Creating degenerate two-dimensional Bose gases with tunable interaction strength

Dissertation
zur Erlangung des Doktorgrades
an der Fakultät für Mathematik, Informatik
und Naturwissenschaften
Fachbereich Physik
der Universität Hamburg

vorgelegt von
Alexandra Mozdzen

Hamburg
2024

Gutachter der Dissertation	Prof. Dr. Henning Moritz
	Prof. Dr. Klaus Sengstock
Zusammensetzung der Prüfungskommission	Prof. Dr. Michael Potthoff
	Prof. Dr. Henning Moritz
	Prof. Dr. Klaus Sengstock
	Prof. Dr. Ludwig Mathey
	Prof. Dr. Ralf Riedinger
Vorsitzender der Prüfungskommission	Prof. Dr. Michael Potthoff
Datum der Disputation	04.09.2024
Vorsitzender des Fach-Promotionsausschusses Physik	Prof. Dr. Markus Drescher
Leiter des Fachbereichs Physik	Prof. Dr. Wolfgang J. Parak
Dekan der Fakultät MIN	Prof. Dr.-Ing. Norbert Ritter

Abstract

This thesis describes the experimental realisation of versatile and highly controllable quantum systems with ultracold quantum gases with the aim to study quantum many-body physics.

In the first part we present the implementation of mesoscopic Fermi-Hubbard-type systems with potassium-40 in a bottom-up approach employing optical tweezers. The experimental setup features an in-vacuo microscope objective with a numerical aperture of 0.75 enabling high-resolution imaging, and allows for tunable interaction strengths via Feshbach resonances as well as for rapid repetition rates due to all-optical cooling schemes. However, reaching quantum degeneracy via Raman-sideband cooling turned out to be very challenging. The achieved 3D ground state fractions of $\sim 40\%$ is not sufficient to make the study of quantum physics in the Hubbard model feasible.

In the main part of the thesis we discuss how the experimental setup was re-designed and re-built in order to create two-dimensional bosonic bulk systems with potassium-39. The key feature is the rare combination of highly tunable interaction strengths via a variety of intra- as well as interstate Feshbach resonances with the ability to study spin mixtures with high-resolution imaging. We have been able to realise a three-dimensional quasi-pure Bose-Einstein condensate of $\sim 5 \cdot 10^3$. The sample is then brought into the quasi-two-dimensional regime by first pre-shaping it with a light sheet-like trap and then transferring it into a single layer of a blue-detuned optical lattice. As a result a degenerate two-dimensional Bose gas of $\sim 3 \cdot 10^3$ with a temperature of $\sim 50\,\mathrm{nK}$ corresponding to $\sim 0.2\,T_{\mathrm{BKT}}$ is created, where T_{BKT} is the BKT critical temperature. Finally, we discuss how 2D quantum droplets might be realised with the setup.

Zusammenfassung

Die vorliegende Arbeit beschreibt die experimentelle Umsetzung vielseitiger und hochgradig kontrollierbarer Quantensysteme mithilfe ultrakalter Quantengase mit dem Ziel, Quanten-Vielteilchenphysik zu untersuchen.

In dem ersten Teil wird die Realisierung von mesoskopischen Fermi-Hubbard-Systemen mit Kalium-40 in einem Bottom-up Ansatz unter Verwendung optischer Pinzetten vorgestellt. Eine der Hauptkomponenten des Aufbaus ist ein im Vakuum platziertes Mikroskopobjektiv mit einer numerischen Apertur von 0,75, welches hochauflösende Abbildungen erlaubt. Der experimentelle Aufbau ermöglicht es zudem, die Wechselwirkungsstärke mithilfe von Feshbach-Resonanzen durchzustimmen sowie durch die Verwendung rein optischer Kühltechniken hohe Wiederholungsraten zu erreichen. Es hat sich jedoch als sehr schwierig erwiesen, mithilfe von Raman-Seitenbandkühlen Quantenentartung zu erreichen. Die erzielte Besetzungswahrscheinlichkeit des 3D Grundzustandes von $\sim 40\%$ ist nicht ausreichend, um die Untersuchung quantenphysikalischer Phänomene im Rahmen des Hubbard-Modells zu ermöglichen.

In dem Hauptteil dieser Arbeit wird erörtert, wie der experimentelle Aufbau umgebaut wurde, um zweidimensionale bosonische Bulk-Systeme mit Kalium-39 zu erzeugen. Das Hauptmerkmal ist die seltene Kombination aus hochgradig durchstimmbaren Wechselwirkungsstärken mithilfe einer Vielzahl an Feshbach-Resonanzen sowohl zwischen gleichen als auch zwischen verschiedenen Spinzuständen mit der Möglichkeit Spinmischungen zu untersuchen und mit hoher Auflösung abzubilden. Es ist uns gelungen, ein dreidimensionales Bose-Einstein-Kondensat aus $\sim 5 \cdot 10^3$ Atomen zu realisieren. Die Atomwolke wird dann in das quasi-zweidimensionale Regime überführt, indem sie mit einer stark anisotropen Dipolfalle vorgeformt und dann in eine einzelne Schicht eines blau-verstimmten optischen Gitters eingeladen wird. Dadurch wird ein entartetes zweidimensionales Bosegas aus $\sim 3 \cdot 10^3$ Atomen mit einer Temperatur von $\sim 50\,\mathrm{nK} \simeq 0.2\,T_{\mathrm{BKT}}$ erzeugt, wobei T_{BKT} der BKT kritischen Temperatur entspricht. Schließlich diskutieren wir, wie 2D Quanten-Droplets mit diesem Aufbau realisiert werden könnten.

Contents

Chapter 1

Introduction

Over the last decades, ultracold quantum gases of neutral atoms have established themselves as one of the major tools to study quantum many-body physics. These isolated, defect-free systems exhibit intrinsic long time and length scales compared to e. g. solid-state systems and have evolved into a versatile and highly controllable platform for e. g. quantum simulations of strongly correlated physics, thanks to groundbreaking milestones and innovations.

A fundamental milestone was the first realisation of Bose-Einstein condensation in dilute quantum gases in 1995 [1, 2], a phase transition solely driven by particle statistics. Reaching quantum degeneracy laid the foundation for studying quantum phenomena where the particle statistics play a fundamental role. In 1999 degeneracy was also achieved for fermionic quantum gases [3] and nowadays, a variety of fermionic and bosonic species are utilised.

The next important accomplishment was the realisation of the first dual-component Bose-Einstein condensate in 1997 by employing two different spin states [4]. The ability to create mixtures allows to increase the complexity of the system which gives rise to new phenomena [5] like different zero-temperature phases [6] or even novel liquid-like states of matter [7, 8]. Mixtures can be prepared with different spin states, different isotopes, or different atomic species which also allows to realise Bose-Fermi mixtures [9, 10].

The achievement of tunable interaction strengths in ultracold gases via Feshbach resonances [11] was another breakthrough: Since their first observation in a Bose-Einstein condensate in 1998 [12, 13] Feshbach resonances have developed into a well-established tool to tune the interaction strength between weakly and strongly interacting, and even to switch between repulsive and attractive interactions. Although not every atomic species exhibits Feshbach resonances suitable for tuning interactions, this feature had a significant impact on the field of ultracold quantum gases as it greatly increases the control

over the system. Feshbach resonances were crucial to reach the strong-coupling regime in 2000 [14], and to observe phenomena like the famous BEC-BCS crossover in 2004 [15–18].

The versatility of ultracold quantum gases is also a consequence of the flexibility given by the optical confinement. Since the first optical confinement of a Bose-Einstein condensate in 1998 [19], huge progress has been made in terms of the potential shaping, not only allowing to study both bulk systems as well as lattice systems [20], but also to change the dimensionality of the system. This gave access to numerous new phases and phenomena such as the realisation of a Tonks-Girardeau gas in one dimension [21, 22] and the observation of the celebrated BKT transition in two dimensions [23].

A new level of precision was achieved with the implementation of microscope objectives. In 2009, the first quantum gas microscope demonstrated single-site resolution in optical lattices [24] and also for bulk systems microscope objectives with high numerical aperture provide unprecedented accuracy for the observation and also manipulation of ultracold quantum gases.

In the experimental work presented in this thesis, we combine these features in order to create highly controllable quantum systems that can be imaged with high spatial resolution.

In chapter 2 we present progress in the early stages of the experimental work and discuss the possibility to realise mesoscopic Fermi-Hubbard systems with K40. This species features multiple suitable spin states with tunable interstate interaction strengths via magnetic Feshbach resonances. Section 2.1 and 2.2 provide an overview of the experimental apparatus built in the course of a previous dissertation [25]. This setup features an in-vacuo microscope objective with high numerical aperture allowing for high-resolution imaging and allows to prepare ultracold fermionic gases. In section 2.3, building on this previous work, we motivate and discuss our work towards an implementation of small, degenerate Fermi-Hubbard-like systems. However, Raman sideband cooling to the vibrational ground state turned out to be very challenging and we did not achieve sufficient ground state fractions to make studying Hubbard systems feasible.

The subsequent main part of this thesis focusses on the realisation of degenerate two-dimensional bosonic bulk systems with K39. The setup combines the ability to prepare spin mixtures with tunable interactions with high resolution imaging and the possibility to reduce the dimensionality and hence represents a promising platform to gain new insights into many-body phenomena.

In chapter 3 and 4 we describe how the experimental setup was re-designed and rebuilt in order to switch from small fermionic tweezer systems to two-dimensional bosonic

bulk systems. In chapter 3 we discuss the realisation of a three-dimensional Bose-Einstein condensate, while chapter 4 focusses on entering the quasi-two-dimensional regime.

Chapter 5 proceeds with the presentation of scientific perspectives, starting with an overview of previous work on two-dimensional bosonic bulk systems with atomic Bose-Einstein condensates. Next, some particularly interesting quantum phenomena that can be studied with Bose mixtures are presented, especially focussing on the potential realisation of two-dimensional quantum droplets in our experimental setup. Finally, chapter 6 provides a conclusion and outlook.

Chapter 2

Creating mesoscopic fermionic systems

In this chapter we will discuss the preparation of small tweezer systems with fermionic potassium. The chapter is divided into two parts.

In the first part we will describe the experimental setup that was designed and built in the course of a previous dissertation [25]. We will present the main components of the apparatus whose key feature are two in-vacuo twin microscope objectives with high numerical aperture that enable a high spatial resolution, both for manipulating as well as for imaging the atomic sample. We will then give an overview of the experimental sequence from generating an atomic beam to trapping atoms in an optical lattice or crossed dipole trap with a temperature of $\sim 25\,\mu\mathrm{K}$. Unless stated otherwise, this part is mostly a partial summary from [25].

In the second part we will focus on our work towards the preparation of Fermi-Hubbard-like systems following a bottom-up approach. First, we will briefly provide research perspectives that motivated us to pursue the investigation of small Fermi-Hubbard-like systems. Then, building on the experimental sequence presented in the first part, we will discuss the technical realisation of these systems. We will mainly focus on our efforts towards reaching the vibrational ground state via Raman-sideband cooling which turned out to be very challenging. In a tweezer array we achieved a 3D ground state fraction of $\sim 40\,\%$ which is not sufficient to efficiently perform experimental studies.

2.1 An apparatus for high resolution imaging and probing of potassium

This section provides a brief overview of the main technical parts of the apparatus. It was designed and set up in the course of a previous dissertation [25] and no significant

changes were made to the vacuum system and the coil assembly. The laser system on the other hand has been improved and expanded over the course of this work. The main changes are marked as such, but not further elaborated here. Details on them will be given in later chapters, the respective references are provided.

2.1.1 Vacuum system

The complete vacuum system of the experiment is shown in fig. 2.1. It can be roughly divided into three sections: the main chamber, the oven and 2D MOT section and the UHV pumping section.

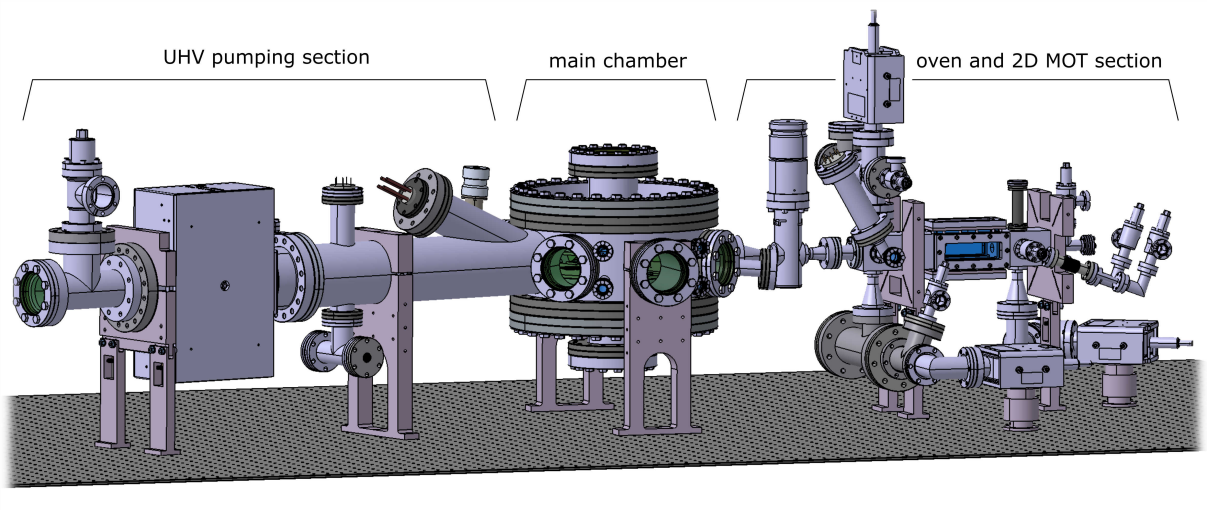

Figure 2.1: Overview of the complete vacuum system of the experiment. The core part is the main chamber in which the degenerate quantum systems are prepared. The key component is a pair of two high-resolution microscope objectives located inside the vacuum. Optical access is provided by eight large as well as several smaller viewports. Furthermore, the main chamber features two in-vacuo antennas allowing to drive RF transitions between the F- and m_F-states. On the right side the main chamber is connected to the oven and 2D MOT section which contains both a K39 as well as an enriched K40 sample. The atoms are transferred to the main chamber in form of an atomic beam created by a 2D MOT. The UHV pumping section shown in the left ensure a low pressure of $\sim 2 \times 10^{-11}$ mbar in the main chamber. Adapted from [25].

Main chamber The main chamber is the core part of the vacuum system. Here, the atomic quantum systems are prepared and investigated. The key components are the in-vacuo high resolution twin microscope objectives enabling the creation of single atom tweezers, single-site addressability and single-site resolution imaging. The microscope objectives share the same housing, but facing opposite directions such that they have a common focal plane. Placing the microscope objectives inside the vacuum chamber circumvents the need to compensate aberrations from the viewport windows and greatly

simplifies the adjustment. It furthermore allows to place the microscope objectives closer to the atoms making it possible to achieve an effective focal length of 20 mm and especially a high numerical aperture of 0.75. Drawback of the in-vacuo microscope objectives is the necessity to use a large steel main chamber: the base flange is an CF300 flange with a corresponding outer diameter of 355.6 mm.

Another implication of the microscope objectives is to split the science position, where the desired quantum systems are created and studied, from the MOT position in order to achieve reasonably large MOT beams which also improves the optical access. Both science and MOT position are located inside the main chamber separated by a short distance of 4 cm.

Optical access to MOT and science position is provided mainly by six CF63 viewports with an outer diameter of 114.3 mm in the horizontal plane, two CF100 viewports with an outer diameter of 152.4 mm as well as several smaller viewports with a small angle to the horizontal plane as can be seen in fig. 2.1.

Additionally, the main chamber features an RF- as well as a microwave antenna. Placing them inside the vacuum chamber ensures a reasonable signal strength at the atom position. Apart from the fact that the sheer spatial distance due to the size of the vacuum chamber reduces the amplitude, the chamber also shields the atoms from antennas outside the chamber as it acts as a Faraday cage. The RF-antenna is essentially a coil with 31 windings printed on a circuit board and was intended to drive transitions between different m_F-states of the ground state manifold.[1] The microwave antenna is a single-loop coil with a large surface area resulting in a low surface resistance in order to achieve large magnetic fields.[2] The microwave antenna was intended to enable transitions between the F-states of the ground state manifold. However, after switching to the bosonic isotope K39 the microwave antenna was also used for the transitions between the m_F-states.

Oven and 2D MOT section In the oven and 2D MOT section the atomic beam is created that is used to load the 3D MOT. It has two separate ovens: one with a K39 sample and one with an enriched sample for K40.[3] Each oven section has an individual valve in order to be able to switch between the atom sources. The 2D MOT chamber features four large rectangular windows allowing for highly elliptical 2D MOT beams. Additionally, there is a small viewport along the axis towards the main chamber to allow for a 'push beam' (see sec. 2.2). A differential pumping stage ensures a high vapour pressure inside

[1] Details on the antenna design can be found in [26].

[2] The design was inspired by [27].

[3] In principle the enriched sample could also be used for K39, but since it is quite expensive it makes sense to use a separate, less expensive sample for K39.

the oven sections to achieve acceptable loading rates while still maintaining a low pressure in the main chamber. The oven and 2D MOT section is separated from the main chamber by a mechanical shutter in order to make maintenance easier.

UHV pumping section The purpose of the UHV pumping section is to ensure a low pressure of $\sim 2 \times 10^{-11}$ mbar in the main chamber in order to achieve a vacuum lifetime in the order of 95 s. This section is not involved in the experimental sequence.

2.1.2 Magnetic coils

There are four main sets of coils which are depicted in fig. 2.2: The MOT coils and the experiment coils, capable of generating high magnetic fields for trapping and tuning interactions, and the Raman coils and the Bias coils to provide quantisation and offset fields.

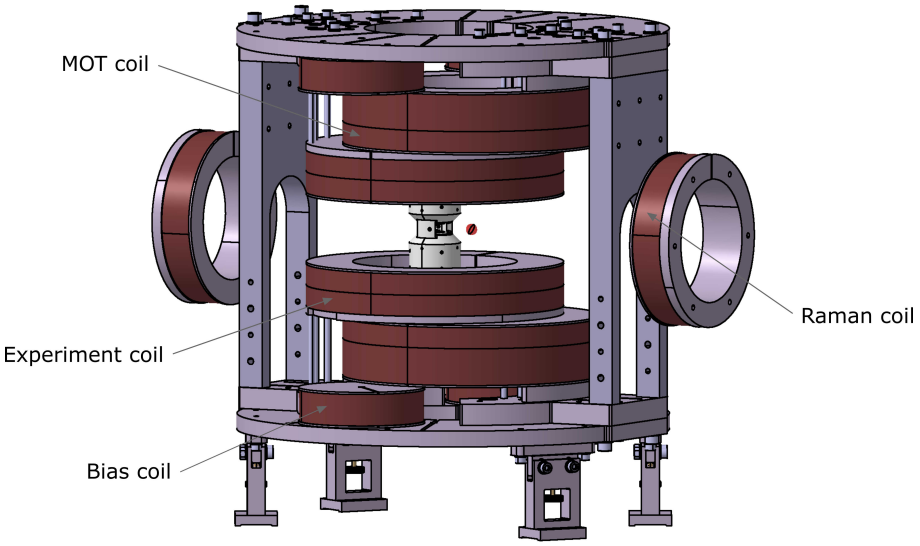

Figure 2.2: Overview of the main coil assembly. The coils are mounted outside the main vacuum chamber. For more clarity the main chamber is not included in the picture. The MOT position is indicated by the red sphere. The science position next to it is surrounded by the white housing of the microscope objectives. The MOT coils and the experiment coils are mainly used for trapping. The experiment coils furthermore provide sufficient magnetic field strength to exploit suitable Feshbach resonances. The Raman coils and the Bias coils address orthogonal horizontal axes and generate much smaller fields, mainly employed as quantisation fields and for alignment. Adapted from [25].

MOT coils The MOT coils are a pair of vertically oriented coils centered around the MOT position. The current direction can be switched for the upper coils such that the MOT coils can be used both in Helmholtz and Anti-Helmholtz configuration. Their main

purpose is to provide the magnetic gradient for the MOT as well as for the magnetic trap that is used to transport the atoms from MOT to science position.

experiment coils The experiment coils are very similar to the MOT coils, also vertically oriented, but centered around the science position. They can be used in Helmholtz and Anti-Helmholtz configuration as well, but since they are closer to the atoms, they can create a higher magnetic field in the atoms plane than the MOT coils. Their main purpose is to create the magnetic gradient for the magnetic trap required for the transport as well as to provide the magnetic field for tuning interactions via Feshbach resonances.

Raman coils The Raman coils are a pair of coils that are oriented perpendicular to the MOT and the experiment coils. They are aligned with the so-called transport axis, i. e. the axis defined by MOT and science position. Both coils have the same current direction and create much weaker fields than MOT and experiment coils. The main purpose is to provide a quantisation axis along the transport axis for optical pumping, imaging and Raman cooling.

Bias coils The Bias coils are intended to provide a magnetic field along the horizontal axis perpendicular to the transport axis. The 2D MOT section and the UHV pumping section of the vacuum system prevent to use the same geometry as for the Raman coils, therefore the Bias coils employ a different design using four coils. The current direction can be set individually for each of these coils allowing to create both offset as well as gradient fields.

2.1.3 Laser system

The two main transitions of potassium are the D1 line at 770.1 nm and the D2 line at 766.7 nm as shown in fig. 2.3, which we mainly utilise for cooling, manipulating and imaging the atoms. For trapping potentials we additionally employ far detuned light at 850 nm, 1064 nm and 532 nm along several axes. The main laser axes are sketched in fig. 2.4.

D2 transition Our D2 laser system is mainly used for the realisation of a 2D and 3D MOT as well as for absorption imaging. Since the MOT scheme requires to address both a cooling as well as a repumping transition, we employ two D2 lasers: The so-called repumper laser is locked to a vapour cell via modulation transfer spectroscopy and is used

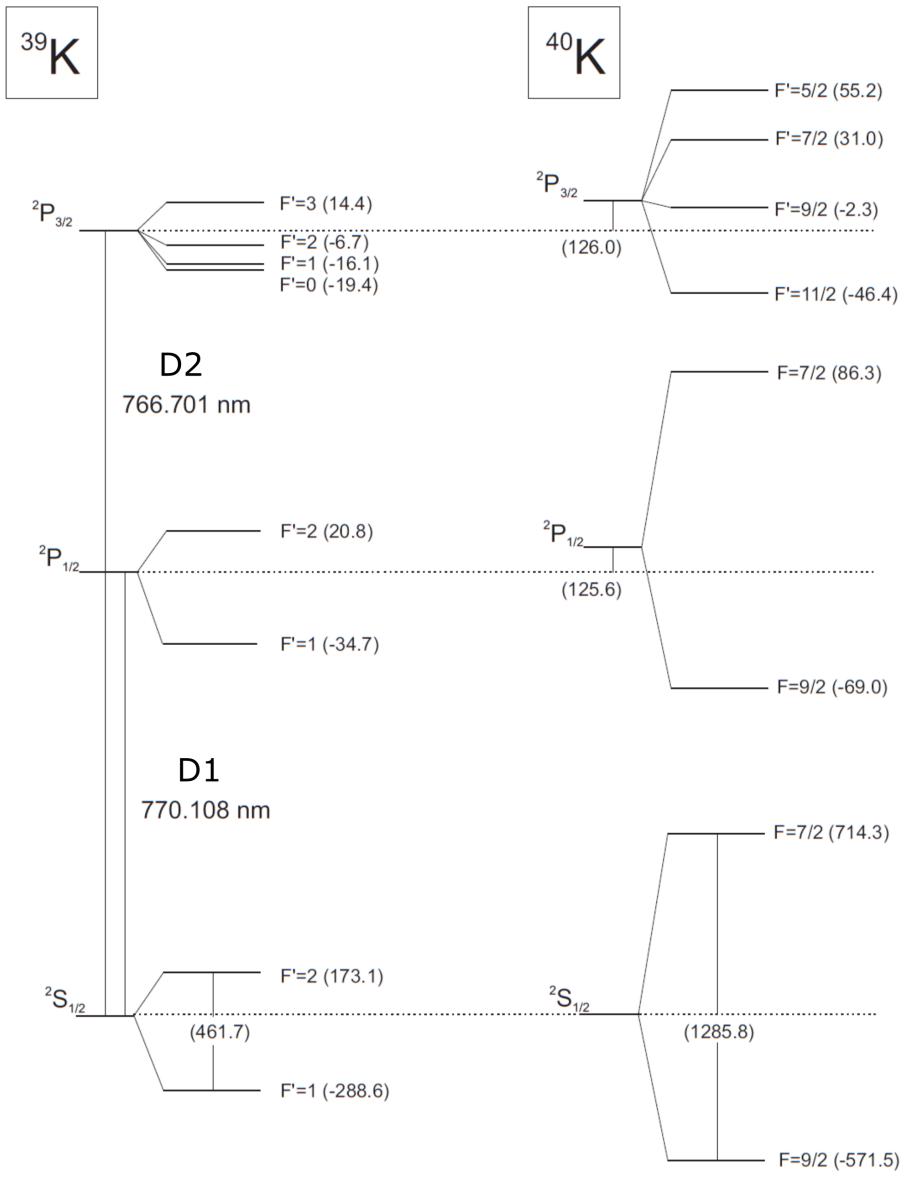

Figure 2.3: Level schemes of K39 and K40. The hyperfine splittings are given in units of MHz. The main transitions are the D1 transition $|4^2S_{1/2}\rangle \leftrightarrow |4^2P_{1/2}\rangle$ and the D2 transition $|4^2S_{1/2}\rangle \leftrightarrow |4^2P_{3/2}\rangle$. Noteworthy are the tight level spacing, especially for K39, and the inverted level structure of K40. More details on the optical properties are given in sec. 3.1.2. Adapted from [28].

to lock the so-called cooler laser via a beat lock.[4] Both lasers address the atoms in the 2D MOT cell (see fig. 2.1) along two orthogonal axes as well as the MOT position in the main chamber along three axes, each retro-reflected to form a proper MOT configuration. The cooler laser can also be applied to the science position along every main axis, mainly to enable absorption imaging for alignment and diagnostics. Additionally, there is an auxiliary D2 beam, the so-called push beam, roughly along the axis defined by 2D MOT and 3D MOT position that allows to transfer momentum to the atomic beam created in the 2D MOT section in order to increase the 3D MOT loading rate.

Note that the difference in the transition frequencies for K39 and K40 can be compensated via an AOM and a different selection of the locking slope of the beat lock such that the D2 laser system is suitable for creating both a K39 as well as a K40 MOT with just minor manual adjustments.

D1 transition The D1 transition is mainly used for molasses cooling, optical pumping and fluorescence imaging. We employ three D1 lasers: The so-called D1 reference laser that solely serves as a frequency reference, the so-called molasses laser mainly used for molasses cooling and the so-called D1 pump laser mainly used for optical pumping. The molasses laser can be modulated via an EOM in order to add a D1 repumping transition for the molasses scheme. Both the molasses and the D1 pump laser are locked to the D1 reference laser via a beat lock while the D1 reference laser is locked to a vapour cell. The locking scheme used to rely on doppler-free absorption spectroscopy, but was rebuilt to a modulation transfer spectroscopy in the course of this thesis. D1 light can be applied along every main axis, in most cases retroreflected beams, in order to enable molasses-like schemes at MOT and science position as well as fluorescence imaging. Along the transport axis, the D1 light is mainly employed for optical pumping and is not retro-reflected.

850 nm 850 nm light is employed to create trapping potentials. It is only applied at the science position along three orthogonal axes, including retroreflectors such that both running wave trap as well as lattice configuration can be realised. The horizontal beams have a Gaussian beam waist of $\sim 30\,\mu m$, the vertical beam a waist of $\sim 50\,\mu m$. The maximal radial trapping frequency is $\sim 1\,kHz$ ($\sim 0.5\,kHz$) for horizontal (vertical) beam(s), the corresponding trap depths are $\sim 100\,\mu K$ ($\sim 30\,\mu K$). While the lattices can be a convenient tool for alignment and diagnostics, we mainly employ the horizontal beams in running wave configuration as a crossed dipole trap in the experiment. Additionally, there used to

[4] For details on the D2 laser system and the locking techniques see [25, 29].

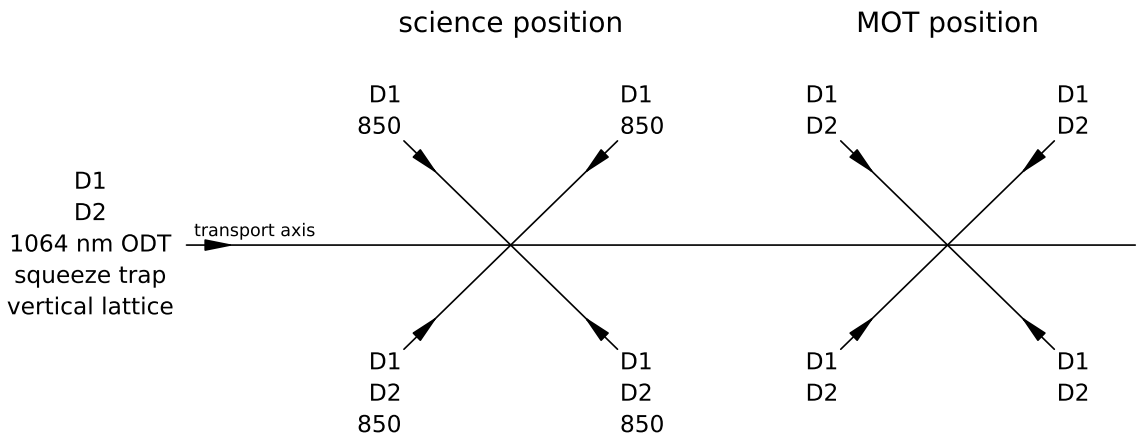

Figure 2.4: Sketch of the main laser axes from top view. Not depicted are the vertical axes both for science and MOT position along which D1 and D2 light can be applied. Additionally, a retroreflected 850 nm beam is implemented along the vertical axis of the science position. MOT and science position are separated by 4 cm and are located in the main chamber.

be an array of 2x2 optical tweezers along the vertical axis that was removed in the course of this thesis. Details on these traps can be found in sec. 2.3.1.

1064 nm The 1064 nm light is used for trapping the atoms. There are two separate optical traps at 1064 nm: the so-called 1064 nm ODT and the so-called squeeze trap which were both set up in the course of this thesis.

The 1064 nm ODT is a deep optical dipole trap at the science position and employed for the collisional loading scheme discussed in sec. 3.6. It has waists of 14.5 µm x 17.0 µm corresponding to a Rayleigh range of ~ 620 µm. The full trap depth is ~ 6 mK, the radial trapping frequencies are 25 kHz and 19 kHz, the axial trapping frequency is 350 Hz. The beam axis has a 5° angle to the transport axis in the horizontal plane.

The squeeze trap is a highly anisotropic dipole trap also at the science position, aligned with the transport axis and part of the setup for the 2D confinement. The squeeze trap will be discussed in detail in chapter 4.

532 nm The purpose of the 532 nm light is to create the so-called vertical lattice at the science position and was also set up in the course of this thesis. The vertical lattice is formed by two interfering beams with a vertical angle of 10° with respect to each other, while the beams are horizontally aligned with the transport axis. The vertical lattice provides the 2D confinement and will be discussed in detail in chapter 4.

2.1.4 Imaging system

One of the key components of the experimental setup are the in-vacuo high-resolution microscope objectives. The high NA of 0.75 allows for a spatially resolved imaging along the vertical axis both with absorption imaging via the D2 transition and fluorescence imaging typically performed on the D1 transition. The corresponding diffraction-limited resolution for the imaging wavelengths of $\sim 767\,\mathrm{nm}$ (D2) and $\sim 770\,\mathrm{nm}$ (D1) is $\sim 0.62\,\mu\mathrm{m}$.

The imaging system consists of two telescopes. The first telescope is formed by one of the microscope objectives and a 2" achromat with a focal length of $f = 1000\,\mathrm{mm}$. The long focal length is chosen due to the large steel chamber and in order to improve the optical access. The microscope objective has an effective focal length of 20 mm, which yields a magnification of the telescope of 50. The diffraction-limited resolution of $\sim 0.62\,\mu\mathrm{m}$ then corresponds to $31\,\mu\mathrm{m}$ behind the first telescope while the employed sCMOS camera features a pixel size of $6.5\,\mu\mathrm{m}$. Placing the camera in the imaging plane of the first telescope would therefore result in a very weak signal. In order to improve the signal-to-noise ratio we employ a second telescope which de-magnifies the imaging beam. It consists of an $f = 500\,\mathrm{mm}$ and an $f = 150\,\mathrm{mm}$ achromat corresponding to a magnification of 0.3, resulting in a total magnification of the imaging system of 15. Thus, the pixel size of $6.5\,\mu\mathrm{m}$ of the camera translates to a effective pixel size of $0.43\,\mu\mathrm{m}$ at the atom plane which roughly matches the diffraction-limited resolution. This increases the signal-to-noise ratio while still maintaining the high spatial resolution as the effective pixel size is slightly smaller than the diffraction-limited resolution.

Furthermore, the experimental setup features auxiliary imagings along every main axis of the science position denoted in fig. 2.4 as well as an additional auxiliary imaging addressing the MOT position. The auxiliary imagings are mostly intended for absorption imaging due to their low NA < 0.07,[5] and are mainly for alignment and diagnostic purposes.

2.2 Overview of the experimental sequence for K40

In this section we briefly discuss the experimental sequence to prepare ultracold K40 atoms in optical traps aiming towards mesoscopic Fermi-Hubbard systems. As small system sizes are associated with an increased need for repetitions, the sequence focusses on short cycle times. We employ all-optical cooling methods which allows to reduce the cycle

[5]The MOT as well as the magnetic trap that are discussed later can be imaged via fluorescence imaging since their atom number is high enough to emit sufficient photon numbers despite the low collection efficiency of the auxiliary imagings.

time by an order of magnitude to $< 2\,\mathrm{s}$ compared to conventional approaches employing evaporative cooling, thus ensuring a rapid repetition rate. The main steps are the initial trapping in a 3D MOT followed by a grey molasses scheme, a magnetic transport from the MOT position to the so-called science position in between the microscope objectives (see sec. 2.1.1) where the atoms are loaded into an optical trap, and finally a Raman sideband cooling scheme to achieve degeneracy.

In the following we provide a brief overview of the experimental steps to obtain ultracold atoms in optical traps. A more detailed discussion of these steps can be found in [25, 29]. The final cooling step, i. e. Raman sideband cooling in optical tweezers, was implemented in the course of this work and will be discussed in sec. 2.3.

- The first step is the generation of an atomic beam via a 2D MOT [30, 31]. Therefore, the oven section, containing the potassium sample, is heated to $\sim 60°\mathrm{C}$ in order to create an atomic vapour which serves as an atom source. The 2D MOT, realised by a static quadrupole field and two orthogonal retroreflected D2 beams, then cools and traps the atoms along two axes, while they can still freely move along the third axis, i. e. towards or away from the main chamber. By applying a so-called D2 push beam along the third axis, the atomic flux towards the main chamber can be increased by one order of magnitude. The push beam furthermore reduces the atom number fluctuation in the following step.

- After reaching the main chamber the atoms are trapped via a 3D MOT [32]: Six circularly polarised, slightly red-detuned D2 beams in combination with a magnetic gradient field create a spatially and velocity dependent radiation force that traps the atoms. Additionally applying near-resonant, blue-detuned D1 light along the same axes reduces the density and leads to a significant increase of the MOT capacity [33] resulting in a maximum loaded atom number of $\sim 3 \cdot 10^7$ with a loading rate of $\sim 7 \cdot 10^6\,\mathrm{s}^{-1}$. The temperature is limited by the Doppler temperature of $\sim 145\,\mu\mathrm{K}$.

- To further cool the atoms a Λ-enhanced grey molasses scheme[6] [36–38] is applied: A Sisyphus cooling mechanism and motionally coupled bright and dark states allow to reach temperatures below the Doppler limit. Note, though, that the molasses cooling scheme exerts no trapping force. This cooling scheme requires a periodic modulation of the polarisation, which is provided by six counter-propagating, circularly polarised, near-resonant D1 beams[7], as well as degenerate m_F-states, i. e. the

[6] A detailed explanation of this scheme can be found in [34, 35].

[7] In principle a grey molasses scheme can also be performed on the D2 transition. In the case of potassium the D2 hyperfine splitting is too narrow to allow for an efficient molasses scheme, though.

absence of magnetic fields. In practice, the magnetic quadrupole field of the previous 3D MOT scheme has a decay time in the order of $\sim 20\,\mathrm{ms}$, though. However, the configuration of the D1 molasses beams, i. e. polarisation and sign of the detuning, is suitable to form a blue-detuned MOT [39] when combined with a quadrupole field. This enables a smooth transition between MOT and grey molasses via a blue MOT which results in higher densities after the grey molasses as the atoms are both cooled and trapped during the decay of the magnetic field. With this cooling step temperatures of $\sim 10\,\mu\mathrm{K}$ are achieved.

- In the next step the atoms are magnetically transported from the MOT position to the science position over a distance of $\sim 4\,\mathrm{cm}$. Therefore, the atoms are optically pumped into the magnetically trapped $|^2S_{1/2}, F = 9/2, m_F = 9/2\rangle$ ground state by applying resonant D1 light and subsequently captured in a magnetic trap created by the MOT coils. The actual transport is then performed by ramping down the gradient field of the MOT coils while simultaneously ramping up a gradient field created by the experiment coils and thus shifting the magnetic trap from the MOT position to science position. The transport is smoothened by using a $\cos^2$- ($\sin^2$-) shaped ramp for the MOT (experiment) coils in order to reduce heating.

- At the science position the atoms are loaded from the magnetic trap into the final optical trap, i. e. either a crossed dipole trap, an optical lattice or into optical tweezers, via a D1 assisted loading scheme: the optical potential is ramped up, blue-detuned D1 light in molasses configuration is applied for $\sim$15 ms while its intensity is linearly decreased and subsequently the magnetic trap is adiabatically ramped down. With this loading scheme $\sim 2 \cdot 10^5$ atoms are loaded into the lattice, $\sim 5 \cdot 10^4$ atoms into the crossed dipole trap, each with a temperature of $\sim 25\,\mu\mathrm{K}$.

2.3 Realising small Fermi-Hubbard systems

The Fermi-Hubbard model is one of the simplest microscopic model of electrons in a solid state system [40]. As it is based on the tight-binding model the Fermi-Hubbard model essentially describes localised fermions in a lattice potential. The Hamiltonian consists of only two terms: a kinetic term, i. e. tunnelling of the particles between the lattice sites described by the tunnelling parameter t, and a potential term, corresponding to an on-site energy term U due to interacting particles on the same lattice site. Despite being conceptually simple, it rapidly becomes more difficult to solve theoretically with increasing system size since the Hilbert space grows exponentially with the number of

lattice sites. Hence, neutral atoms in optical lattices, featuring a high degree of control over t and U, prove highly useful as quantum simulators for Hubbard systems.

In contrast to quantum gas microscopes where large number of atoms are trapped in optical lattices we were focussing on a bottom-up approach: keeping the single site addressability and single site imaging, but generating small flexible potentials that are assembled site by site by using optical microtraps. The tunnelling parameter t can be controlled by changing the shape of the potential while a Feshbach resonance allows to tune the onsite interaction U. Starting from the smallest instances, where the observed dynamics can be compared to theoretic solutions to validate and calibrate the experiment, the system size and thus the complexity can then be gradually increased to observe how many body effects emerge.

The flexible potential geometry enables to easily implement different tunnelling rates between different pairs of neighbouring sites. This is of particular interest for the study of topological systems such as the Su-Schrieffer-Heeger model [41] where topologically protected states are localised on the edges of a one dimensional chain of lattice sites with alternating tunnel coupling strength [42]. By extending the potential to ladder type systems and modulating the positions of the lattice sites, even complex tunnelling can be introduced. This gives rise to artificial gauge fields [43] which would allow to implement and study for example the Harper-Hofstadter model [44–47].

Another exciting research direction arises when considering the t,t' Hubbard model which includes not only nearest-neighbour tunnelling t, but also next-nearest neighbour tunnelling t'. Within this model a plaquette, i. e. 2×2 lattice sites, features a quantum critical point where a crossing of the ground state energies of atom number $N = 2, 3, 4$ occurs, suggesting that the plaquette is the fundamental building block for d-wave superconductivity. [48]

To be able to generate such a plaquette potential we started out with four sites. Each site is created by an individual optical tweezer [49–51], i. e. an optical microtrap, providing a nearly harmonic potential. The experimentally critical part is to cool the atoms to the motional ground state of these potentials in order to achieve a quantum degenerate system. To ensure a high repetition rate we employ an optical cooling scheme, i. e. Raman sideband cooling, to remove all motional quanta of the atom in the tweezer [52–54]. While we achieved ground state fractions close to 90% in a 1D lattice[8] with this cooling technique, it turned out that we did not achieve high enough ground state fractions in the tweezer potentials to efficiently perform experimental studies, especially

[8]The 1D lattice was used to set up and pre-optimise the Raman sideband cooling scheme since the larger atom number exhibits a larger signal and requires less statistics.

considering increasing system sizes.

Nonetheless, in the following we will give some details on the creation of the tweezer potentials, the detection of atoms in tweezers and on Raman sideband cooling in a tweezer.

2.3.1 Creating and loading into the tweezer potentials

Initially, we set up four optical tweezers, i. e. four tightly focussed optical dipole traps, the minimum required to investigate the quantum critical point in the t,t' Hubbard model.[9] Each tweezer is created by an individual laser beam that is focussed down to a waist of $\sim 0.7\,\mu\text{m}$ by one of the two high NA microscope objectives, where the beam angle on the objective determines the tweezer position. In our setup the four beams are completely independent which allows to independently set position and depth of each tweezer, giving full control over each site and thus also full flexibility on the geometry.[10] Details on the plaquette potential and its stability can be found in [55].

The atoms are loaded into the tweezers with the D1 assisted loading scheme briefly described in sec. 2.2 with a small adaption: The size of the tweezer potentials is on the same length scale as the interference pattern of the molasses beams. To avoid a spatial dependence of the loading efficiency the position of the interference pattern is modulated by 'shaking' the retro-reflectors of the molasses beams via a piezo [53]. With this scheme one or zero atoms are loaded into each tweezer with a loading probability of 50%: Due to light-assisted collisions atoms scatter pairwise out of the tweezer. Odd initial numbers result in one atom in the tweezer, even initial numbers result in an empty tweezer.[11]

2.3.2 Tweezer detection

To detect whether a tweezer is occupied or not the atom needs to be imaged via fluorescence imaging. Conveniently, the Raman sideband cooling process, discussed in the following section, is associated with fluorescence. However, despite the high NA of the microscope objective, not enough photons were collected to get a reliable signal. This is due to a large background signal, probably originating from light that is scattered by the in-vacuo objectives. Instead a molasses imaging scheme proved to be more effective: The atoms are illuminated with D1 molasses light along the x' and y' axis as well as

[9] The setup was designed to allow for a future extension for increasing the system size.

[10] While this is useful for small system sizes, using independent beams becomes impracticable when increasing the systems size since the required laser power scales badly with the number of sites because every additional site requires an additional beamsplitter cube to add the additional laser beam to the setup.

[11] The loading probability can be increased via a 'blue-shielding' scheme [56, 57].

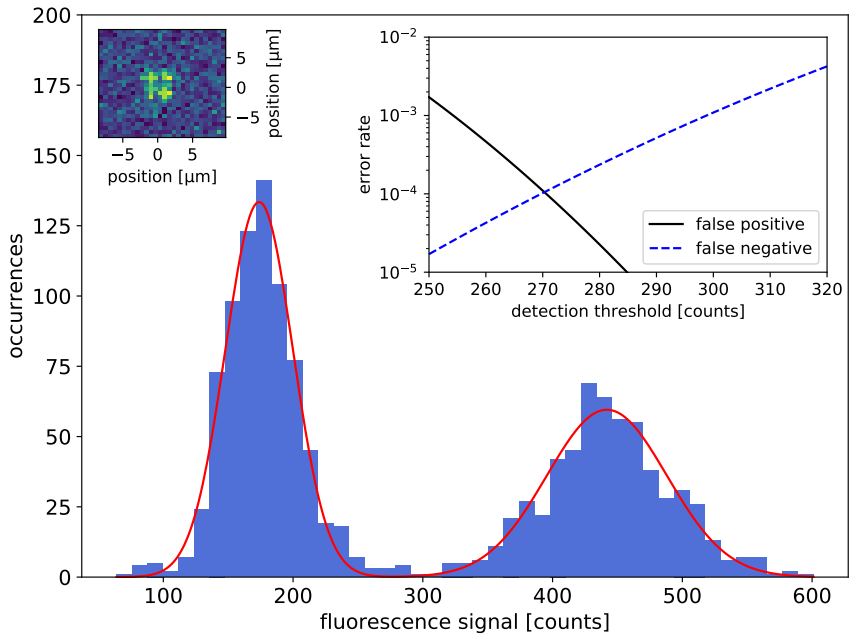

Figure 2.5: Histogram of the detected fluorescence signal when imaging a tweezer via molasses imaging. The left peak corresponds to an empty tweezer, the right peak corresponds to one atom in the tweezer. By fitting the two peaks with a Gaussian (red line) the false positive and false negative error rates can be calculated as plotted in the right inset. The left inset exemplarily shows an image of a plaquette with one atom per site.

D1 F repump light[12] along the transport axis. Thereby, a 2D molasses is formed which yields enough fluorescence to reliably detect the tweezer occupation.[13] A histogram of the collected fluorescence signal in units of camera counts is shown in fig. 2.5. It features two peaks: The left peak is present even when the tweezer potential is disabled. We hence attribute it to dark counts of the camera. The right peak only occurs when properly applying the previously described loading scheme with enabled tweezer potential. Accordingly, we attribute it to the fluorescence of a single atom. The separability of the two peaks depends on the molasses parameters, and only after optimisation the peaks are clearly distinguishable allowing to binarise the signal into an occupation number of zero or one by defining a detection threshold.

To determine the detection fidelity of this scheme one would need to know the true occupation for each fluorescence image. As this is not known, we instead estimate the error rates by modelling the two fluorescence count peaks as Gaussian shaped probability distributions. The false positive (negative) error rate is then derived by calculating the

[12]The repumper for the molasses scheme is modulated onto the molasses beam via an EOM. Therefore, the additional D1 F pump beam along the transport axis is not required for the molasses scheme. However, we experimentally found that it enhances the signal.

[13]We cannot apply a 3D molasses since the third molasses axis equals the imaging axis and hence would saturate the camera.

part of the distribution of the empty (occupied) tweezer that is above (below) the detection threshold. The thereby determined error rates are plotted in fig. 2.5 (right inset). It is apparent that the false positive error rate is particularly low since it has a much higher slope than the false negative error rate. This is due to the fact that the width of the zero atom peak is much lower, i. e. nearly half the width of the atom peak. However, these low false positive error rates are probably too optimistic as the right wing of the zero atom peak shows a slower drop-off than predicted by the Gaussian model. Thus, we conservatively estimate the error rates to be $\lesssim 10^{-3}$. The error rates can be further reduced by defining two different detection thresholds for identifying a site as empty or occupied. This increases the statistical error, though, since every measurement run with a fluorescence signal in between the two thresholds is not taken into account.

2.3.3 Raman sideband cooling

The Raman sideband cooling scheme

To prepare a degenerate quantum system the atoms need to be cooled to the motional ground state of the respective tweezer potential. This can be achieved via Raman sideband cooling[14]. A scheme of the cooling process is depicted in fig. 2.6. The basic idea is to lower the vibrational level by driving a coherent two-photon transition, the so-called Raman transition, that allows to address specific vibrational levels. Thereby, motional quanta can be removed one by one over several iterations until the atom reaches the motional ground state.

The Raman transition requires two Raman beams, both detuned from the D2 line by some ten GHz, that couple the states $|^2S_{1/2}, F = 9/2, m_F = -9/2\rangle$ and $|^2S_{1/2}, F = 7/2, m_F = -7/2\rangle$ via a virtual state indicated in fig. 2.6 by the dotted horizontal line. Due to the state being virtual the Raman transition has a very narrow linewidth allowing to address a single vibrational level $|n\rangle$ of the harmonic potential. The relative detuning of the two Raman beams determines which Δn is addressed. A transition with $\Delta n = 0$ is referred to as carrier transition, transitions with $\Delta n \neq 0$ as sidebands. To be able to drive the sidebands the Raman beams need to transfer a sufficient momentum kick which is why the Raman beams cannot be parallel, but are orthogonal to each other. For increasing $|\Delta n|$ the overlap of the wave functions decreases which makes transitions with $|\Delta n| > 1$ inefficient. Therefore, only one motional quantum per iteration is removed.

The Raman transition is a coherent transition and hence leads to Rabi oscillations between the states $|^2S_{1/2}, F = 9/2, m_F = -9/2, n\rangle$ and $|^2S_{1/2}, 7/2, -7/2, n-1\rangle$. To break

[14] A detailed explanation of Raman sideband cooling can be found in [58].

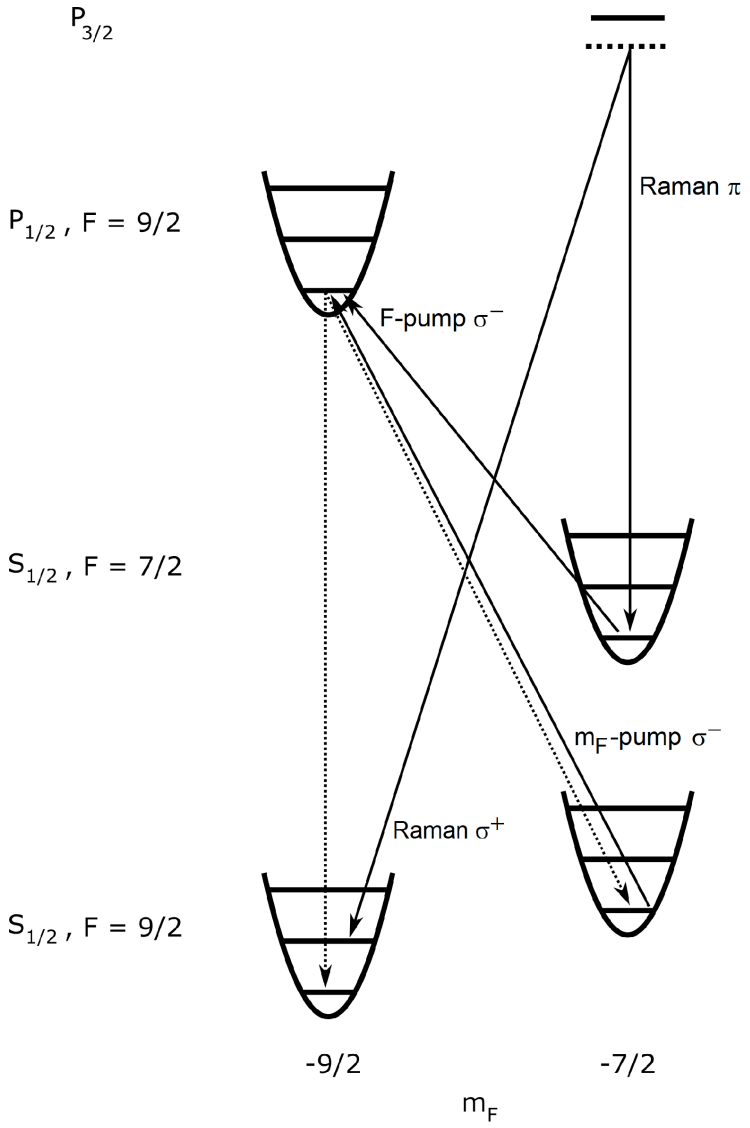

Figure 2.6: Raman sideband cooling scheme. The cooling is achieved by reducing the vibrational level via the coherent two-photon Raman transition $|^2S_{1/2}, F = 9/2, m_F = -9/2, n\rangle \rightarrow |^2S_{1/2}, F = 7/2, m_F = -7/2, n-1\rangle$. Subsequently, the atom is pumped to the state $|^2P_{1/2}, F = 9/2, m_F = -9/2\rangle$ from where it decays back to the state $|^2S_{1/2}, F = 9/2, m_F = -9/2\rangle$, but with a lower vibrational level. The motional quanta can thus be removed one by one until the atom reaches the ground state of the harmonic potential. As the atom can decay from $|^2P_{1/2}, F = 9/2, m_F = -9/2\rangle$ to $|^2S_{1/2}, F = 9/2, m_F = -7/2\rangle$ the scheme requires an additional pumping beam denoted as 'm_F-pump'. Adapted from [25].

the coherence and in order to pump the atom back into the initial state, D1 F-pump light is simultaneously applied. The pumping beam drives the transition $|^2S_{1/2}, 7/2, -7/2\rangle \rightarrow |^2P_{1/2}, 9/2, -9/2\rangle$ from where the atom can decay back to the state $|^2S_{1/2}, 9/2, -9/2\rangle$. As the atom can also decay to the state $|^2S_{1/2}, 9/2, -7/2\rangle$, we additionally employ a repumper that drives the transition $|^2S_{1/2}, 9/2, -7/2\rangle \rightarrow |^2P_{1/2}, 9/2, -9/2\rangle$. For these transitions the atom is unlikely to change its motional state when operating in the so-called Lamb-Dicke regime (see e. g. [58]). In total, the atom then changes its state from $|^2S_{1/2}, 9/2, -9/2, n\rangle$ to $|^2S_{1/2}, 9/2, -9/2, n-1\rangle$ over the course of one iteration, i. e. loses one motional quantum per iteration and can thus be cooled to the motional ground state which is then dark to the Raman transition.

Optimisation

As only a single atom is trapped within a tweezer, it is non-trivial to measure a temperature to assess the cooling success and optimise the parameters for the Raman sideband cooling. In our experiment, we used three different approaches to estimate the temperature that are presented in the following.

Spilling technique For the so-called spilling technique, the trapping depth is adiabatically lowered such the number of vibrational levels in the trapping potential is decreased. The lower the final trapping potential, the lower the remaining number of levels. Atoms above the threshold level get spilled out of the trap. Hence, the survival probability after the spilling corresponds to the motional state of the atom before the spilling.

This technique is fast and convenient for a rough optimisation. However, spilling down to low n and especially calibrating the relation between the set final trap depth and the number of remaining vibrational levels is challenging. Hence, this method is unfavourable for atoms in a low mean vibrational level $\bar{n}$.

Release and recapture Another method is the so-called release and recapture technique [59] where the trapping potential is switched off for $\sim 10\,\mu s$ and then switched back on. The probability to recapture the atom in the trapping potential depends on its initial velocity which again depends on its energy. Performing several iterations yields an energy distribution that can be used to estimate the mean occupied vibrational level $\bar{n}$.

The release and recapture technique is an easy and fast method to extract an estimate for the temperature, but has a drawback when optimising Raman sideband cooling: The extracted temperature is only meaningful when assuming thermal equilibrium. Raman

sideband cooling, on the other hand, addresses the vibrational levels n_x, n_y and n_z individually. Consequently, the technique provides an estimate on the overall Raman cooling efficiency, but it does not allow to differentiate between the different axes.

Raman spectra As a third method we employed Raman spectra. The basic idea is to use the Raman transition as a diagnostic tool since the ground state of the trapping potential is dark to the red sideband $|n\rangle \rightarrow |n-1\rangle$. Therefore, after applying the Raman cooling scheme, a $\pi/2$ Raman pulse with variable frequency f_{probe} of one of the Raman beams is applied to drive the transition $|^2S_{1/2}, F = 9/2, m_F = -9/2\rangle \rightarrow |^2S_{1/2}, 7/2, -7/2\rangle$. Depending on f_{probe}, which determines the relative detuning of the two Raman beams, the carrier transition $|n\rangle \rightarrow |n\rangle$, the blue sideband $|n\rangle \rightarrow |n+1\rangle$ or the red sideband $|n\rangle \rightarrow |n-1\rangle$ is driven. A subsequent resonant, so-called blowout pulse on the D2 line then removes all remaining atoms in the state $|^2S_{1/2}, 9/2, -9/2\rangle$ that were not affected by the Raman transition. In the last step the remaining atoms that were hidden from the blowout pulse in the state $|^2S_{1/2}, 7/2, -7/2\rangle$ are imaged via D1 fluorescence imaging. Hence, a Raman spectrum essentially probes the probability that an atom is affected by the Raman transition at a variable relative detuning of the Raman beams.

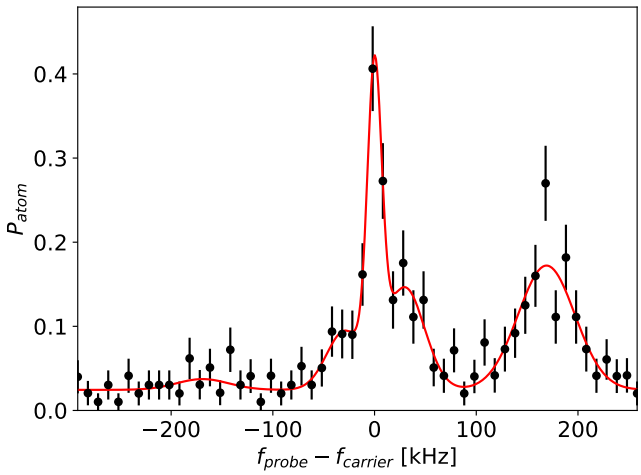

Figure 2.7: Raman spectrum after Raman sideband cooling in a tweezer. A $\pi/2$ Raman pulse is applied where the frequency f_{probe} of one of the Raman beams is varied. The frequency f_{carrier} at which the carrier transition is driven acts as a reference. Subsequently, all atoms that were not addressed by the Raman transition are removed via a blowout pulse and the remaining atoms are then imaged. Plotted is the corresponding probability to detect an atom in the tweezer (black). The axial sidebands are visible at a detuning of $\sim 30\,\text{kHz}$. The radial trapping frequencies are degenerate and visible at a detuning of $\sim 170\,\text{kHz}$. To extract the amplitude of the sidebands, the data is fitted (red) with a sum of five Gaussians where the position of the sidebands is forcibly symmetric. The mean vibrational level per axis and thus the ground state fractions can then be derived from the ratio of the fitted amplitudes of the sidebands. Radially ground state fractions of 91.3% are achieved, axially a ground state fraction of 43.3%, yielding a 3D ground state fraction of 36.1%.

A thereby derived Raman spectrum is shown in fig. 2.7. It was taken after Raman sideband cooling in a tweezer potential and features five peaks: The central one corresponds to the carrier transition. To the left, i. e. at lower frequencies, are the red sidebands, to the right, i. e. at higher frequencies, the blue sidebands. The spectral distance of the sidebands to the carrier corresponds to the trapping frequency.[15] As the tweezer potential has two degenerate radial trapping frequencies and one axial trapping frequency, the spectrum features two red and two blue sidebands.[16] The axial sidebands are closer to the carrier than the radial ones due to the lower trapping frequency. As can be seen in the plot, the amplitude of the red sidebands are lower than the amplitudes of the blue sidebands. This so-called sideband asymmetry is caused by atoms in the motional ground state. While these atoms contribute to the blue sideband, they are not addressed by the red one as the ground state is dark to the red sideband. Hence, from the amplitude ratio $r = A_r/A_b$ of red and blue sidebands the mean vibrational level $\bar{n} = r/(1-r)$ can be derived [52] as well as the ground state fraction, i. e. the probability $P_{GS} = 1 - r$ that an atom is in the motional ground state.[17]

This method yields more information compared to the previously described methods since it allows to differentiate between non-degenerate axes and to directly extract the ground state fraction. However, this method is much more time-consuming.

Performance

While we achieved ground state fractions of 87% in a 1D lattice, cooling in three dimensions turned out to be more difficult. As assessed from the fitted data shown in fig. 2.7 we were able to get a ground state fraction of up to 91% in the radial axes, but only 43% in the axial direction yielding a 3D ground state fraction of 36%. When increasing the axial trapping frequency by an additional confinement, resulting in all three trapping frequencies being nearly degenerate, the achieved 3D ground state fraction was slightly higher with 40%, but still similar. In principle this could be compensated via reasonable post-selection and accordingly taking more statistics, but in practice this gets unfeasible for increasing atom number N as the ground state fraction of the total system scales with $(P_{GS})^N$.

Despite thorough investigation of potential issues such as laser frequency noise, lattices formed by surface reflections, fictitious magnetic fields, and heating from intensity

[15] Hence, Raman spectra are also a useful tool to extract the trapping frequencies.

[16] 1D Raman spectra as taken in 1D lattices or Raman spectra in a tweezer with all three trapping frequencies being degenerate result in a total of three peaks: a carrier, one red sideband and one blue sideband.

[17] This relation can be easily derived from the Maxwell-Boltzmann statistics.

instabilities, we were not able to exceed a ground state fraction of $\sim 40\%$. This is surprising since we are not aware of any factor that should fundamentally limit the ground state fraction in our system to such relatively low values. With rubidium, strontium and sodium ground state fractions of more than 90% were achieved in optical tweezers [53, 60, 61]. With potassium Raman sideband cooling was successfully performed in a 3D lattice with a resulting ground state fraction of 72% [62]. After we performed our measurements on Raman cooling described above, ground state fractions of 69% [63, 64] were furthermore reported for potassium in a tweezer array. The lower ground state fractions achieved in our setup might be connected to spurious interference from the lens surfaces of our in-vacuo microscope objectives or to transitions from the $4p$- to the $5p$-manifold at $\sim 852\,\mathrm{nm}$ [65] which is very close to the wavelength of $\sim 850\,\mathrm{nm}$ we employ for the tweezer potentials.[18] Although these transitions are dipole-forbidden, the high intensity at the atom position due to the small focal waist of the tweezers of $< 1\,\mu\mathrm{m}$ might result in a non-negligible transition probability.

[18] In contrast to our setup, the experimental setup of [63, 64] employs 1064 nm light for the trapping potential.

Chapter 3

Realising a K39 BEC

In the previous chapter we introduced the experimental apparatus and described how we prepared small Fermi-Hubbard systems employing the fermionic potassium isotope K40. As it proved very challenging to achieve the required high ground state fractions, we then decided to take a new direction towards two-dimensional bosonic bulk systems.

In this chapter we will discuss how the experimental setup introduced in the previous chapter was adapted in order to make a three-dimensional K39 Bose-Einstein condensate. We will first give an overview on the bosonic potassium isotope K39, focussing on why it is the most favorable choice for our research endeavour and on its main properties, especially in comparison to the previously employed K40. We will see that the optical properties are very similar and although switching from K40 to K39 requires some technical modifications of the laser system, the main changes arise from switching from small tweezer systems to large bulk systems as this requires significant adaptions of the experimental sequence: For small tweezer systems we focussed on short cycle times as these systems are associated with an increased need for repetitions, which prevents to employ non-optical cooling techniques such as evaporation. Bulk systems, on the contrary, require to focus on large atom numbers instead which are, on the one hand, favorable in terms of an enhanced signal and on the other hand, also for achieving high phase-space densities via evaporation. Consequently, while the experimental sequence for K40 and K39 is similar up to the three-dimensional magneto-optical trap, it significantly differs for the steps thereafter.

Hence, after introducing the atomic species, we will discuss the re-designed experimental sequence allowing to prepare a three-dimensional Bose-Einstein condensate. We will first give a brief overview of the sequence and then discuss improvements and the main steps after the three-dimensional magneto-optical trap in more detail.

3.1 The atomic species

3.1.1 Why K39?

As we were not designing a bosonic ultracold quantum gas experiment from scratch, but re-building an existing quantum gas experiment that was operating with fermionic potassium K40, it appears natural that we employ the same element and switched to the bosonic isotope K39.[1] However, K39 is not only most convenient from a technical point of view, but also the most suitable choice to enable a combination of spin mixtures and tunable interactions.

As an alkali metal, K39 possesses one valence electron and thus a hydrogen-like structure. This simplifies the manipulation making alkali metals the most common choice for ultracold quantum gas experiments. Almost all alkali metals have been used to realise degenerate bosonic systems. Only francium has not been employed as it is one of the most unstable naturally occurring elements with a half-life on less than half an hour [66]. Every other alkali metal, i. e. lithium, sodium, potassium, rubidium and caesium, has been successfully utilised to study ultracold Bose gases (see sec. 5.1). However, most of these elements are not well suited for our experimental setup as we are especially interested in spin mixtures with tunable interactions while most alkali metals only provide one of these features.

Cs133, the only stable isotope of caesium[2], features a variety of intrastate Feshbach resonances, especially a low-field, broad Feshbach resonance in the energetically lowest-lying state $|6S_{1/2}, F = 3, m_F = 3\rangle$ and thus features easily tunable intrastate interactions. However, Cs133 suffers from high two- and three-body loss rate coefficients which, especially in combination with the high mass[3], makes it very challenging to achieve (quasi-)condensation in any state other than the absolute ground state where inelastic two-body losses are energetically suppressed [67].[4] Hence, Cs133 is not suitable for the study of spin mixtures.

Rb87[5] as well as Na23, which is the only stable isotope of sodium, both allow to use

[1] K41, the other bosonic isotope of potassium, has a substantially lower natural abundance which makes K39 more favorable.

[2] Cs135 is radioactive, but with a half-life of $\sim 10^6$ years. However, the natural abundance is extremely low.

[3] The high mass reduces the thermal de Broglie wavelength and hence the phase-space density. Therefore, the temperature required to achieve degeneracy is much lower for species with a high mass.

[4] Only very recently, a BEC in the $|6S_{1/2}, F = 3, m_F = 2\rangle$ state has been realised [67].

[5] Rubidium has two naturally occuring isotopes: Rb85 and Rb87, both of them are bosonic. While the natural abundance of Rb85 is higher, it suffers from an extremely large, negative background scattering length [68]. Therefore, Rb87 is typically preferred.

a spin degree of freedom. However, although Feshbach resonances are reported for both species [11, 69], to our knowledge all of them are narrow and hence not suitable for tuning interactions as they are associated to severe losses.

Hence, lithium[6] and potassium are the only atomic species in the group of the alkali metals that are suitable to create bosonic spin mixtures while also featuring Feshbach resonances that are suitable for tuning the interaction strength. However, although suitable intra- as well as interstate Feshbach resonances are reported both for Li7 [70] and K39 (see sec. 3.7.1), Li7 suffers from high three-body loss coefficients. Especially for scattering lengths in the order of $10^2\,a_0$, where a_0 is the Bohr radius, as required for evaporation, the three-body loss coefficients for Li7 are more than one order of magnitude higher than for K39 [71, 72] limiting the density and making the preparation of Li7 more difficult. [73, 74].

Therefore, of all alkali metals, K39 provides the highest flexibility in terms of tunable interactions for bosonic spin mixtures. Note, though, that the tunability is, nonetheless, subject to some constraints as the intra- and interstate scattering lengths cannot be tuned individually. The achievable combinations of the intra- and interstate coupling strengths depend on the properties, e. g. the location, of the respective Feshbach resonances.[7] Details on the viable regimes are given in sec. 4.6.2.

3.1.2 From K40 to K39

The main general properties of K39 and K40 relevant in the context of this thesis are stated in tab. 3.1. The most fundamental difference is that K40 follows Fermi-Dirac statistics, while K39 follows Bose-Einstein statistics. Consequently, K40 is subject to Pauli blocking

	K39	K40
statistics	bosonic	fermionic
natural abundance	93.258 %	0.012 %
lifetime	stable	$1.28 \cdot 10^9$ y
nuclear spin	3/2	4
s-wave scattering length	$\sim -33\,a_0$	$\sim 170\,a_0$

Table 3.1: General properties of K39 and K40. The background s-wave scattering length is approximated by the triplet scattering length [75]. Data is taken from [28].

[6] Lithium has only one bosonic isotope which is Li7.

[7] Most notably, K39 does not yield a regime where all three scattering length of any spin combination of the lowest hyperfine state are positive. Nonetheless, K39 allows to study spin mixtures with attractive as well as repulsive interstate interactions when focussing on strongly imbalanced spin mixtures.

and will form a Fermi gas in a degenerate bulk system. K39 atoms, on the other hand, are able to occupy the same states, and will undergo a phase transition to Bose-Einstein condensation in a degenerate 3D bulk system. An important consequence of the different statistics is that K39 allows for an efficient spin-polarised evaporation which is prevented for K40 due to Pauli blocking.

The level schemes of K39 and K40, depicted in fig. 3.1, exhibit the same basic structure. The main transitions are the D1- and D2-line, the respective optical properties are stated in tab. 3.2. A noteworthy difference is the normal hyperfine structure of K39 as opposed to the inverted hyperfine structure of K40. Due to the lower nuclear spin, the hyperfine ground states $F = 1$ and $F = 2$ exhibit less Zeeman states than the hyperfine ground states $F = 9/2$ and $F = 7/2$ of K40. Furthermore, the lower nuclear spin results in a tighter level spacing of K39. This can be convenient from a technical point of view as it allows to employ the same laser, tuned via an offset lock, for several transitions. However, the hyperfine states in the D2 manifold are separated only by a few Γ or by even less than Γ. This makes it challenging to address these states without being affected by the respective other states as we will see e. g. in sec. 3.5. As the transition frequencies are shifted between the two isotopes, switching from K40 to K39 requires some technical modifications of the laser system that are not further discussed here.[8]

	D1	D2
wavelength	770.1 nm	766.7 nm
natural linewidth Γ	$2\pi \cdot 5.96$ MHz	$2\pi \cdot 6.04$ MHz
recoil temperature	0.4 µK	0.4 µK
Doppler temperature	145 µK	145 µK

Table 3.2: Optical properties of potassium. Within the given precision the values are valid for both K39 and K40. Data is taken from [28].

Both isotopes feature Feshbach resonances that allow for tunable interactions. Despite the larger number of Zeeman states, K40 exhibits only few suitable Feshbach resonances, the most relevant being between the two lowest-lying Zeeman states at ~ 200 G [77], while intrastate resonances are suppressed due to Pauli blocking. K39 features a variety of suitable Feshbach resonances, both inter- as well as intrastate, that are discussed in more detail in sec. 3.7.1.

[8] For a brief discussion see [76].

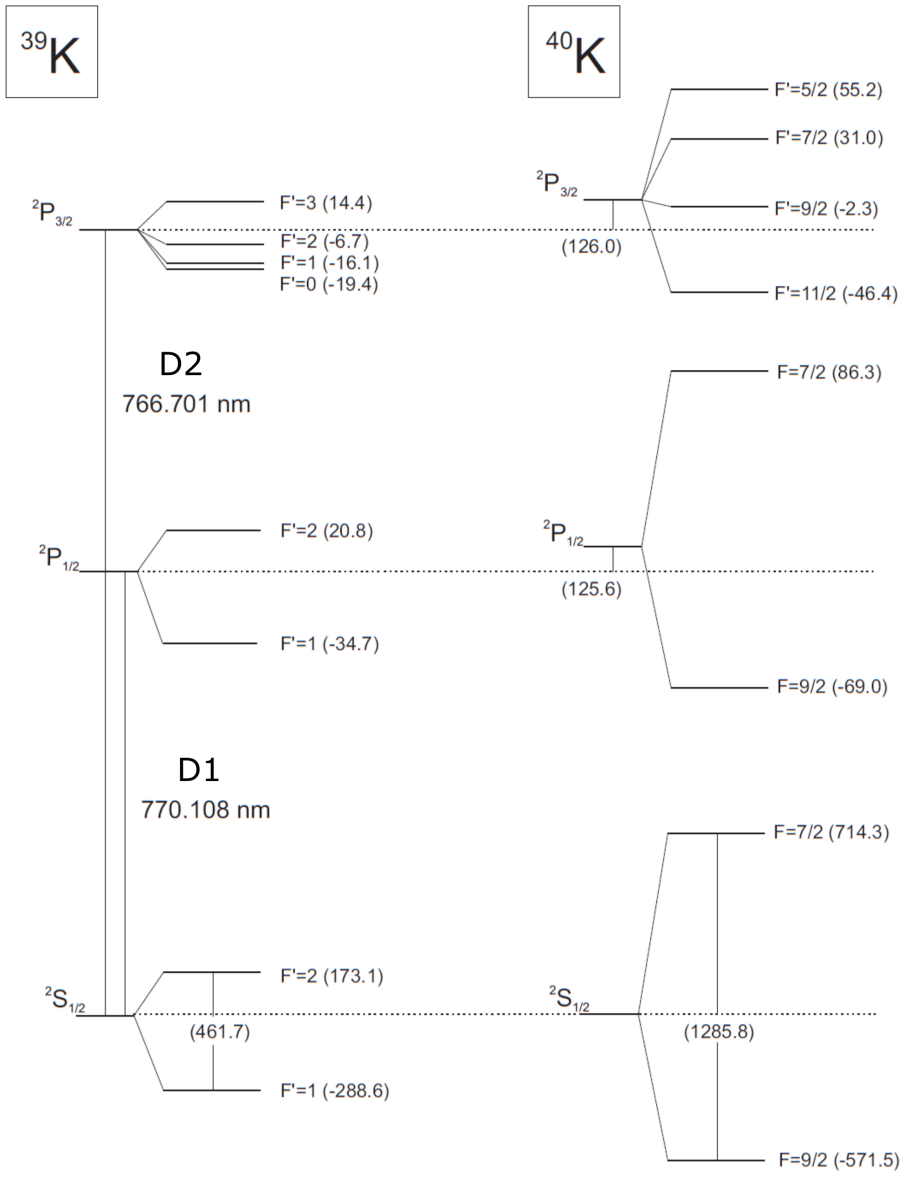

Figure 3.1: For convenience we again present the level scheme of K39 and K40 already shown in fig. 2.3. The hyperfine splittings are given in units of MHz. Adapted from [28].

3.2 Overview of the experimental sequence for K39

In contrast to the experimental sequence to prepare small tweezer systems with K40 presented in sec. 2.2 where we focussed on short cycle times, the K39 sequence aims towards 2D bulk systems and hence focusses on achieving larger atom numbers. The central cooling step is evaporation where large atom numbers are then translated to high phase space densities allowing to cross the threshold of Bose-Einstein condensation. Thus, while the steps of the K39 sequence up to the three-dimensional magneto-optical trap (MOT) are essentially the same as for the K40 sequence, the steps thereafter differ significantly: The 3D MOT is followed by a hybrid MOT and a subsequent grey molasses phase to further cool the atoms which are then magnetically transported to the science position located between the two microscope objectives. There the atoms are loaded from the magnetic confinement into a far-detuned optical dipole trap via a collisional loading scheme and evaporated in a crossed dipole trap to achieve quantum degeneracy resulting in a 3D BEC. The collisional loading scheme is chosen and optimised to provide large atom numbers for the evaporation, while the previous steps are optimised to achieve high densities required for the collisional loading scheme. The degenerate atomic sample is then transferred from the three-dimensional into a quasi-two-dimensional regime.

In the following we provide an overview of the experimental sequence and parameters to prepare a K39 BEC. A more detailed discussion of individual steps and implemented improvements and schemes is given in the subsequent sections. The transformation from a three-dimensional to a quasi-two-dimensional system will be discussed in chapter 4, an overview of the corresponding experimental steps is given in sec. 4.6.1

- In a first step an atomic beam, generated via a 2D MOT [30, 31], is used to load a 3D MOT [32] where three pairs of counter-propagating beams create a cooling force via Doppler cooling [78–81] and in combination with a magnetic quadrupole field also a trapping force.
  The cooling light addresses the D2 transition $|^2S_{1/2}, F = 2\rangle \rightarrow |^2P_{3/2}, F = 3\rangle$ and is red-detuned typically by $\sim 5.5\,\Gamma$. Additionally, repumping light on the D2 transition $|^2S_{1/2}, F = 1\rangle \rightarrow |^2P_{3/2}, F = 2\rangle$ is applied which is also red-detuned by $\sim 1.5\,\Gamma$. The vertical magnetic gradient is typically $9.5\,\mathrm{G/cm}$.
  With these parameters a loading rate of up to $\sim 8 \cdot 10^9\,\mathrm{atoms/s}$ is achieved. The loading process saturates already after $\sim 1.7\,\mathrm{s}$ at an atom number of $\sim 9 \cdot 10^9$. The achieved phase-space density is $\sim 4 \cdot 10^{-9}$.

- The 'red' MOT is directly followed by a hybrid MOT [33] where the red-detuned D2 cooling light is replaced by blue-detuned D1 cooling light. Thereby, a different cooling scheme is applied that allows to reach higher phase-space densities. A more detailed explanation is given in sec. 3.3.
  This hybrid MOT scheme is applied for 50 ms during which the vertical magnetic gradient is ramped to a higher value of typically 15.5 G/cm. The D1 cooling light addresses the transition $|^2S_{1/2}, F = 2\rangle \rightarrow |^2P_{1/2}, F = 2\rangle$ and is blue-detuned typically by $\sim 9\,\Gamma$. The D2 repumper addresses the same transition as for the 'red' MOT and is red-detuned by $\sim 1.75\,\Gamma$ which is barely different compared to the 'red' MOT phase. However, it is crucial to reduce the intensity of the repumper, typically by a factor of 4. Compared to the previous 'red' MOT the central density is increased by a factor of ~ 5, the temperature is decreased even by a factor of ~ 10. The achieved phase-space density is then $\sim 5.4 \cdot 10^{-7}$.

- The third step is a Λ-enhanced grey molasses scheme[9] [36–38], i. e. a polarisation gradient cooling scheme with motional coupling of bright and dark states which is not trapping, but allows to further cool the atoms.
  As required for the grey molasses scheme, the magnetic field is switched off and D1 cooling light is applied as well as D1 repumping light which is modulated onto the cooling light via an EOM. Just as the hybrid MOT, the molasses scheme requires blue-detuned cooling light, the detuning is typically $\sim 9\,\Gamma$. After a waiting time of 24 ms during which the cooling efficiency increases due to the decay of the magnetic field, the D1 light is ramped down within 5 ms in order to reduce the photon scattering rate towards the end of the cooling scheme.
  During this step, the central density decreases by a factor of ~ 4, partially due to atom losses, partially due to an expansion of the cloud since the molasses does not exert a trapping force. However, the temperature is significantly reduced to $\sim 13\,\mu$K, resulting in a phase-space density of $\sim 3.3 \cdot 10^{-5}$.

- The fourth step is a magnetic transport of the atoms from the MOT position to the science position. Therefore, the atoms are first optically pumped into the state $|^2S_{1/2}, F = 2, m_F = 2\rangle$ as this is the ground state in which the atoms have the highest magnetic moment and hence experience the strongest confinement by the magnetic trap. For the optical pumping we apply a quantisation field of ~ 4 G and employ an F-pump beam as well as an m_F-pump beam. The F-pump beam is resonant to the D1 transition $|^2S_{1/2}, F = 1\rangle \rightarrow |^2P_{1/2}, F = 2\rangle$ from where the atoms

[9] A detailed explanation of this scheme can be found in [34] or [35].

can then decay to the desired $|^2S_{1/2}, F = 2\rangle$ state. The m_F-pump beam is resonant to the D2 transition $|^2S_{1/2}, F = 2\rangle \rightarrow |^2P_{3/2}, F = 3\rangle$ from where the atoms can also decay to the $|^2S_{1/2}, F = 2\rangle$ state. It is circularly polarised in order to transfer the atoms into the desired m_F-state. We achieved best results when applying both pumping beams for 15 µs and the D1 F-pump light for additional 20 µs.
After the optical pumping the atoms are captured in a magnetic trap by switching on a quadrupole field with a vertical gradient of 22.5 G/cm. After a short waiting of 4 ms for the magnetic field to settle, the magnetic trap is tightened by increasing the gradient to 85 G/cm within 200 ms. A further discussion of the behaviour of the atoms in the magnetic trap can be found in sec. 3.5.
The transport is then performed by slowly shifting the magnetic trap from MOT to science position by ramping down the field created by the MOT coils centered on the MOT position while simultaneously ramping up a gradient field generated by the experiment coils centered on the science position. The MOT (experiment) coil current ramp is $\cos^2$- ($\sin^2$-) shaped in order to smoothen the transfer and performed within 500 ms to reduce heating. This step, especially capturing the atoms in the magnetic trap, decreases the phase-space density to $\sim 1.1 \cdot 10^{-6}$.

- After the transport to the science position the atoms are loaded from the magnetic trap into a tightly focussed 1064 nm optical dipole trap (ODT). In contrast to the magnetic trap, optical traps allow to exploit Feshbach resonances which is necessary to achieve a sufficient collision rate for an efficient evaporation in the following step. The atoms are loaded into the 1064 nm ODT via elastic collisions. In order to increase the density and hence the collision rate, the magnetic trap is tightened by increasing the magnetic gradient to 99 G/cm within 100 ms, while the ODT is switched on and ramped to a depth of ~ 6 mK. After a loading time of 2 s the magnetic trap is then ramped down within 100 ms. A more detailed discussion of the loading scheme can be found in sec. 3.6.
  With this scheme $\sim 1.1 \cdot 10^6$ atoms are loaded into the ODT with a temperature of ~ 500 µK yielding a phase-space density of $\sim 1.6 \cdot 10^{-4}$.

- In the final step quantum degeneracy is achieved via evaporation. A more detailed discussion of this step can be found in sec. 3.7. The atoms are first transferred either to the $|^2S_{1/2}, F = 1, m_F = +1\rangle$ state or the $|^2S_{1/2}, F = 1, m_F = -1\rangle$ state depending on which of these states is preferred for the subsequent experiment. Both states exhibit suitable intrastate Feshbach resonances to achieve sufficiently high scattering rates for the evaporation. Typically, we prepare the atoms in the

$|^2S_{1/2}, F = 1, m_F = -1\rangle$ state as this is favorable for studying spin mixtures. Due to the optical density of the atomic cloud in the 1064 nm ODT, optical pumping is not very effective, instead the spin preparation is realised via RF transfers.
After the spin preparation, the atoms are transferred from the single-beam 1064 nm ODT into a 850 nm crossed dipole trap (CDT). While the 1064 nm ODT is well adapted to the collisional loading scheme, it is less favorable for the evaporation due to the axially and radially drastically different trapping frequencies. The actual evaporation is then performed in the 850 nm CDT which is ramped down from its full depth of $\sim 100\,\mu$K to a relative depth of 4.5 % within 2.7 s. During the transfer into the 850 nm CDT as well as during the evaporation a magnetic gradient of $\sim 25\,$G/cm is applied in order to reduce the effective trap depths without lowering the trapping frequency.
With this procedure $\sim 1.9 \cdot 10^5$ atoms are loaded into the full depth 850 nm CDT. The achieved temperature is $\sim 10\,\mu$K yielding a phase-space density of $\sim 4.2 \cdot 10^{-2}$. During the evaporation in the 850 nm CDT the atomic cloud crosses the condensation threshold and forms a quasi-pure BEC of $\sim 5 \cdot 10^3$ atoms.

3.3 Hybrid MOT

The hybrid MOT [33] is a specific MOT configuration with increased phase-space density compared to the typically used type-I red-detuned MOT. Eventually, its purpose is to improve the collisional loading.

Motivation

For an effective collisional loading from the magnetic trap into the 1064 nm optical dipole trap a high density n_b in the magnetic trap is required (see sec. 3.6). n_b is in turn determined by temperature and density n_f of the atom cloud loaded into the magnetic trap. The phase-space density in the 3D MOT is not sufficient for directly loading into the magnetic trap due to the comparatively high temperature.[10] Hence, the atoms are cooled via a Lambda-enhanced grey molasses before loading them into the magnetic trap.[11] The grey molasses requires the absence of magnetic fields, while the MOT scheme, on the other hand, requires a magnetic quadrupole field. Therefore, a waiting time Δt in between 3D

[10] For K39 the temperatures achieved with a typical red MOT scheme are rather high due to the tight level spacing of the D2 manifold [87].

[11] The presence of dark states in this scheme significantly reduces the heating caused by photon scattering which enables much lower temperatures of $\sim 13\,\mu$K. The absence of magnetic fields is required in order to protect the 'darkness' of the dark states.

MOT and molasses phase needs to be introduced, whose time scale is set by the decay time of the magnetic field. During this waiting time - and also during the molasses - the atoms are not trapped, the cloud expands and thus the density decreases. Accordingly, the corresponding final density n_f depends on Δt, T and the initial density n_0.

We substantially increased the final density and hence the density in the magnetic trap by two measures: We reduced Δt by reducing the eddy currents in our experimental setup (see sec. 3.4) and we significantly reduced T and increased n_0 by introducing a hybrid MOT subsequent to the MOT.

The hybrid MOT scheme

The hybrid MOT is a hybrid in two respects: it combines the typical red-detuned MOT (red MOT) with a blue-detuned MOT (blue MOT) [39] and it employs both the D1 and the D2 transition.

Red MOT A red MOT utilizes light that is red-detuned to a type-I transition, i. e. a transition $F \to F'$ with $F' > F$, to induce a trapping force as well as a cooling force. The cooling mechanism is simply Doppler cooling [78–81]. The trapping force is provided by a magneto-optical scheme that relies on a magnetic gradient causing a spatially and m_F-state dependent energy shift, and on a $\sigma^{\pm}\sigma^{\mp}$ polarisation configuration. This leads to a spatially dependent absorption probability resulting in a restoring force. This is typically performed in a type-I system, i. e. in our case on the D2 line, such that there are no dark states where the atoms elude the cooling and trapping forces. The sign of the cooling force depends on the sign of the detuning, but is independent of the polarisation. The sign of the trapping force, on the other hand, depends on the sign of the detuning *and* on the orientation of the polarisation.[12] Therefore, trapping can also be achieved with blue-detuned light by reversing the polarisation. This is exploited to create a blue MOT.

Blue MOT While a blue MOT utilizes the same trapping mechanism as a red MOT, the cooling mechanism cannot be adopted. Instead it relies on polarisation gradient cooling (PGC). For type-I transitions PGC is strongly suppressed in the presence of magnetic fields. However, type-II transitions, i. e. transitions $F \to F'$ with $F' \leq F$, are more robust in that respect: For low magnetic fields in the order of a few Gauss the PGC

[12] It also depends on the sign of the Landé-factor g' of the excited state, but that can only be changed by addressing a different transition.

scheme still exerts a significant cooling force [82].[13]

In contrast to Doppler cooling, PGC in type-II systems requires blue-detuned light. Furthermore, in blue MOTs PGC and Doppler cooling compete against each other due to the different sign of the respective cooling force. Above the equilibrium velocity the atoms are heated by the Doppler mechanism. Hence, blue MOTs require a lower initial velocity. However, due to exploiting dark states, photon scattering is significantly reduced and thus much lower temperatures and higher densities are achieved.[14]

Hybrid MOT The hybrid MOT is a mixture of red and blue MOT: the cooler light is blue-detuned to a type-II transition on the D1 line, while the repumping light is red-detuned to a type-I transition on the D2 line. The predominant cooling mechanism stems from the cooler and is PGC which yields the advantages of a blue MOT, i. e. a lower temperature as well as a higher density, while the repumper mainly provides additional trapping. Just as the blue MOT the hybrid MOT requires a lower initial velocity for the PGC to outweigh the heating caused by the Doppler mechanism. Hence, the hybrid MOT cannot replace the red MOT, but is introduced as a subsequent step.

Blue MOT with K39? Potassium, especially K39, has a tight level spacing that prevents to address the hyperfine states individually. This makes the system more complex compared to other species as for example rubidium.[15] Fully analysing the cooling/heating, anti-/trapping contributions for every configuration of cooler and repumper in terms of detuning, polarisation and addressed transition would go beyond the scope of this thesis, though.

In our experimental setup, we did not observe a properly operating blue MOT with K39.[16] However, the number of viable configurations is limited in our setup: The D1 repumper is implemented by modulating the D1 cooler light via an EOM, i. e. the orientation of the polarisation is forcibly the same for D1 cooler and D1 repumper. Decoupling these parameters might allow to find a suitable blue MOT configuration.

Performance While we cannot compare the experimental performance of the hybrid MOT scheme to the blue MOT scheme, the absence of a dark state for the type-I transition

[13]Note, that the cooling force is reduced with respect to the cooling force in the absence of magnetic fields and decreases with increasing magnetic field.

[14]In contrast to Doppler cooling PGC exhibits velocity dependent motional coupling of dark and bright states which is why dark states are advantageous for PGC, but need to be avoided for Doppler cooling.

[15]This also applies to the analysis.

[16]For K40 the inverted level structure allows to find a suitable blue MOT configuration. Also, the level spacing of the D1 transitions is three times larger than for K39 which significantly reduces the contribution from nearby transitions.

in the hybrid MOT scheme suggests a higher temperature compared to a type-II blue MOT due to increased photon scattering. However, the simulations in [82] indicate that the hybrid MOT is favorable in terms of the trapping force: According to the simulations the strength of the trapping force increases significantly with increasing ratio g'/g where g' (g) is the g-factor of the excited (ground) state. This ratio is a factor of 4 higher for the D2 transition addressed in the hybrid MOT compared to the D1 transition addressed in the blue MOT.

Compared to the red MOT we gained a factor of ~ 5 in the density and reduced the temperature by a factor of ~ 10 yielding an improvement of the phase-space density of more than two orders of magnitude.

3.4 Eddy currents: achieving shorter decay times

The decay times of the magnetic fields in our experimental setup are limited by eddy currents: When switching off the coil current the changing magnetic field induces current loops in electrically conducting components of the experimental setup.[17] These eddy currents in turn generate a secondary magnetic field and hence, the decay time of the magnetic field is given by the decay time of the eddy currents. We were able to reduce the measured $1/e^2$ decay time from $\sim 30\,\mathrm{ms}$ to $\sim 10\,\mathrm{ms}$ by altering the path of the dominant eddy currents by cutting one of the breadboards used for mounting the optics such that a current flow in a continuous circle is prevented.[18] This allowed to reduce the temperature and to increase the density in the magnetic trap (see sec. 3.3 and 3.5) which was crucial for the collisional loading of the optical dipole trap (see sec. 3.6).

The dominant component: the upper breadboard

In our case the main contribution is given by the so-called upper breadboard, i. e. a horizontally mounted, 25 mm thick aluminium breadboard with a size of 700 mm x 900 mm located right above the upper coils which is used to mount optics. This can be concluded from the following considerations:

Approximating the coil current I_{coil} as a step function where the current is switched off immediately at $t = 0$, the corresponding eddy currents as well as the secondary magnetic flux induced by them can each be estimated by an exponential decay with time constant

[17] This section exemplarily describes the scenario of switching off the coil current. The case of switching on the coil current is completely analogous.

[18] Note that for technical reasons the time-dependent magnetic flux was not measured at the atom position. However, FEM simulations performed with *COMSOL Multiphysics* indicate that the decay time at the atom position is even stronger reduced.

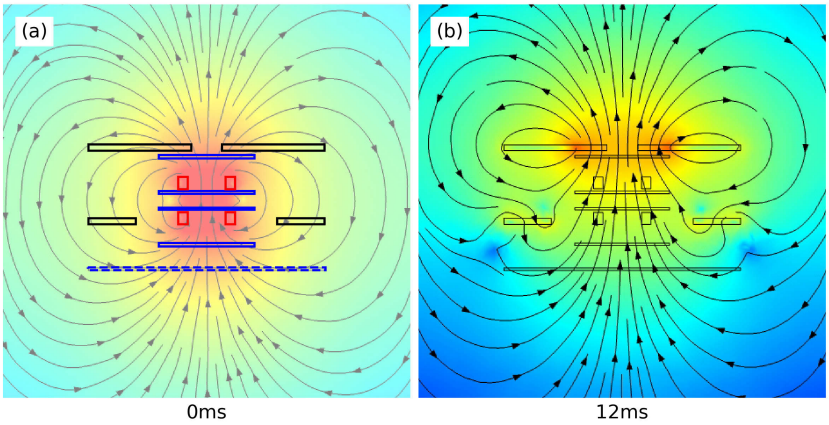

Figure 3.2: Simulation of the magnetic flux for an uncut upper breadboard. Depicted is a cut through the experimental setup in front view. The magnetic flux is indicated by a logarithmic colour scale covering nearly four orders of magnitude where red (blue) corresponds to a high (low) flux. **(a)**: The magnetic flux induced by the coils. Highlighted are the components of the experimental setup that are included in the simulation: the horizontally oriented pair of copper coils (red) that are generating the initial magnetic field, the upper and the lower breadboard made of aluminium (black), parts of the steel vacuum chamber (blue, solid) and the surface of the optical table also made of steel (blue, dashed). **(b)**: The magnetic flux induced by eddy currents 12 ms after switching off the coil current. It is clearly visible that the main contribution stems from the upper breadboard.

$\tau = L/R$ where L and $R = l/\sigma A$ are the inductance and resistance of the conducting component, respectively. l corresponds to the path length of the current, A to the cross-sectional area of the current and σ to the electrical conductivity of the component [83]. Accordingly, the dominant eddy currents in terms of amplitude and decay time are induced in thick components with high conductivity that are close to the (horizontally aligned) high-field coils and have a comparably large horizontal area.

Consequently, the most relevant parts of our experimental setup are the upper breadboard, the so-called lower breadboard, also made of aluminium and located around the vacuum chamber, parts of the steel vacuum chamber, and the surface of the optical table which is also made of steel. However, it is to be expected that the dominant contribution stems from the upper breadboard: The breadboards are made of aluminium which has a roughly one order of magnitude higher electrical conductivity than stainless steel resulting in a significantly larger time constant for the eddy currents within the breadboards. From these breadboards the lower one is less critical than the upper one since it is much further away from the coils. Furthermore, the lower breadboard is actually composed of two separate breadboards, hence it can be essentially considered as cut twice.

Finite element method (FEM) simulations performed with *COMSOL Multiphysics* confirm that the secondary magnetic field induced by the eddy currents in the upper breadboard are dominant as can be seen in fig. 3.2. Note that the experimental setup

also includes copper gaskets that are not included in the simulation in favour of the computing time. Their contribution is negligible compared to the breadboards: Although the conductivity of copper is roughly twice as high as of aluminium, the gaskets are more than one order of magnitude thinner than the breadboards and also the relevant width is more than one order of magnitude lower, leading to a significantly shorter decay timescale.

Cutting the breadboard: why does it help?

As previously discussed the dominant eddy currents stem from the upper breadboard. The amplitude and the decay time of these currents could be significantly reduced by cutting the breadboard which can be explained by considering the geometry of the eddy currents in the upper breadboard which are illustrated in fig. 3.3.

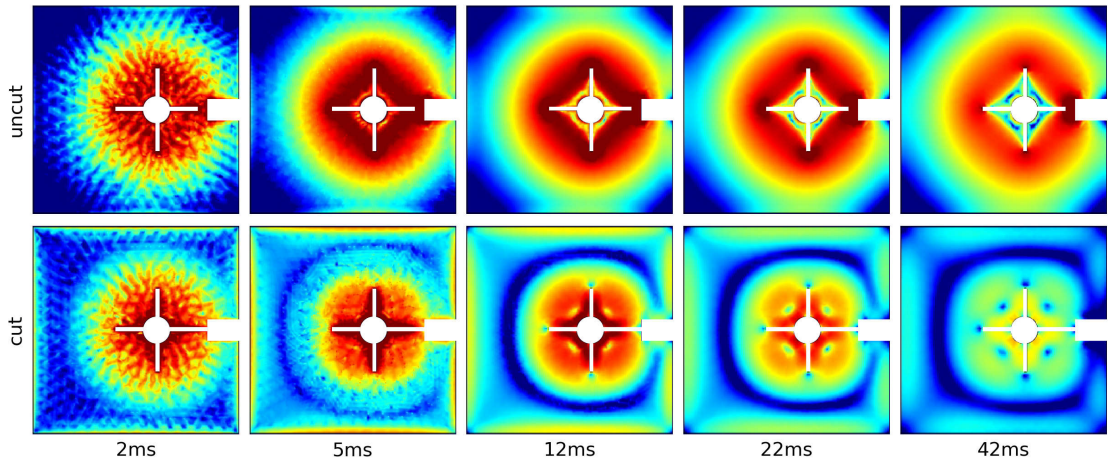

Figure 3.3: Simulated current density in the cut and uncut upper breadboard (top view) located above the upper coils for different times after switching off the coil current. The logarithmic colour scale covers two orders of magnitude where red (blue) corresponds to a high (low) current density. In the uncut breadboard (top row), the eddy currents can form a closed loop around the central cut-out resulting in a rather slow decay time. The cut breadboard (bottom row) prevents such a circular current loop and instead causes an inner current close to the cut-out and an outer current close to the edges. These inner and outer currents have opposite directions causing a clearly visible C-shaped zero-crossing of the current density. The altered geometry of the eddy currents results in a much faster decay time.

Details on the breadboard The shape of the original upper breadboard can be seen in fig. 3.3 (top row). The basic shape is rectangular with edge lengths of 700 mm and 900 mm. It has a circular cut-out roughly in the middle which is centered on the top viewport of the vacuum chamber to allow optical access along the vertical axis. Accordingly, it is also roughly centered on the upper coils. The diameter of the cut-out is 120 mm, which is smaller than the diameter of the coils of ~ 200 mm. The original breadboard already

features two additional slits to increase the effective diameter of the cut-out to 400 mm which were intended to reduce eddy currents. The breadboard furthermore exhibits a square-shaped cut-out on the side with an edge length of 100 mm in order to grant physical access to the mechanical shutter used to separate the oven and 2D MOT section from the main chamber (see sec. 2.1.1).

In order to reduce the amplitude and the time scale of induced eddy currents the breadboard was cut such that one of the original slits extends to the square-shaped cut-out at the edge as can be seen in fig. 3.3 (bottom row)

Geometry of the eddy currents in the uncut upper breadboard In accordance with Lenz's law the geometry of the eddy current is such that the secondary magnetic field it induces opposes the change of the initial magnetic field. Since the initial magnetic field is turned off this essentially means that the eddy current tries to keep up the magnetic field, i. e. the geometry of the eddy current follows the geometry of the coil current. Hence, the uncut breadboard exhibits roughly circular eddy currents around the central cut-out as depicted in fig. 3.3 (top row). The slits cause a deviation from the circular shape as they exceed the radius of the coils below, but do not prevent a closed loop current around the central cut-out. Due to this approximately circular current flow close to the coils, the breadboard essentially acts as another coil that is switched on when the actual coils are switched off. The close proximity of the breadboard to the coils results in a rather large secondary magnetic field generated by the eddy currents and the low resistance of the thick breadboard leads to rather long decay times.

Geometry of the eddy currents in the cut upper breadboard In the cut upper breadboard the eddy currents cannot follow a circular path anymore, but instead are forced to follow the edges of the connected cut-outs and the edges of the breadboard as shown in fig. 3.3 (bottom row). Essentially, the current path can be considered to consist of an outer and an inner C-shaped part that are connected around the square shaped cut-out. Importantly, the inner and outer current have opposite directions, resulting in a zero-crossing of the current density. As a direct consequence, the secondary magnetic fields induced by inner and outer current partially cancel each other which reduces the total amplitude. According to Lenz's law this effect is minimised which is why the current paths are as far away from each other as possible, i. e. much more localised on the edges of the breadboard than in the uncut case. The different geometry of the eddy currents compared to the uncut case reduces the inductivity and significantly increases thee path length which in turn increases the resistance. Consequently, the eddy currents decay much

faster. According to the simulation, after 22 ms the maximum current density of the cut breadboard is ∼5 times lower than compared to the uncut case, after 42 ms even ∼15 times lower.

Decay times

Complementary to the simulations, we measured the magnetic flux via a Hall sensor in dependence of the time after switching off the coil current in order to extract the decay time. We considered four different configurations: the uncut and the cut breadboard where both lower and upper coil were employed, and furthermore the uncut breadboard with both coils individually where the respective other coil was disconnected from the power supply and hence open-circuited. Note that the magnetic flux was not measured at the atom position, but at the height of the upper breadboard ∼20 cm away from the central cut-out. A measurement position significantly closer to the atom position is prevented by the size of vacuum chamber. However, we are mainly interested in comparing the different configurations.

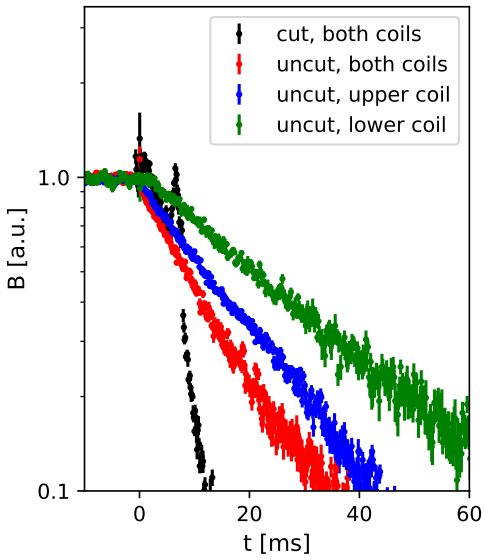

Figure 3.4: The magnetic flux B at time t after switching off the coil current for different configurations of un-/cut breadboard and connected coils. Depicted is the vertical component of the magnetic flux as measured with a Hall sensor at the height of the upper breadboard ∼20 cm away from the central cut-out. For comparison the respective offset of each curve was subtracted and the curves were normalised to their respective initial value. The decay of the magnetic field is significantly faster after cutting the breadboard. More details are given in the main text.

The corresponding data is shown in fig. 3.4. As can be seen the time evolution of the magnetic flux roughly follows an exponential decay. The $1/e$ decay times τ as well as the $1/e^2$ decay times τ_2 as determined from the data are listed in tab. 3.3. The cut breadboard exhibits the shortest decay time constant: cutting the breadboard reduced τ by a factor of 2, τ_2 even by a factor of 3. Comparing the uncut configurations reveals that when using only one of the coils the time constant increases, just slightly for the upper coil and by a factor of 2.5 for the lower coil compared to using both coils (red). While the reason is not understood at present, we suspect that this might be connected to cancellation of fields in an approximately symmetric setup which is broken when using only one coil.

In the cases of an uncut upper breadboard we obtain $\tau_2/\tau \approx 2$ as expected for a

	cut, both coils	uncut, both coils	uncut, upper coil	uncut, lower coil
$1/e$ time τ [ms]	7.96	13.24	16.90	32.05
$1/e^2$ time τ_2 [ms]	10.48	29.56	35.84	57.55
τ_2/τ	1.3	2.2	2.1	1.8

Table 3.3: Decay times of the magnetic field derived from the measured time-dependent magnetic flux shown in fig. 3.4. For a purely exponential decay, one obtains $\tau_2/\tau = 2$.

pure exponential decay. However, the ratio is significantly lower after cutting the upper breadboard. As the measured magnetic flux is given by the sum of all secondary magnetic fields induced by several eddy currents with different time scales, this indicates that the upper breadboard is no longer determining the time scale.

The simulations depicted in fig. 3.5 (d) support the hypothesis that the cut upper breadboard is no longer the dominant component. The magnetic flux is overall much lower than compared to uncut case and the lower breadboard becomes relevant. The changed weighting of the eddy currents of upper and lower breadboard as well as the altered path of the eddy current in the upper breadboard results in a more complex geometry of the secondary magnetic field. The different geometry further reduces the magnetic flux at the atom position. According to the simulation the magnetic flux at the atom position at $t = 12\,\mathrm{ms}$ is a factor of ~ 20 lower with a cut upper breadboard compared to the uncut case. So while the measurement at the position of the upper breadboard already indicates a decrease of the decay time constant by a factor 2-3, the simulation indicates an even stronger improvement at the atom position.

Vertical shift of the atom position

Apart from prolonging the decay time of magnetic fields, the eddy currents induced in our setup have another important effect: For magnetic confinements they introduce a vertical shift of the atom position due to the asymmetry of our setup both for cut and uncut upper breadboard.

In the uncut case, the main contribution to the secondary magnetic field stems from the upper breadboard. Consequently, while the coil pair and hence the symmetry axis of the initial magnetic field is centered on the atom position, the symmetry axis of the secondary field is strongly shifted towards the upper breadboard as can be seen in fig. 3.5 (b). This effect is less pronounced for the cut breadboard since the amplitude of the eddy currents is reduced and due to the lower breadboard becoming relevant as illustrated in fig. 3.5 (d).

Nonetheless, this shift has important consequences, especially when using a quadrupole

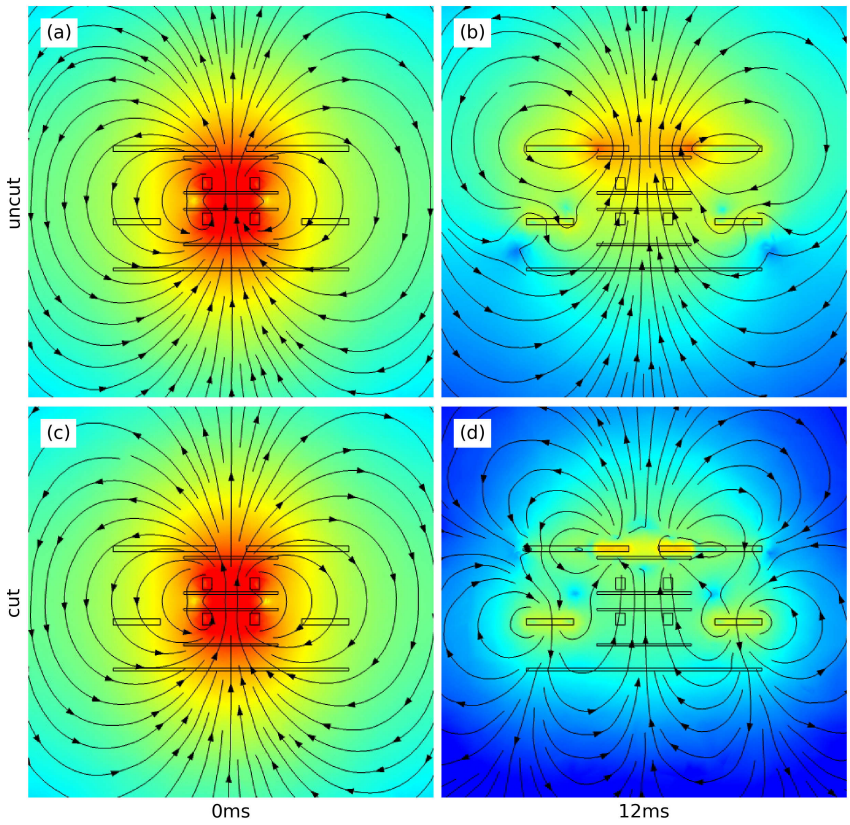

Figure 3.5: Simulated magnetic flux induced by the coils (0 ms) and by the eddy currents 12 ms after switching off the coil current both for cut and uncut upper breadboard. Shown is a cut through the experimental setup in front view. The magnetic flux is indicated by a logarithmic colour scale covering more than four orders of magnitude where red (blue) corresponds to a high (low) flux. The data from (a) and (c) was already shown in fig. 3.2 and is included for comparison. **(a),(c)**: At t=0 the magnetic field is determined by the coils. The magnetic dipole field generated by the exemplarily displayed Helmholtz configuration is not affected by the geometry of the upper breadboard. **(b)**: The secondary magnetic field is mainly determined by the uncut upper breadboard which essentially acts as a coil featuring a dipole field similar to the initial field. The main differences are the reduced amplitude due to the decay of the magnetic field and the vertical shift of the symmetry axis of the magnetic field since it is now centered roughly around the upper breadboard. **(d)**: For the cut breadboard the overall amplitude is much lower compared to the uncut case due to the lower decay time. The eddy currents in the upper breadboard are reduced to such an extent that the lower breadboard becomes relevant. This, together with the altered path of the eddy currents in the upper breadboard, results in a more complex geometry of the secondary magnetic field. The different geometry further reduces the magnetic flux at the atom position. Although the eddy currents still cause a vertical shift of the atom position for magnetic confinements, this effect is less pronounced than for the uncut breadboard.

field, e. g. for the MOT or the magnetic trap. In these cases the magnetic zero and thus the atom position is suddenly shifted when switching on or off the coils. Although the magnetic zero moves back as the eddy currents decay, the sudden jump heats the atomic sample. However, the vertical shift can be partially compensated with a time-dependent offset field (see sec. 3.5).

3.5 Magnetic trap

The magnetic trap is required for the magnetic transport from the MOT position to the science position. After the grey molasses, the atoms are therefore optically pumped into the magnetically trapped $|2, 2\rangle$ state and, subsequently, caught in the magnetic trap by suddenly switching on the coil current to the so-called catch current. Then, the magnetic gradient is slowly increased to the transport value. This two-step gradient ramp up is chosen in order to decouple the catch process from the transport. Subsequently, the atoms are transported from the MOT position to the science position by shifting the magnetic trap by simultaneously ramping down (up) the magnetic gradient at the MOT (science) position. After the transport the atoms are loaded from the magnetic trap into an optical trap via a collisional loading scheme (see sec. 3.6).

In order for this loading scheme to be efficient, a high density of the atom cloud in the magnetic trap is required. The density can be increased by increasing the magnetic gradient leading to a stronger confinement and, more importantly, by reducing the temperature. It is therefore important to optimise the mode matching, i. e. to adjust the catch gradient to the temperature, determined by the molasses phase, and to the size of the atom cloud, given by the expansion time before switching on the magnetic trap. When the size of the atom cloud at the time it is caught by the magnetic trap matches the equilibrium size in the magnetic trap determined by temperature and magnetic gradient, then heating e. g. due to breathing excitations is minimised. In our system the quality of the mode matching is limited by the switching time, though, or more precisely by the time scale for the build-up of the magnetic field due to eddy currents (see sec. 3.4).

A further consequence of the eddy currents is a vertical shift of the symmetry axis and thus of the magnetic zero when switching on or off the magnetic field. This vertical offset is time-dependent since it is determined by the time-dependent eddy currents. This results in a 'sloshing' of the atom cloud, i. e. an oscillation of the center position as shown in fig. 3.6 which heats the atom cloud. Although the symmetry axis shifts along the vertical axis we also observe a less pronounced sloshing along the transport axis,

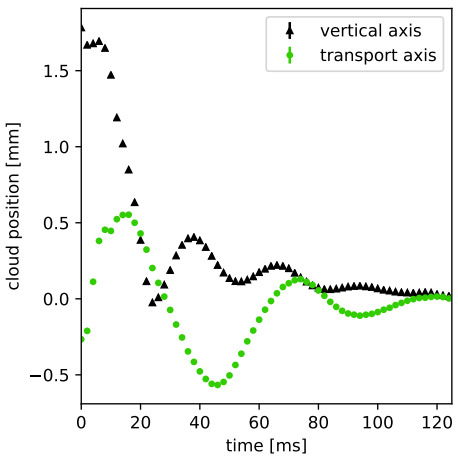

Figure 3.6: Center position of the atomic cloud after catching the atoms in a magnetic trap. Due to eddy currents the magnetic zero experiences a time-dependent shift which causes an oscillation of the center position.

i. e. the axis along which the magnetic transport is performed. This oscillation is slower because of the lower magnetic gradient compared to the vertical axis due to the geometry of the quadrupole field. The horizontal sloshing is not affected by the strength of the quantisation field applied during the optical pumping which is oriented along the transport axis and is switched off shortly before the magnetic trap is switched on. This indicates that the Raman coils that are used to create the quantisation field do not induce significant eddy currents. Instead, we suspect that the eddy currents in the upper breadboard induced by the MOT coils used to generate the magnetic trap also introduce a horizontal shift since the cut-out in this breadboard is not centered around the MOT position, but around the science position. However, the sloshing can be partially compensated by a simultaneous linear ramp of the current through offset coils. With this compensation the vertical temperature is reduced by $\sim 40\%$, the horizontal temperature by $\sim 20\%$. The peak density increases by a factor of ~ 2, the corresponding phase-space density by a factor of ~ 3.

In order to optimise the mode matching as well as the sloshing compensation, the temperature is a useful figure-of-merit. Especially for the sloshing compensation the temperature is a more convenient figure-of-merit than e. g. the peak density since the temperature can be obtained individually for the different axes.[19] In the following we will explain how the temperature in the magnetic trap is derived.

3.5.1 Thermometry

In contrast to optical traps the magnetic trap cannot be switched off in a fast way due to eddy currents that limit the decay time of any magnetic field (see sec. 3.4). This prevents to acquire meaningful time-of-flight measurements which is a common method to extract the temperature since this method requires a sudden release of the atoms.[20] Instead, the temperature can be extracted from in situ images of the atoms in the magnetic trap since the temperature is related to the density distribution as can be derived from the Maxwell-Boltzmann statistics:

[19] Due to the small background scattering length of potassium, the thermalisation time in the magnetic trap is in the order of a few seconds. Hence, the temperature extracted for different axes is not necessarily the same.

[20] Although it introduces a systematic error for low magnetic gradients one can still use time-of-flight measurements as a figure of merit for the temperature. For high gradients on the other hand the trajectory of the atoms after switching off the magnetic field is significantly affected by the remaining magnetic field.

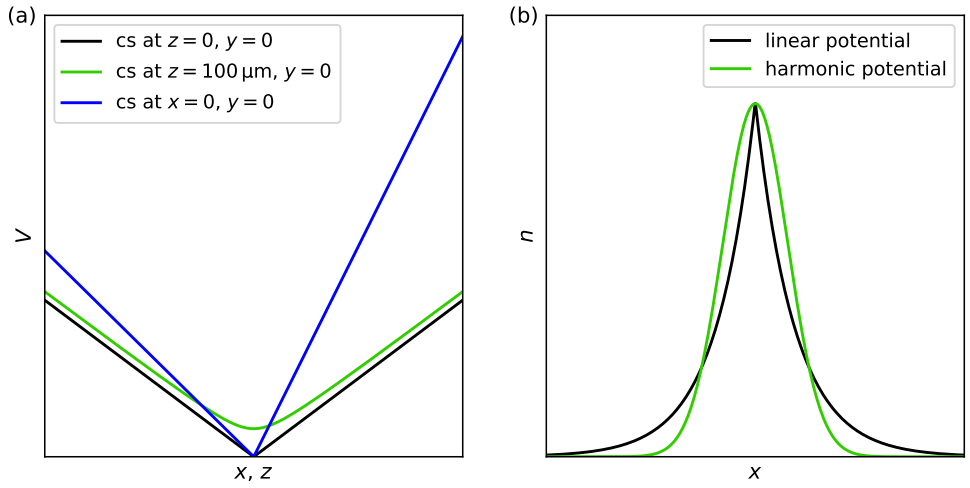

Figure 3.7: **(a)** Cross-section (cs) through the calculated potential V given by the magnetic trap including gravity. **(b)** Calculated density distribution n in a linear trapping potential as given by the magnetic trap for $y = z = 0$ (black). For comparison the density distribution in a harmonic potential (green) is shown as well.

Assuming thermal equilibrium the probability distribution $f(\mathbf{x},\mathbf{p})$ is given by

$$f(\mathbf{x},\mathbf{p}) = N' \exp\left[-\frac{E(\mathbf{x},\mathbf{p})}{k_B T}\right] \tag{3.1}$$

where N' is a normalisation constant such that $\int\int f(\mathbf{x},\mathbf{p}) d\mathbf{x} d\mathbf{p}$ is unity. Integrating over the momentum $\mathbf{p}$ and proper normalisation yields the spatial density distribution

$$n(\mathbf{x}) = n_0 \exp\left(-\frac{V(\mathbf{x})}{k_B T}\right) \tag{3.2}$$

where n_0 is the central density. The potential $V(\mathbf{x})$ is given by the magnetic potential $V_{\text{mag}}(\mathbf{x}) = g_F m_F \mu_B B(\mathbf{x})$ as well as by the gravitational potential and is plotted in fig. 3.7(a). Its shape is predominantly determined by the quadrupole field generated by the MOT or experiment coils in Anti-Helmholtz configuration. Close to the center of the respective coil pair the magnetic field strength can be approximated by

$$|B| = B' \sqrt{(x/2)^2 + (y/2)^2 + z^2} \tag{3.3}$$

where B' is the magnetic gradient in the vertical direction. Due to the coil geometry this axis is tighter confined than the radial direction. The vertical axis furthermore displays an asymmetry caused by the additional gravitational potential. Along the main axes, e. g. for $x = y = 0$, eq. 3.3 simplifies to a linear relation. In contrast to most optical traps where

the approximately harmonic potential leads to a Gaussian density distribution $n(x) \propto \exp(-V_{\mathrm{harm}}(x)/k_B T) \propto \exp(-x^2)$, the corresponding linear potential of the magnetic trap results in an exponential decay $n(x) \propto \exp(-V_{\mathrm{magn}}(x)/k_B T) \propto \exp(-x)$ as depicted in fig. 3.7(b).

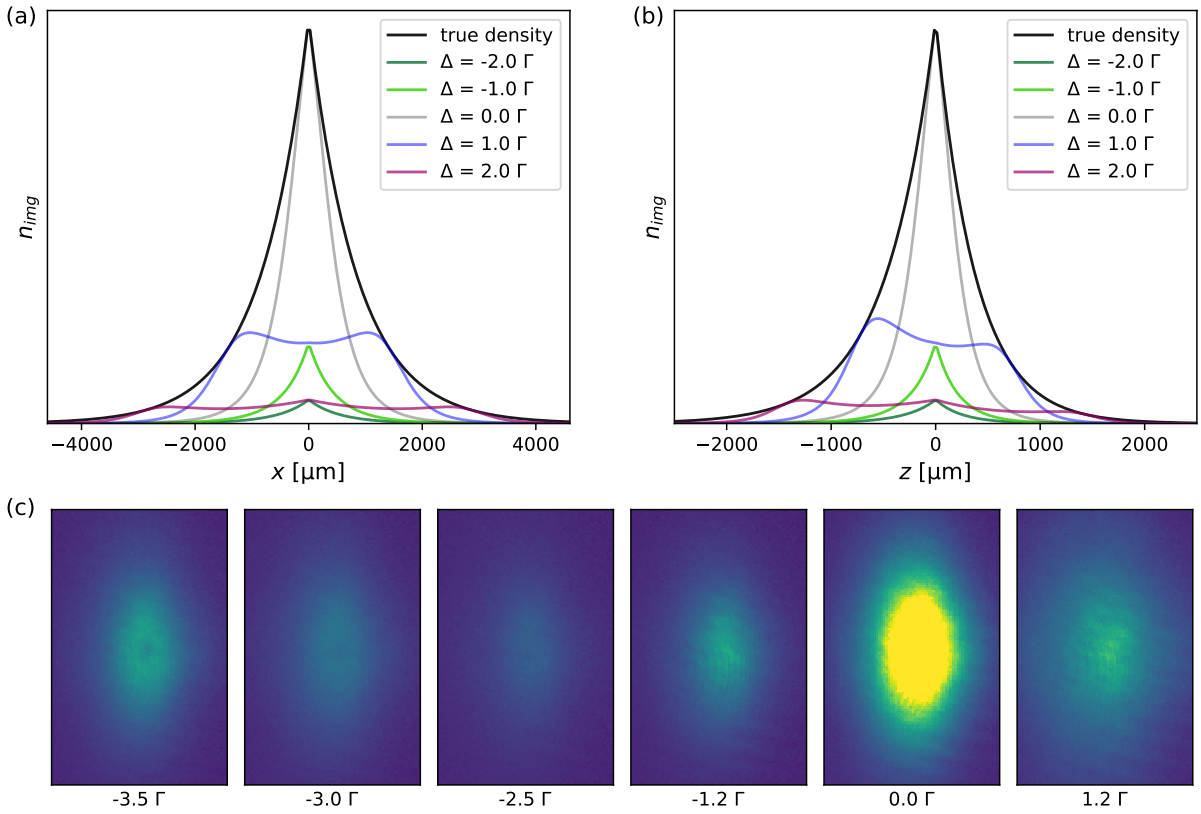

Figure 3.8: **(a),(b)** Cross-section at $y = z = 0$ (a) and at $x = y = 0$ (b) through the calculated imaged density distribution, i. e. taking into account that the effective imaging detuning is spatially dependent due to the Zeeman effect. The calculation is performed for different nominal imaging detunings Δ which is referenced to the resonance of the imaging transition at the trap center, i. e. $B = 0$. For comparison a cross-section through the true density distribution (black) neglecting any effect from the imaging is shown as well. **(c)** Images of the density distribution of the atom cloud in the magnetic trap for different nominal imaging detunings. The images are rotated by 90°, i. e. gravity acts along the horizontal axis of the images. The density distribution is derived by extracting the optical density via absorption imaging. Details on the observed shapes are given in the main text.

While eq. 3.2 describes the true density distribution it does not describe the imaged density distribution since it does not take into account that the magnetic gradient affects the imaging: The magnetic field introduces a Zeeman shift of the imaging transition, i. e. the spatially dependent gradient field results in a spatially dependent scattering rate $\gamma(\mathbf{x}) = \frac{\Gamma}{2} \cdot s \left[1 + s + (2\Delta(\mathbf{x})/\Gamma)^2\right]^{-1}$ where Γ is the natural linewidth, s the saturation

parameter and Δ the difference between the laser frequency and the resonance frequency of the imaging transition. Assuming $s \ll 1$ the imaged density distribution can be approximated by

$$n_{\text{img}} = n_{0,\text{img}} \exp\left(-\frac{V(\mathbf{x})}{k_B T}\right) \cdot \frac{1}{1 + \left(\frac{2\Delta(\mathbf{x})}{\Gamma}\right)^2}. \tag{3.4}$$

This means that depending on the detuning of the imaging light, different parts of the atom cloud are imaged as can be seen in fig. 3.8: When the imaging light is resonant to the transition frequency at the center position, i. e. the zero-field value, the central part of the cloud is imaged properly while the atoms in the outer parts of the cloud absorb less photons. Hence, the cloud appears smaller and neglecting the spatial dependence of the detuning would underestimate the temperature of the atoms. When the imaging light is blue-detuned with respect to the zero-field value, the resonance position moves away from the center to the outer parts of the cloud. The center becomes more transparent and the cloud appears to be ring shaped. When the imaging light is red-detuned with respect to the zero-field value, then no part of the atom cloud is resonant. The detuning with respect to the zero-field value is lowest at the center position, i. e. the scattering rate is highest at the center position and decreases with increasing distance to the center. Accordingly, the shape of the imaged density distribution is similar to the case where the imaging light is resonant at the center position, but has a smaller amplitude. One could think that it thus makes sense to rather use red-detuned than blue-detuned light, but that is not necessarily true since we cannot consider the atom as a pure 2-level system. The level spacing of the D2 manifold of K39 is very tight. When the imaging light is red-detuned to the imaging transition $|^2S_{1/2}, F = 2\rangle \rightarrow |^2P_{3/2}, F = 3\rangle$, one also sees an effect of the transition $|^2S_{1/2}, F = 2\rangle \rightarrow |^2P_{3/2}, F = 2\rangle$ to which the light is blue-detuned. Hence, a ring-like shape also occurs in the case of red-detuned light as illustrated in fig. 3.8.

Another effect that needs to be considered is that we cannot image tomographically, i. e. the 2D density distribution derived from the absorption images are not cross-sections through the atom cloud, but the density integrated over the line of sight as plotted in fig. 3.9. The integration broadens the distribution and flattens the center. Especially higher detunings result in a nearly Gaussian shape. Higher temperatures increase the size of the atom cloud and thus lead to a more pronounced detuning effect. Hence, even for a slight detuning of $0.25\,\Gamma$ higher temperatures result in a nearly Gaussian-shaped imaged density distribution. That also means that the shape of the density distribution is a convenient indicator: only for low temperatures the imaged density distribution displays not a Gaussian shape but the expected exponentially decaying wings.

With the true density distribution derived from the Maxwell-Boltzmann distribution

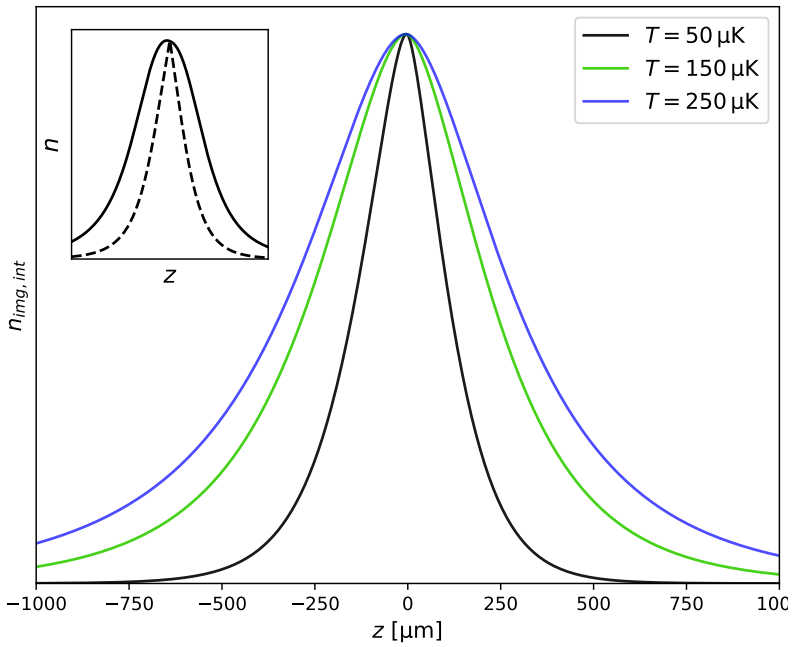

Figure 3.9: Cross-section at $x = 0$ through the calculated imaged density distribution of the atom cloud in the magnetic trap including the effect of the spatially dependent imaging detuning and including the line-of-sight integration along y. The calculation assumes a nominal imaging detuning of $\Delta = 0.25\,\Gamma$ and is performed for different temperatures T. To emphasize the effect of the line-of-sight integration a direct comparison between a cross-section at $x = y = 0$ (black, dashed) and a cross-section at $x = 0$ including the line-of-sight integration along y (black, solid) is depicted in the inset. Both cross-sections include the effect of the spatially dependent imaging detuning.

and taking into account the detuning effect and the line of sight integration the observed density distribution derived from absorption imaging can be explained and the temperature can be extracted by fitting to the measured density distribution as illustrated in fig. 3.10. It stands out that a fit to the two-dimensional data has to compromise between the vertical and the radial axis. This indicates that the atom cloud is not fully thermalised even after the magnetic transport. Hence, it makes sense to extract the temperatures separately for the vertical and the radial axis by integrating over the respective other axis and performing separate fits to the respective one-dimensional data. While the 2D fit yields a temperature of 91 µK, the 1D fits yield temperatures of $T_{\mathrm{vert}} = 89\,\mu\mathrm{K}$ and $T_{\mathrm{rad}} = 77\,\mu\mathrm{K}$ revealing that the temperature assigned to the vertical axis is higher than the temperature assigned to the radial axis. This is consistent with the fact that the sloshing movement explained above is more pronounced along the vertical axis than along the horizontal axis as was shown in fig. 3.6, and also with the fact that the sloshing movement caused by the decaying eddy currents is a limiting factor for the temperature of the atoms in the magnetic trap.

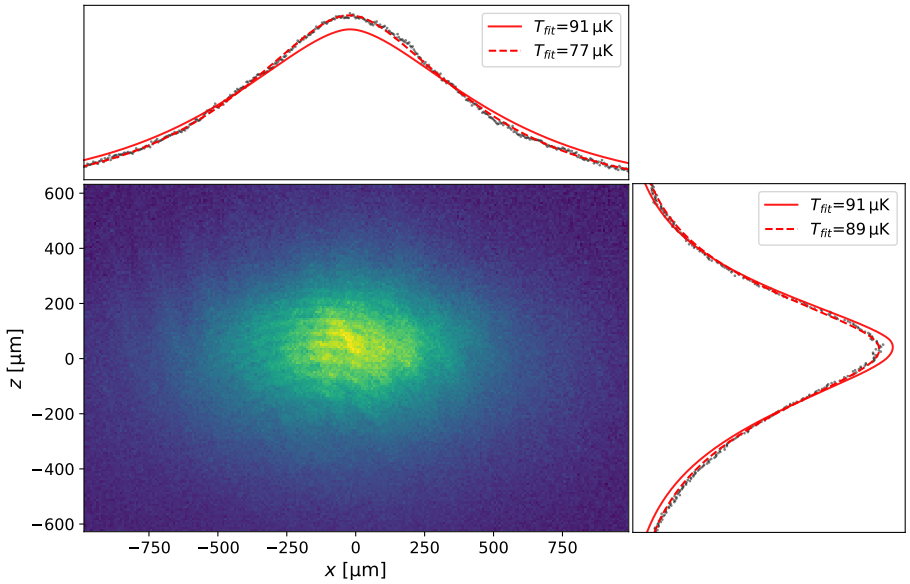

Figure 3.10: Density distribution of the atoms in the magnetic trap derived via absorption imaging after the transport to the science position and without sloshing compensation. Also shown are the linesums of the density distribution (black). The temperature is extracted by fitting to the data according to eq. 3.4 including the line-of-sight integration along y. For comparison two different fits are plotted: the linesums of a two-dimensional fit (red, solid) yielding a total temperature and two separate one-dimensional fits to the respective linesums (red, dashed) yielding different temperatures for the vertical and the radial axis. Details are given in the main text.

3.6 Collisional loading of the optical dipole trap

After the atoms are transported to the science position they are transferred from the magnetic trap to an optical dipole trap. In the following we will discuss the dynamics of our loading scheme and experimentally characterise the loading behaviour. Then, we will describe this behaviour with a simple model to understand the effect of the trap parameters. This allows us to infer the limitations of our current setup as well as potential improvements. A brief summary of the results can be found at the end of this section.

3.6.1 Motivation and concept

Transferring the atoms from the magnetic trap into an optical dipole trap decouples the atom position from the magnetic zero and thus allows to use the magnetic field as a free parameter. This is crucial to enable the use of Feshbach resonances in order to tune the interaction strength which is a key feature of our experiment.

While in principle it is possible to perform evaporation in the magnetic trap, e. g. RF evaporation, this scheme is inefficient for K39 due to a low background scattering length resulting in a low scattering rate in the magnetic trap. Therefore, we first transfer the

atoms from the magnetic trap into an optical trap and then perform the evaporation. Hence, the loading process aims to achieve good initial conditions for the subsequent evaporation (see sec. 3.7.3), i. e. low temperatures and in particular high atom numbers.

The loading scheme we apply is collisional loading: An optical 'dimple', i. e. an optical dipole trap much smaller than the reservoir, here given by the atom cloud in the magnetic trap, and with a depth much larger than the reservoir's temperature, is applied simultaneously to the magnetic trap as sketched in fig. 3.11. The atoms undergo elastic collisions where one of the two involved atoms has a chance to scatter into the dimple. That way, the optical trap is loaded non-adiabatically.[21]

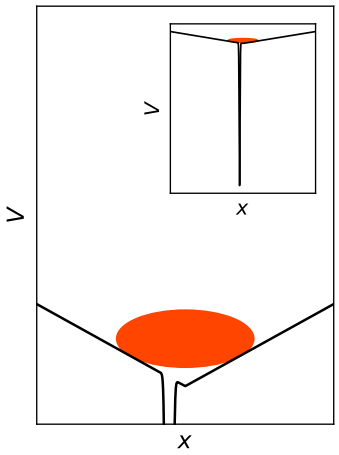

Figure 3.11: Combined magnetic and optical potential. Both potential depths and lengths are roughly to scale.

Since this scheme relies on elastic collisions, its efficiency depends on the collision rate. This has two main implications: First, a high density in the magnetic trap is required. To achieve this, it was crucial to introduce the hybrid MOT (see sec. 3.3), to reduce the time scale of the eddy currents (see sec. 3.4) and to reduce the temperature in the magnetic trap by reducing an observed sloshing movement (see sec. 3.5).

Second, it sets an essential requirement for the optical trap depth connected to the Ramsauer-Townsend effect [84]: Species with a small negative background scattering length, such as K39, feature the so-called Ramsauer minimum where the elastic cross-section in dependence of the collision energy drops by several orders of magnitude. For K39 the Ramsauer minimum is located at $\sim 400\,\mu\mathrm{K}$ and has a full width of $\sim 700\,\mu\mathrm{K}$:[22] Roughly in between $200\,\mu\mathrm{K}$ and $900\,\mu\mathrm{K}$ the cross-section is more than one order of magnitude lower

[21] One might wonder whether the D1 assisted loading scheme mentioned in sec. 2.2 is a reasonable alternative, but that is not the case. Compared to the collisional loading scheme it results in a lower temperature, but more importantly also in a much lower atom number. This is due to applying the near-resonant D1 light which introduces light-assisted collisions limiting the density. While the lower temperature achieved with the D1 assisted loading is more favorable when preparing small systems where the atom number is less relevant, the higher atom number achieved with the collisional loading scheme is favorable when striving for larger system sizes.

[22] Note that the position of the Ramsauer minimum depends on the scattering length [85]. The stated position assumes the background scattering length, i. e. $B = 0$. One might wonder whether the magnetic gradient of the trap introduces a shift of the Ramsauer minimum. However, the magnetic field in the relevant region is small due to the small size of the atomic cloud, and the $|2, 2\rangle$ state used here does not feature a Feshbach resonance that could introduce a significant scaling of the scattering length with the magnetic field in the relevant regime. Therefore, the position of the Ramsauer minimum is not shifted and nearly constant over the extent of the atomic cloud.

than the cross-section that corresponds to the background scattering length $a_{bg} \approx -33\,a_0$ [86]. [87, 88] The temperature in the magnetic trap is $\sim 100\,\mu\text{K}$, i. e. below this regime, but the energy from the optical potential the atoms gain at the location of the optical trap adds to the collision energy. That means the trap depth needs to be at least $\sim 1\,\text{mK}$ in order to get past the Ramsauer minimum.

The pre-existing 850 nm crossed dipole trap that is later on in the sequence utilised for the evaporation has a trap depth one order of magnitude below this limit. Hence, another optical trap was set up in the course of this work: a tightly focussed 1064 nm single-beam optical dipole trap (1064 nm ODT) with waists of $14.5\,\mu\text{m} \times 17.0\,\mu\text{m}$ and a corresponding Rayleigh range of 620 µm. With a maximum power[23] of 17 W a trap depth of $\sim 6\,\text{mK}$ is achieved, the corresponding measured radial trapping frequencies are 25 kHz and 19 kHz, the corresponding axial trapping frequency is 350 Hz. A discussion of the trap parameters can be found in sec. 3.6.3.

3.6.2 Loading dynamics

The dynamics of the collisional loading scheme are described in detail in [89] and can be briefly summarised as follows: the atoms in the magnetic trap follow periodic trajectories. Which trajectories are populated depends on the temperature in the magnetic trap. When the optical trap is non-adiabatically switched on it cuts out a certain region in the phase-space. Since the optical trap is much smaller than the magnetic trap this initially loaded atom number in the optical trap is small. With elapsing loading time atoms with a trajectory through the optical trap can scatter into the trap. The high trapping frequencies of the ODT lead to an increased density at the position of the optical trap enhancing the local scattering rate and thus the loading rate. This process can be sustained by re-thermalisation of the atoms in the magnetic trap due to scattering events which re-populate the trajectories through the ODT.

During this loading process losses can occur, mainly due to inelastic scattering events and Majorana spin-flip transitions [90] to magnetically anti-trapped spin states. One might think that the latter is irrelevant due to the optical confinement, but in fact it introduces an evaporation process due to the finite trapping potential for anti-trapped spin states. This can be easily avoided by introducing a spatial offset between the magnetic trap center and the ODT trap center as sketched in fig. 3.11 since Majorana transitions only occur close to the magnetic zero. The offset should be small, though, since the density in the magnetic trap and hence the loading rate increases towards the trap center.

[23] The maximal achievable power is slightly higher, allowing to use up to 19.4 W for short measurements. The stated maximum power of 17 W refers to the maximum long-term stable power setting.

However, our system differs from the description above in two main aspects: First, due to the low background scattering length of K39 the scattering rate in the magnetic trap is much lower leading to a thermalisation time in the order of a few seconds which is much longer than the time scales given by the loading and loss rates. Therefore, the re-population of the trajectories through the ODT is suppressed on the time scale relevant for the loading process, similar to [91]. Second, we do not switch on the ODT suddenly, but linearly ramp to the final depth within 100 ms.[24] For these reasons, the loading behaviour is altered compared to the description in [89].

In the following we will explore this behaviour in more detail. The experimentally loaded atom number N in dependence of the loading time t and for different trap parameters is shown in fig. 3.12. The observed behaviour of these loading curves can be explained by the three main effects that are relevant in our system: The first effect is the scattering from the magnetic trap into the ODT described by a loading rate $\Gamma(t)$. The second effect is the depletion of the trajectories that pass the ODT as explained above which leads to a decrease of the loading rate over time, $\dot{\Gamma}(t) < 0$, and the third effect are density dependent losses. While the depletion of the trajectories already causes a saturation of the loading curve, the competition with the losses yields an actual peak feature resulting in a maximum atom number $N_{\max}$ loaded after the respective optimal loading time $t_{\max}$. The data shown in fig. 3.12 already illustrates that these quantities depend on the trap parameters.

To discuss this more quantitatively we describe the loading process with the following simple model: At $t = 0$ the ODT is switched on and cuts out part of the phase-space resulting in an initial atom number N_0.[25] For the subsequent dynamics we then assume an exponentially decreasing loading rate $\Gamma(t)$, and two-body losses with a rate Γ_{loss}:

$$\dot{N}(t) = \Gamma(t) + \Gamma_{\text{loss}} = \Gamma_0 \exp(-t/\tau) - KN^2 \quad \text{with} \quad N(t=0) = N_0 \tag{3.5}$$

Fitting our measured data to this model shows good agreement[26] as can be seen in fig. 3.12 (a) and allows to extract Γ_0, $N_{\max}$ and $t_{\max}$ plotted in fig. 3.12 (b), (c).[27]

[24] The ramp time is mainly determined by the simultaneous ramp of the magnetic gradient from the value set by the magnetic transport to the value desired for the loading process.

[25] Since we perform an adiabatic ramp, short compared to the loading time, instead of a sudden switch on N_0 is higher than one would expect from a cut-out in the phase-space, but the qualitative behaviour is basically the same.

[26] Assuming a linearly decreasing loading rate or three-body losses yields similar results indicating that our model is not sensitive to the exact shape of the loading or the loss rate.

[27] Note that Γ_0 is directly obtained from the fit since it is one of the free parameters, next to N_0, τ and K, while $N_{\max}$ and $t_{\max}$ are the peak values of the fitted curves, i. e. derived from the fitted curve.

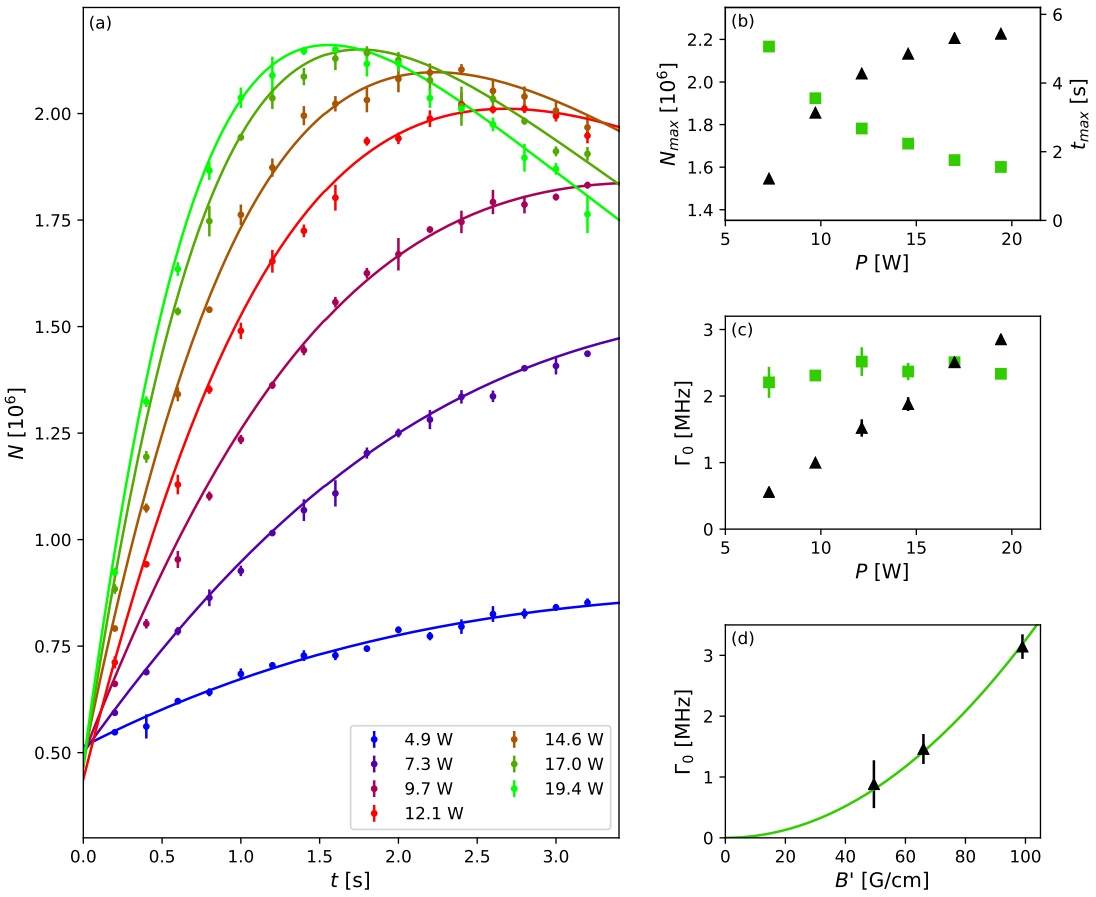

Figure 3.12: Performance of the collisional loading scheme for different settings. **(a)** Loaded atom number N (dots) in dependence of the loading time t for different ODT powers P. For each loading curve a fit (solid lines) with a model described by the differential equation $\dot{N}(t) = \Gamma_0 \exp(-t/\tau) - KN^2$ and the initial condition $N(t = 0) = N_0$ is performed. **(b)** Maximum loaded atom number $N_{\max}$ (black triangles) and the corresponding loading time $t_{\max}$ (green squares) in dependence of the ODT power P extracted from the fitted curves in (a). **(c)** The initial loading rate Γ_0 as derived by fitting to the loading curves as shown in (a) (black triangles) in dependence of the ODT power P. Also plotted is the initial loading rate rescaled to $P = 17\,\mathrm{W}$ (green squares) assuming the scaling $\Gamma_0 \propto P^{3/2}$ derived in eq. 3.7 and including the power dependence of the elastic cross-section. The latter is only relevant for the first data point, though. The rescaled initial loading rate is roughly constant supporting the validity of the derived power scaling. **(d)** Fitted initial loading rate Γ_0 for different magnetic gradients B' (black triangles). Also shown is a quadratic fit (green, solid) with one free parameter $\Gamma_0 = c \cdot B'^2$.

For further analysis, especially regarding the effect of the trap parameters, it is useful to consider also a theoretical estimate for the initial loading rate which is given by the initial atom number N_b in the magnetic trap, modified by a spatial factor V_r and a temporal factor t_r, and by the scattering rate Γ_{sc} at the ODT position as will be explained in the following [91]:

$$\Gamma_0 \simeq N_b \cdot V_r \cdot t_r \cdot \Gamma_{sc} \simeq N_b \cdot \frac{w}{l_b} \cdot \frac{t_{ODT}}{t_b} \cdot n_b \sigma \bar{v} \tag{3.6}$$

The spatial factor accounts for the fact that only a fraction of the atoms in the magnetic trap has a trajectory through the ODT and can be estimated by the ratio of the trap's length scales $V_r \simeq w/l_b$. The length scale of the ODT can be estimated by its waist w, while the length scale of the magnetic trap can be estimated by the $1/e^2$-length of the density distribution $l_b \simeq 2k_BT/(\mu_B B')$ determined by the temperature T and the magnetic gradient B'.

The temporal factor refers to the atom fraction that is at a generic time in the dipole trap[28] and can be estimated by the fraction of time an atom spends in the ODT. Therefore, the transit time t_{ODT} through the ODT is compared to the 'oscillatory' time t_b in the magnetic trap $t_r \simeq t_{ODT}/t_b$. $t_{ODT} \simeq 1/\bar{\omega}$ can be estimated by the inverse of the mean trapping frequency $\bar{\omega}$, while $t_b \simeq l_b/\bar{v_b}$ can be estimated via the mean velocity $\bar{v_b} = \sqrt{8k_BT/\pi m}$ in the magnetic trap.

The scattering rate at the ODT position is given by $\Gamma_{sc} = n_b\bar{\sigma v}$ where n_b is the density in the magnetic trap, σ the elastic cross-section and v the relative velocity of the scattering atom pairs. σ and v are both determined by the collision energy E in the center-of-mass frame which can be estimated by the ODT depth U_0. For high trap depths as used for the collisional loading scheme, σ becomes nearly constant and the scattering rate can be estimated by $\Gamma_{sc} \simeq n_b\sigma\bar{v}$.

Eq. 3.6 is just an estimate, e. g. not taking into account the fraction of the scattering events where no atom is scattered into the ODT and accordingly, the loading rate is overestimated. However, it still gives a reasonable estimate; with the ODT parameters stated above, $N_b \approx 3.8 \cdot 10^8$, $l_b \approx 360\,\mu\text{m}$, $T \approx 120\,\mu\text{K}$ in the magnetic trap, $n_b \approx 2.4 \cdot 10^{10}\,\text{cm}^{-3}$, $\sigma \approx 8\pi(33a_0)^2$ and $\bar{v} \approx 1.8\,\text{m/s}$ a loading rate of $\sim 7\,\text{MHz}$ is estimated for the full ODT power of 17 W compared to a fitted loading rate of $\sim 2.5\,\text{MHz}$.

3.6.3 ODT parameters

In the following, we will qualitatively investigate the effect of the relevant ODT parameters, namely the laser power P and the waist[29] w, on the loading performance. Therefore, we again employ our model $\dot{N}(t) = \Gamma_0 \exp(-t/\tau) - \Gamma_{\text{loss}}$ with $\Gamma_{\text{loss}} = KN(t)^2$ and the initial condition $N(t=0) = N_0$ and derive how the loading and the loss term scale with the ODT parameters:

P and w affect the trap depth $U_0 \propto Pw^{-2}$ and both trapping frequencies $\omega_{rad} \propto P^{1/2}w^{-2}$ and $\omega_{ax} \propto P^{1/2}w^{-3}$ as can be easily derived from the Gaussian beam profile.[30]

[28] in the dipole trap, but not trapped

[29] For simplicity we assume equal radial waists for the scaling analysis.

[30] The different waist scalings for the radial and the axial trapping frequency stem from the fact that

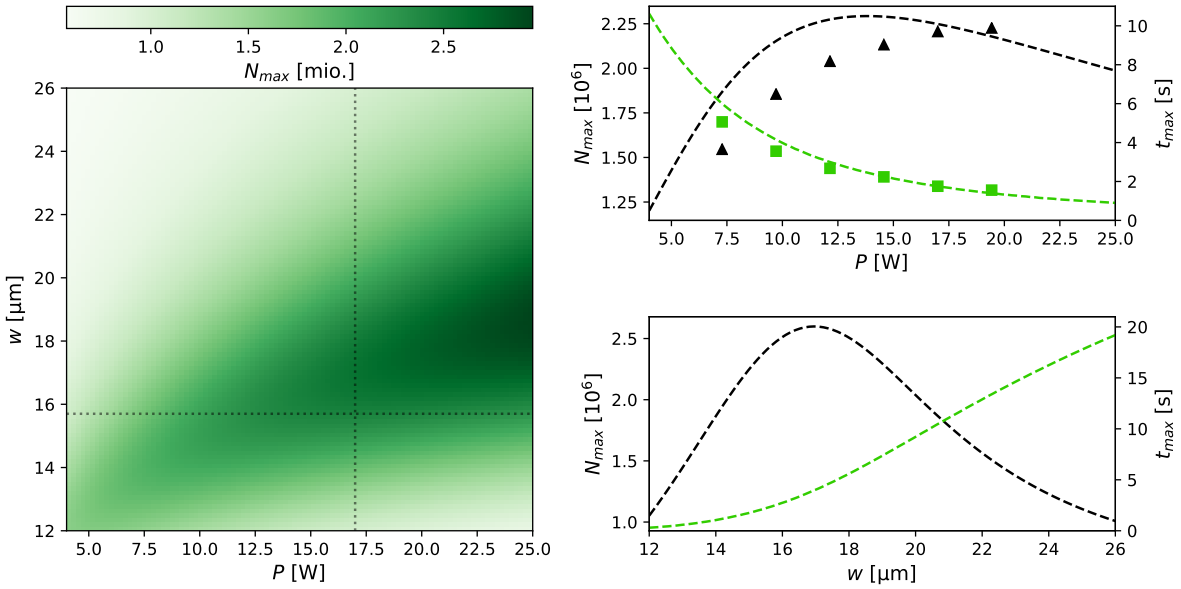

Figure 3.13: Simulated performance of the collisional loading scheme in dependence of power P and waist w of the optical trap. The maximal loaded atom number $N_{\max}$ and the corresponding loading time $t_{\max}$ were derived by modelling the loading behaviour with the differential equation $\dot{N}(t) = \Gamma_0 \exp(-t/\tau) - \Gamma_{\text{loss}}$ with $\Gamma_{\text{loss}} = KN^2$ and the initial condition $N(t=0) = N_0$, with Γ_0, τ, K and N_0 given by the fits shown in fig. 3.12, but rescaled according to eq. 3.7 and 3.8. Our settings, $P = 17\,\text{W}$ and $\bar{w} = 15.7\,\mu\text{m}$, are marked (black, dotted) in the 2D plot on the left. Cross-sections through the 2D plot along these lines are provided on the right where both the maximal loaded atom number $N_{\max}$ (black) as well as the corresponding loading time $t_{\max}$ (green) are shown. For comparison the measurement data presented in fig. 3.12 (b) is also included. The results of this simulation are discussed in the main text.

These parameters again affect the spatial factor $V_r \propto w$ and the temporal factor $t_r \propto \bar{\omega}^{-1}$ with $\bar{\omega} = (\omega_{rad}^2 \omega_{ax})^{1/3}$, as well as the mean relative velocity $\bar{v} \propto U_0^{1/2}$. Although n_b only depends on the magnetic trap, we do introduce a scaling $n \propto \bar{\omega}^3$ to account for the density enhancement caused by the ODT. Hence, the loading rate scales with

$$\Gamma_0 \propto P^{3/2} w^{-14/3} \tag{3.7}$$

This power scaling is in excellent agreement with our measurement data as can be seen in fig. 3.12 (c). The rescaled loading rate shown there does include the changing elastic cross-section. This mainly affects the first data point, though, validating the assumed constant cross-section in eq. 3.7.

The loss rate on the other hand scales with $\Gamma_{\text{loss}} \propto n^2 \propto \bar{\omega}^6$ yielding

$$\Gamma_{\text{loss}} \propto P^3 w^{-14} \tag{3.8}$$

the radial confinement is determined directly by the waist while the axial confinement is determined by the Rayleigh range $z_r \propto w^2$.

The loss rate scales much stronger with power and waist than the initial loading rate, indicating that low powers and high waists are favorable. However, this does not take into consideration the different time dependencies: The loading rate decreases with elapsing time while the loss rate increases due to the increasing density, resulting in a parameter-dependent optimal loading time $t_{\max}$. Furthermore, the loss term depends on the atom number, $\Gamma_{\text{loss}} \propto N(t)^2$, i. e. on the solution of the differential equation, while the loading term is independent of $N(t)$. Hence, a simple comparison of the scalings derived in eq. 3.7 and 3.8 is not sufficient to deduce a reasonable parameter regime. Instead we use our model (eq. 3.5) with the fit values from the measured loading curve at 17 W in fig. 3.12 as a reference[31] and rescale the parameters Γ_0 and K according to eq. 3.7 and 3.8. Numerically integrating the differential equation then allows to extract $N_{\max}$ for variable parameters P and w.

The results of this simulation are shown in fig. 3.13. Comparing these results to our measurement data in fig. 3.12 (b) reveals quantitative differences, mainly a saturation already at lower powers. This is to be expected, though, since the simulation is based on a simplified model with an estimated loading rate. However, the simulation and measurement results are in qualitative agreement, suggesting that the simulation is a valid basis to find suitable ODT parameters:

While there is an optimal waist for a chosen power and vice versa, in general higher waists and higher powers are advantageous. Hence, we use the maximal available power of 17 W. The simulation indicates that our waists of 14.5 µm and 17 µm are close to the optimum for that power. Although we did not systematically study the effect of the waist, that is in agreement with measurements we performed.

3.6.4 Magnetic trap parameters

Next, we will analyse how the loading performance is affected by the quadrupole trap which is characterised by the magnetic gradient B'. Since the gradient is adiabatically changed between the final value of the magnetic transport to B' for the collisional loading, B' affects both the length scale $l_b \propto T/B'$ as well as the temperature T.

Due to the adiabaticity the phase-space density $\rho \propto n_b T^{-3/2}$ is constant where $n_b \propto l_b^{-3} \propto (B'/T)^3$ which yields $T \propto B'^{2/3}$. Accordingly, $V_r \propto l_b^{-1} \propto B^{1/3}$ is affected as well as $t_b \approx l_b/\bar{v} \propto l_b/T^{1/2} \propto B'^{-2/3}$ and $\Gamma_{sc} \propto n_b \propto B'$. Hence, the loading rate scales with

$$\Gamma_0 \propto B'^2 \tag{3.9}$$

[31] The results are similar when using a different measured loading curve as reference.

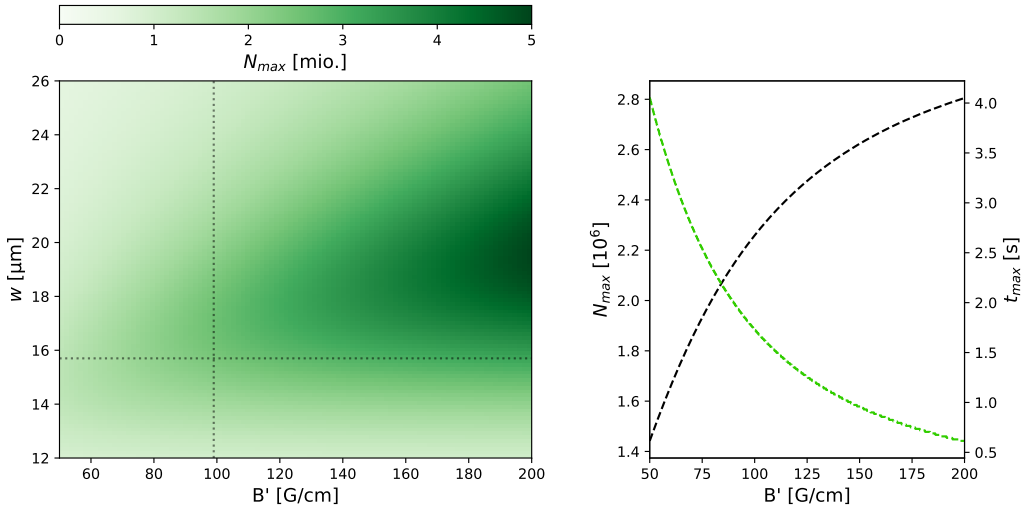

Figure 3.14: Simulated performance of the collisional loading scheme in dependence of the magnetic gradient B' and the ODT waist w. The maximal loaded atom number $N_{\max}$ and the corresponding loading time $t_{\max}$ were derived by modelling the loading behaviour with the differential equation $\dot{N}(t) = \Gamma_0 \exp(-t/\tau) - \Gamma_{\text{loss}}$ with $\Gamma_{\text{loss}} = KN^2$ and the initial condition $N(t=0) = N_0$, with Γ_0, τ, K and N_0 given by the fits shown in fig. 3.12, but rescaled according to eq. 3.7 and 3.8, 3.9 and 3.10. Our settings, $B' = 99\,\text{G/cm}$ and $\bar{w} = 15.7\,\mu\text{m}$, are marked (black, dotted) in the 2D plot on the left. A cross-sections through the 2D plot along at $w = 15.7\,\mu\text{m}$ is provided on the right where both the maximal loaded atom number $N_{\max}$ (black) as well as the corresponding loading time $t_{\max}$ (green) is shown. The results of this simulation are discussed in the main text.

This scaling is in agreement with our measurements as can be seen in fig. 3.12 (d).

The loss rate Γ_{loss} is proportional to n^2 and thus also scales quadratically with the magnetic gradient:

$$\Gamma_{\text{loss}} \propto B'^2 \tag{3.10}$$

We perform a simulation analogous to the previous section where the effects of the ODT parameters were discussed and employ our model with according to eq. 3.9 and 3.10 rescaled parameters Γ_0 and K.

The results are shown in fig. 3.14. In contrast to the ODT parameters each featuring a finite optimum when the respective other parameters are fixed, $N_{\max}$ starts to saturate with increasing gradient. This can be explained by the depletion of the trajectories through the ODT. Accordingly, the saturation threshold can be increased by increasing the ODT waist and thus the number of trajectories through the ODT. In any case it is favorable to use the maximum viable gradient. In our setup this gradient is limited to $\sim 100\,\text{G/cm}$ mainly due to the large vacuum chamber setting a rather high lower limit for the distance of the quadrupole coils to the atom position.

3.6.5 Summary

With the described collisional loading scheme we load up to $\sim 2.2 \cdot 10^6$ atoms within $\sim 2\,\mathrm{s}$ from the magnetic trap with a gradient of $\sim 100\,\mathrm{G/cm}$ into a single-beam 1064 nm optical dipole trap with waists of $14.5\,\mu\mathrm{m} \times 17\,\mathrm{um}$ and a laser power of 17 W. The achieved temperature in the ODT is $\sim 500\,\mu\mathrm{K}$ and depends on the optical trap depth. The experimentally observed loading behaviour can be well described with a simple model $\dot{N}(t) = \Gamma_0 \exp(-t/\tau) - KN(t)^2$ with the initial condition $N(t=0) = N_0$ which assumes an exponentially decreasing loading rate and two-body losses. Simulations based on that model indicate that our loaded atom number is limited by the laser power, when the ODT waist is accordingly adapted, and especially by the magnetic gradient. Measurements from before and after reducing the temperature in the magnetic trap (see sec. 3.5) also indicate that the loaded atom number can be improved by further reducing the temperature and thus increasing the density in the magnetic trap. Note that for other atomic species re-thermalisation in the magnetic trap might become relevant provided that the background scattering length is high enough. In that case, the trajectory depletion becomes negligible and the loading behaviour is significantly altered, leading to higher atom numbers.

3.7 Evaporation

So far only optical cooling techniques were discussed. Optical techniques suffer from a density limitation, though: At high densities, as achieved after loading into the 1064 nm ODT, the atom cloud gets optically dense which prevents to properly optically address the atomic sample. Hence, to reach degeneracy we employ evaporative cooling which is a non-optical cooling technique: The mean energy is reduced by non-optically removing hot particles from the trap. The high scattering rate required for a sufficiently fast re-thermalisation is ensured by exploiting Feshbach resonances. In the following we will discuss which Feshbach resonances are suitable for evaporation, describe how the spin states exhibiting the respective Feshbach resonance are prepared and elaborate on the experimental evaporation procedure.

3.7.1 Selecting a Feshbach resonance

Feshbach resonances are an important tool in the field of ultracold quantum gases as they allow to tune the scattering length and thus the interaction strength. A more detailed

discussion of the theoretical background, applications, and related experiments can be found in the highly recommendable review by Chin *et al.* [11]. Here we only give a brief overview:

A Feshbach resonance occurs when two molecular potentials, one of them representing an open, the other a closed channel, have a relative energy such that a bound state of the closed channel is energetically close to the threshold of the open, so-called entrance channel. In that case two colliding atoms with a small energy in the entrance channel couple to the molecular bound state which leads in the resonance case to a divergence of the scattering length a. Hence, the scattering length can be controlled by tuning the energy difference of entrance and closed channel. When the magnetic moments of the two channels are different, this can be done via a magnetic field B.

The scattering length associated to a magnetically tunable Feshbach resonance can be locally described by $a(B) = a_{bg}\,(1 - \Delta/(B - B_0))$ and hence are characterised by three parameters: The center position B_0 is the magnetic field at which the scattering length diverges and where the sign of the scattering length flips. That means one side of the resonance features a positive scattering length, corresponding to repulsive interaction, while the other side features a negative scattering length, corresponding to attractive interaction. Further away from the center position, the absolute value of the scattering length gets smaller and eventually approaches the background scattering length a_{bg}. The width Δ corresponds to the magnetic field difference between B_0 and the zero crossing of the scattering length. Only one side of a Feshbach resonance features such a zero crossing; which side depends on the sign of a_{bg}. Note that a_{bg} weakly depends on B and can therefore only locally be assumed to be constant.

Overview of K39 Feshbach resonances and selection criteria

For K39 all spin combinations of the $F = 1$ hyperfine manifold exhibit Feshbach resonances at experimentally accessible magnetic field strength as can be seen in fig. 3.15. In principle the evaporation scheme only requires repulsive interactions, i. e. a positive scattering length, in order to be in a stable regime[32]Therefore, to first order any intrastate Feshbach resonance could be used for evaporation.

However, in order to choose a suitable resonance there are further aspects to consider:

[32]For attractive interactions the atom cloud gets unstable in the sense that the density increases with time resulting in severe two- and three-body losses. Note, though, that this is a simplification. Due to delocalisation, i. e. a kinetic energy term counteracting the attractive interaction term, there is also a stable regime for attractive interactions. However, this regime lies within the weakly interacting regime and is hence irrelevant for the evaporation where high scattering lengths are required.

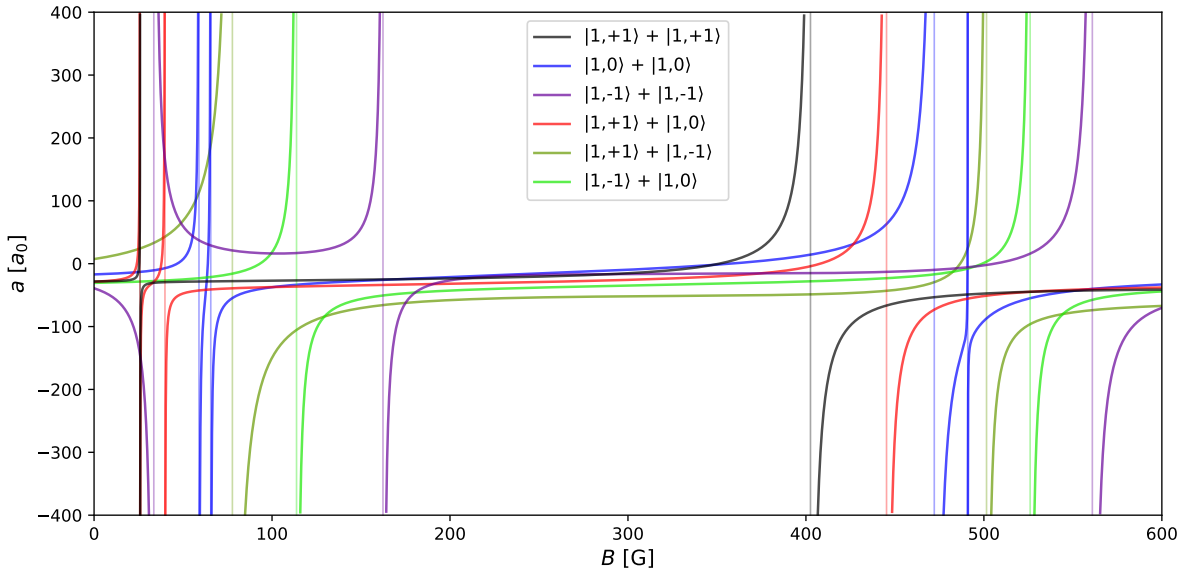

Figure 3.15: Scattering length a in dependence of the magnetic field B for all spin combinations of the $F = 1$ manifold of K39. The data for the Feshbach resonances is taken from [92]. The effective scattering length when considering multiple resonances, especially when close to each other, is calculated according to [93], but with $a_{bg} = a_{bg}(B)$. However, $a_{bg}(B)$ is approximated to be stepwise linear between the resonances.

First of all, the width of the resonances is of great importance. There are two types of Feshbach resonances: closed channel dominated resonances with a width typically below 1 G, hence also called narrow resonances, and entrance channel dominated resonances with a width typically much larger than 1 G, also called broad resonances.[33] [11] When utilising Feshbach resonances for tuning the scattering length as in our case, broad resonances are much more suitable since narrow resonances suffer from a higher loss rate compared to broad resonances [94]. Furthermore, for broad resonances the scattering length scales more weakly with the magnetic field which reduces the effect of magnetic field fluctuations.

Second, independent of the properties of the Feshbach resonances, one also needs to take the spin preparation into account. Usually, edge states are favorable since they are typically easier to prepare, e. g. via Landau-Zener sweeps.

Third, one also needs to consider how to proceed after the evaporation. When tuning the magnetic field for subsequent experiments and for imaging the sample, it is favorable to stay in a stable regime and to avoid crossing the resonance positions where the scat-

[33]Note that the classification does not rely on the width Δ, but can be expressed by a dimensionless resonance strength parameter s_{res} being much larger or smaller than 1, which depends on Δ, but also on further parameters such as the background scattering length or the difference of the magnetic moments of closed and entrance channel. Hence, although rarely, there are resonances with a width much larger than 1 G that are nevertheless more closed channel dominated.

tering length diverges. Accordingly, it makes sense to choose a Feshbach resonance in a magnetic field regime that is appropriate for imaging. Furthermore, many experiments make use of a second spin state. Thus, it is advantageous to use an intrastate Feshbach resonance for evaporation that is close to an interstate Feshbach resonance for subsequent measurements such that the interstate resonance is within the repulsive and hence stable regime of the intrastate resonance. Analogous, one also needs to consider the positions of the intrastate resonances of the second spin state.

Feshbach resonances suitable for evaporation

Considering the criteria above we found the most convenient Feshbach resonances for the evaporation to be the $|1,+1\rangle + |1,+1\rangle$ resonance at $\sim 400\,\mathrm{G}$ and the $|1,\text{-}1\rangle + |1,\text{-}1\rangle$ resonance at $\sim 560\,\mathrm{G}$:

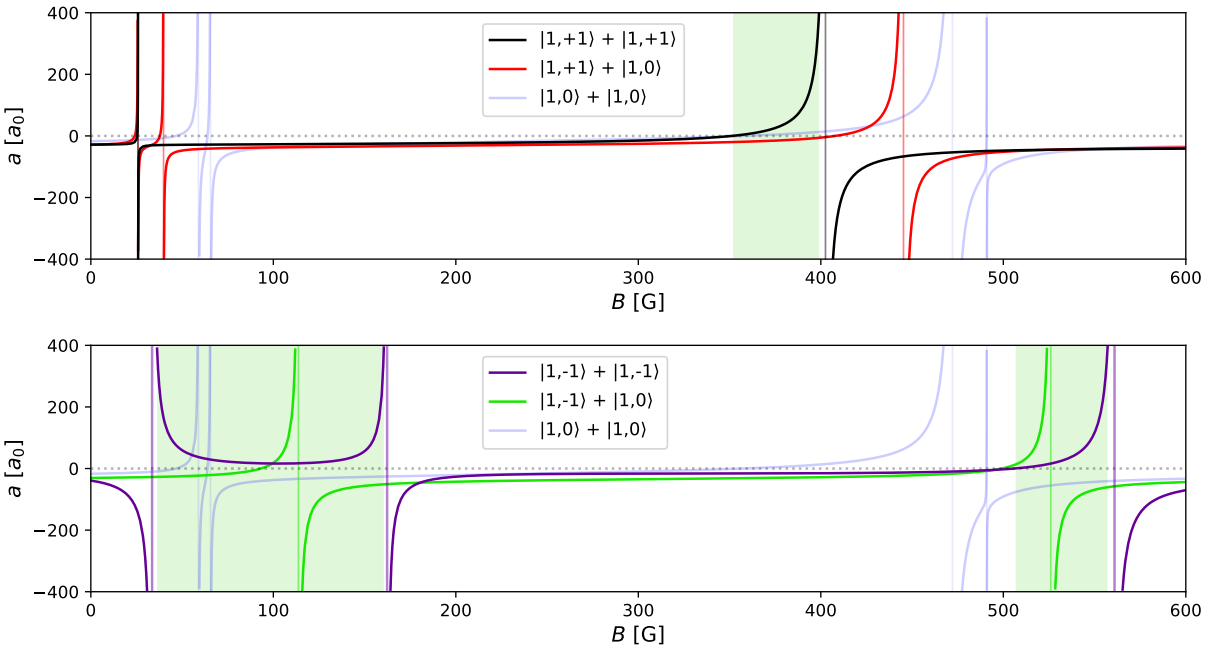

Figure 3.16: Scattering length a in dependence of the magnetic field B for selected spin combinations. The data is the same as in fig. 3.15. **Top:** Relevant Feshbach resonances when evaporating in the $|1,+1\rangle$ state. **Bottom:** Relevant Feshbach resonances when evaporating in the $|1,\text{-}1\rangle$ state. The regimes where the respective intrastate scattering length is positive as required for evaporation are shaded in green. The respective regime of the $|1,+1\rangle$ state (top) around 25 G has a width of only $\sim 0.5\,\mathrm{G}$ and is hence barely visible.

The $|1,+1\rangle$ state is in our case the easiest to prepare: After the magnetic transport the atoms are in the $|2,+2\rangle$ state and the atoms can thus be transferred to the $|1,+1\rangle$

state with a single RF π-pulse. Up to 600 G the $|1,+1\rangle$ state features two intrastate Feshbach resonances, at $\sim$26 G and at $\sim$400 G as shown in fig. 3.16 (top). The first one is a narrow Feshbach resonance and thus inconvenient, the latter on the other hand is a broad resonance and thus suitable. In the regime with positive scattering length there is no interstate Feshbach resonance, though. Hence, the $|1,+1\rangle + |1,+1\rangle$ resonance at $\sim$400 G is the most convenient choice in the case that no second spin state is required.

If subsequent experiments on the other hand do require a second spin state, then the $|1,\text{-}1\rangle + |1,\text{-}1\rangle$ resonance at $\sim$560 G is the most convenient Feshbach resonance for evaporation. Up to 600 G the $|1,\text{-}1\rangle$ state features three intrastate resonances: at $\sim$34 G, at $\sim$160 G and at $\sim$560 G. All of these are broad resonances and the corresponding regimes with positive scattering length are marked in fig. 3.16 (bottom). As a second spin state only the $|1,0\rangle$ state is suitable since $|1,\text{-}1\rangle + |1,+1\rangle$ can scatter into $|1,0\rangle + |1,0\rangle$ which acts as a severe loss channel. Up to 600 G there are two $|1,\text{-}1\rangle + |1,0\rangle$ resonances, at $\sim$115 G and at $\sim$525 G, both in the regime with repulsive $|1,\text{-}1\rangle + |1,\text{-}1\rangle$ interaction. Hence, all three intrastate resonances have a suitable interstate resonance on their respective repulsive side. One could think that the lower field resonances are more convenient since the intra- and interstate resonances are further apart yielding a weaker tuning of the intrastate scattering length in the region of the interstate resonance. But that does not take into account the imaging: It is much more favorable to image the atomic sample at high magnetic fields, i. e. deeper in the Paschen-Back regime to achieve more closed imaging transitions [76]. When using the lower field resonances one would need to cross the resonance positions with diverging scattering length to reach a reasonable imaging field and the necessity to ramp the field by a few 100 G would introduce a rather high lower limit for the time in between the actual experiment and imaging. Hence, it is favorable to use the resonance at $\sim$560 G for evaporation. Note, though, that the $|1,0\rangle + |1,0\rangle$ interaction is attractive in the region of the interstate resonance. Accordingly, it is not recommendable to use high densities of atoms in the $|1,0\rangle$ state.[34]

[34] It would be also possible to work with the $|1,0\rangle$ state and the $|1,+1\rangle$ as a second spin state using the $|1,0\rangle + |1,0\rangle$ resonance at $\sim$470 G for evaporation and the $|1,0\rangle + |1,+1\rangle$ resonance at $\sim$445 G for tuning the interstate scattering length. This is less favorable, though, due to the smaller distance of both intrastate resonances to the interstate resonance.

3.7.2 Spin preparation

After loading the 1064 nm ODT the atoms are in the $|2,2\rangle$ state[35] while the state favorable for evaporation and subsequent experiments is $|1,+1\rangle$ or $|1,-1\rangle$ as discussed in sec. 3.7.1. While the experimental sequence for K40 allowed to prepare the desired spin states by optical pumping (see sec. 2.2), this is not an option for the K39 sequence. The high density and hence also high optical density in the 1064 nm ODT prevents efficient optical pumping. Instead we employ RF π-pulses via the single-loop in-vacuo antenna (see sec. 2.1.1) for the spin preparation.

The preparation of the $|1,+1\rangle$ state simply requires a single π-pulse for the transfer $|2,2\rangle \rightarrow |1,+1\rangle$ (see fig. 3.17 (a)). The transfer is performed at a few Gauss to provide a quantisation axis. The Rabi rate of the transfer is $2\pi \cdot 5.3\,\mathrm{kHz}$. Since the atoms can undergo hyperfine changing collisions in the $F = 2$ manifold, which is especially relevant in the 1064 nm ODT due to the high density, it is advantageous to perform the spin transfer as soon as possible after the collisional loading scheme.

Preparing the $|1,-1\rangle$ state requires additional RF transfers. We start out with the transfer $|2,2\rangle \rightarrow |1,+1\rangle$ just as for preparing the $|1,+1\rangle$ state and then proceed with two further π-pulses for the transfer $|1,+1\rangle \rightarrow |2,0\rangle \rightarrow |1,-1\rangle$ (see fig. 3.17 (b)). A more conventional Landau-Zener scheme $|1,+1\rangle \rightarrow |1,0\rangle \rightarrow |1,-1\rangle$ showed poor performance which we attribute to fast decoherence due to $|1,+1\rangle$+$|1,-1\rangle \leftrightarrow$ |1,0⟩+|1,0⟩ scattering. This hypothesis is supported by the fact that we found a reasonable performance of the $|1,+1\rangle \rightarrow |1,0\rangle$ transfer, but still poor performance for the $|1,0\rangle \rightarrow |1,-1\rangle$ transfer at fields of $\sim 200\,\mathrm{G}$ where |1,0⟩+|1,0⟩ $\rightarrow |1,+1\rangle$+$|1,-1\rangle$ scattering is energetically forbidden while $|1,+1\rangle$+$|1,-1\rangle \rightarrow$ |1,0⟩+|1,0⟩ scattering is still allowed.

Since it is technically more convenient, we use the same RF transfer frequency for the first transfer $|2,2\rangle \rightarrow |1,+1\rangle$ and the second transfer $|1,+1\rangle \rightarrow |1,0\rangle$ and instead tune the magnetic field to achieve resonance. Since the $|1,+1\rangle$ state is spin-protected the additional time for the magnetic ramp does not introduce significant losses. In the $|2,0\rangle$ state on the other hand the atoms can undergo hyperfine changing collisions. Hence it is advantageous to minimise the time the atoms spend in that state. Accordingly, we use the same magnetic field for second and third transfer, use a second RF transfer frequency instead and perform the third transfer right after the second transfer. The Rabi rate for both, second and third transfer is $2\pi \cdot 2.2\,\mathrm{kHz}$.

[35] The atoms were transferred to the $|2,2\rangle$ state for the magnetic transport since this is the ground state in which the atoms have the highest magnetic moment and thus experience the strongest confinement in the magnetic trap. The collisional loading scheme used to then load the atoms from the magnetic trap into the 1064 nm ODT does not affect the state.

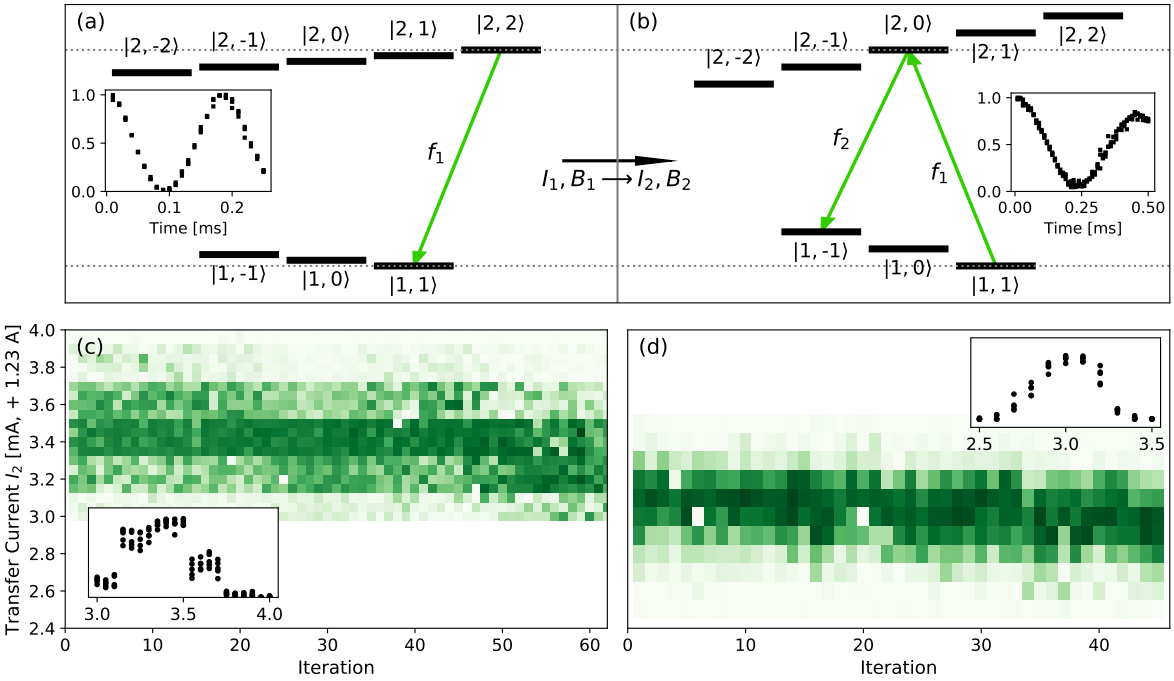

Figure 3.17: Spin preparation scheme. **(a)** Preparing the $|1,+1\rangle$ state is achieved with a single RF π-pulse with frequency f_1 driving the transition $|2,2\rangle \rightarrow |1,+1\rangle$. The inset shows the Rabi oscillation of this transfer, where the y-axis corresponds to the $|2,2\rangle$ population. **(b)** For preparing the $|1,-1\rangle$ state two additional RF π-pulses are applied. The transfer $|1,+1\rangle \rightarrow |2,0\rangle$ utilises the same RF transition frequency f_1 as the previous transfer shown in (a). Instead of tuning the frequency, the transfer current I, i. e. the magnetic field B is adapted. The third transfer $|2,0\rangle \rightarrow |1,-1\rangle$ then utilises the same transfer current as the second one and instead of tuning the current, a second RF transition frequency f_2 is employed in order to minimise the time in between second and third transfer. The inset shows the Rabi oscillation exemplarily of the third transfer $|2,0\rangle \rightarrow |1,-1\rangle$. The y-axis corresponds to the $|2,0\rangle$ population. **(c),(d)** Typical transfer spectra of the third transfer $|2,0\rangle \rightarrow |1,-1\rangle$ in dependence of the time. The range of the x-axis corresponds to several hours, the range of the y-axis corresponds to $\sim 8\,\mathrm{mG}$. The inset shows a single transfer spectrum corresponding to a vertical cut through the 2D plot. The data was taken before (c) and after (d) improving the coil current resolution. Before, the quantised coil current steps are clearly visible. Adapted from [76]. More details are given in the main text.

The RF transitions are quite narrow and thus sensitive to the magnetic field stability. To achieve sufficient short-term stability a synchronisation of the experimental cycle with the electricity grid is necessary as well as a coil current stability of $\sim 10^{-4}\,\mathrm{A}$ which requires choosing a suitable current power supply. Furthermore, we had to reduce the quantisation steps of the 16-bit analog channel used to control the coil current.[36] (see fig. 3.17 (c)-(d)) Long-term stability is ensured with an automated procedure taking brief transfer spectra every few hours, extracting the center current of the respective transfer and adapting the transfer currents accordingly for the subsequent experimental runs.

[36]The analog channel has an output range of 10 V while the coil current supply's input range is only 5V. By adding a voltage divider we were able to improve the current resolution by a factor of 2.

3.7.3 Evaporation

Evaporation is a widely used cooling technique allowing to achieve Bose-Einstein condensation. In the following we will give an overview on this technique, focussing on the aspects relevant for this thesis. A more detailed discussion is given in [95]. We will then describe our evaporation procedure, briefly show how evaporation can be utilised for the atom number calibration and finally, present the observed performance.

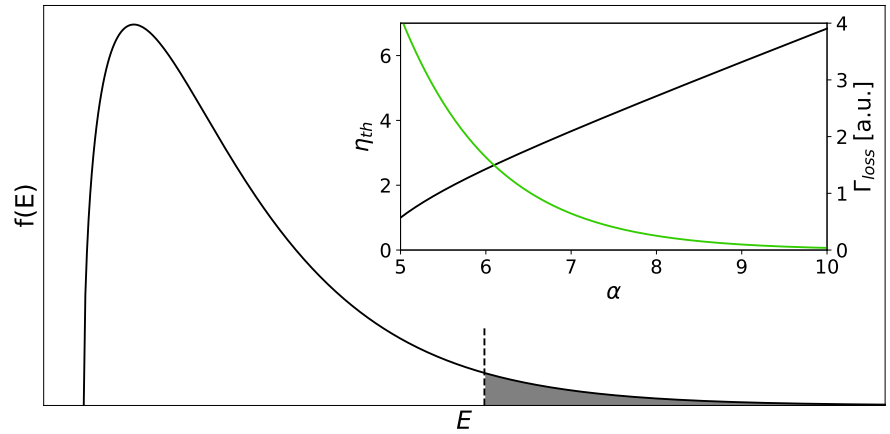

Figure 3.18: Energy distribution $f(E)$ of a thermal cloud. The position of the vertical dashed line corresponds to the cut-off by the trap depth and is determined by the parameter α. Atoms with a higher energy, i. e. in the grey shaded tail of the Maxwell-Boltzmann distribution, escape the trap and thus lower the mean energy of the remaining atoms. Elastic scattering events restore the thermal distribution, i. e. re-populate the tail of the Maxwell-Boltzmann distribution, while shifting the peak of the distribution to lower values corresponding to a lower temperature. Continuously lowering the trap depth then leads to a continuously decreasing temperature, resulting in an increasing phase space density. **Inset:** The theoretically expected efficiency η_{th} (black) as well as the estimated initial evaporation loss rate Γ_{loss} (green) in dependence of the parameter $\alpha = U/k_B T$. While high values of α increase the efficiency η_{th}, i. e. the gain in phase space density for a given atom number loss, the evaporation loss rate Γ_{loss} decreases, i. e. the evaporation slows down, making it more difficult to compete against heating processes and inelastic losses.

The idea of the evaporation technique is to reduce the mean temperature of the atomic sample by removing those atoms with high energy. For a thermal cloud that means the tail of the Maxwell-Boltzmann distribution is cut off, as sketched in fig. 3.18, and the sample re-thermalises through elastic scattering which re-populates the tail of the Maxwell-Boltzmann distribution such that the thermal distribution is restored, but with a lower mean temperature. Thereby, continuously cutting off the tail and re-thermalising the sample reduces the temperature at the cost of an atom number loss. Given that the scattering rate is high enough to ensure a re-thermalisation faster than the evaporation rate, the final temperature is only limited by the initial atom number and losses due to

inelastic collisions, as the temperature can be lowered further and further by removing more atoms.

For optical traps evaporation occurs naturally due to the finite trap depth U: Individual atoms can gain enough energy via elastic collisions to escape the trap. For low temperatures the evaporation rate scales with $\exp(-\alpha) = \exp(-U/k_B T)$, which means the evaporation rate decreases with decreasing temperature T and freezes out for $\alpha \approx 10$ [96]. Therefore, the trap depth needs to be lowered to maintain the evaporation process which is called forced evaporative cooling. For large α and when the trap depth is reduced such that α stays constant[37] the achieved phase space density ρ can be expressed as:

$$\rho = \rho_i \cdot \left(\frac{N_i}{N}\right)^{\eta} \tag{3.11}$$

where N is the atom number, the index i denotes the initial conditions, and the exponent η characterises the efficiency of the evaporation process. For a fixed gain in phase space density a higher η corresponds to a lower atom number loss. For harmonic traps and large α the theoretical efficiency is $\eta_{th} = \alpha + (\alpha - 5)/(\alpha - 4) - 4$ [96] and is shown in fig. 3.18 (inset). Theoretically, the efficiency can therefore be increased by increasing α, which in turn is determined by the rate with which U is lowered. However, this does not take into account other loss channels. A high α means to cut a smaller part of the Boltzmann tail before re-thermalisation, hence the higher theoretical efficiency, but this also reduces the evaporation rate and hence slows down the process which is disadvantageous when considering a counteracting heating rate and inelastic losses. Consequently, the optimal α needs to be determined experimentally.

α also affects how the scattering rate changes over the course of the evaporation. There are two counteracting effects: lowering the trap depths reduces the trapping frequency which lowers the scattering rate via the density. On the other hand the temperature decreases with the ongoing evaporation which again increases the density and thus the scattering rate.[38] Assuming an energy-independent scattering cross-section, the first effect dominates for reasonably large α and the scattering rate decreases with decreasing U meaning that no runaway evaporation is achieved [96]. However, the scattering rate can be easily kept high enough, i. e. reasonably higher than the evaporation rate, by adjusting

[37] For an exponential lowering of the trap depth U, α is approximately constant. We found that the performance of an exponential ramp is similar compared to the analytically found ramp shape keeping α constant [96].

[38] The temperature also affects the mean velocity counteracting the effect on the density. However, the density scales much stronger with the temperature than the mean velocity does, hence the increasing density is the dominant effect of the decreasing temperature.

the scattering length via a suitable Feshbach resonance.

The final phase space density also depends on the initial conditions. For fixed trap parameters, the initial phase space density scales with $\rho_i \propto N_i T_i^{-3}$. Hence, the final phase space density scales with $\rho \propto T_i^{-3} N_i^{\eta+1}$. For a typical efficiency $\eta \simeq 3$, the phase space density scales stronger with the initial atom number than with the initial temperature. Accordingly, the optical trap loading (see sec. 3.6) was optimised for low temperatures and especially for high atom numbers.

Experimental evaporation procedure

After the atoms are transported to the science position, they are transferred from the magnetic trap into a 1064 nm high-power, single-beam optical dipole trap (see sec. 3.6). While this trap is adapted for the applied collisional loading scheme, it is not well suited for the evaporation. Since the Rayleigh range, determining the on-axis confinement, is much larger than the beam waists, determining the radial confinement, the 1064 nm ODT exhibits a weak axis with a ~ 60 times lower trapping frequency compared to the other axes. Therefore, the thermalisation time is axially much longer than radially. While low scattering rates due to low trapping frequencies can be easily compensated by adapting the scattering length via Feshbach resonances, this is not favorable for vastly different trapping frequencies. When increasing the scattering length to achieve a reasonable axial thermalisation time, the much higher radial trapping frequencies will enhance inelastic losses and hence reduce the efficiency. Hence, we instead employ the pre-existing 850 nm crossed dipole trap (CDT) for evaporation. Since the two beams are crossed under $2 \cdot 45°$ the trapping frequencies differ only by a factor of $\sqrt{2}$.[39]

Experimentally, when evaporating in the $|1, +1\rangle$ state we found best results when loading the atoms from the 1064 nm ODT into the full depth 850 nm CDT with an evaporation-like scheme and then evaporating in the 850 nm CDT to achieve degeneracy. The scheme is depicted in fig. 3.19 (top). When preparing the $|1, -1\rangle$ state we introduce an intermediate step and lower the 1064 nm ODT depth to $\sim 30\%$ before performing the spin transfer $|1, +1\rangle \rightarrow |2, 0\rangle \rightarrow |1, -1\rangle$ as we found best performance of the spin transfer in the reduced depth 1064 nm ODT compared to the full depth 1064 nm ODT as well as compared to the 850 nm CDT. After the spin transfer the procedure is the same as for the $|1, +1\rangle$ state: the atoms are loaded from the reduced depth 1064 nm ODT trap into the full depth 850 nm CDT and subsequently evaporated to degeneracy as shown

[39] In principle the 1064 nm single-beam ODT can be upgraded to a crossed dipole trap. Due to technical reasons the crossing angle is limited to $2 \cdot 5°$, though, still resulting in one comparatively weak axis.

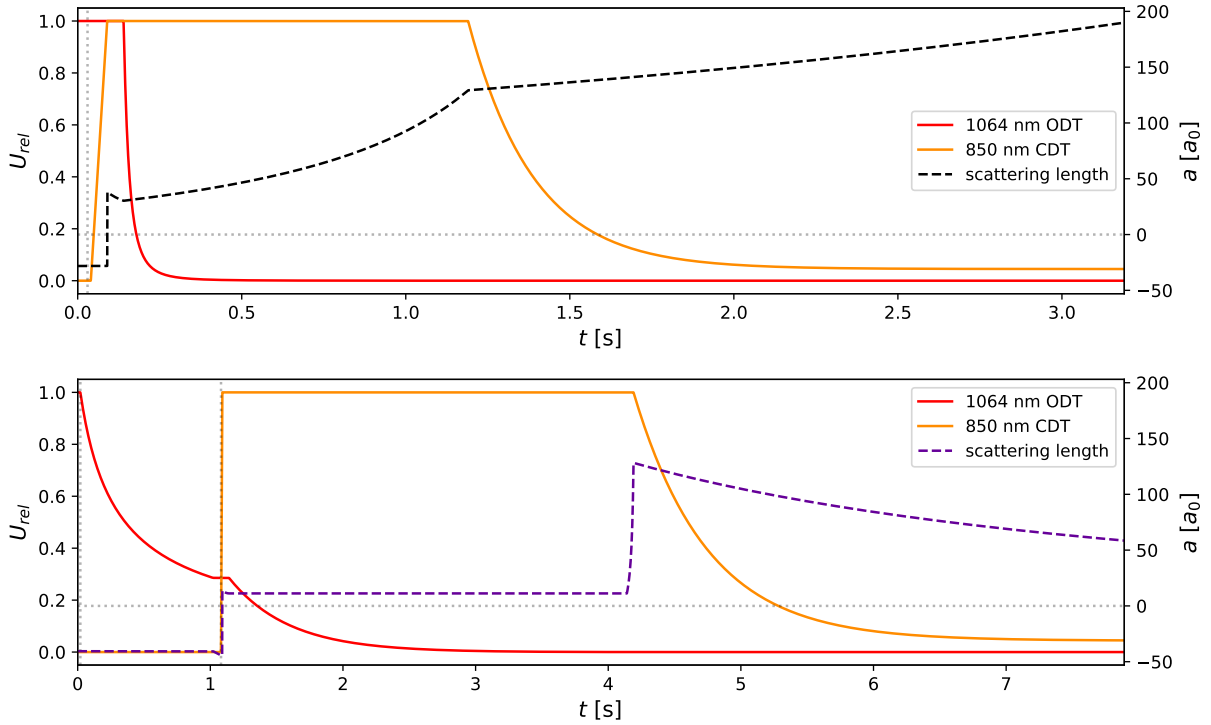

Figure 3.19: Experimentally optimised evaporation scheme for the $|1,+1\rangle$ (top) and the $|1,-1\rangle$ (bottom) state. Depicted are the relative trap depth U_{rel} of the 1064 nm ODT (red, solid) where full depth $U_{\mathrm{rel}} = 1$ corresponds to ~ 6 mK, and of the 850 nm CDT (orange, solid) where full depth corresponds to ~ 100 µK, as well as the intrastate scattering length a of the $|1,+1\rangle$ state (black, dashed) and of the $|1,-1\rangle$ state (purple, dashed) in dependence of the time t. $t = 0$ corresponds to the end of the collisional loading scheme, i. e. the end of the rampdown of the magnetic trap. The vertical dashed lines correspond to the times of the RF transfers. **Top:** After a short waiting time for the magnetic field to settle, the atoms are transferred from the $|2,+2\rangle$ state into the $|1,+1\rangle$ state. The magnetic field and thus the scattering length is fixed by the transfer. Afterwards, the 850 nm crossed dipole trap is ramped up and the scattering length is increased for the subsequent evaporation-like loading from the 1064 nm ODT into the 850 nm CDT. The ramp shape for lowering the 1064 nm ODT to zero is chosen such that $\alpha = U/k_BT = \text{const.}$ [96]. During the loading the scattering length is further increased. Subsequently, the atom are evaporated in the 850 nm CDT: The scattering length is slowly increased and the trap depth is lowered exponentially until Bose-Einstein-condensation is achieved. **Bottom:** After a short waiting time for the magnetic field to settle, the atoms are transferred from the $|2,+2\rangle$ into the $|1,+1\rangle$ state. Afterwards, the 1064 nm ODT trap depth is lowered to $\sim 30\%$ for the subsequent second and third RF transfer $|1,+1\rangle \rightarrow |2,0\rangle \rightarrow |1,-1\rangle$. The magnetic field and thus the scattering length is fixed by the respective transfer. After the transfers the atoms are loaded from the 1064 nm ODT into the 850 nm CDT: The 850 nm CDT is ramped up, the scattering length is tuned to positive, but rather low values as discussed in the main text, and the 1064 nm ODT is ramped down with a ramp shape keeping $\alpha = U/k_BT$ constant. For the actual evaporation step the scattering length is then increased and the 850 nm CDT is exponentially ramped down until Bose-Einstein-condensation is achieved.

in fig. 3.19 (bottom). The experimentally optimised scattering length employed for the $|1,-1\rangle$ state when loading the atoms from the 1064 nm ODT into the 850 nm CDT is with $\sim 10\,a_0$ rather low. We suspect that this is connected to the closeby $|1,-1\rangle + |1,0\rangle$ Feshbach resonance. Remaining atoms in the $|1,+1\rangle$ state scatter quickly with atoms in the $|1,-1\rangle$ state into the $|1,0\rangle$ state. These atoms can participate in the evaporation process from the 1064 nm ODT into the 850 nm CDT. While the $|1,-1\rangle + |1,-1\rangle$ scattering length is very low, the $|1,-1\rangle + |1,0\rangle$ scattering length is with $\sim 180\,a_0$ rather high, supporting the hypothesis that the evaporation is mainly driven by atoms in the $|1,0\rangle$ state. Scattering events involving atoms in the minority $|1,0\rangle$ state are much more likely, resulting in a higher relative evaporation loss rate of these atoms compared to atoms in the $|1,-1\rangle$ state. Thus, when evaporating with enhanced interstate scattering length between the desired spin state and the remaining minority fraction instead of an enhanced intrastate scattering length, the spin polarisation is improved over the course of the evaporation.

While loading the 850 nm CDT and during the evaporation we additionally apply a magnetic gradient. This reduces the effective trap depth without lowering the trapping frequency. Hence, a higher density is maintained, especially at the end of the evaporation where the effect of the gradient is largest due to the low trap depth.[40] This is particularly advantageous when evaporating in a single-beam trap to support the weak axis. Although we found slightly better results when applying a gradient of $\sim 25\,\mathrm{G/cm}$, the performance is not sensitive to the exact value of the gradient.

Atom number calibration

By imaging the atom cloud via absorption imaging we can derive the atom number N from the optical density, the temperature T from time-of-flight measurements and the condensate fraction N_0/N from fitting a bimodal distribution to the imaged density distribution for different times of the evaporation. The phase space density ρ is given by

$$\rho = n \cdot \lambda_{th}^3 \tag{3.12}$$

where n is the density and $\lambda_{th} = (2\pi\hbar^2/mk_BT)^{1/2}$ the thermal de Broglie wavelength with the atomic mass m and the Boltzmann constant k_B. The density can be estimated by the peak density n_0 in a 3D harmonic trap potential $V(\mathbf{r})$ from the normalisation condition

[40] Note that the magnetic gradient results in a spatially dependent scattering length. However, due to the small size of the atomic cloud, the variation in the relevant region is typically less than 0.1%.

of the Boltzmann distribution $N = n_0 \int \exp(-V(\mathbf{r})/k_B T) d\mathbf{r}$ yielding

$$n_0 = N\bar{\omega}^3 \left(\frac{m}{2\pi k_B T}\right)^{3/2} \tag{3.13}$$

where $\bar{\omega}$ is the mean trapping frequency.[41] Note that his expression does not take into account the effect of interactions, which is a valid approximation as the imaging is performed at low scattering length of $\sim 20\, a_0$. For known trap parameters, the central phase space density can therefore be estimated from the measured atom number and temperature.

However, the measured atom number is only an approximation. Since the imaging is performed at high magnetic fields, the imaging transition is not closed, meaning that the measured atom number needs to be calibrated by introducing a correction factor. A suitable method for the calibration is to compare the phase space density calculated according to eq. 3.12 with the measured condensate fraction as shown in fig. 3.20. For a 3D harmonic oscillator the critical temperature T_C at which condensation occurs is

$$k_B T_C = \frac{\hbar\bar{\omega} N^{1/3}}{[\zeta(3)]^{1/3}} \approx 0.94 \hbar\bar{\omega} N^{1/3} \tag{3.14}$$

where $\zeta(s)$ denotes the Riemann zeta function [97]. Hence, for a 3D harmonic oscillator the critical phase space density characterising the condensation threshold is $\rho_C = \zeta(3) \approx 1.2$. By matching this critical phase space density to a condensate fraction of $N_0/N \simeq 10^{-2}$ an atom number calibration is obtained.[42] Note that this is just an estimate, though. For an accurate calibration finite size effects and interaction shifts have to be included [98].

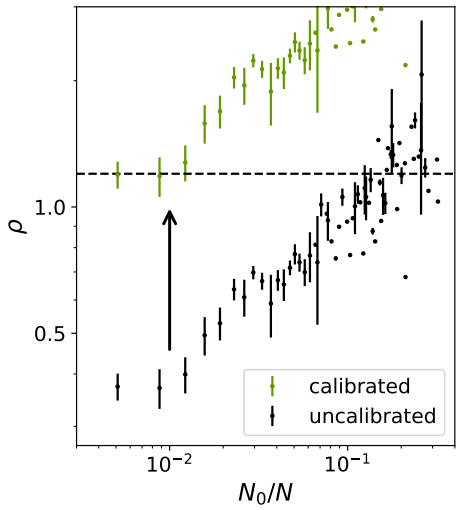

Figure 3.20: Phase space density ρ calculated according to eq. 3.12 with uncalibrated (black) and calibrated (green) atom number in dependence of the condensate fraction N_0/N.

[41] This only holds true for a thermal cloud, though. Above the condensation threshold the density is increasingly underestimated by this approximation.

[42] This is the threshold at which we can observe a condensate fraction. Note that the error of the measured condensate fraction is on the same order of magnitude.

Performance

With the calibrated atom number the performance of the evaporation can be estimated. The mean efficiency estimated from initial atom number and phase space density in the 1064 nm ODT directly before evaporating into the 850 nm CDT and from the atom number in the 850 nm CDT at $\rho = 1$ is ~ 4.1 (~ 2.2) for the for the $|1, -1\rangle$ ($|1, +1\rangle$) state.

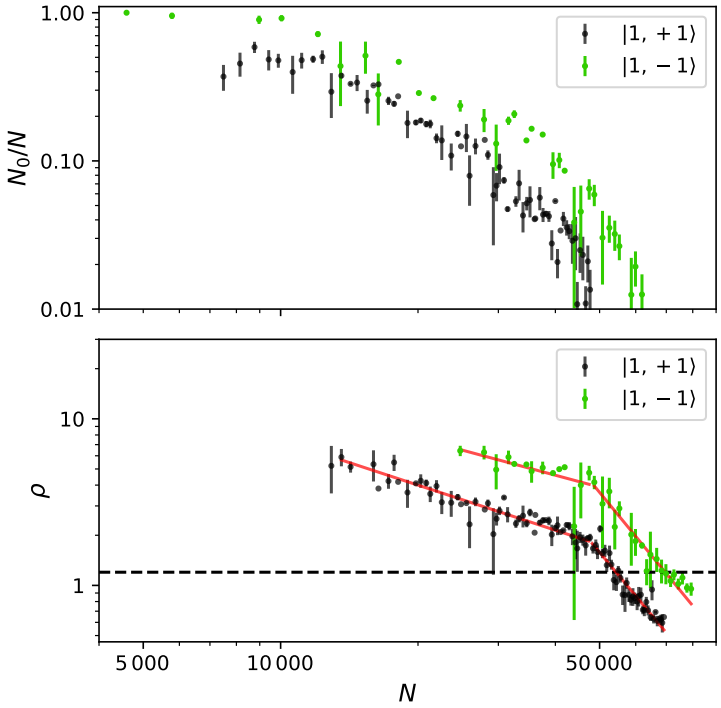

Figure 3.21: Condensate fraction N_0/N (top) and phase space density ρ (bottom) versus atom number N during the last stages of the evaporation in the 850 nm CDT for the $|1, +1\rangle$ (black) and the $|1, -1\rangle$ (green) state. Direction of time is from right to left. N_0/N is extracted from the bimodal distribution of the imaged density, ρ is calculated according to eq. 3.12, N is corrected according to the calibration method shown in fig. 3.20 for each spin state independently. The data for the two spin states was taken six months apart. Also shown is a fit (red) to extract the slope corresponding to the efficiency. Both spin state exhibit a similar initial performance with a fitted efficiency of ~ 3.3 with a subsequent flattening to a fitted value of ~ 0.9 (~ 0.7) for the $|1, +1\rangle$ ($|1, -1\rangle$) state. The efficiency for significant condensate fractions is underestimated, though, as the optical density of the BEC results in an underestimated atom number.

The condensate fraction and the phase space density during the final phase of the evaporation in the 850 nm CDT is shown in fig. 3.21. As can be seen the efficiency in the final phase is with ~ 3.3 similar for both spin states. With a rising condensate fraction the efficiency drops to ~ 0.9 (~ 0.7) for the $|1, +1\rangle$ ($|1, -1\rangle$) state: In this regime, the cloud can no longer be described by a Boltzmann distribution such that the scalings derived above are no longer valid. More importantly, the BEC is optically dense such that the measured and calibrated atom number and therefore also the calculated phase

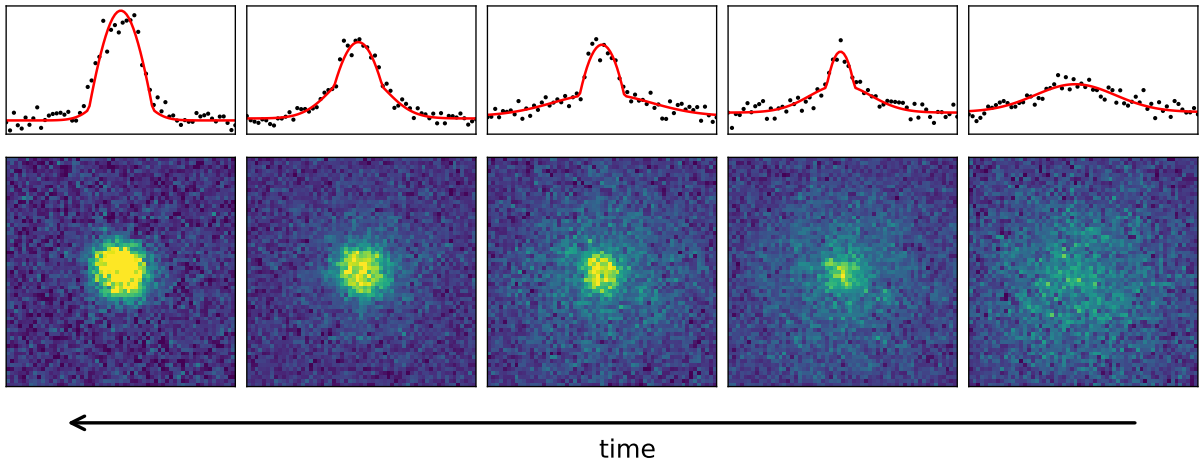

Figure 3.22: Measured density profile of the atom cloud at different times of the evaporation in the 850 nm CDT. Also depicted is a cross-section through the respective density profile. The condensation threshold is reached in between the first and second image from the right. It is clearly visible how the shape of the density distribution changes from Gaussian above the condensation threshold to a bimodal distribution below the condensation threshold. With ongoing evaporation the thermal fraction decreases until it vanishes as can be seen in the leftmost image. In the degenerate regime, the atom cloud can be approximated with a Thomas-Fermi density distribution.

space density is underestimated for a significant condensate fraction. We conservatively estimate an atom number of $\sim 5 \cdot 10^3$ in the condensate.

Chapter 4

From 3D to 2D

In the previous chapter we described how we adapted and extended the experimental setup and re-designed the experimental sequence to achieve a three-dimensional K39 Bose-Einstein condensate. In this chapter we will address the transformation from a three-dimensional to a two-dimensional system. Therefore, we will first motivate the significance of the dimensionality and present the fundamental theoretical aspects of a 2D Bose gas. We will then introduce the conditions under which a 3D atomic cloud exhibits thermodynamically 2D behaviour, which is called the quasi-2D regime. We will then briefly discuss different experimental setups to realise such a quasi-2D system and explain why we chose the concept of a vertical lattice loaded from a light-sheet-like trap. After describing the design and realisation of this setup we will finally provide an overview of the degenerate 2D Bose system that can be created by utilising this setup.

4.1 Fundamentals of 2D Bose gases

In this section we provide a brief theoretical overview of some key aspects of 2D Bose gases. In particular, we will discuss the significance of dimensionality for the occurrence and nature of phase transitions from the normal to the superfluid state, as 2D systems exhibit the celebrated BKT transition whose discovery lead to the Nobel Prize in Physics being awarded to Kosterlitz and Thouless in 2016. We will then introduce the concept of a quasi-2D system, i. e. the conditions to experimentally realise a thermodynamically two-dimensional system, and discuss how the behaviour of such a system can be described in the low temperature regime.

Effects of the dimensionality

The dimensionality is a fundamental property of a system which has a significant impact on the system's behaviour. Arguably, the most fundamental difference when going to lower dimensions is the enhanced role of fluctuations which can be intuitively understood by the reduced number of nearest neighbours. While thermal and quantum fluctuations are more costly and hence stronger suppressed in 3D, they are less costly in lower dimensions which has an important consequence: In 2D, and also in 1D, fluctuations are strong enough to destroy true long-range order at any non-zero temperature T. More formally, the Mermin-Wagner theorem [99–102] states that for a dimension $d \leq 2$ true long-range order is impossible for a system with continuous Hamiltonian symmetry and short-ranged interactions that is in the thermodynamic limit and at $T \neq 0$. Accordingly, there are no phase transitions with spontaneously broken continuous symmetry. This especially includes the well-known Bose-Einstein condensation (BEC) where the spontaneously broken continuous symmetry is given by the arbitrarily chosen phase of the macroscopic wave function which emerges at the transition.

The absence of BEC in 2D uniform systems can be easily seen when considering the effect of the dimensionality on the density of states $g(E)$ which scales with energy E as $g(E) \propto E^{(d/2-1)}$ [97]. Here, the 2D case immediately stands out as it is the only case where the dependence on E drops out and the density of states becomes constant. With the density of states we can express the average total atom number N in the system as [97]

$$N = N_0 + \int_0^\infty dE\, g(E) f^0(E) \tag{4.1}$$

where $f^0(E)$ is the well-known Bose distribution function. N_0 is the number of atoms in the ground state, while the integral corresponds to the number of atoms in excited states. In 3D the integral is finite for any given temperature T. That means the number of excited states saturates and an atom number exceeding the maximum number of excited states leads to a macroscopic population of the ground state corresponding to BEC. For $d \leq 2$, on the other hand, the integral in eq. 4.1 diverges due to the different scaling of the density of states, i. e. the number of available excited states does not saturate. Thus, in an infinite uniform 2D or 1D system Bose-Einstein condensation can only occur at zero temperature.

Berezinskii-Kosterlitz-Thouless transition

In contrast to the 1D case, an infinite uniform 2D system can still exhibit a superfluid state which is not connected to BEC, but to the so-called BKT transition [103, 104]. At low temperatures the interaction energy becomes dominant and the interactions result in a suppression of density fluctuations[1] which manifest in the second-order correlation function. Low-energy long-wavelength excitations are thus mainly given by phase fluctuations. These phase fluctuations, i. e. phonons, destroy true long-range order which manifests in a vanishing first-order correlation function $g_1(r)$ for $r \to \infty$. However, a unique feature of 2D systems is that, below a critical temperature, they can still exhibit a *quasi-long-range order* which allows for the emergence of a superfluid state. This quasi-long-range order corresponds to a slow algebraic decay of $g_1(r)$ for long distances[2] r in the superfluid state, i. e. below the BKT critical temperatures T_{BKT}, as opposed to an approximately exponential decay in the normal state, i. e. above T_{BKT}, and as opposed to a Gaussian shape at high temperatures in the non-degenerate regime [105]. This results in the formation of a quasi-condensate which can be understood as 'local' Bose-Einstein condensates without global phase correlations, i. e. as a condensate with fluctuating phase. [106]

Recalling the Mermin-Wagner theorem this BKT transition cannot be connected to a spontaneously broken continuous symmetry, but instead belongs to the class of topological phase transitions. While there are no discontinuities in thermodynamic quantities besides the remarkable universal jump of the superfluid density (see e. g. [105]) which classifies the transition as of 'infinite order', the BKT transition is connected to a change of the system's topology. This cannot be explained by the long-wavelength phononic excitations, but with a different kind of phase fluctuations, namely vortices. These are topological defects around which the phase field smoothly changes by $n2\pi$ where the integer n is called the charge or vorticity. At the vortex center the superfluid density vanishes as the velocity field cannot be well defined at this point due to the phase winding. Hence vortices correspond not only to phase fluctuations, but also to density fluctuations. These are just small scale fluctuations, though, since the size of the vortices is given by the healing length. Density fluctuations on larger scales are still suppressed by interactions and the BKT transition is determined by the effect of the vortices on the phase field: Below T_{BKT} the free energy associated with a free vortex is positive. Consequently, free vortices are suppressed and vortices occur as bound pairs with opposite charge, i. e. opposite sense of rotation. Thus, the phase winding around the bound pair is zero, the resulting phase fluctuations are

[1] More precisely, density fluctuations at lengthscales larger than the healing length are suppressed.

[2] Here, 'long distances' refers to distances that are large compared to the healing length and compared to the thermal wavelength.

limited to small scales and the phase field is only locally affected. That means although true long-range order is destroyed by phonons, neither phonons nor vortices cause sufficient phase fluctuations to destroy the quasi-long-range order and the system's topology is equivalent to the topology of a BEC with true long-range order. Above T_{BKT}, on the other hand, the free energy associated to free vortices becomes negative and free vortices become energetically favorable. The vortex pairs break up and free vortices emerge. Hence, the effect of the vortices on the phase field can no longer be considered as local, the phase ordering is destroyed and the topology of the system is altered, corresponding to a normal state.

Although the BKT transition is driven by vortices and their effect on the phase field, the suppression of density fluctuations is a crucial requirement for the emergence of the superfluid BKT state. Thus, in contrast to BEC, the BKT transition can only occur in interacting systems.

BEC in 2D systems

The statement that Bose-Einstein condensation (BEC) at non-zero temperature does not occur in 2D is not universally valid. While it is true for infinite uniform system, the situation is different for an harmonically trapped gas. The harmonic trap breaks the continuous Hamiltonian symmetry which is one of the conditions of the previously stated Mermin-Wagner theorem and alters the density of state which in the harmonically trapped case scales as $g(E) \propto E^{(d-1)}$ [106]. In this case $g(E)$ is no longer constant for a two-dimensional system and the integral in eq. 4.1 becomes finite, the number of excited states saturates and BEC at non-zero temperature is restored. This only holds true in an ideal, i. e. non-interacting gas, though, as BEC in 2D is extremely sensitive to interactions [105, 107].

However, BEC at non-zero temperature can still occur in interacting 2D systems due to finite size effects. Decaying phase correlations can effectively not be distinguished from true long-range order when the phase coherence length is much larger than the system size, resulting in the emergence of a true condensate.[3] The slow algebraic decay of the first-order correlation function associated with the BKT state results in such large phase coherence lengths. Hence, while a BKT state in an infinite system is associated with a quasi-condensate, a system with realistic parameters in a BKT state typically also exhibits a finite true condensate fraction.

The difference between condensate and quasi-condensate is subtle. Local correlations

[3] Here, we presume that the system is in a degenerate regime where density fluctuations are suppressed by interactions.

as well as the Thomas-Fermi density profile are the same for quasi-condensate and condensate, the difference lies in the phase coherence properties [106]. Whether the character of a system is more that of a quasi-condensate or more that of a condensate is often differentiated by how the phase coherence length compares to the system size or equivalently on the phase fluctuations on the length scale given by the Thomas-Fermi radius. For our parameters we expect to be more on the condensate side.

	uniform gas		harmonic confinement	
	infinite system	finite system	infinite system	finite system
ideal	no BKT no BEC	no BKT BEC	no BKT BEC	no BKT BEC
interacting	BKT no BEC	BKT BEC	BKT no BEC	BKT BEC

Table 4.1: Basic overview of which 2D systems support BEC and BKT states based on the considerations in [105]. We emphasize that these considerations do not reflect the full picture. A comprehensive analysis is beyond the scope of this thesis and the presented table is only intended to provide an orientation. Note that a confinement always introduces a finite system size. The data for an infinite, harmonically trapped gas is derived by considering an appropriately defined thermodynamic limit.

Quasi-2D Bose gases

Since we are living in a three-dimensional world we cannot create truly two-dimensional systems. However, we can create atomic gases that are kinematically 2D by tightly confining the motion of the atoms in one spatial direction, here chosen to be y [108]. This can be achieved by suppressing excitations along y, i. e. by a macroscopic population of the ground state in that axis. This limits the atomic motion to zero-point oscillations and enables the decomposition of the 3D wave function

$$\psi_{3\mathrm{D}}(x,y,z) = \psi_{2\mathrm{D}}(x,z) \cdot \phi_0(y) \tag{4.2}$$

into a 2D wave function $\psi_{2\mathrm{D}}(x,z)$ that contains the main dynamics and the ground state wave function[4] $\phi_0(y)$ along y which is not affected by the in-plane dynamics. To realise this, a strong confinement along y is needed as it introduces an energy gap between the ground state and the first excited state. In order to suppress excitations this energy gap needs to be large compared to all relevant energy scales of the system. For ultracold gases the confinement is typically harmonic and accordingly the energy gap is given by

[4]For an harmonic confinement the ground state wave function corresponds to a Gaussian.

the trapping frequency ω_y. The relevant energy scales for bosonic systems are given by the temperature T and by the chemical potential μ. This yields

$$\hbar\omega_y \gg k_B T, \mu. \tag{4.3}$$

A system fulfilling this condition is considered to be *quasi-2D*.[5] Although kinematically 2D, quasi-2D systems are typically collisionally 3D since the harmonic oscillator length $a_{ho,y} = \sqrt{\hbar/(m\omega_y)}$ with the atomic mass m is usually much larger than the 3D scattering length a_{3D}.

As the chemical potential corresponds to the interaction energy $\mu = gn$ for uniform systems in the low temperature regime with coupling constant g and density n, the condition $\hbar\omega_y \gg \mu$ can also be expressed in terms of the corresponding characteristic length scales $\xi \gg a_{\mathrm{ho,y}}$ where $\xi = \hbar/\sqrt{mgn}$ is the healing length. This expression is quite intuitive: $a_{\mathrm{ho,y}}$ corresponds to the system size along y while ξ is the minimal length scale over which the wave function spatially changes. Hence, it is apparent that the y-component of the wave function cannot be changed by the dynamics and can thus be separated out for $\xi \gg a_{\mathrm{ho}}$.[6]

Scattering in 2D and quasi-2D

The dimensionality is also of importance for the scattering properties of a system. In the following we will therefore briefly revisit the 3D case, before turning to the true 2D case. Finally, we will consider the quasi-2D regime where we will see that it is in principle equivalent to the true 2D case, but in practice typically exhibits a more 3D scattering character. A thorough description of the 3D scattering problem can be found e. g. in [97, 110]. A more detailed discussion of scattering in true 2D can be found in [111, 112], the quasi-2D case is presented in [106, 108]. Here, we only give a brief overview which mainly follows [106, 112].

Scattering in 3D In the following we consider elastic collisions of two atoms that are interacting via a short-range potential $U(r)$. The scattering problem is then described by

[5] Especially in early research 'quasi-2D' is also used for system with $\hbar\omega_y \lesssim k_B T$. Due to the phenomenon of transverse condensation these systems already start showing a macroscopic ground state population [109].

[6] In this picture it can also be intuitively understood that binary spin mixtures allow to create 3D systems with 2D spin dynamics as the intra- and interstate coupling constants g_{ii} and g_{ij} correspond to separate density and spin healing lengths ξ and ξ_s.

the Schrödinger equation

$$\left[-\frac{\hbar^2}{2m^*}\nabla^2 + U(r)\right]\psi(\mathbf{r}) = E\psi(\mathbf{r}) \tag{4.4}$$

where $E = \hbar^2 k^2/(2m^*)$ is the scattering energy with relative momentum $\mathbf{k}$, m^* is the reduced mass and $\mathbf{r} = \mathbf{r}_1 - \mathbf{r}_2$ corresponds to the relative coordinate of the two atoms. For $r \to \infty$ the wave function is composed of an incident plane wave and a scattered spherical wave which in the three-dimensional case reads

$$\psi_{3\mathrm{D}}(\mathbf{r}) \approx e^{i\mathbf{kr}} + f(k,\theta,\varphi)\frac{e^{i\mathbf{kr}}}{r}. \tag{4.5}$$

$f(k,\theta,\varphi)$ is the so-called scattering amplitude and is of central importance. It can be derived by solving the (3D) Schrödinger eq. 4.4 and determines the differential cross-section $d\sigma/d\Omega = |f(k,\theta,\varphi)|^2$. In the low-temperature regime we can assume that only the spherically symmetric s-wave scattering occurs as scattering through higher partial waves (angular momentum quantum number $l > 0$) is energetically suppressed. Accordingly, in this regime the scattering amplitude $f(k)$ is independent of θ and φ. In the low energy limit the scattering amplitude takes a finite value $f(k)_{k\to 0} = -a_{3\mathrm{D}}$, where $a_{3\mathrm{D}}$ is called the s-wave scattering length, and the total cross-section takes the form $\sigma = 4\pi a_{3\mathrm{D}}^2$ or in the case of identical bosons $\sigma = 8\pi a_{3\mathrm{D}}^2$.

Furthermore, in the ultracold limit the scattering amplitude is directly related to the coupling constant g used to express the interaction energy since the mean-field interaction energy is given by the sum of all pair interactions in the weakly interacting regime. In the three-dimensional case this yields $g_{3\mathrm{D}} = (4\pi\hbar^2/m)a_{3\mathrm{D}}$.

Scattering in true 2D In true 2D the wave function describing the relative motion is different to the 3D case stated in eq. 4.5. The general structure, i. e. the composition of incident plane wave and scattered circular wave, stays the same, but due to the different geometry the 2D case reads

$$\psi_{2\mathrm{D}}(\mathbf{r}) \approx e^{i\mathbf{kr}} - f(k,\varphi)\sqrt{\frac{i}{8\pi kr}}e^{i\mathbf{kr}}. \tag{4.6}$$

Again, assuming only s-wave scattering as justified for low temperatures one can derive the scattering amplitude by solving the (2D) Schrödinger eq. 4.4 which yields

$$f(k) = \frac{2\pi}{\ln(1/ka_{2\mathrm{D}}) + i\pi/2}. \tag{4.7}$$

where $a_{2D} > 0$ is the 2D scattering length. Note that unlike the 3D case the 2D scattering amplitude does not take a finite value in the low energy limit $k \to 0$. For $ka_{2D} \ll 1$ the logarithmic term in the denominator is dominating and the scattering amplitude becomes real. The corresponding coupling constant is then given by $g = 2\pi\hbar^2/(m \ln(1/k_c a_{2D}))$ where k_c is the characteristic momentum, e. g. the thermal momentum in the case of a thermal gas or the inverse healing length in the case of a (quasi-)condensate. Thus, the logarithmic dependency yields a remarkable result: For sufficiently low temperature and density $k_c a_{2D} \ll 1$ the interaction in true 2D is always repulsive since $g > 0$.[7]

Scattering in quasi-2D In contrast to true 2D systems, collisions in quasi-2D systems typically exhibit a 3D character since typically $a_{3D} \ll a_{ho,y}$, where $a_{ho,y}$ is the harmonic oscillator length along the tightly confined axis y. Nevertheless, quasi-2D scattering can be mapped to true 2D scattering as the scattered wave is constrained by the tight harmonic potential $V_{con}(y)$ providing the quasi-2D confinement. As previously shown (see eq. 4.2) the 3D wave function can be decomposed into a 2D component and into the ground state wave function $\phi_0(y)$ along y which remains unaffected by the interactions. Accordingly, for $r \to \infty$ the wave function of two interacting atoms is similar to eq. 4.6 and can be written as

$$\psi(\mathbf{r}) \approx \phi_0(y) \left(e^{i\mathbf{kr}} - f(k,\varphi) \sqrt{\frac{i}{8\pi kr}} e^{i\mathbf{kr}} \right). \tag{4.8}$$

The quasi-2D confinement also affects the Schrödinger equation which gets modified to

$$\left[-\frac{\hbar^2}{2m^*} \nabla^2 + U(r) + V_{con}(y) - \frac{\hbar\omega_y}{2} \right] \psi(\mathbf{r}) = E\psi(\mathbf{r}). \tag{4.9}$$

Once more, we assume that only s-wave scattering occurs and find the scattering amplitude by solving the modified Schrödinger equation which yields

$$f(k) = \frac{4\pi}{\sqrt{2\pi} a_{ho,y}/a_{3D} + \ln(B/(\pi a_{ho,y}^2 k^2)) + i\pi} \tag{4.10}$$

where $B \approx 0.915$ is a numerical factor. One clearly sees that the quasi-2D scattering amplitude has the same structure as the true 2D scattering amplitude shown in eq. 4.7. By comparing both equations one can express $a_{2D} = \sqrt{\pi/B}\, a_{ho,y} \exp(-\sqrt{\pi/2}\, a_{ho,y}/a_{3D})$

[7] Unless $a_{2D} \to \infty$ as is the case in the presence of a bound state with binding energy $E_0 \to 0$.

in terms of a_{3D} and $a_{ho,y}$. The corresponding coupling constant then reads

$$g = \frac{4\pi\hbar^2}{m} \frac{1}{\sqrt{2\pi}\, a_{ho,y}/a_{3D} + \ln(B/(\pi a_{ho,y}^2 k^2))}. \tag{4.11}$$

For $a_{3D} \ll a_{ho,y}$ the first term in the denominator dominates over the logarithmic term and the expression for the coupling constant simplifies to

$$g = \frac{\hbar^2}{m}\tilde{g} = \frac{\hbar^2}{m}\sqrt{8\pi}\frac{a_{3D}}{a_{ho,y}} \tag{4.12}$$

where we defined the dimensionless coupling constant $\tilde{g}$. We emphasize that eq. 4.12 only holds true in the weakly-interacting regime. Close to Feshbach resonances the assumption $a_{3D} \ll a_{ho,y}$ is not valid and the coupling constant is described by eq. 4.11. Note that due to the additional logarithmic term in the denominator the transition between repulsive and attractive interaction, i. e. $g > 0$ and $g < 0$, is not located at the position of the Feshbach resonance as is the case for g_{3D}, but is slightly shifted. For typical parameters that means that there is a regime with repulsive interactions, $g > 0$, although $a_{3D} < 0$.

Furthermore, we point out that the equivalence of the true 2D and quasi-2D scattering problem as implied by the same structure of the scattering amplitudes also implies that the quasi-2D scattering exhibits the same peculiar feature as the previously discussed true 2D case: Due to the logarithmic term one can always find a sufficiently low, finite k, which is determined by temperature in the thermal case and by the density in the (quasi-)condensed case, below which the interaction is repulsive, $g > 0$, regardless of the value and especially the sign of a_{3D}. That means in principle one could switch from attractive to repulsive interactions by lowering the temperature. However, for realistic parameters the temperature required to switch the sign of g is unrealistically low and hence, in practice, the logarithmic term is negligible in the weakly-interacting regime. The coupling constant is then well approximated by eq. 4.12 corresponding to a more 3D scattering character.

Low-temperature description

In this section we will briefly discuss the mean-field description of a weakly-interacting 2D Bose gas in the low-temperature regime. Following [97] we will first derive the well-known Gross-Pitaevskii equation (GPE) which is one of the main tools to theoretically study such a system and will then utilise the GPE to infer some basic properties of the system, i. e. the density distribution and the nature of the elementary excitations.

Gross-Pitaevskii equation We consider a system of N bosons of mass m in an external confinement $V(\mathbf{r})$ and with pairwise interaction described by the interaction potential $U(\mathbf{r}-\mathbf{r}')$. In second quantisation the corresponding Hamiltonian reads

$$\hat{H} = \int d\mathbf{r} \left[\hat{\Psi}^\dagger(\mathbf{r},t) \left(-\frac{\hbar^2}{2m}\nabla^2 + V(\mathbf{r}) \right) \hat{\Psi}(\mathbf{r},t) + \frac{1}{2} \int d\mathbf{r}' \hat{\Psi}^\dagger(\mathbf{r},t) \hat{\Psi}^\dagger(\mathbf{r}',t) U(\mathbf{r}-\mathbf{r}') \hat{\Psi}(\mathbf{r}',t) \hat{\Psi}(\mathbf{r},t) \right] \tag{4.13}$$

where $\hat{\Psi}^\dagger(\mathbf{r},t)$ and $\hat{\Psi}(\mathbf{r},t)$ represent the creation and annihilation field operators. Assuming contact interactions the interaction term can be expressed in terms of the previously introduced coupling constant g which resolves the double integral:

$$\hat{H} = \int d\mathbf{r}\, \hat{\Psi}^\dagger(\mathbf{r},t) \left(-\frac{\hbar^2}{2m}\nabla^2 + V(\mathbf{r}) + \frac{g}{2}\hat{\Psi}^\dagger(\mathbf{r},t)\hat{\Psi}(\mathbf{r},t) \right) \hat{\Psi}(\mathbf{r},t) \tag{4.14}$$

The time evolution of the field operators can be derived by the Heisenberg equation of motion [106]

$$i\hbar \frac{\partial \hat{\Psi}}{\partial t} = \left[\hat{\Psi}, \hat{H} \right]. \tag{4.15}$$

Assuming the low temperature regime, where the atomic sample as previously discussed forms a (quasi-)condensate, and using the Bogoliubov approximation [113] we can write the field operator as

$$\hat{\Psi}(\mathbf{r},t) = \psi_0(\mathbf{r},t) + \delta\hat{\psi}'(\mathbf{r},t) \tag{4.16}$$

where ψ_0 corresponds to the (quasi-)condensate wave function and $\delta\hat{\psi}'$ to the remaining non-condensed fraction. At $T = 0$ we can neglect $\delta\hat{\psi}'$ and combining eq. 4.14, 4.15 and 4.16 yields the well-established time-dependent Gross-Pitaevskii equation [110]

$$i\hbar \frac{\partial \psi_0(\mathbf{r},t)}{\partial t} = \left(-\frac{\hbar^2}{2m}\nabla^2 + V(\mathbf{r}) + g|\psi_0(\mathbf{r},t)|^2 \right) \psi_0(\mathbf{r},t) \tag{4.17}$$

with the normalisation condition $\int d\mathbf{r}|\psi_0(\mathbf{r},t)|^2 = N$ implying that $|\psi_0(\mathbf{r},t)|^2$ corresponds to the density $n(\mathbf{r},t)$ of the system. In the equilibrium case the time dependence of the wave function can be simply expressed as $\psi_0(\mathbf{r},t) = \phi_0(\mathbf{r})\exp(-i\mu t/\hbar)$ where μ is the chemical potential. By inserting this into eq. 4.17 one obtains the famous stationary GPE [114, 115]:

$$\mu\phi_0(\mathbf{r}) = \left(-\frac{\hbar^2}{2m}\nabla^2 + V(\mathbf{r}) + g|\phi_0(\mathbf{r})|^2 \right) \phi_0(\mathbf{r}) \tag{4.18}$$

The GPE is a well-established tool for the description of a (quasi-)condensate and is useful to derive fundamental properties of a system e. g. by employing a variational ansatz as we will do in sec. 5.4. It is also referred to as the non-linear Schrödinger equation as its

form is comparable to the Schrödinger equation with an additional non-linear mean-field term accounting for interactions.

Note that the derivation of the GPE sketched above does not assume a specific dimension. Nevertheless, the dimension is of great importance. Calculating the energy functional associated to eq. 4.18 reveals a unique feature of quasi-2D systems: In contrast to the 3D case both the kinetic energy as well as the interaction energy exhibit the same scaling with the system size, i. e. the behaviour of the system is independent of its size. This is referred to as scale invariance.[8]

Thomas-Fermi approximation An interesting quantity that can be obtained from the Gross-Pitaevskii equation (GPE) is the density distribution of the (quasi-)condensate. In the limit of large atom numbers N the kinetic energy term of the GPE (eq. 4.18) becomes small compared to the interaction energy term and can be neglected. This is known as the Thomas-Fermi approximation [97] and yields

$$\mu\phi_0(\mathbf{r}) = \left(V(\mathbf{r}) + g|\phi_0(\mathbf{r})|^2\right)\phi_0(\mathbf{r}). \tag{4.19}$$

As this transforms the differential eq. 4.18 into a mere algebraic equation this can be easily solved for the density $n(\mathbf{r}) = |\phi_0(\mathbf{r})|^2$ and one obtains

$$n(\mathbf{r}) = \left(\mu - V(\mathbf{r})\right)/g \tag{4.20}$$

for $\mu > V(\mathbf{r})$ and $g > 0$.[9] For $\mu < V(\mathbf{r})$ the solution for eq. 4.19 is given by $\phi_0(\mathbf{r}) = 0$. Accordingly, the so-called Thomas-Fermi density distribution is determined by the shape of the potential, i. e. a parabola in the case of the typical harmonic confinement, and the extent of the cloud is given by the condition $V(\mathbf{r}) = \mu$ which for harmonic potentials yields the so-called Thomas-Fermi radius

$$r_{\mathrm{TF},i} = \sqrt{\frac{2\mu}{m\omega_i^2}} \tag{4.21}$$

with $i = x,y,z$ and where ω_i is the trapping frequency along i. Calculating r_{TF} for a specific trap requires to determine the chemical potential μ which can be obtained from the normalisation condition $N = \int n(\mathbf{r})d\mathbf{r}$ with the parabolic Thomas-Fermi density

[8] Note that the scale invariance only holds true as long as the interaction coupling parameter g is independent of the density, i. e. in the weakly-interacting regime. The scale invariance is a unique feature of the quasi-2D regime and does not occur in the true 2D regime.

[9] For attractive interactions, $g < 0$, the system is not in a stable regime and the cloud collapses (see sec. 5.2).

distribution $n(\mathbf{r}) = n_0(1 - r^2/r_{\mathrm{TF}}^2)$ for $0 < r < r_{\mathrm{TF}}$ and $n(\mathbf{r}) = 0$ for $r > r_{\mathrm{TF}}$. By using eq. 4.21 and expressing the peak density as $n_0 = \mu/g$ one derives for the three-dimensional case [97]

$$\mu_{3D} = \frac{\hbar\bar{\omega}}{2}\left(\frac{15Na_{3\mathrm{D}}}{\bar{a}_{ho}}\right)^{2/5} \tag{4.22}$$

where $\bar{\omega} = (\omega_x\omega_y\omega_z)^{1/3}$ is the mean trapping frequency, $a_{3\mathrm{D}}$ the 3D scattering length and $\bar{a}_{\mathrm{ho}}$ the mean harmonic oscillator length.

In the quasi-2D case the density distribution along the tightly confined axis is not determined by the Thomas-Fermi distribution, but instead by the ground state wave function of the 2D confinement. For an harmonic 2D confinement this yields a Gaussian density distribution where the length scale is given by the harmonic oscillator length. The radial density distribution on the other hand is again given by the Thomas-Fermi distribution. Analogous to the 3D case the 2D chemical potential can be derived by integrating over the 2D parabolic density distribution which yields

$$\mu_{2D} = \hbar\bar{\omega}\sqrt{\frac{N\tilde{g}}{\pi}} \tag{4.23}$$

where $\bar{\omega} = \sqrt{\omega_x\omega_z}$ is the mean of the radial trapping frequencies and $\tilde{g}$ the 2D dimensionless coupling constant (see eq. 4.12).

Elementary excitations Another fundamental property that can be derived from the Gross-Pitaevskii equation (GPE) are the elementary excitations of the system which are included by allowing a small perturbation of the wave function $\psi(\mathbf{r},t) = \psi_0(\mathbf{r},t) + \delta\psi(\mathbf{r},t)$. Using this, the excitation modes can be found by linearising the corresponding time-dependent GPE (eq. 4.17) and searching for periodic solutions. Hence, we make the ansatz $\delta\psi(\mathbf{r},t) = \exp(-i\mu t/\hbar)[u(\mathbf{r})\exp(-i\omega t) - v^*(\mathbf{r})\exp(i\omega t)]$ and insert this into the equations obtained from linearising the GPE which yields the Bogoliubov equations. [97] For a uniform Bose gas $u(\mathbf{r})$ and $v(\mathbf{r})$ can be expressed as plane waves with coefficient u_k and v_k, respectively. With this ansatz we can solve the Bogoliubov equations which allows to derive the energy of the excitations [97]

$$\epsilon_k = \frac{\hbar^2}{2m}\sqrt{k^2(k^2 + 4\tilde{g}n)} \tag{4.24}$$

where k is the wavevector of the excitation and $\tilde{g} = gm/\hbar^2$ the previously introduced dimensionless coupling constant. The result is the same as obtained from the Bogoliubov

approach[10] and is thus referred to as the Bogoliubov excitation spectrum.

For small k the term k^2 is negligible compared to the term $4\tilde{g}n$ yielding a linear dispersion relation $\omega_k = \epsilon_k/\hbar = \sqrt{gn/m}k$. That means low-energy excitations correspond to phonons that propagate at the Bogoliubov speed of sound

$$c_0 = \sqrt{gn/m} \tag{4.25}$$

which in the weakly interacting regime is equal to the Landau critical velocity. For high k the excitation spectrum approaches a quadratic behaviour corresponding to free particles. The characteristic momentum separating the phonon and particle regimes is given by the inverse of the healing length.

4.2 Experimental realisation of a quasi-2D system

As previously explained a system is considered as quasi-2D if the condition $\hbar\omega_y \gg k_B T, \mu$ (see eq. 4.3) is fulfilled which requires a tight confinement along y. To realise such quasi-2D systems with ultracold gases different setups can be employed. In the following we will present common methods and discuss which one is the most suitable for our experiment.

Light sheet The first method used to create a two-dimensional atomic sample in 2001 in the group of Ketterle is a so-called light sheet [116], which is a red-detuned highly anisotropic optical dipole trap created by using cylindrical lenses. The small beam axis leads to a tight confinement ensuring the desired high trapping frequency ω_y while still keeping the chemical potential μ low by means of the low trapping frequencies along the other axes given by the large beam diameter in one and the Rayleigh range of the tight focus in the other direction. The advantage of such a light sheet is the conceptually rather simple experimental setup. On the other hand, the trapping frequency of the tight confinement is typically in the order of $\sim$1 kHz, i. e. rather limited. This sets a tight upper

[10] While the approach sketched above is a classical field approach, the Bogoliubov approach takes the quantum nature of the excitations into account. A full description of the Bogoliubov approach can be found e. g. in [97]. A brief sketch: Starting from the Hamiltonian in eq. 4.14 we can use the ansatz in 4.16 and express $\delta\hat{\Psi}$ in terms of the single-particle state annihilation and creation operators $\hat{a}_{\mathbf{k}}$, $\hat{a}^\dagger_{\mathbf{k}}$ characterised by the momentum $\hbar\mathbf{k}$. Using the Bogoliubov approximation and assuming that $\delta\hat{\Psi}$ is small we replace $\hat{a}_0$, $\hat{a}^\dagger_0$ by $\sqrt{N_0}$, where N_0 corresponds to the atom number in the condensed state, and neglect all terms that are more than quadratic in $\hat{a}_{\mathbf{k}}$ and $\hat{a}^\dagger_{\mathbf{k}}$ for $\mathbf{k} \neq 0$. Applying the Bogoliubov transformation and diagonalising the Hamiltonian then yields the Bogoliubov excitation spectrum.

bound to the temperature one needs to achieve and also limits the chemical potential and thus the atom number and especially the scattering length that can be used.

TEM_{01}-like mode Another approach is the use of a blue-detuned Hermite-Gaussian TEM_{01}-like mode [117, 118]. This can be created by imprinting a phase shift of π between the upper and lower half of a Gaussian beam by passing it through a phase-plate. Focussing such a beam leads to an intensity pattern close to a TEM_{01} mode at the focus position. The atoms are trapped in the nodal plane and experience a trapping frequency not given directly by the overall beam waist, but by the smaller length scale given by the distance of the two intensity maxima. Hence, higher trapping frequencies can be achieved.

A drawback of this method is that the shape of the intensity pattern and hence the trapping frequency is sensitive to production-related imperfections as well as to the alignment of the phase-plate. Another downside is the low loading efficiency. Since the blue-detuned light is anti-trapping, there is no density enhancement in the nodal plane when loading the atoms from the crossed dipole trap into the 2D confinement, i. e. the TEM_{01}-like mode cuts out a part of the atom cloud. Since the atom cloud is typically much larger than the distance between the intensity maxima, a large part of the atoms are lost.[11]

Optical lattice The method we chose for our experiment is - as nowadays widely used - to create the strong confinement by an optical lattice [119–122], which from now on we will refer to as the vertical lattice[12]. High trapping frequencies can be achieved since the smallest length scale is set by the lattice spacing $d = \lambda/(2\sin(\alpha))$ where α is half the crossing angle between the two interfering beams. Since the lattice does not require a phase plate its intensity pattern is more robust than the TEM_{01}-like mode. What needs to be considered, though, is that in contrast to the TEM_{01}-like mode the optical lattice consists of several layers, in which the atoms can be trapped. When loading a typical spherical atom cloud into the lattice, several layers would be occupied which would result in a blurring of the signal as the lattice spacing is on the order of the depth of view.[13] To prevent this we decided to introduce an intermediate step. Instead of loading the atoms directly into the vertical lattice, they are first loaded into a light sheet-like trap, which in

[11] The loading efficiency can be increased by employing an accordion scheme which refers to the dynamic adjustment of the distance between the intensity maxima which can be realised via a digital mirror device (DMD)[118]. Thus, the trap can be loaded with a large spacing in order to increase the loading efficiency. Then the trap can be compressed in order to enter the 2D regime. However, this comes at the cost of a rather low power efficiency, since the DMD basically acts as a diffraction grating.

[12] The vertical orientation is chosen to counteract gravity.

[13] Even with a larger depth of view the signal would get blurred since the layers behave slightly different in terms of vertical trapping frequency and in-plane potential (see sec. 4.6.4).

the following will be referred to as the squeeze trap. The squeeze trap is not supposed to provide enough vertical confinement to enter the quasi-2D regime, as opposed to the light sheet trap mentioned above - hence the different name - but the vertical confinement is supposed to be tight enough to pre-shape the atom cloud into a pancake-like shape. The reduced vertical cloud size allows to then load the atoms from the squeeze trap into a single layer of the vertical lattice.[14]

There are two variations of an optical lattice: using red-detuned light where the atoms are trapped at the antinodes of the interference pattern or using blue-detuned light where the atoms are trapped at the nodes. With red-detuned light already the individual lattice beams can be used to trap atoms which is advantageous in terms of alignment. On the other hand the intensity profile introduces a significant confinement in the xz-plane while blue-detuned light introduces a (much lower) anti-trapping confinement in the xz-plane.[15] This means a red-detuned lattice yields an upper limit for the aspect ratio of vertical and radial trapping frequency which ultimately limits the scattering length that can be used to remain in the quasi-2D regime. A blue-detuned lattice on the other hand does require an additional radial confinement, but allows to decouple vertical and radial confinement enabling very low radial trapping frequencies or even flat potentials, i. e. box traps [126–128].[16] We therefore decided for a blue-detuned vertical lattice and use the pre-existing 850 nm crossed dipole trap (CDT) at low depth as an additional confinement in the xz-plane.

Although in principle the additional radial confinement is only required for the vertical lattice, the 850 nm CDT is also used to support the squeeze trap. The experimental sequence is roughly as follows: After a BEC is created in the CDT as described in chapter 3, the atoms are loaded into the squeeze trap while ramping down the 850 nm CDT to a lower value. The strong anisotropy of the squeeze trap results in a pancake-like shape of the atomic sample, which is then loaded into one layer of the vertical lattice while still keeping the 850 nm CDT as radial confinement. A more detailed description of the

[14] Instead of using a fixed vertical lattice one could also use an accordion lattice [123–125], i. e. a lattice with adjustable lattice spacing. By being able to load the lattice using a larger lattice spacing the relative alignment of squeeze trap and vertical lattice needs to be less precise and the requirements for the squeeze trap to be able to load into a single layer of the vertical lattice are less strict which is especially interesting for Fermi gases. However, compared to the fixed lattice this requires a more complex experimental setup, since one needs to introduce a method to dynamically adjust the distance between and, depending on the setup, angle and focus position of the two lattice beams.

[15] Even though the atoms are trapped in the nodes of a blue-detuned optical lattice, they still have a ground state energy which depends on the lattice trapping frequency and thus on the lattice intensity, which radially decreases due to the Gaussian beam shape. For more details see sec. 4.6.4.

[16] One might wonder whether the heating rate due to spontaneous emission is lower for blue-detuned lattices as the atoms are trapped in the dark regions, but it turns out that the heating rate is the same for blue- and red-detuned lattices [129].

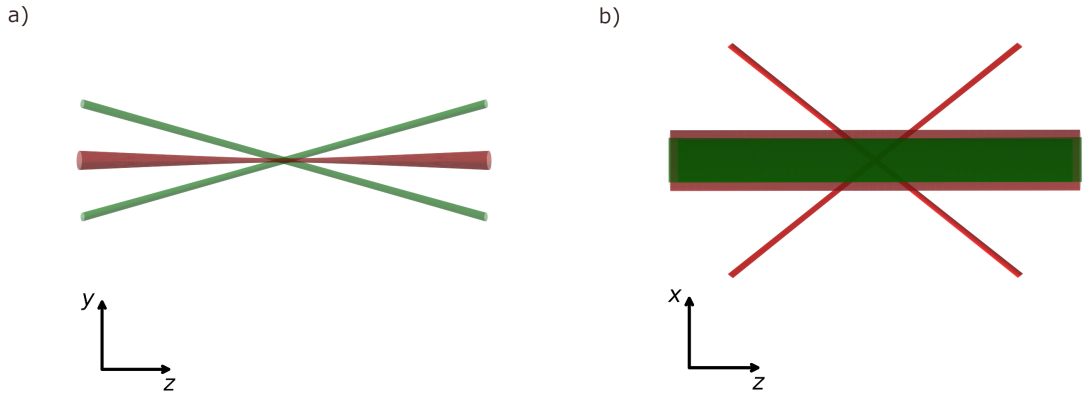

Figure 4.1: Sketch of the beam arrangement. **(a)** Side view on upper and lower vertical lattice beam (green) providing the 2D confinement and squeeze trap beam (dark red) enabling single layer loading. **(b)** Top view on vertical lattice beams (green), squeeze trap beam (dark red) and the 850 nm crossed dipole trap beams (red) that are providing the radial confinement. In the following the x axis will also be referred to as horizontal axis, y as vertical and z as longitudinal.

procedure will be given in sec. 4.6.

The advantage of applying the low depth 850 nm CDT in addition to the squeeze trap is support against gravity as well as reduced heating during the transfers from the 850 nm CDT into the squeeze trap and from the squeeze trap into the vertical lattice: The radial trapping frequency of the 850 nm CDT is much higher than the radial trapping frequency of squeeze trap and vertical lattice. That means for all three stages, 3D BEC in the 850 nm CDT, pancake-like atom cloud in the squeeze trap as well as quasi-2D gas in the vertical lattice, the radial position is determined by the 850 nm CDT and thus nearly independent of the exact radial alignment of squeeze trap and vertical lattice which prevents the excitation of sloshing modes during the transfers. One might wonder whether supporting the squeeze trap with the 850 nm CDT is unfavorable in view of the increased vertical Thomas-Fermi radius due to the higher radial trapping frequency; a larger vertical extent of the atom cloud would make it more difficult to load into a single lattice layer. However, for radial trapping frequencies below $2\pi \times 330$ Hz, as is the case for the low depth 850 nm CDT, the vertical cloud size is not determined by the Thomas-Fermi radius, but by the vertical harmonic oscillator length which is not affected by the radial confinement.

4.3 Design considerations

In the previous section we explained the concept of our 2D setup: a blue-detuned optical lattice with fixed lattice spacing ('vertical lattice'), loaded from a red-detuned highly

anisotropic dipole trap ('squeeze trap'), while the radial confinement is provided by a pre-existing 850 nm crossed dipole trap (CDT). The laser light for the 2D setup is provided by an ALS 1064/532 dual output fiber laser from Azurlight Systems. The 532 nm output is used for the vertical lattice, the 1064 nm output for the squeeze trap. Further considerations and requirements for developing a design for the vertical lattice and squeeze trap will be discussed in the following.

4.3.1 Vertical lattice

2D criterion The purpose of the vertical lattice is to provide the 2D confinement, so first and foremost, the 2D condition $\hbar\omega_y > k_B T, \mu$ (see eq. 4.3) needs to be fulfilled. As the temperature T is usually smaller than μ for BECs with typical interaction strengths, the lower bound for the lattice trapping frequency ω_y is given by the chemical potential μ which can be calculated according to eq. 4.23 and depends on the radial trapping frequencies ω_x and ω_z, the atom number N and the 3D scattering length a. Using that ω_x and ω_z are given by the pre-existing 850nm CDT and are in the order of 150 Hz, we can calculate the minimum vertical trapping frequency for variable N and a as plotted in fig. 4.2. Considering that the atom number of our BEC is typically in the order of $\sim 10^4$

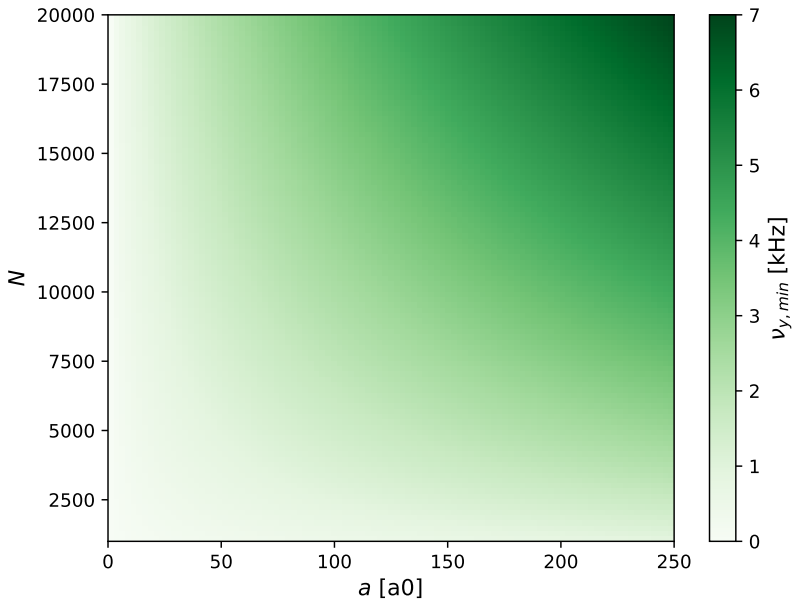

Figure 4.2: The minimum trapping frequency $\nu_{\mathrm{y,min}} = \omega_{\mathrm{y,min}}/2\pi$ of the vertical lattice that fulfills the 2D criterion $\hbar\omega_y > \mu_{\mathrm{2D}}$ for various atom numbers N and 3D scattering lengths a assuming radial trapping frequencies of 150 Hz. Note that in order to achieve a quasi-2D system the criterion $\hbar\omega_y > k_B T$ also needs to be satisfied. However, for BECs with typical interaction strengths the temperature T is usually smaller than μ.

and in order to be able to use a wide range of scattering lengths we set a lower limit for the trapping frequency of $\omega_{\mathrm{y,min}} = 2\pi \times 5\,\mathrm{kHz}$.

Trap depth Second, the radial and vertical trap depths need to be reasonably larger than the temperature T and the chemical potential μ in order for the atoms to be trapped. As usually $T < \mu$ for BECs with typical interaction strengths and since μ is in the order of $\sim 100\,\mathrm{nK}$, we set a minimum trap depth of 1 µK. While this will be easily exceeded for the vertical lattice when achieving the required high vertical trapping frequency, this criterion is quite relevant for the radial confinement. Since the geometry of the 850 nm CDT is already set, the radial trapping frequencies solely depend on the trap depth. Hence, while the 2D condition demands the radial trapping frequencies to be as low as possible, the minimum trap depth sets a lower limit of $\sim 2\pi \cdot 150\,\mathrm{Hz}$.

Homogeneity Third, as discussed in sec. 4.2 using an optical lattice for the 2D confinement yields flexibility in terms of the radial confinement. To fully exploit this, i.e. allowing to freely adapt the radial confinement, especially including the possible future implementation of a flat potential, we require the radial potential given by the vertical lattice to be nearly homogeneous. Due to the Gaussian beam profile, i. e. the radially decreasing intensity I of the lattice beams, this requires the radial extent of the vertical lattice to be reasonably larger than the cloud size. Any inhomogeneity of the intensity results in a spatially dependent chemical potential μ since the chemical potential is affected by the coupling constant $\tilde{g}$ which in turn is affected by the harmonic oscillator length which again depends on the intensity via the vertical trapping frequency ω_y. The dependence is quite weak, though: $\mu_{2D} \propto I^{1/8}$. Within our parameter range the cloud size, estimated by the 2D Thomas-Fermi radius given by eq. 4.21, is in the order of 10 µm. Accordingly, we set a minimum radial trap size of 100 µm. With this lower bound, the extent of the atom cloud is smaller than 0.1 waists of the Gaussian beam profile and hence the intensity decreases by less than 2 % over the cloud size yielding a variation of less than 0.3 % of the 2D chemical potential.

Radial symmetry Last, to obtain a radially roughly symmetric system, we demand equal radial trapping frequencies of the vertical lattice. Since in the xz-plane the trap can be basically considered as a crossed dipole trap formed by the equal lattice beams, this is equivalent to the diameters of the two in-plane trap axes having the same size. One of these diameters is given by half the length of the intersection region which can be geometrically determined to be $r_{\mathrm{intersection}} = w_{\mathrm{ver}}/\sin\alpha$ with the vertical waist w_{ver} and

half the crossing angle α of the lattice beams. The other diameter is simply given by the horizontal waist w_{hor} of the lattice beams. Accordingly, the ratio of the beam waists is supposed to be $w_{\mathrm{ver}}/w_{\mathrm{hor}} = \sin\alpha$. Thus, this criterion sets the ellipticity of the lattice beams.

Technical considerations In addition to the requirements set above there are also some technical considerations: In order to get a small lattice spacing and thus a tight vertical confinement, a large crossing angle 2α of the lattice beams is advantageous. The optical access sets an upper limit of 5° for α, though.

Additionally, in order to increase the intensity and thus the vertical trapping frequency, a small vertical waist is desirable. A lower limit is obviously set by aberrations, but also by the size of the vacuum chamber which gives a rather high lower limit for the focal length and diameter of the focussing lens that can be used.

Finally, also the achievable laser power is naturally limited by the availability of high-power lasers, but also of suitable high-power fibers.

Taking into account the above criteria we decided for the vertical lattice parameters stated in tab. 4.2.

wavelength	λ	532 nm
half the crossing angle	α	5°
vertical beam waist	w_{ver}	25 µm
horizontal beam waist	w_{hor}	290 µm
laser power	P	400 mW
lattice spacing	d	3.05 µm
trap depth	U_0	8.4 µK
trapping frequency	ω_y	$2\pi \times$ 9.7 kHz
anti-trapping	ω_{at}	-$2\pi \times$ 5.4 Hz
chemical potential	μ_{2D}	89 nK
Thomas-Fermi radius	$r_{\mathrm{TF,2D}}$	6.5 µm

Table 4.2: Design values for the vertical lattice. Chemical potential and Thomas Fermi radius are calculated for 10^4 atoms, a scattering length of $30a_0$ and radial trapping frequencies of 150 Hz.

4.3.2 Squeeze trap

Vertical cloud size The purpose of the squeeze trap is to decrease the vertical size of the atom cloud sufficiently to enable loading into a single layer of the vertical lattice. Hence, the main requirement is that the vertical cloud size is smaller than the lattice

spacing d. The cloud size can be estimated via the 3D Thomas-Fermi radius by combining eq. 4.21 and eq. 4.22. Accordingly, in order to achieve a small cloud size a high ratio of vertical to radial trapping frequencies is favorable. Increasing this ratio one approaches the quasi-2D regime, though, where this estimate is no longer valid. Close to the quasi-2D regime the vertical cloud size can instead be estimated by the harmonic oscillator length $a_{\mathrm{ho,y}}$ of the tightly confined axis which is the length at which the density drops to $1/e$. Hence, we demand $\max\left[2r_{\mathrm{TF,3D}}, 4a_{\mathrm{ho,y}}\right] < d = 3.05\,\mu\mathrm{m}$.

Trap depth Second, in order for the atoms to be trapped the trap depth needs to be larger than the temperature and the chemical potential. Accordingly, just as with the vertical lattice we set a lower limit for the trap depth of 1 µK.

Radial symmetry Third, we also prefer the squeeze trap to be radially symmetric in the xz-plane which is equivalent to equal radial trapping frequencies. To estimate these trapping frequencies we consider a highly elliptical beam with waists $w_y \ll w_x$ propagating along z. The intensity profile is then given by

$$I(x,y,z) = I_0 \exp\left(-\frac{2x^2}{w_{x,0}^2} - \frac{2y^2}{w_{y,0}^2}\right) \frac{w_{x,0}}{w_x(z)} \frac{w_{y,0}}{w_y(z)} \tag{4.26}$$

with waist $w_i(z) = w_{i,0}(1+(z/z_{R,i})^2)^{1/2}$ where z_R is the Rayleigh range. Since $z_{R,x} \gg z_{R,y}$ due to the ellipticity the term $(z/z_{R,x})^2$ can be neglected:

$$I(x,y,z) \simeq I_0 \exp\left(-\frac{2x^2}{w_{x,0}^2} - \frac{2y^2}{w_{y,0}^2}\right) \frac{1}{\sqrt{1+(z/z_{R,y})^2}} \tag{4.27}$$

Taylor expanding this to second order and using that the optical potential is proportional to the intensity yields:

$$U \simeq -U_0 \left[1 - 2\frac{x^2}{w_{x,0}^2} - 2\frac{y^2}{w_{y,0}^2} - \frac{1}{2}\frac{z^2}{z_{R,y}^2}\right] \tag{4.28}$$

This yields the trapping frequencies

$$\omega_x \simeq \sqrt{\frac{4U_0}{m w_{x,0}^2}}, \quad \omega_z \simeq \sqrt{\frac{U_0}{m z_{R,y}^2}} \tag{4.29}$$

where $w_{x,0}$ corresponds to the horizontal beam waist w_{hor} of the squeeze trap and $z_{R,y}$ to the Rayleigh range $z_{R,ver}$ of the vertical waist of the squeeze trap. Thus, in order to

get equal radial trapping frequencies the condition $w_{\mathrm{hor}} = 2z_{R,ver} = 2\pi w_{\mathrm{ver}}^2/\lambda$ needs to be fulfilled.

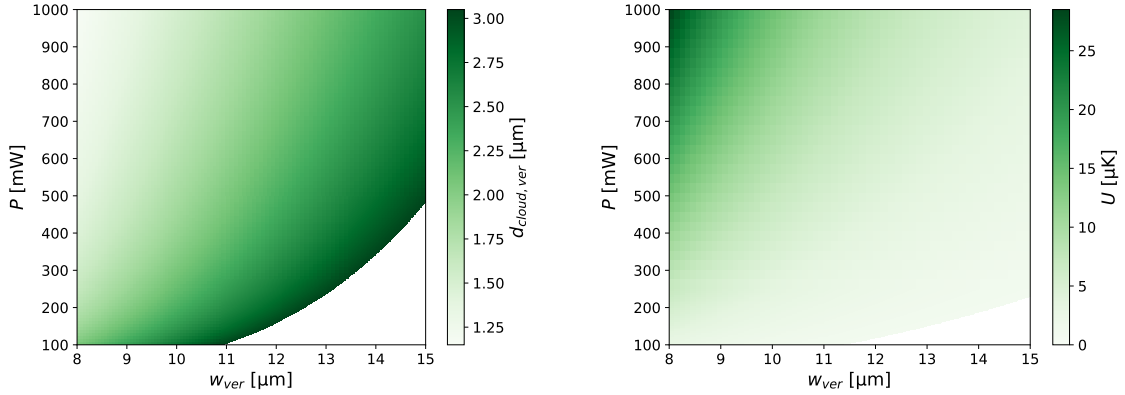

Figure 4.3: The vertical cloud size $d_{\mathrm{cloud,ver}}$ in and trap depth U of the squeeze trap for various laser powers P and vertical waists w_{ver} of the squeeze trap. $d_{\mathrm{cloud,ver}}$ is estimated by $\max\left[2r_{\mathrm{TF,3D}}, 4a_{\mathrm{ho,y}}\right]$ where $r_{\mathrm{TF,3D}}$ is the 3D Thomas-Fermi radius and $a_{\mathrm{ho,y}}$ the vertical harmonic oscillator length. For the calculations the horizontal squeeze trap waist is adapted such that the radial trapping frequencies of the squeeze trap are equal. Only the regimes fulfilling the requirements are plotted.

The parameter regimes fulfilling the requirements above are plotted in fig. 4.3. As can be seen low vertical waists and high laser powers are favorable. However, from a technical point of view the achievable laser power is limited and also the vertical waist underlies technical limitations. A lower bound is set by the occurrence of severe aberrations. Also, the size of the vacuum chamber sets a lower limit for the focal length of the focussing lens. Hence, a small focal waist requires a large beam waist on the focussing lens whose size is limited by the need for optical access e. g. for the beam paths of the vertical lattice. These considerations lead to the design parameters for the squeeze trap stated in tab. 4.3.

wavelength	λ	1064 nm
vertical beam waist	w_{ver}	10.6 µm
horizontal beam waist	w_{hor}	660 µm
laser power	P	500 mW
trap depth	U	6.2 µK
vertical trapping frequency	ω_y	$2\pi \times 1.1$ kHz
radial trapping frequency	ω_r	$2\pi \times 17$ Hz
harmonic oscillator length	$a_{\mathrm{ho,y}}$	0.5 µm
Thomas-Fermi radius	$r_{\mathrm{TF,3D}}$	0.3 µm

Table 4.3: Design values for the squeeze trap. The Thomas Fermi radius is calculated for 10^4 atoms and a 3D scattering length of $30a_0$.

4.4 Generating the squeeze trap and the vertical lattice

In this section we discuss the technical implementation of the vertical lattice and the squeeze trap. We will focus on two aspects: the employed beam shaping scheme and the setup designed to split the vertical lattice beam into an upper and a lower beam that interfere at the atom position to create the lattice. We will present experimentally achieved beam and trap parameters and compare them with the design values derived in the previous section.

Preliminary considerations The first question for the technical implementation of the vertical lattice is whether to split the lattice beam into two before or behind a common focussing lens. When splitting the beam into two parallel beams before the focussing lens the intersection automatically lies within the focal plane, which is convenient in terms of alignment. On the other hand, the beams have to pass the lens quite off-center to achieve a reasonable crossing angle, which would introduce additional aberrations. Furthermore, the longer the focal length, the larger the required lens diameter to maintain the same crossing angle. This setup is thus only suitable for rather short focal lengths which is not compatible with the lower bound set by the size of our vacuum chamber. Hence, in our setup the lattice beam first passes the focussing lens and is then split into an upper and lower lattice beam interfering at the intersection to form the vertical lattice.

4.4.1 Beam shaping

Considerations and concept As stated in sec. 4.3, we have to use rather long focal lengths for the focussing lenses, i. e. $f = 400\,\mathrm{mm}$ for the squeeze trap due to the size of the vacuum chamber and $f = 750\,\mathrm{mm}$ for the vertical lattice due to the additional space required in between focussing lens and vacuum chamber for the setup that splits the lattice beams (see sec. 4.4.2). That means in order to achieve the desired small vertical focal waists, the beam waists and thus the optics before the focussing lenses have to be rather large. Hence, we have to compromise between preserving optical access for other optical setups[17] and truncating the beams as little as possible as a truncated beam increases the focal waist. Furthermore, it is favorable to use as few optical elements as possible in order to increase the stability and to preserve space, while the necessity to create highly elliptical beams requires additional optics.

[17] The squeeze trap, the vertical lattice and the 1064 nm ODT for the collisional loading (see sec. 3.6) enter the vacuum chamber through the same viewport, but under different angles and hence cannot be superimposed.

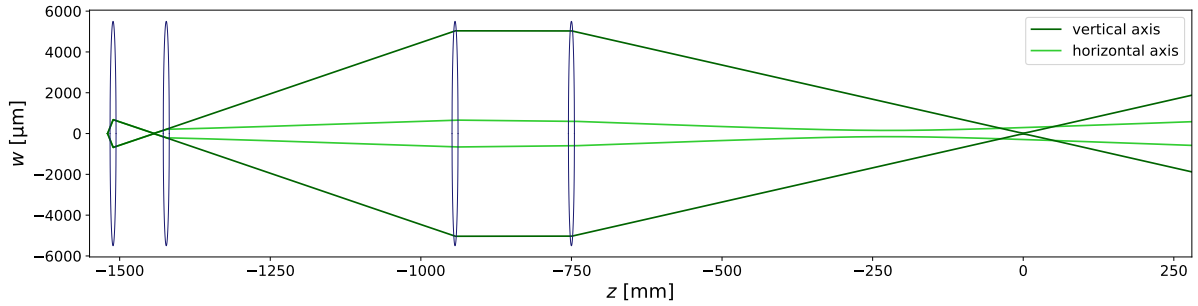

Figure 4.4: Beam shaping of the vertical lattice beam to achieve the desired elliptical beam at the atom position $z = 0$. The general concept is explained in the main text. Depicted is the beam size w in dependence of the position z along the beam axis with respect to the atom position both in the vertical (dark green) as well as in the horizontal (light green) plane. The leftmost point refers to the position of the fiber tip which delivers the lattice beam. The first lens is an f = 8 mm achromat which focusses the beam down to a waist of 16.8 µm corresponding to a divergence of 10.1 mrad. The second lens is an f = 22.19 mm cylindrical lens reducing the divergence in the horizontal beam axis while the vertical axis is not affected. The third lens is an f = 500 mm achromat which collimates the beam in the vertical axis. The fourth lens is an f = 750 mm achromat that focusses the vertical beam axis down to a waist of 25.2 µm at the atom position. The horizontal waist at the atom position is 291.9 µm and can be adjusted by adjusting the position of the cylindrical lens.

The conceptually most simple beam shaping would employ two telescopes: a first telescope affecting both beam axes specified to adjust e. g. the vertical axis and a second telescope with cylindrical lenses to adjust the respective other axis in order to achieve the desired elliptical beam. Together with the lens to collimate the beam behind the fiber and the focussing lens this would require a total of six lenses, two of them cylindrical.

To reduce the number of lenses and the overall size of the setup we instead use the beam shaping design depicted in fig. 4.4 and fig. 4.5. The key idea is to abandon the constraint that the beam has to be focussed in both axes at the atom position: While it has to be focussed in the tight, i. e. the vertical axis, the horizontal axis can exhibit a slight con- or divergence without detrimental consequences as elaborated below. In that case a total of four lenses, one of them cylindrical, is sufficient to achieve the desired elliptical beam at the atom position.

Details on the beam shaping design The beam shaping designs for vertical lattice and squeeze trap are shown in fig. 4.4 and fig. 4.5. While the values for positions and focal lengths of the lenses differ, the general setup is the same for vertical lattice and squeeze trap. It consists of four lenses where the second one is cylindrical and oriented such that it only affects the horizontal axis.

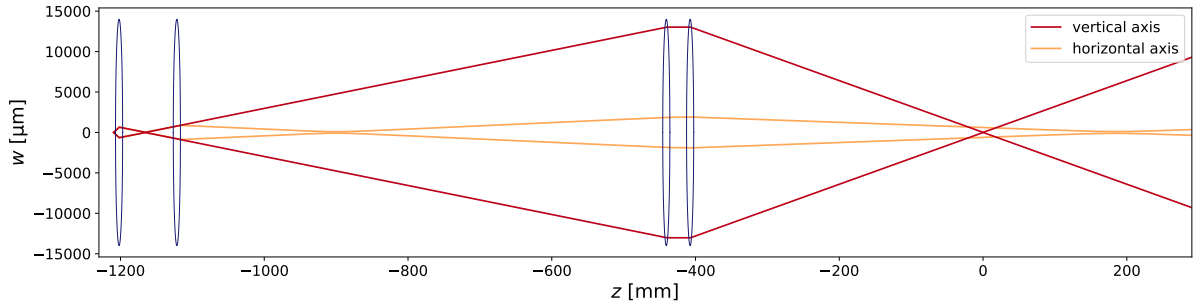

Figure 4.5: Beam shaping of the squeeze trap to achieve the desired elliptical beam at the atom position $z = 0$. The general concept is explained in the main text. Depicted is the beam size w in dependence of the position z along the beam axis with respect to the atom position both in the vertical (dark red) as well as in the horizontal (light red) plane. The leftmost point refers to the position of the fiber tip which delivers the squeeze trap beam. The first lens is an f = 6.24 mm asphere which focusses the beam down to a waist of 18.9 µm corresponding to a divergence of 18.0 mrad. The second lens is an f = 40 mm cylindrical lens reducing this divergence in the horizontal beam axis while the vertical axis is not affected. The third lens is an f = 750 mm achromat which nearly collimates the beam in the vertical axis. The fourth lens is an f = 400 mm achromat that focusses the vertical beam axis down to a waist of 10.6 µm at the atom position. The horizontal waist at the atom position is 604.3 µm and can be adjusted by adjusting the position of the cylindrical lens.

The design of the vertical axis is rather conventional: The small vertical waist is achieved with a large, nearly collimated beam on the focussing lens, i. e. the fourth lens. Typically, this large collimated beam would be achieved by collimating the beam emitted by the fiber and magnifying it with a telescope. To save space and to reduce the number of lenses we instead place the first lens behind the fiber not at the focal distance, but further away from the fiber. That way an intermediate focal spot with a reduced divergence compared to the fiber output is created already after the first lens. Although reduced, the divergence is still large enough to result in a large beam waist on the third lens which then nearly collimates the beam.

The lowering of the divergence is important in order to reduce aberrations caused by the subsequent lenses[18] which sets a lower limit for the waist of the intermediate focal spot.[19] The distance between first lens and fiber is obviously also limited by the occurrence of aberrations especially when using aspheric lenses.

In order to achieve an elliptical beam the beam shaping in the horizontal axis is altered with respect to the vertical axis via the cylindrical second lens: it further reduces

[18]The diameter of high-quality aspheric lenses is production-related rather small. Therefore, only the first lens in our setup is an aspheric lens. For the subsequent lenses the larger beam waist prevents to use aspheric lenses. Accordingly, these lenses are more prone to introduce spherical aberrations, especially in the case of high numerical apertures.

[19]This lower limit depends on which lens is used after the intermediate focal spot.

the divergence to achieve a smaller beam waist on the third and fourth lens compared to the vertical axis, and thus a larger beam waist at the atom position. This also shifts the focus position causing the beam to be horizontally con- or divergent at the atom position. Allowing a small con-/divergence, which is negligible in terms of potential gradient and inhomogeneity (see discussion below), enables to adjust the horizontal beam waist by adjusting the position of the cylindrical lens.

Note that it is possible to place the cylindrical lens such that the astigmatism vanishes. According to ray optics this should not be the case since the vertical and horizontal intermediate foci are at different positions due to the cylindrical lens. However, the Rayleigh range of the desired horizontal waists are in the order of the focal length of the respective focussing lens. Hence, ray optics is no longer valid and Gaussian beam optics has to be considered instead which explains why the horizontal and vertical focal spots can be both located at the atom position. This is not favorable, though, as this would fix the position of the cylindrical lens, forfeiting this degree of freedom and thus the flexibility to adjust the horizontal waist at the atom position.[20]

Discussion The beam shaping design described above allows to keep the beam path in general and especially the parts with large beam waists short. Also, it uses only four lenses and especially minimises the number of cylindrical lenses which typically cannot be manufactured with as good quality as spherical lenses, and are not commonly available as doublets and hence are more likely to cause aberrations.

On the downside, one might think that the horizontal con- or divergence at the atom position is disadvantageous in terms of confinement along the beam axis and inhomogeneity, but these are minor effects:

The radial confinement for the vertical lattice is given by the 850 nm crossed dipole trap and is thus not affected.[21] For the squeeze trap the confinement along the beam axis is dominated by the Rayleigh range of the much tighter vertical focal waist. The calculated shift of the potential minimum caused by the astigmatism is $\sim 0.6\,\mu$m which is well below the cloud size.

The con- or divergence causes inhomogeneity, though, in the sense that the trapping frequencies change along the beam axis as the horizontal waist and thus, the intensity

[20] Also, the horizontal waist is then set by the focal length of the cylindrical lens since the other lenses are fixed by the vertical axis. That means in order to achieve the desired horizontal waist one would need a customised cylindrical lens.

[21] In case of the future implementation of a flat in-plane potential via a DMD, the small potential gradient introduced by the divergence can be compensated by the DMD.

changes. As stated in sec. 4.3.1 for the vertical lattice this mainly affects the 2D chemical potential which depends only weakly on the intensity of the lattice beams. For the designed beam shaping shown in fig. 4.4 the horizontal waist changes by ∼0.1 % over the trap size causing the 2D chemical potential to change by ∼0.01 %, which is an order of magnitude lower than the effect of the Gaussian beam profile. For the squeeze trap the trapping frequency is mainly relevant for the vertical cloud size which is given by the harmonic oscillator length $a_{\mathrm{ho,y}} \propto w_{\mathrm{hor}}^{1/4}$. For the designed beam shaping presented in fig. 4.5 the horizontal waist w_{hor} changes by ∼0.15 % over the size of the vertical lattice causing the harmonic oscillator length to change by ∼0.04 %. Hence, the vertical size of the atom cloud is well below the lattice spacing as required.

4.4.2 Splitting the lattice beams

So far we only considered a single 532 nm beam, while two interfering beams are required to create the optical lattice. To achieve this we built a separate setup whose purpose is to split the incoming single 532 nm beam into two lattice beams, the so-called upper and lower beam, that interfere at the atom position. In order to increase the stability of the vertical lattice it is favorable to minimise the number of non-common components of upper and lower beam. Hence, the setup to split the lattice beam is placed behind the last lens of the beam shaping discussed above, i. e. behind the focussing lens of the vertical lattice.

A picture of the setup is shown in fig. 4.6. Its central component is a one inch polarising beamsplitter cube that splits the beam entering the setup from the right into the two lattice beams. The other components are mainly mirrors needed to achieve the vertical distance of the two lattice beams that is required for the lattice beams to intersect at the desired angle of 2 x 5° at the position of the atoms. The lower lattice beam path additionally includes a wave plate to align the polarisation of the two lattice beams. Otherwise, the two lattice beams would have orthogonal polarisations due to the polarising cube and would therefore not interfere.

The surface of the cube with the actual beamsplitter coating acts as a symmetry plane. Hence, every fluctuation of beam position or angle caused by common optical elements, i. e. before the cube, translates into a symmetric fluctuation of the two lattice beams while the symmetry plane stays the same. That means fluctuations of common optical elements translate into a fluctuation of the lattice spacing, but not to an actual displacement of the lattice.[22] For that reason the setup is designed to minimise the

[22] This holds true for the central layer. Due to the changing lattice spacing any other layer will move in

Figure 4.6: Setup for splitting the lattice beams: The beam enters from the right and is reflected by two mirrors onto a polarising beamsplitter cube which performs the actual splitting. Each of the two lattice beams is then again reflected by two mirrors and exits the box on the left side of the picture. The mirrors are oriented such that the beams intersect $\sim 400\,\mathrm{mm}$ behind the box under the desired crossing angle of $2\,\mathrm{x}\ 5°$. Since the cube is polarising the lower beam path includes a wave plate attached to the output port of the box to align the polarisation of the two lattice beams and to thus achieve full interference.

number of optical elements behind the cube. Although one could further reduce this number by utilising a non-polarising beamsplitter (NPB) instead of the polarising cube and thus making the wave plate unnecessary, the polarising beamsplitter cube is more favorable: It allows to balance the power of the two lattice beams by adding another wave plate before the splitting setup. To further increase the stability three of the walls of the casing including the two that have the optics attached to them are machined from one piece. Also, solid, one-piece, non-adjustable mounts are employed where possible. Only the last mirror of each lattice beam is adjustable to provide enough degrees of freedom to adjust position and angle of the two lattice beams. Furthermore, these mirrors are mounted specifically to three-knob adjusters, so that the path lengths can be adjusted as well. While this gives the necessary degree of freedom to ensure that both focal spots are at the intersection, this is not precise enough to equalise the path lengths

space. The displacement will be much smaller, though, than the displacement of the lattice beams with respect to the symmetry plane.

on the order of the wavelength. That means although in principle an intensity node would be in the center of the lattice due to the phase jump in one of the beams due to being reflected by the cube, in reality there will be an additional random phase shift due to the path lengths difference of the two lattice beams such that the 'central' layer will not be at the center.[23]

The setup is designed to be compact in order to preserve optical access while still limiting the truncation to keep the small focal waist. The relation between truncation and increase of the focal waist is shown in fig. 4.7. The largest truncation occurs at the mirror right after the cube where, according to the designed beam shaping, the beam is truncated after 1.88 waists. Considering 90 % of the surface of the optics as clear aperture to account for non-perfect alignment the beam is truncated after 1.69 waists corresponding to an increase of the focal waist by $\sim 3\,\%$.

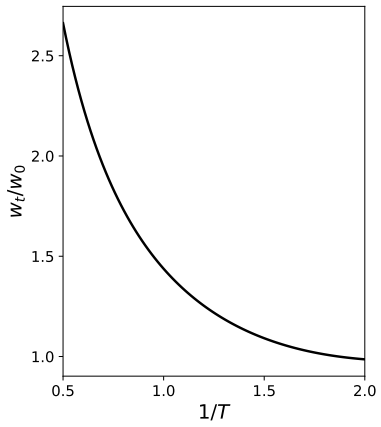

Figure 4.7: The relative focal waist, i. e. the focal waist w_t of a truncated Gaussian beam normalised to the focal waist w_0 in case of no truncation in dependence of the inverse truncation $1/T = D_t/D_b$ where D_t is the limiting aperture diameter and D_b is the Gaussian beam diameter measured at the $1/e^2$ intensity point of the unfocussed beam.

4.4.3 Final setup

A picture of the final 2D setup is shown in fig. 4.8. The squeeze trap and vertical lattice enter the vacuum chamber along the transport axis (see fig. 2.4) from the same direction. In principle that is not a necessity, but in our case it is convenient in order to allow for maximum optical access and hence resolution of the imaging along that axis which is set up on the other side of the chamber. Although the squeeze beam and the vertical lattice beams are not superimposed vertically, they are horizontally aligned. This is achieved with a carefully sized mirror which reflects the squeeze beam into the chamber while the lattice beams pass above and below the mirror.

Besides the lenses for the beam shaping and the box for splitting the lattice beams discussed above the setup includes polarising beamsplitters to purify the polarisation as well as photodiodes as part of the power stabilisation. In addition, the squeeze trap path includes a dichroic mirror to superimpose the squeeze trap light with D2 imaging light.

[23] Vertical shifts of the lattice on the order of the lattice spacing can be enabled by a simple upgrade of the setup: adding rotatable glass plates or translatable wedged glass plates in the paths of the lattice beams would allow to tune the relative phase of the lattice beams and thus to vertically shift the layers.

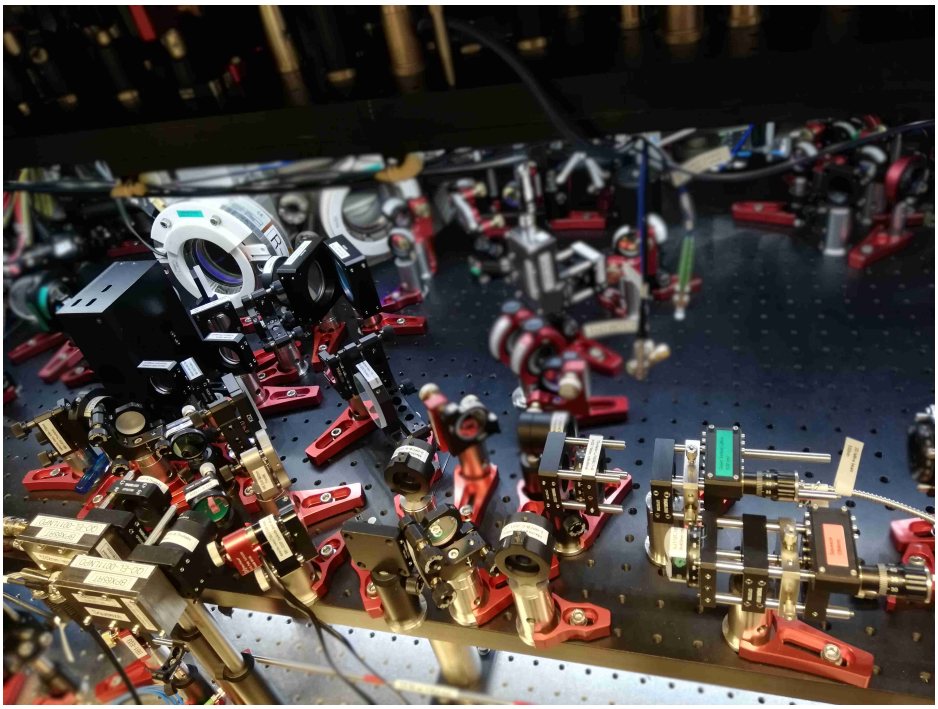

Figure 4.8: Picture of the final 2D setup as implemented in the experiment. The light for the squeeze trap and the vertical lattice are delivered via the fibers on the right side of the picture and passes the optics explained in the main text before entering the vacuum chamber through the same viewport.

To minimize the effect of this dichrioc mirror on the beam profile and waist of the squeeze trap the setup is chosen such that the squeeze trap is transmitted through the mirror while the imaging light is reflected. Furthermore, to ensure that the focus position of squeeze trap and vertical lattice can be reasonably well adjusted each focussing lens is mounted on a translation stage. Finally, to reliably adjust the relative position of the squeeze trap and vertical lattice with the sub-micron precision required to vertically align the squeeze trap with one of the lattice layers, the squeeze trap path features a motorised mirror mount with a step size of 0.7 µrad corresponding to a shift of 130 nm per step at the atom position.

4.4.4 Performance

Vertical lattice

The parameters that were actually achieved for the vertical lattice beams with the setup described in the previous section are stated in tab. 4.4.

upper beam, vertical waist	w_{ver}	21.0 µm
upper beam, horizontal beam waist	w_{hor}	268 µm
lower beam, vertical waist	w_{ver}	21.5 µm
lower beam, horizontal beam waist	w_{hor}	267 µm
laser power per beam	P	290 mW
vertical trapping frequency	ω_z	$2\pi \times 6.5$ kHz

Table 4.4: Measured values for the vertical lattice. The beam waists were obtained by fitting a 2D Gaussian function to the beam profile at the focus position in a test focus outside the vacuum chamber. The trapping frequency was obtained via a parametric heating measurement. Details on the measurements are given in the main text.

Beam waists To acquire the beam waists of the lattice beams the beam profile at the focus position was measured with a camera and fitted with a 2D Gaussian. An exemplary image of the beam profile can be seen in fig. 4.9. The measured beam waists are with

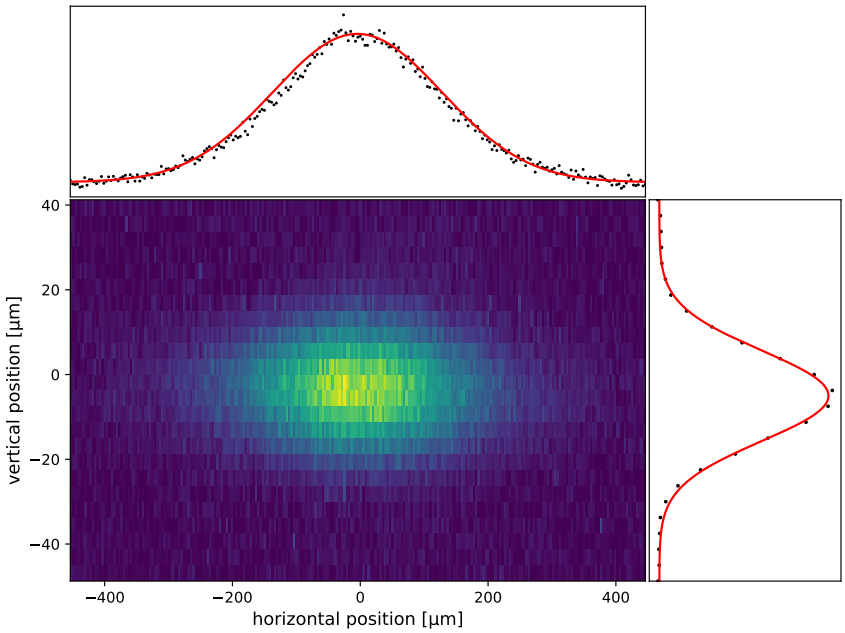

Figure 4.9: Beam profile of the lower lattice beam at the focus position measured with a camera. The beam profile of the upper lattice beam looks similar. The beam waists of 21.0 µm x 268 µm for the upper and 21.5 µm x 267 µm for the lower beam are obtained by fitting a 2D Gauss function to the measured intensity distribution. For a better comparison the vertical and horizontal linesums of measured (black dots) and fitted (red line) data are presented as well.

21.0 µm x 268 µm and 21.5 µm x 267 µm for upper and lower beam smaller than the design values of 25 µm x 290 µm which is favorable as it increases the vertical trapping frequency. The deviation is probably due to a slightly different position of the asphere, i. e. the first lens of the beam shaping, since the size of the vertical focal waist is quite sensitive to this parameter. The vertical waists of the upper and lower lattice beam are slightly different

which mainly affects the radial anti-trapping. This effect depends on the lattice layer and is on the order of only a few percent. Thus, the anti-trapping is still much lower than the radial confinement provided by the 850 nm crossed dipole trap, hence this effect is negligible (for details see sec. 4.6.4). The lattice depths one would expect for the measured beam waists is 7.8 µK, the expected vertical trapping frequency is $2\pi \times 9.3$ kHz which is fairly close to the design values.

Vertical trapping frequency To measure the trapping frequency we modulate the intensity of the vertical lattice with variable modulation frequency while observing the temperature of the trapped atomic gas [130]. This amplitude modulation causes parametric heating, i. e. an increase of the temperature that can be determined from time-of-flight absorption images. Varying the frequency of the sinusoidal modulation with a modulation amplitude of 20 % and a modulation time of 180 ms we obtain the spectrum shown in fig. 4.10. When the modulation frequency is twice the trapping frequency the atoms are parametrically excited [131] resulting in a temperature peak at, in our case, a modulation frequency of 13 kHz, indicating a trapping frequency of $2\pi \times 6.5$ kHz. This is lower than expected for the measured beam waists indicating a longitudinal and horizontal misalignment in the order of 110 µm of the vertical lattice with respect to the 850 nm crossed dipole trap (see sec. 4.5.2), but within the requirement of exceeding a lower limit of $2\pi \times 5$ kHz.

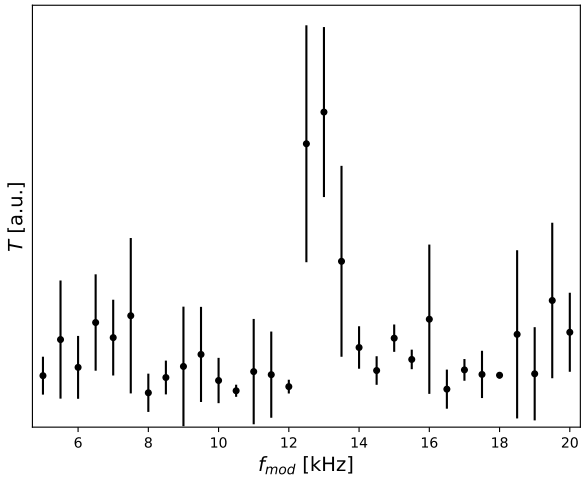

Figure 4.10: The approximate temperature T deduced from the cloud size after a time-of-flight absorption measurement in dependence of the intensity modulation frequency f_{mod} of the vertical lattice for a laser power of 290 mW per lattice beam and a modulation amplitude of 20 %. Due to parametric heating the temperature peaks at twice the trapping frequency, indicating a trapping frequency of $2\pi \times 6.5$ kHz.

Squeeze trap

The parameters that were achieved for the squeeze trap beam are stated in tab. 4.5.

vertical waist	w_{ver}	11.8 µm
horizontal beam waist	w_{hor}	372 µm
laser power	P	480 mW
vertical trapping frequency	ω_z	$2\pi \times 1.04$ kHz

Table 4.5: Measured values for the squeeze trap. The horizontal waist was adapted according to the measured vertical waist to achieve an in-plane aspect ratio of the atom cloud of roughly 1:2. The horizontal beam waist was derived from the beam profile at the focus position, the vertical beam waist from the beam caustic. The trapping frequency was extracted by measuring the sloshing mode. Details on the measurements are given in the main text.

Beam waist The horizontal beam waist of the squeeze trap beam was obtained by imaging the beam profile at the focus position, shown in fig. 4.11, and fitting a 2D Gaussian to the measured intensity profile. To derive the vertical waist, however, this procedure

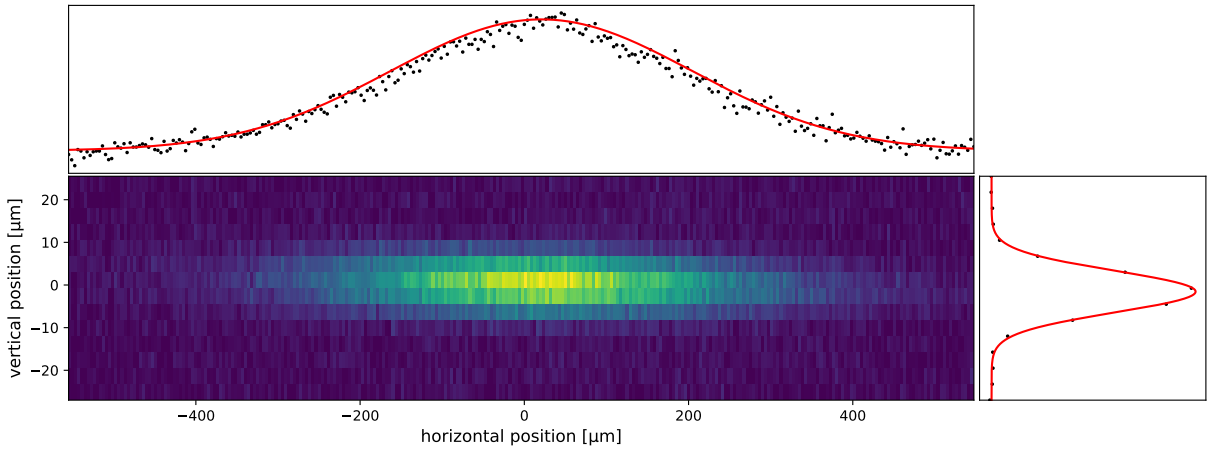

Figure 4.11: Beam profile of the squeeze trap beam at the focus position. The horizontal beam waist of 372 µm is obtained by fitting a 2D Gauss function to the intensity distribution. Also shown are the linesums of measured (black dots) and fitted (red line) data, confirming the Gaussian profile at the focus position. Since the small beam waist is on the order of 2-3 px the vertical focal waist of 11.8 µm was not extracted directly from the beam profile at the focus position, but by fitting to the beam caustic.

was used to obtain the beam waist for several positions along the beam axis to acquire the beam caustic. The vertical beam waist of 11.8 µm was then extracted from a fit to the measured beam caustic, the fit suggests an M^2 factor of 1.18. Note that the fit only includes data for distances of up to 200 µm to the focus position. Further away the squeeze trap beam exhibits significant aberrations as can be seen in fig. 4.12. This is compatible

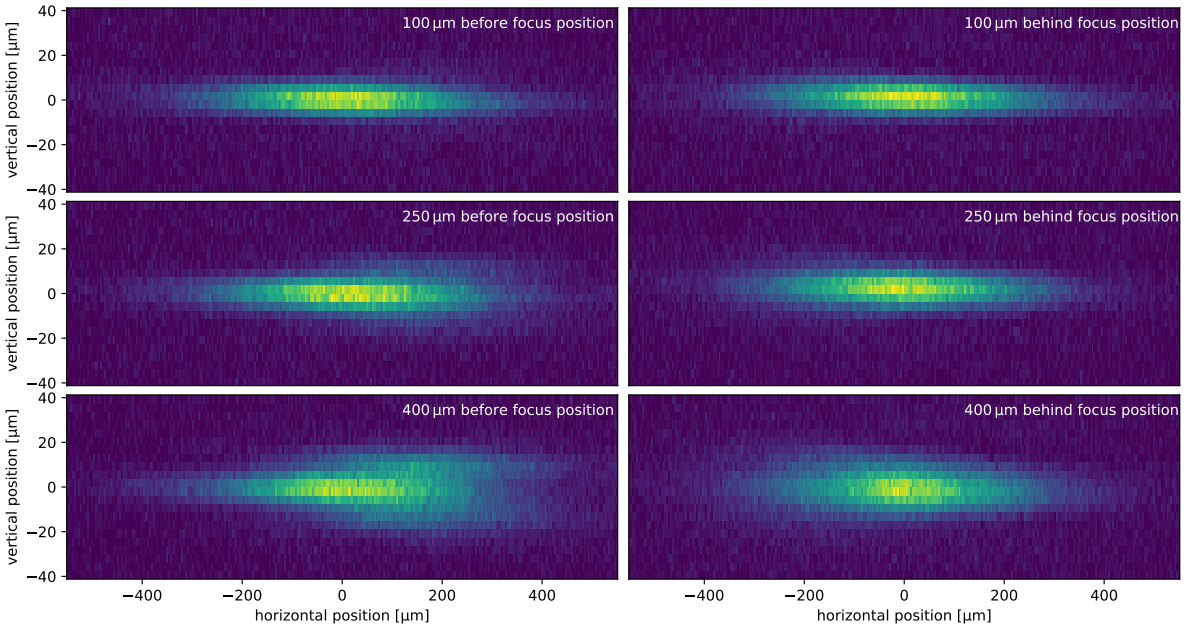

Figure 4.12: Beam profile of the squeeze trap beam at different distances to the focus position. For distances $\gtrsim 250\,\mu m$ the beam exhibits significant aberrations. However, within distances of 200 µm, which is well above the size of the atom cloud, the beam profile is well described by a Gaussian.

with the vertical focal waist being slightly higher than the design value. However, the observed aberrations are not relevant for our system since the squeeze trap only acts as an intermediate step and since the aberrations occur at distances larger than the size of the vertical lattice. Over the size of the vertical lattice, which is much larger then the size of the atom cloud estimated by the Thomas-Fermi radius, the squeeze trap beam profile is well approximated by a Gaussian.

The slightly higher vertical focal waist would require a quite large horizontal waist of 820 µm when demanding a radial symmetric trap. This would reduce the trapping frequency by $\sim 25\%$ compared to the design value. As a compromise between ellipticity and, via intensity, the trapping frequency the horizontal beam waist was instead adapted to 372 µm yielding an aspect ratio of 1:2.2. The expected trap depths for these parameters is 9.5 µK, the expected trapping frequency is $2\pi \times 1.2\,\mathrm{kHz}$.

Vertical trapping frequency To measure the trapping frequency of the squeeze trap we excite a monopole mode ('breathing' mode) [132] with the following procedure: a BEC is loaded into the squeeze trap at $\sim 30\,\%$ of its full depth, supported by the 850 nm crossed dipole trap. Afterwards, the 850 nm CDT is adiabatically turned off and the squeeze trap depth is suddenly increased. After a subsequent variable evolution time the atoms are released from the squeeze trap and imaged along the squeeze beam axis via absorption

imaging after 4 ms time-of-flight, from which the cloud size and position, especially in the tightly confined direction that we are interested in, can be extracted.

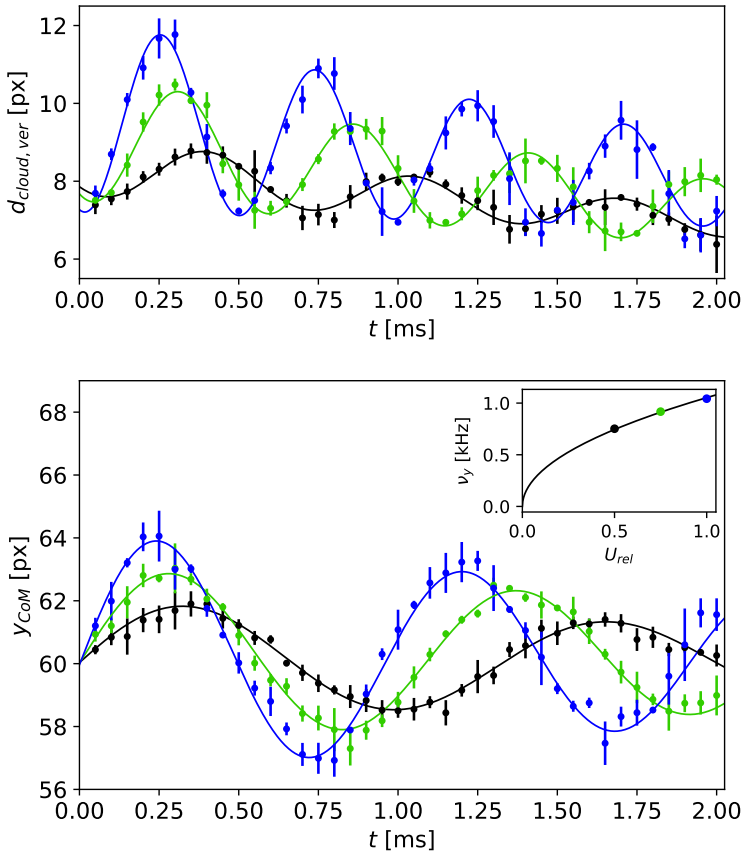

Figure 4.13: Oscillation of the cloud size $d_{\mathrm{cloud,ver}}$ corresponding to the monopole or 'breathing' mode (top) and oscillation of the center-of-mass position y_{CoM} corresponding to the dipole or 'sloshing' mode (bottom) in the tightly confined (vertical) axis of the squeeze trap after quenching the squeeze trap to 50 % (black), 75 % (green) or 100 % (blue) of the maximum trap depth. The respective trapping frequency is extracted by fitting with a damped sine (solid lines). The trapping frequencies ν extracted from the sloshing mode in dependence of the relative trap depth U_{rel} (inset, errorbars are smaller than the marker size) follow the expected square root behaviour (solid line). Details are given in the main text.

The quenching of the squeeze trap excites a breathing mode, i. e. a collective excitation of the atoms in the squeeze trap, that can be observed as an oscillation of the size of the atom cloud as shown in fig. 4.13 (top). To get an intuition one can consider the classical picture: due to the non-adiabatic quench the atoms gain energy and start oscillating in the trap. At the time of the quench there is a certain spatial distribution and a narrow momentum distribution. After $T/4$ the spatial distribution is mapped onto the momentum distribution and vice versa and thus after $T/4$ the spatial distribution, i. e. the cloud size, is narrow. After $T/2$ the system has undergone another Fourier transformation and the spatial distribution is mapped back to the initial distribution. Accordingly, we would

expect the cloud size to oscillate with twice the trapping frequency. This naive picture does not take interactions into account, though. While the factor of 2 is hence altered by the interactions in the 3D case, where the oscillation frequency strongly depends on the interaction strength, in the 2D case there is a 'hidden', so-called Pitaevskii-Rosch symmetry [133] that to first order leads to a pre-factor of 2 also for an interacting gas. However, taking the theoretical treatment one step further and considering the quantum anomaly [134, 135] reveals a weak dependence on the interaction strength resulting in a deviation from the classical value of twice the trapping frequency [136–139]. However, this deviation is low, below 10 %, and hence half the frequency of the breathing mode can be used as a good estimate for the trapping frequency.

A more precise method is to measure the frequency of the dipole oscillations ('sloshing' mode), i. e. the center-of-mass oscillations as shown in fig. 4.13 (bottom). The sloshing mode is excited by the same procedure as the breathing mode and since both cloud size and position can be extracted from the absorption images, monopole and dipole oscillations can be acquired simultaneously. Note, that the signal of the sloshing mode can be weak, especially if the position of the atom cloud is very well aligned to the trap center. However, if a suitable signal-to-noise ratio is achieved, it is favorable to extract the trapping frequency from the sloshing mode since its frequency, which equals the trapping frequency after the quench, does not depend on the interaction strength [136].

The breathing and the sloshing mode in the squeeze trap in the tightly confined direction are presented in fig. 4.13. The oscillations were measured for three different trap depth, corresponding to a laser power of 240 mW (black), 360 mW (green) and 480 mW (blue) where the latter is considered the maximum trap depth. To extract the trapping frequency the data was fitted with a damped sine with a frequency equal to twice (once) the trapping frequency for the breathing (sloshing) mode. The fit function for the breathing mode additionally includes a linearly decreasing offset to account for a decreasing atom number. Although the sloshing measurement is more reliable than the breathing measurement as discussed above, the fitted trapping frequencies from both modes are in agreement, the deviation is less than 3 %. Furthermore, the fitted trapping frequency in dependence of the trap depths is well described by the expected square root behaviour as can be seen in fig. 4.13 (inset).

The extracted trapping frequency ω_y in the tightly confined axis of the squeeze trap at full depth is $2\pi \times 1.04\,\mathrm{kHz}$ which is slightly lower than the design value and than expected for the measured beam waists. However, the corresponding harmonic oscillator length - which is the relevant parameter for the vertical cloud size since our squeeze trap already approaches the quasi-2D regime - is 0.5 µm which is well within the requirements.

4.5 Alignment

In this section, we explain the alignment procedure for the squeeze trap and the vertical lattice. We will start with the alignment of the squeeze trap and the vertical lattice with respect to the atom position determined by the 850 nm crossed dipole trap. We will estimate the required accuracy for the alignment of the different axes and discuss the respective alignment steps. We will then proceed to the subsequent relative alignment of squeeze trap and vertical lattice. This step is of particular importance as it determines the 'singlicity', i. e. how well loading into the vertical lattice is limited to a single layer. We will explain how the singlicity can be measured and present data on the achieved stability.

4.5.1 Squeeze trap

Required alignment precision

Before elaborating on the alignment procedure, we first discuss the alignment precision we need to achieve. While the required vertical precision of a few µm is determined by the adiabaticity of the transfer from the 850 nm crossed dipole trap (CDT) into the squeeze trap, the required horizontal (longitudinal) precision of 200 µm (500 µm) is given by the achieved vertical trapping frequency.

Vertical alignment precision The squeeze trap is loaded from the 850 nm CDT by adiabatically ramping up the squeeze trap while simultaneously ramping down the 850 nm CDT to $\sim 1\,\%$ of its maximum depth. The reduced depth 850 nm CDT is then kept to support the squeeze trap against gravity. If the center of the squeeze trap is not aligned with the center of the 850 nm CDT the total potential gets deformed and the center of the combined trap and accordingly also the atoms shift during the transfer. Thus, a limit for the acceptable squeeze trap displacement is given by the deformation of the combined trap: If the trap centers are too far apart, a double-well like feature will appear, but if the displacement is on the order of the beam waist or smaller, both trap potentials can be considered parabolic and the total potential can therefore also be considered parabolic. In this case the atoms will still move between the center positions of the traps during the transfer, but for a sufficiently slow timescale the transfer will be adiabatic.

To further limit the tolerable displacement one can estimate and limit this timescale. For a rough estimate we demand that the velocity of the center-of-mass motion during the transfer due to the displacement is much smaller than the velocity given by the relevant length and time scales, namely the Thomas-Fermi radius and the trapping frequency, and

limit the transfer time to ∼100 ms. For the vertical axis this yields a required alignment precision of a few µm.

Radial alignment precision For the radial, i. e. horizontal and longitudinal, alignment the situation is different: The radial atom position is determined by the 850 nm CDT, the trap center of the combined squeeze trap and 850 nm CDT barely depends on the displacement. Here, the limiting factor is given by the vertical cloud size. A radial displacement of the squeeze trap leads to a lower intensity of the squeeze trap beam at the atom position, which reduces the effective vertical trapping frequency and therefore increases the vertical cloud size. If the center positions of squeeze trap and 850 nm CDT are too far apart, the cloud size exceeds the lattice spacing and it is no longer possible to load the atom cloud into a single lattice layer. The dependence of the vertical cloud size on the radial displacement is shown in fig. 4.14. From this data we derive a required alignment precision of 200 µm in the horizontal and 500 µm in the longitudinal axis.

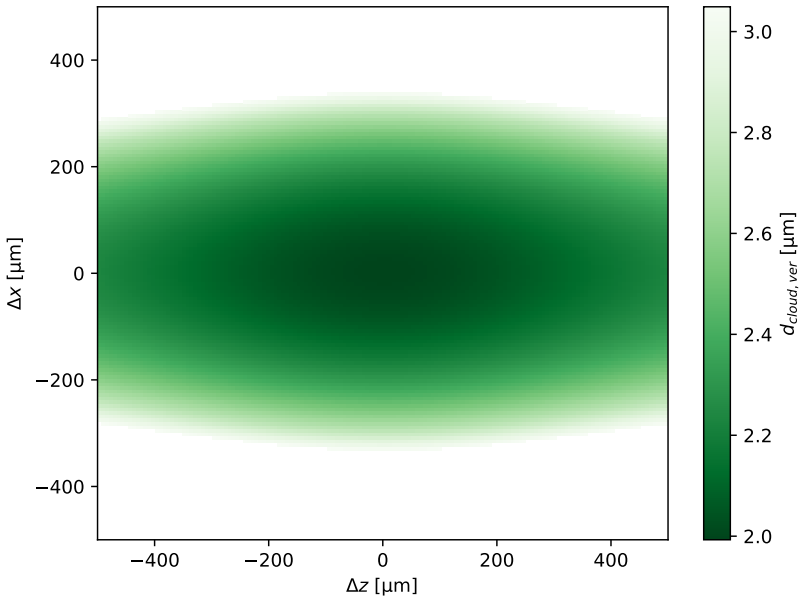

Figure 4.14: The vertical cloud size $d_{\mathrm{cloud,ver}}$ in the squeeze trap supported by the 850 nm crossed dipole trap in dependence of the longitudinal and horizontal displacements Δz and Δx of the squeeze trap. Only the regime where the vertical cloud size is smaller than the lattice spacing of the vertical lattice is plotted giving an impression of the required alignment precision. In this regime the relevant length scale is the harmonic oscillator length, not the Thomas-Fermi radius. Hence, the required alignment precision for the squeeze trap without support of the 850 nm crossed dipole trap is the same.

Adjustment screws To align the vertical and horizontal position of the squeeze beam the squeeze beam path includes a motorised mirror mount with a step size of 0.7 µrad

which translates to $\sim 130\,\mathrm{nm/stp}$ at the atom position.[24] To allow for a longitudinal alignment, i. e. along the squeeze beam axis, the focussing lens of the squeeze beam is mounted on a manual translation stage enabling to shift the focal plane with a resolution of $\sim 10\,\mu\mathrm{m}$.

Coarse alignment

For the first coarse alignment we make use of an already implemented D2 absorption imaging along the squeeze beam axis. We superimpose the squeeze beam with the D2 imaging beam such that the squeeze beam passes the imaging path and can be seen on the camera. Then we use the BEC in the 850 nm CDT as a position reference for the focus of the squeeze beam[25] by superimposing the imaged squeeze beam focus with the imaged atom cloud on the camera (see fig. 4.15) in all three axis. The imaging lens introduces a

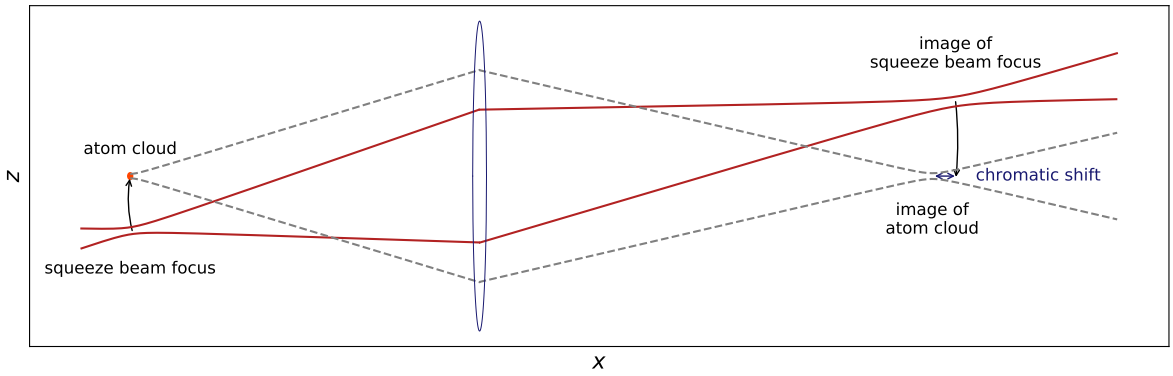

Figure 4.15: Imaging path of atom cloud and squeeze trap beam. A pre-existing absorption imaging along the squeeze beam axis is used to image the squeeze beam as well. This allows for a coarse alignment of the squeeze trap using the atom cloud in the 850 nm crossed dipole trap as reference by superimposing the image of the squeeze beam focus with the image of the atom cloud. The imaging lens introduces a chromatic shift that has to be accounted for.

chromatic shift, though, as squeeze beam and imaging beam have different wavelengths. In our case the chromatic shift causes a shift of the image position on the order of 2.5 mm and can be compensated by shifting the camera, which is mounted on a translation stage.

The longitudinal precision of this procedure is given by the Rayleigh range of the squeeze beam, the depth of focus of the imaging and by the uncertainty of the chromatic

[24] For technical reasons this mirror mount is located before the focussing lens with quite some distance in between. That means adjusting the vertical and horizontal position with that mirror mount causes the squeeze beam to go off-center through the focussing lens. For very small angles, i. e. for the fine alignment, this is negligible. For the rough alignment another mirror mount is used that is much closer to the focussing lens. That mirror mount has resolution of 0.08 mrad/tick which translates to ca. 12 µm/tick at the atom position.

[25] This refers to the position of the vertical focus since this determines the center of the squeeze trap.

shift. In our case the latter is dominant, yielding an estimated longitudinal precision of 1.5 mm, i. e. $\sim 3.5\, z_{R,\mathrm{squeeze}}$. The lateral, i. e. vertical and horizontal, precision is determined by the longitudinal precision and the angle between imaging and squeeze beam, yielding a lateral precision in the order of 10 - 100 µm. That means the horizontal displacement is below half a waist and already within the required precision. Therefore, the next alignment step concentrates on the vertical and longitudinal axes.

Fine alignment: longitudinal axis

The second alignment step utilises the acceleration force exerted by the squeeze trap potential and allows to achieve the required longitudinal alignment precision while also improving the vertical alignment.

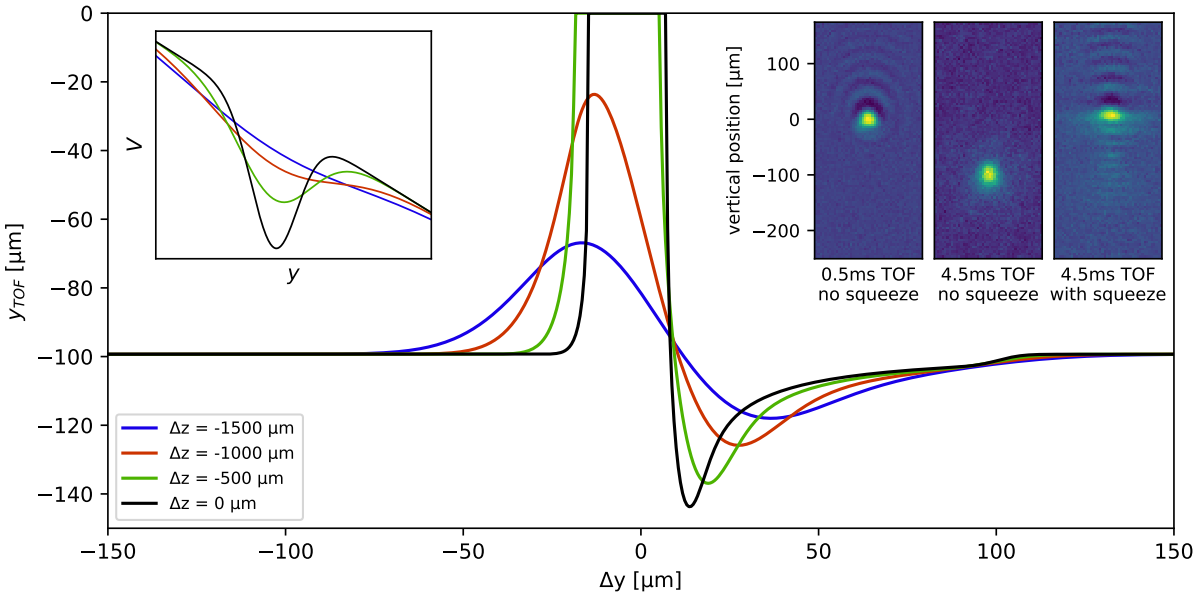

Figure 4.16: For the second alignment step the atom cloud is released from the 850 nm crossed dipole trap and imaged after a subsequent time-of-flight during which the squeeze trap is present. When the atom cloud (partially) passes the squeeze trap during the time-of-flight it experiences an additional acceleration and its trajectory is altered. The main plot shows the calculated position y_{TOF} of the atom cloud after 4.5 ms time-of-flight in dependence of the vertical displacement Δy of the squeeze trap. The different curves correspond to different longitudinal displacements Δz of the squeeze trap. Positive (negative) values of Δy correspond to the squeeze trap being below (above) the 850 nm CDT. $y_{\mathrm{TOF}} = 0$ corresponds to the atom position in the 850 nm CDT which acts as a reference, y_{TOF} without the squeeze trap present is -99 µm. The bend around $\Delta y \approx 100$ µm marks the displacement at which the atom cloud just reaches the squeeze trap potential within the time-of-flight. The cut-off around $\Delta y = 0$ corresponds to the atoms being trapped in the squeeze trap. **Left inset:** sum of gravitational and squeeze trap potential V in dependence of the vertical position y. For large Δz the potential minimum vanishes and the atoms cannot be trapped. **Right inset:** Images of the atom cloud after a negligible time-of-flight as reference for the atom position in the 850 nm CDT as well as after 4.5 ms time-of-flight with and without squeeze trap present. The data was taken after the second alignment step.

We prepare a BEC in the 850 nm CDT and observe the vertical position y_{TOF} of the atom cloud after a fixed time-of-flight during which the squeeze trap is present. As soon as the squeeze trap potential lies within the distance the atoms cover during the time-of-flight, they experience an additional acceleration and the covered distance changes. The dependence on the vertical displacement Δy for different longitudinal displacements Δz is plotted in fig. 4.16. When the squeeze trap is below the 850 nm CDT, $|y_{\mathrm{TOF}}|$ increases. For the full squeeze trap depth and a vertical displacement of 100 µm this effect is in the order of 10 µm, i. e. clearly detectable. With decreasing Δy the effect gets larger until the squeeze trap is close enough to trap the atoms.

To gain information about the longitudinal axis the squeeze trap depth is reduced until the atoms can no longer be trapped due to the vanishing potential minimum when the trap is shallow compared to the gravitational potential gradient (see fig. 4.16 left inset). Although the atoms are not trapped, they are slowed down by the squeeze trap potential. Hence, the vertical squeeze trap position can be adjusted such that $|y_{\mathrm{TOF}}|$ is minimised. By adjusting the longitudinal squeeze trap position the effective trap depth (waist) is increased (decreased), such that Δz can be optimised by further minimising $|y_{\mathrm{TOF}}|$ until the atoms get trapped again. For each iteration step of longitudinal and vertical alignment the squeeze trap depth is reduced until the effective trap depth is in the order of the temperature, i. e. the atoms cannot be properly trapped anymore.

The lower trap depth limit given by the temperature limits the precision of this alignment procedure in our case to ~ 300 µm longitudinally and ~ 5 µm vertically. On top of this uncertainty there is a systematic error to the vertical position in the order of 5 µm due to the gravitational shift of the potential minimum. After this alignment step the horizontal and longitudinal position is within the required precision and the atoms can be trapped in the squeeze trap. To achieve the desired alignment precision along the vertical axis, a third alignment step is required.

Fine alignment: vertical axis

Being able to trap the atoms in the squeeze trap gives rise to new, more precise alignment methods. While we decided for a straightforward approach we also briefly discuss further alignment methods.

For the final alignment step we directly image the atoms in the squeeze trap with absorption imaging where we use the atom position in the 850 nm CDT as reference which allows to align the vertical as well as the horizontal position. Since the imaging is the same for both traps the precision of this method solely depends on the imaging resolution.

An estimate for the achieved accuracy is given by the effective pixel size of the respective imaging. For our setup the effective pixel size is 4.2 µm which is within the required precision. Note, though, that the effective pixel size is a conservative estimate. By increasing the temperature of the sample the vertical cloud size can be increased to several pixels which allows for a sub-pixel fit.

An alternative alignment method is to minimise the amplitude of the sloshing mode, i. e. the center-of-mass motion after transferring the BEC from the 850 nm CDT to the squeeze trap. The displacement is directly connected to the amplitude of the sloshing mode and by using the full squeeze trap depth the gravitational shift of the potential minimum becomes negligible. The precision is mainly given by the imaging resolution which makes this method more favorable for larger waists, i. e. in our case for the horizontal and longitudinal axes which are already aligned. A further disadvantage is that this method is rather time-consuming since it is necessary to measure a full oscillation of the sloshing mode for every vertical position setting.

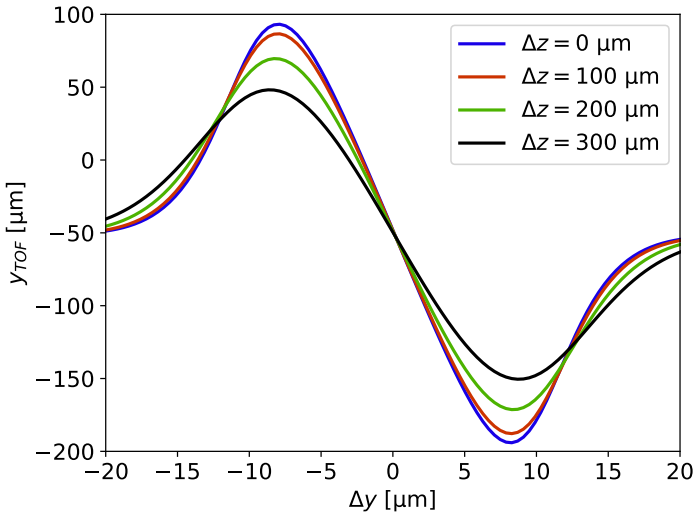

Figure 4.17: The vertical position y_{TOF} after 3 ms time-of-flight in dependence of the vertical displacement Δy of the squeeze trap after an evolution time of T/4 in the squeeze trap with full depth of 9.5 uK for different longitudinal displacements Δz. Positive (negative) vertical displacements correspond to the squeeze trap being below (above) the 850 nm crossed dipole trap. y_{TOF} without squeeze trap is -51.5 µm.

To avoid these disadvantages this method can be altered to enhance the signal: Instead of observing the sloshing mode in situ, the amplitude can be extracted by transforming the displacement into momentum via a $T/4$ evolution in the squeeze trap and then effectively

performing another Fourier transformation via a time-of-flight measurement. In the limit of short evolution times, this method basically probes the local curvature of the potential. In view of this, it is intuitive that the signal is roughly shaped like the derivative of a Gaussian as can be seen in fig. 4.17.

However, that means that the optimum position $\Delta y = 0$ does not yield a peak, but a strong slope in the signal. Therefore, while the signal amplitude is enhanced which increases the precision and while this alignment procedure is less time-consuming since only one data point per vertical displacement is required, this method is more difficult in the sense that a precise reference is required.

4.5.2 Vertical lattice

In this section, we focus on the alignment of the vertical lattice with respect to the atom position determined by the 850 nm crossed dipole trap. The relative vertical position of vertical lattice and squeeze trap will be aligned separately (see sec. 4.5.3). Before discussing the alignment procedure, we will first estimate the required accuracy of the alignment of the vertical lattice.

Required alignment precision

Radial alignment precision The most important concern is to fulfill the requirement set for the vertical trapping frequency ν_y. Since the intensity and hence the trapping frequency decreases with larger distance to the center of the lattice, this sets an upper limit for the horizontal and longitudinal displacement Δx and Δz of the atom position determined by the 850 nm CDT with respect to the center of the vertical lattice given by the intersection.[26] Simply demanding that $\nu_y(\Delta x, \Delta z) \geq 5\,\mathrm{kHz}$ yields a maximum displacement Δx and Δz of $\sim 140\,\mu\mathrm{m}$ as illustrated in fig. 4.18. Assuming a maximum misalignment of the focus position with respect to the center of the lattice of half the Rayleigh range, i. e. 1.3 mm as well as demanding that central, first and second layer achieve the required trapping frequency slightly tightens this limit to 130 µm.

Vertical alignment precision One the one hand, a requirement for the alignment accuracy for the vertical axis is determined by the required longitudinal precision as the longitudinal position of the intersection solely depends on the vertical position of the

[26] We emphasize that the longitudinal displacement Δz refers to the intersection of the lattice beams, not to the focus position.

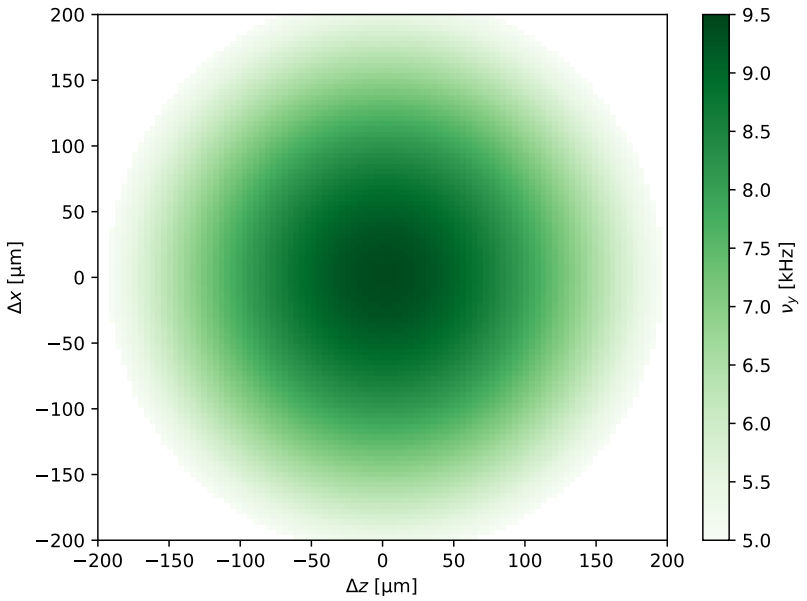

Figure 4.18: Vertical trapping frequency ν_z of the vertical lattice in the central layer in dependence of the longitudinal and horizontal distance Δz and Δx between the atom position determined by the 850 nm CDT and the center of the vertical lattice. Only the regime where the vertical trapping frequency is above the desired minimum value of 5 kHz is plotted giving an impression of the required radial alignment precision.

single lattice beams. Considering half the crossing angle of the lattice beams of 5 ° and demanding a longitudinal precision of 130 µm one geometrically derives a required vertical precision of 10 µm. On the other hand, a limit is also given by the required precision of the squeeze trap since it is the squeeze trap that will be moved in a separate subsequent alignment step for the relative vertical alignment of vertical lattice and squeeze trap. This tightens the limit to ~ 5 µm.

Adjustment screws To adjust the horizontal and vertical position of the single lattice beams the beam paths include adjustable mirror mounts. In order to ensure reproducible shifts of the lattice beams, the beams are imaged on a camera after passing the vacuum chamber.[27] This allows for a resolution of ~ 3 µm. The focal position can be adjusted by the position of the common focussing lens that is mounted on a manual translation stage with a resolution of ~ 10 µm. Additionally, the focal position of the single lattice beams can be adjusted individually as the adjustable mirror mounts mentioned before are three-knob adjusters.

[27] The lattice beams are imaged individually. Due to the high NA of the lattice and due the size of the vacuum chamber it is not possible to image the lattice behind the chamber.

Coarse alignment

Since we cannot image the lattice directly we align both lattice beams individually. For the first coarse alignment we set up a temporary imaging roughly along the lattice beam axes and image the atoms in the 850 nm CDT to obtain a reference position. It is crucial to minimise aberrations due to low quality imaging lenses, due to a tilt of the imaging lens with respect to imaging and lattice beams and due to being off-center on the imaging lens.[28] After setting up the temporary imaging the coarse alignment is basically the same as for the squeeze trap: The imaged focus position of the lattice beams is superimposed with the imaged atom position in the 850 nm CDT corrected for the chromatic shift.

The precision of this alignment step is mostly determined by the uncertainty of the chromatic shift, the imaging depth and the angle between imaging and lattice beam and is for our setup $\sim 150\,\mu m$ horizontally and vertically, and $\sim 1\,mm$ for the focus position.

Fine alignment

In contrast to the squeeze trap beam, the lattice beams are blue-detuned and hence anti-trapping which makes the alignment more difficult. We can not use the fine alignment methods described in sec. 4.5.1 as they are based on trapping the atoms. Instead, we observe the effect of the lattice beams on the atoms trapped in the 850 nm CDT: We load atoms into the 850 nm CDT at a shallow depth of $\sim 3\,\mu K$ while a single full depth lattice beam is present and scan the vertical position of the lattice beam until the atom number is affected.[29] The shape of the measured signal is shown in fig. 4.19. When the lattice beam is ~ 20 - $30\,\mu m$ below the atom position it counteracts gravity, which leads to an increase of the atom number. When the lattice beam gets closer and is centered on the atom position it effectively decreases the trap depth and hence pushes the atoms out of the trap, causing a decrease of the atom number. The horizontal alignment only changes the effective height of the lattice beam potential. The lattice beam is then aligned by iteratively optimising vertical and horizontal position to be centered on the loss feature, where the power of the lattice beam is reduced after every iteration in order to reduce the width of the loss feature. This also reduces the signal amplitude, though, giving a lower limit for the lattice beam power. For our setup this limit was given by half the lattice power corresponding to $\sim 1\,\mu K$ potential height.

[28] Since imaging and lattice beam axes are similar, but not the same, spherical aberrations due to being off-center on the imaging lens cannot be avoided. Nonetheless, it is highly recommended to minimise these aberrations.

[29] For this measurement we rely on the fact that horizontally the lattice beam is already within a waist distance of the atom position due to the coarse alignment.

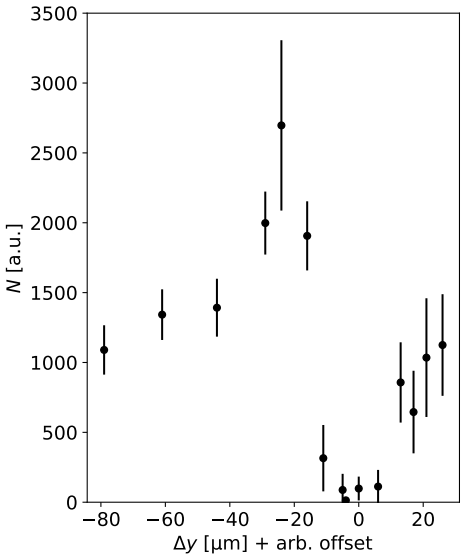

Figure 4.19: The atom number N in the shallow 850 nm crossed dipole trap when a single lattice beams is present with the vertical displacement Δy with respect to the center of the 850 nm CDT. Lower values of Δy correspond to a lower lattice beam position. The lattice beam is anti-trapping and has a similar waist as the 850 nm CDT beams. Hence, in effect it reduces the potential depth resulting in a loss of atoms when properly aligned. The atom number peak next to the loss feature occurs when the lattice beam is slightly below the 850 nm CDT. In that case it stabilises it against gravity resulting in an increased atom number.

However, a lower limit for the lattice beam power is also useful in the sense that it limits the vertical displacement: The gravitational shift of the potential minimum of the shallow 850 nm CDT introduces a systematic error that increases with lower lattice beam power due to the asymmetry of the signal. For half the lattice beam power this systematic error is $\sim 3\,\mu$m.[30] Note that this error occurs for both lattice beams in the same direction and hence does not translate to a longitudinal displacement of the lattice center. The precision of this alignment method is determined by the width of the loss feature and is in the order of $\sim 5\,\mu$m vertically and $\sim 100\,\mu$m horizontally which is within the desired accuracy. Using this alignment procedure for both lattice beams individually ensures that the intersection is at the atom position. We then use the intersection as a reference to align the focus position where we conservatively estimate an achieved accuracy of half the Rayleigh range.

[30]Since it is known that the error is roughly one lattice spacing and since also the direction is known this can be compensated for when performing the relative alignment of squeeze trap and vertical lattice.

4.5.3 Relative alignment of squeeze trap and vertical lattice

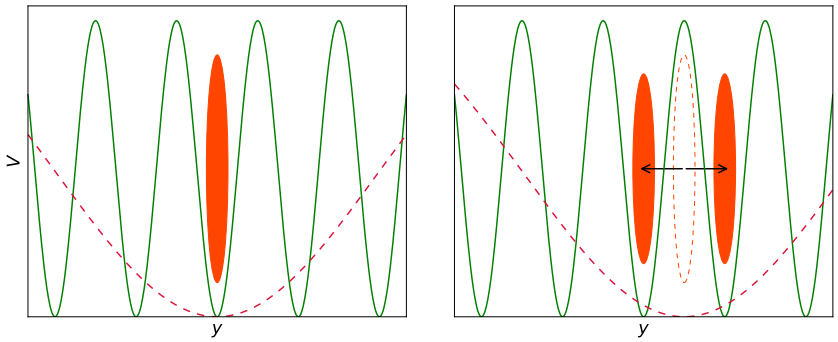

Figure 4.20: Sketch of the potential V of squeeze trap (red, dashed) and vertical lattice (green, solid) along the vertical axis y. **Left:** When both traps are vertically aligned with respect to each other, the atom cloud is loaded into a single layer. **Right:** When the traps are vertically misaligned with respect to each other, two layers are occupied.

Required alignment precision We previously described how squeeze trap and vertical lattice were each aligned onto the atom position given by the 850 nm crossed dipole trap. Both traps are therefore also aligned relative to each other within the precision given by the discussed alignment methods. While this suffices for the horizontal and longitudinal axes, the vertical axis requires a much more accurate alignment since this is the lattice axis. The vertical relative alignment of squeeze trap and vertical lattice defines into which layer the atoms are loaded and, even more importantly, whether just one or more layers are occupied (see fig. 4.20). Accordingly, the vertical relative alignment needs to be accurate to a length scale well below the lattice spacing.

The relative position is adjusted by vertically shifting the squeeze trap via a motorised mirror mount. As stated in sec. 4.5.1 the effective step size is ~ 130 nm, which provides a sufficient resolution. To ensure that the squeeze trap is well aligned with one of the lattice layers we measure how many layers are occupied with a technique that we will in the following refer to as a singlicity measurement [140].

Singlicity measurement Measuring the occupation of the individual layers is non-trivial since we cannot resolve two occupied layers in-situ. Hence, the main idea of the singlicity measurement is to increase the spatial separation by performing two Fourier transformations in the $(y,\ p_y)$ phase space. The first one transforms the two spatially distinct layers into two distinct momentum classes via time evolution in a harmonic trap. The second one transforms the momentum classes back to spatially separated atom clouds with a resolvable distance via a time-of-flight. This technique therefore allows to measure the relative occupation of multiple layers with a single absorption image.

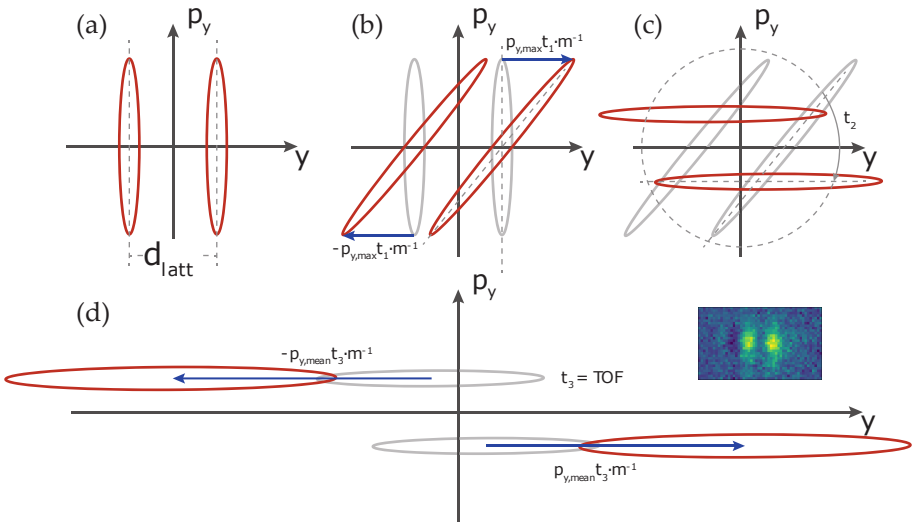

Figure 4.21: Sequence of the singlicity measurement in phase space representation in the case of two occupied lattice layers. **(a)** The measurement starts at t=0 with atoms trapped in the vertical lattice. Two layers are occupied corresponding to two atom clouds with a spatial distance given by the lattice spacing d_{latt} which can not be resolved with our imaging. **(b)** The lattice is switched off and the atom clouds are allowed to expand for a short time t_1 in order to decrease the density. **(c)** The squeeze trap is flashed on for the time t_2 to provide a harmonic potential, causing a rotation in phase space. t_2 is chosen such that the original spatial distribution is translated to a momentum distribution. Thus, the originally spatially distinct layers were transformed to two distinct momentum classes. **(d)** The squeeze trap is switched off and a time-of-flight is performed to spatially separate the two momentum classes. **Inset:** Typical image as derived by the described singlicity measurement for a misaligned squeeze trap. Figure adapted from [140]

The sequence is as follows: The atoms are prepared in the vertical lattice. When the squeeze trap is misaligned with respect to the vertical lattice, then two adjacent lattice layers are occupied, i. e. there are two atom clouds spatially separated by the lattice spacing $d_{\mathrm{latt}} = 3\,\mu\mathrm{m}$ (see fig. 4.21 (a)). The vertical lattice is switched off which leads to a rapid expansion of the atom clouds (see fig. 4.21 (b)) and since the lattice is tightly confining along y, the expansion is mainly along y. Due to the expansion the density decreases such that interactions become negligible, which happens rather fast. Accordingly, the expansion time t_1 is short enough that the center-of-mass motion due to gravity is negligible. Suitable values for t_1 depend on the scattering length and in agreement with our rather low scattering lengths we experimentally found best results for a rather short time $t_1 = 50\,\mu\mathrm{s}$.

In the next step the squeeze trap is flashed on for a short time t_2. Due to the harmonic potential, the force acting on the atoms is spatially dependent and the atoms undergo a rotation in phase space where the angular velocity is given by the trapping frequency of the squeeze trap (see fig. 4.21 (c)). t_2 is chosen such that the spatial layers are transformed to separable momentum classes, meaning $t_1 = 0$ would yield $t_2 = T/4$ and the longer t_1,

the shorter t_2. We found best results for $t_2 = 220\,\mu s$ which is close to $T/4 = 240\,\mu s$ in agreement with our rather low value for t_1.

The last step is a time-of-flight, i. e. the squeeze trap is switched off again and the different layers spatially separate due to the different mean momenta (see fig. 4.21 (d)). The atom clouds also expand, but much less than during t_1 due to the momentum distribution now being much more narrow. After $t_3 = 3\,ms$ the atoms are imaged via absorption imaging. Here, t_3 is chosen such that the atom clouds corresponding to different lattice layers are clearly distinguishable (see fig. 4.21 (d) inset).

Fitting a double or triple Gaussian (depending on the number of expected occupied layers) to the density distribution obtained from the absorption imaging allows to extract the relative occupation of the layers.[31] The relative occupation can then be used as a figure-of-merit for the relative alignment of squeeze trap and vertical lattice.

Alignment stability Since the occupation of a second lattice layer depends on the relative vertical displacement Δy between squeeze trap and vertical lattice, the singlicity measurement can also be used to assess the stability of the relative vertical alignment. In this case, the squeeze trap is aligned such that two layers are equally occupied which increases the sensitivity of the measurement. The relative occupation of the layers is then measured every 5.5 s over 30 h via the singlicity measurement described above. To relate the relative occupation of the two layers with the relative vertical alignment the data is compared with a simple simulation assuming that the atom cloud in the squeeze trap is of Gaussian shape in the vertical axis[32] and assuming that the occupation of each lattice layer is determined by the integral of the density distribution in the squeeze trap over the spatial extent of the respective layer. This allows to translate the measured relative occupation into the vertical displacement Δy between squeeze trap and vertical lattice.

The time series of Δy is presented in fig. 4.22. Here, $\Delta y = 0$ corresponds to the squeeze trap being centered on an intensity maximum of the vertical lattice corresponding to two equally occupied layers. Note that Δy is given in units of the lattice spacing such that the Δy axis covers the extent of one lattice layer. The data shows that the vertical alignment is quite stable. On the long term squeeze trap and vertical lattice barely move with respect to each other. The moving mean over 9 min (red solid line) changes by less than $0.05\,d_{\mathrm{latt}}$. However, the fluctuations are dominated by short-term fluctuations. Exemplarily, a time

[31] This is not only useful to adjust the relative vertical alignment of squeeze trap and vertical lattice, but can also be used to optimize cooling parameters since a higher temperature will increase the cloud size and hence the occupation of lattice layers adjacent to the targeted layer.

[32] This is a reasonable assumption since the Thomas-Fermi radius is smaller than the harmonic oscillator length.

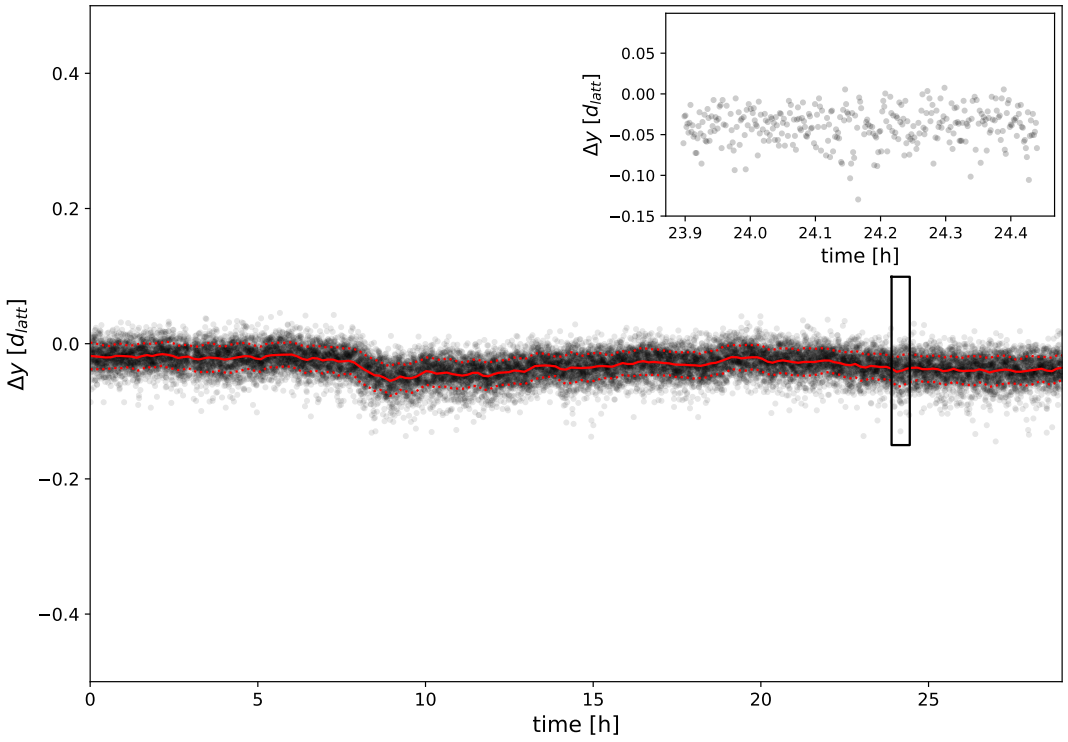

Figure 4.22: Stability measurement of the relative vertical alignment of squeeze trap and vertical lattice. Each data point (black) corresponds to a single singlicity measurement. The moving mean over 9 min (red solid line) and the corresponding standard deviation (red dashed lines) are plotted as well. The inset is a magnification of the data within the black rectangle. Details are given in the main text.

frame of ~ 30 minutes at around $t = 24$ h is shown magnified in the inset of fig. 4.22. The standard deviation over this time frame is $0.02\, d_{\mathrm{latt}} = 60$ nm. The maximum deviation from the mean value is $0.09\, d_{\mathrm{latt}} = 270$ nm. Using the same simulation explained above, but with the squeeze trap being centered on a lattice layer, this deviation corresponds to 99.3% of the atoms being loaded into the targeted lattice layer. Hence, the relative vertical alignment is stable at least over a few days, most likely even longer since there is no onset of a long-term drift. In case the necessity arises, the singlicity measurement can be used to implement a feedback loop as it provides a fast and simple method to verify the relative vertical alignment.

Distinguishing between lattice layers While the singlicity measurement allows to center the squeeze trap on a lattice layer, it does not give any information about which layer is loaded. Practically, we know from the precision of the vertical alignment that the atoms are loaded into the central or one of the first two layers and, as will be explained in sec. 4.6.4, any of these layers is suitable. In principle one could measure the trapping

frequency in different layers, but for central and first two layers the trapping frequency barely differs. Hence, this is not a suitable method to distinguish between these layers. Another way in which the layers differ is the in-plane potential (see sec. 4.6.4). However, when using an additional harmonic potential as radial confinement, as we do, the in-plane potential becomes essentially negligible and the layers in question essentially behave the same. On the one hand this means that we cannot distinguish between central, first and second layer, but on the other hand this also means, that any of these layers is a suitable choice. In a contrary case of a box potential as radial confinement the in-plane potential becomes relevant and it becomes favorable to load into the central layer. In that case the layers can be identified by the density distribution in the box potential.

4.6 Final system

4.6.1 Preparing a 2D BKT cloud

In chapter 3 it was explained how we prepare a three-dimensional BEC of $\sim 5 \cdot 10^3$ K39 atoms, where the last step was evaporation in the 850 nm CDT. Proceeding from there we utilise the 2D setup discussed throughout this chapter to create a 2D BKT cloud via the following procedure:

Subsequent to the evaporation where the 850 nm CDT was ramped down to 4.5 % of its full depth of $\sim 100\,\mu$K, the magnetic gradient applied for the evaporation is ramped down and the magnetic field is adapted such that the scattering length nearly vanishes. The atomic cloud is then transferred into the squeeze trap by ramping down the 850 nm CDT to 1 % relative depth within 100 ms while simultaneously ramping up the squeeze trap to full depth. Due to the strong anisotropy of the combined squeeze trap and reduced 850 nm CDT the atomic cloud takes a pancake-like shape, but is not yet in the quasi-2D regime. The sample is then loaded from the squeeze trap into the vertical lattice by simultaneously ramping down the squeeze trap and ramping up the vertical lattice, again within 100 ms. The pancake-like shape in the squeeze trap ensures that just one layer of the vertical lattice is occupied in this step. The scattering length is then slightly increased and a waiting time of 100 ms is introduced to allow for thermalisation which also results in some final evaporation.

With this procedure we achieve a spin-polarised 2D BKT cloud of $\sim 3 \cdot 10^3$ atoms in the $|1, -1\rangle$ state with a temperature of ~ 50 nK corresponding to $\sim 0.2\,T_{\mathrm{BKT}}$ where T_{BKT} is the BKT critical temperature in our harmonic radial confinement calculated according to [105] for a scattering length of $20\,a_0$.

It is also possible to prepare a 2D BKT cloud in the $|1,+1\rangle$ state by evaporating in that state (see sec. 3.7.3) and then following the procedure described above. This is favorable when aiming for studying spin-polarised system e. g. to measure Tan's contact [141]. Tunable interactions are in that case enabled via the $|1,+1\rangle + |1,+1\rangle$ Feshbach resonance at $\sim 400\,\mathrm{G}$.

However, we are more interested in the physics of spin mixtures (see sec. 5.2). As discussed in sec. 3.7.1 it is favorable to prepare the 2D BKT cloud in the $|1,-1\rangle$ state in that case. The spin mixture is then prepared by applying an RF pulse that transfers atoms from the $|1,-1\rangle$ state into the $|1,0\rangle$ state. For the RF pulse we employ the same in-vacuo single-loop antenna that is also utilised to prepare the spin state for the evaporation step (see sec. 3.7.2), but with a different matching circuit. By varying the length of the RF pulse the ratio of the two spin components can be adapted.[33]

4.6.2 Spin mixtures: viable regimes for K39

For K39 two different suitable regimes for spin mixtures exist: To exploit tunable interstate interactions it is favorable to utilise the $|1,-1\rangle + |1,0\rangle$ Feshbach resonance at $\sim 525\,\mathrm{G}$. However, while the intrastate scattering length of the $|1,-1\rangle$ is positive in the respective magnetic field regime corresponding to repulsive interactions, the intrastate scattering length of the $|1,0\rangle$ state is negative corresponding to attractive interactions, which means that the $|1,0\rangle$ component is not stable. Hence, this regime is only suitable for strongly imbalanced spin mixtures where the $|1,0\rangle$ state acts as the minority component with accordingly low density as is the case for the polaron measurements performed by [76] summarised in sec. 5.3.[34]

When striving for balanced spin mixtures one has to go to lower magnetic fields around $\sim 55\,\mathrm{G}$. Within a range of $\sim 10\,\mathrm{G}$ both intrastate interactions are repulsive as required for the single components to be stable.[35] However, this regime is far away from the interstate Feshbach resonances, i. e. the interstate scattering length is nearly constant. Thus, while

[33] Note that at magnetic fields corresponding to a high scattering length the Rabi oscillation is strongly damped which limits the achievable ratio. Hence, balanced spin mixtures can only be prepared in a regime with low scattering lengths.

[34] Note that no binary spin mixture consisting of any combination of $|1,-1\rangle$, $|1,0\rangle$ or $|1,+1\rangle$ yields a regime where both intrastate as well as the interstate interactions are repulsive.

[35] Note that according to the theoretical data on Feshbach resonances from [92] a $|1,+1\rangle$, $|1,0\rangle$ spin mixture also exhibits a regime where both intrastate interactions are repulsive. This regime is around $\sim 380\,\mathrm{G}$ with a total width $\sim 40\,\mathrm{G}$. However, the intrastate scattering length of the $|1,0\rangle$ state is particularly low in that range, $< 15\,a_0$. Moreover, the data from [92] does partially not agree with the theoretical data from [8].

the intrastate scattering lengths can be tuned, the interstate interaction is fixed to weakly attractive. Nonetheless, this regime is particularly interesting as it covers the transition from a mean-field stable, where the intrastate repulsion exceeds the interstate attraction, to a mean-field instable spin mixture, where the interstate attraction exceeds the intrastate repulsion. Hence, this regime allows to study the mean-field collapse of 2D binary spin mixtures as well as beyond mean-field effects as proposed in sec. 5.4.

4.6.3 Imaging

To probe the 2D setup we use the high-resolution imaging along the vertical axis through the microscope objective with an NA of 0.75 corresponding to a diffraction-limited resolution of $\sim 0.62\,\mu\text{m}$ for the imaging wavelength of $\sim 767\,\text{nm}$. Due to the high density of the atom cloud we cannot employ fluorescence imaging as photoassociation would lead to severe losses. Instead we use absorption imaging since this technique allows to apply much shorter imaging times.

Imaging can be performed at both low and high magnetic fields ($\sim 500\,\text{G}$). Currently, we typically prepare strongly imbalanced spin mixtures for which we utilise the interstate Feshbach resonance at $\sim 525\,\text{G}$. Hence, we typically use the high-field imaging, which is described in [76], in order to avoid time delays before the imaging due to magnetic field ramps. Note that the imaging is spin-dependent. Hence, when preparing a spin mixture the two spin states can be imaged separately.

The main observable of the experiment is the density distribution $n(x,z)$ which is derived via absorption imaging along the vertical axis where the atoms are illuminated on a cycling transition on the D2 line. By taking two consecutive images with and without atoms the final $I_f(x,z)$ and initial intensity $I_i(x,z)$ of the imaging beam, i. e. after and before passing the atomic sample, can be obtained. Since according to the Beer-Lambert law $n(x,z) \propto -\ln[I_f(x,z)/I_i(x,z)]$ this allows to derive the density distribution.

The density distribution can be derived for both in-situ and time-of-flight images. Performing a 2D TOF imaging, where the atom cloud is released from the radial confinement while the vertical lattice providing the 2D confinement is still present, allows for a longer time-of-flight since the atoms are levitated against gravity and are thus kept within the imaging plane of the microscope objective. Performing 3D TOF measurements on the other hand, where the atoms are also released from the 2D confinement, limits the usable time-of-flight, but has the advantage that interactions are almost immediately switched off. This is caused by the rapid expansion along the vertical axis due to the previous tight confinement which significantly reduces the 3D density on a time scale much faster than

the radial expansion of the cloud. Hence, we typically perform 3D TOF measurements. A more detailed discussion of 2D and 3D TOF measurements can be found in [105].

Integrating over the measured density distribution allows to derive the atom number N. The imaging needs to be calibrated, though, which was done by observing the 3D condensation threshold as described in sec. 3.7.3 which employed the same imaging. Furthermore, the temperature T can be estimated via 3D TOF measurements. Due to the harmonic radial confinement the density at the edges of the cloud are low and the cloud exhibits a thermal component. This allows to obtain an estimate for the temperature via the well-established method of a Gaussian fit to the thermal wings after a time-of-flight [142].

4.6.4 Radial potential created by the vertical lattice

The lattice potential is created by two interfering laser beams crossing under an angle of $2\,\mathrm{x}\,5^\circ$ with beam waists and power as stated in tab. 4.4. Assuming equal lattice beams a vertical lattice as shown in fig. 4.23 is formed where each intensity node is a lattice layer into which the atoms can be loaded. This section is intended to provide a better understanding on how the in-plane lattice potential is shaped, how the lattice layers differ from each other and which layers are suitable to provide the 2D confinement. A brief conclusion is provided at the end of the section.

Vertical trapping frequency The most obvious difference between the lattice layers is the vertical trapping frequency ω_y. Due to the Gaussian beam shape the intensity I reduces away from the center position. Accordingly, the vertical trapping frequency as well as the effective trap depth decrease towards higher layers and hence it is favorable to load the atoms into the central layer (0th layer) as it provides the strongest confinement. However, due to $\omega_y \propto \sqrt{I}$ and due to the Gaussian intensity distribution, the decrease of ω_y is small for the first layers. The trapping frequency of the first layer is only 2% and the trap depth only 4% lower than for the central layer. The second layer is also reasonably close to the central layer, the trapping frequency is 8%, the trap depth 12% lower compared to the central layer. Hence, in respect of the vertical trapping frequency, central, first and second layer are similarly well-suited. Note that although ω_y notably decreases towards higher layers, the requirements set in sec. 4.3.1 are fulfilled even for third and fourth layer.

Longitudinal trapping potential for layers ≥ 1 In first approximation, the in-plane potentials can be considered to be flat as the lattice layers are located at the intensity

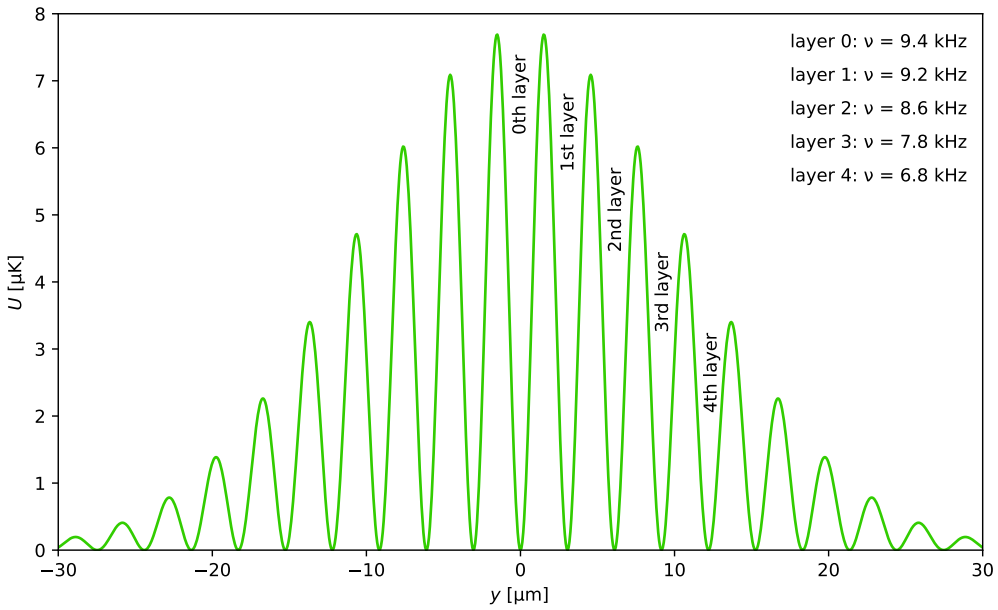

Figure 4.23: Potential U created by the lattice beams in dependence of the vertical position y. The potential is calculated for the longitudinal and horizontal center position. Furthermore, the calculation assumes equal waists and power of the lattice beams as well as the same path length, i. e. a phase shift of π due to the cube that is splitting the lattice beam. Vertical trapping frequency ν and effective trap depth decrease for higher layers due to the Gaussian beam shape.

nodes of the vertical lattice. However, assuming equal intensities of the lattice beams total destructive interference only occurs in the central layer as it acts as a symmetry plane. For higher layers, on the other hand, total destructive interference only appears at the center of the longitudinal axis $z = 0$. For any position in layers ≥ 1 where $z \neq 0$ the lattice beams do not have the same intensity and can therefore only partially interfere destructively as can be seen in fig. 4.24. The remaining intensity creates a potential which is maximal at the center positions of the individual lattice beams, resulting in a confining potential along z. This effect gets stronger with higher layers as the beam center positions are farther apart the higher the layer which again leads to a higher ratio of the beam intensities at the beam center positions. We emphasize that this effect only occurs along z, not along the horizontal axis x.

The potential along z for different layers is illustrated in fig. 4.25 (a). The plot also includes the ground state potential explained below. The potential is trapping for layers ≥ 1, the corresponding physical trapping frequencies ν are in the order of up to a few 10 Hz. This is considerably lower than the trapping frequency of the 850 nm CDT. Due to the quadratic summation the increase of the longitudinal trapping frequency for layers ≤ 4 is below 2.5%. Hence, this effect is negligible in our setup. However, it will become relevant in sec. 5.4 where the possibility to study 2D quantum droplets with our experimental

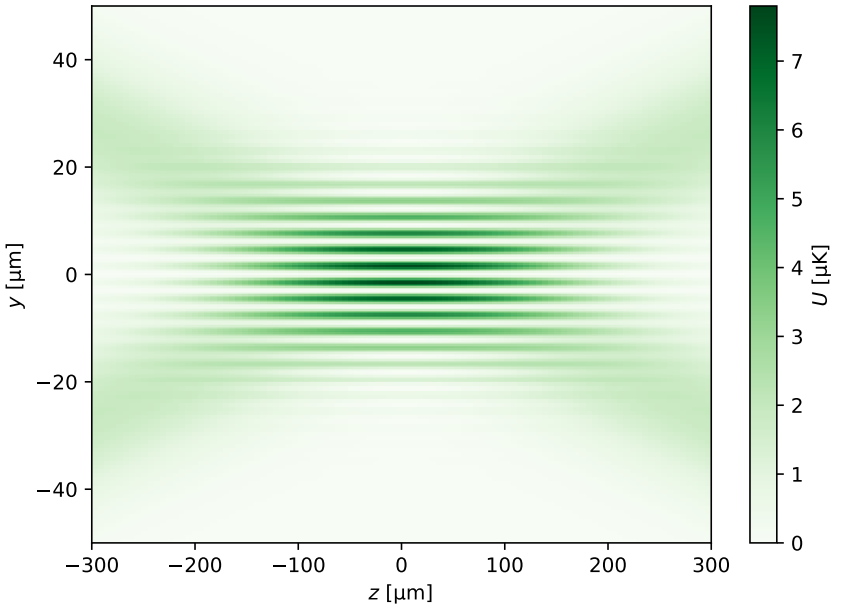

Figure 4.24: Potential U created by the lattice beams in dependence of vertical and longitudinal position y and z. The calculation assumes $x = 0$ as well as equal waists and power of the lattice beams. Total interference only appears at the symmetry planes defined by $y = 0$ and by $z = 0$. At any other position the lattice beams do not have the same intensity and can thus only partially interfere destructively. The remaining intensity creates an potential in any layer except the central layer. The potential is maximal at the center position of each lattice beam, not at $z = 0$, causing a confining potential along the longitudinal axis.

setup is discussed.

Anti-trapping ground state potential Although the light intensity is zero in the central plane, the in-plane potential of the central layer is not flat since another effect comes into play. Just as the intensity and thus the trapping frequency decreases vertically it also decreases radially, i. e. horizontally and longitudinally. This affects the ground state energy $\hbar\omega_y/2$ which hence also decreases radially, resulting in an effective anti-trapping potential, in the following referred to as the ground state potential. A comparison between the in-plane potential of central, first and second layer with and without including the ground state potential is shown in fig. 4.26. As can be seen the longitudinal trapping potential for layers ≥ 1 explained above is still dominating. Hence, layers ≥ 1 feature an in-plane potential which is trapping along z while being anti-trapping along x. The central layer, in contrast, exhibits a radially nearly symmetric anti-trapping in-plane potential.

The potential along x at $z = 0$, which is given by the ground state potential, is illustrated in fig. 4.25 (b). The corresponding trapping frequency ν slightly decreases with higher layers due to the decreasing intensity. ν is in the order of $\sim -5\,\mathrm{Hz}$ which is

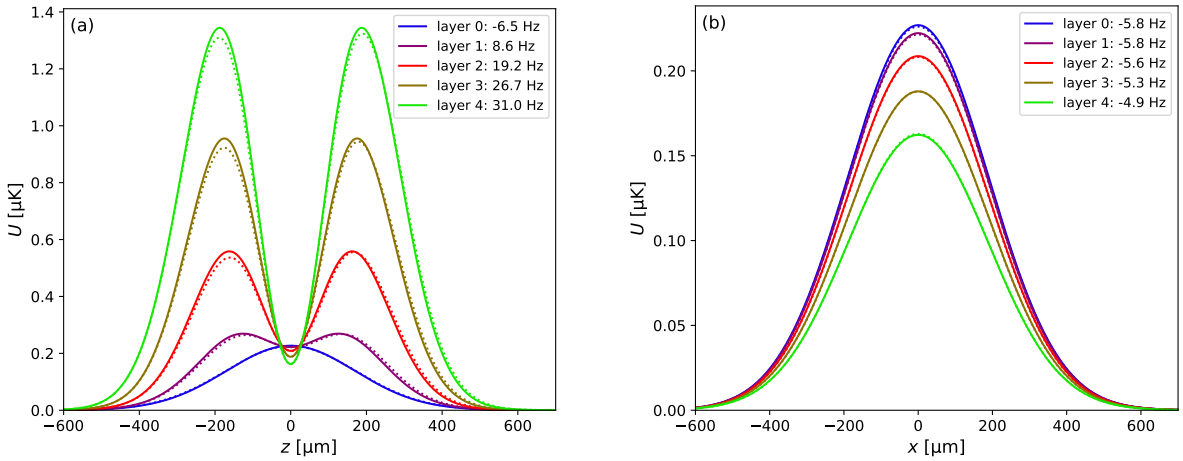

Figure 4.25: Potential U created by the lattice beams depending on the longitudinal (a) and horizontal (b) position z and x for different lattice layers. The calculation is performed for equal lattice beam waists (solid lines) as well as for slightly different lattice beam waists (dotted lines) as stated in tab. 4.4. The corresponding trapping frequencies ν for equal waists are stated in the legend. The trapping frequencies for slightly different waists differ by less than 2%. Horizontally the potential is anti-trapping with lower trapping frequency for higher layers. Longitudinally, only the central layer is anti-trapping while every other layer is trapping with higher trapping frequencies for higher layers.

much smaller than the radial trapping frequency of the 850 nm CDT. Accordingly, for our setup the ground state potential is negligible.

Imperfections So far we only considered equal lattice beams. In reality the beam waists are slightly different as stated in tab. 4.4 and there will be imperfections in power balancing and polarisation. All of these effects result in remaining intensity and thus have an effect on the in-plane potential.

Remaining intensity caused by imperfect polarisation is symmetric and will lead to an additional anti-trapping potential with the same shape and similar order of magnitude as the anti-trapping ground state potential. Accordingly, it mainly affects the central layer and first layer, as their respective trapping frequencies are in the same order of magnitude, as well as the horizontal axis of the other layers since their longitudinal axis is dominated by the confining potential as discussed above. Assuming 5% wrong polarisation the trapping frequencies corresponding to the anti-trapping ground state potential would increase by $\sim$35%. That means the order of magnitude does not change and the anti-trapping would be negligible compared to the radial confinement provided by the 850 nm CDT.

Unequal beam waists and a power imbalance have basically the same effect. The remaining intensity is asymmetric in the longitudinal axis, though, as illustrated in fig. 4.25. However, while the asymmetry results in a slight deformation of the in-plane potential,

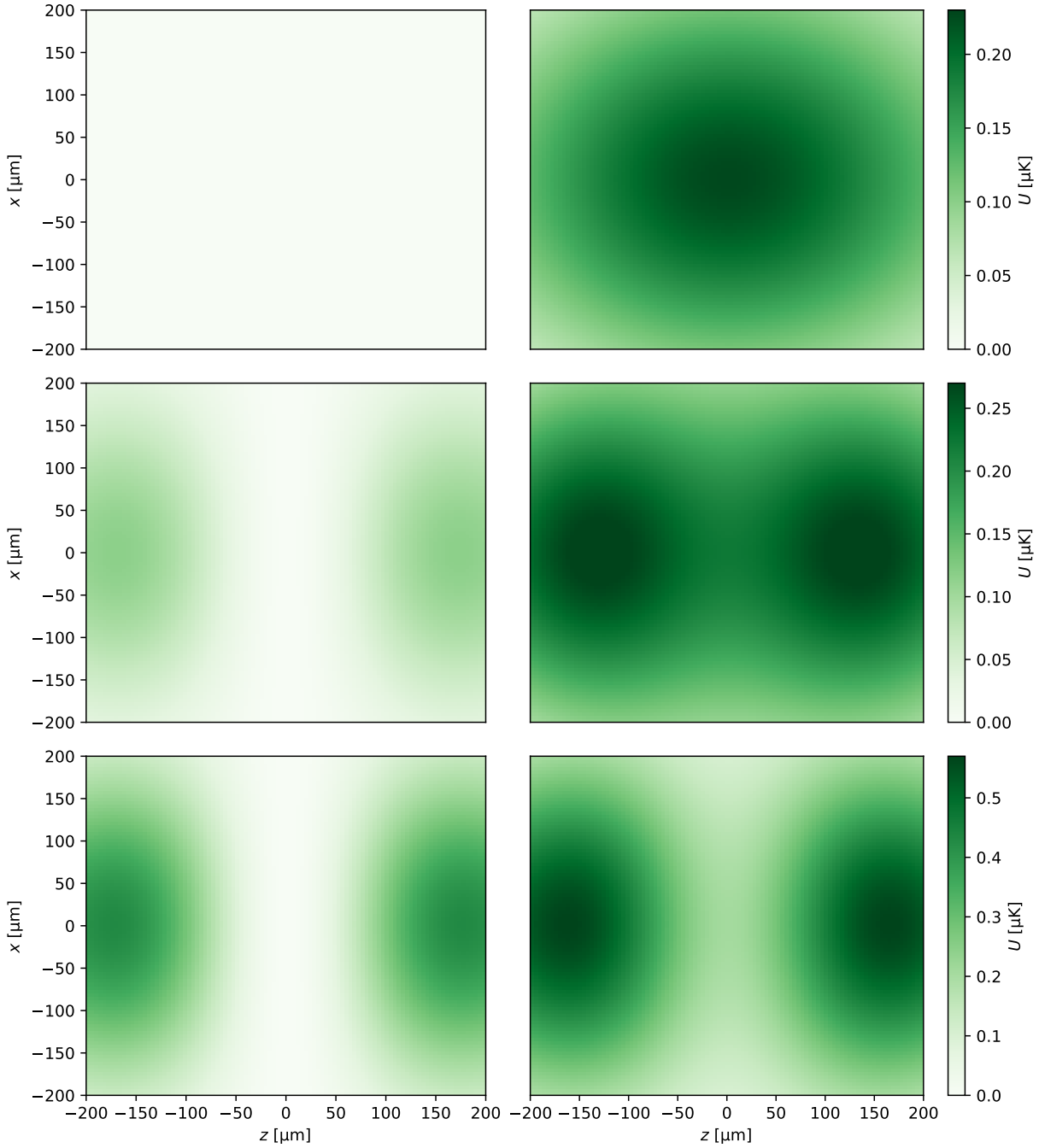

Figure 4.26: The in-plane potential U for different lattice layers with (right column) and without (left column) including the ground state potential. The lattice beams propagate from left to right. For the calculation equal waists and power of the lattice beams are assumed. The first row shows the central layer (0th layer), second row shows the first layer, third row the second layer. Cross-sections through these 2D potentials at $x = 0$ and $z = 0$ are provided in fig. 4.25. When purely considering the potential proportional to the light intensity, the central layer exhibits a flat potential while any other layer features a confining potential along the longitudinal axis. Including the ground state potential adds an anti-trapping potential resulting in a saddle potential at the atom position for layers other than the central layer. However, the corresponding trapping frequencies are much smaller then the trapping frequency of the radial confinement provided by the 850 nm CDT which is not included in the plots. Hence, the in-plane potential is only relevant in free space or when desiring a flat potential.

the center of the trap where the atoms are located barely changes. For the beam waists as stated in tab. 4.25 and assuming a power imbalance of 5% the trapping frequencies of the in-plane potential caused by the lattice beams decrease by less than 5%. Hence, the effect of the observed unequal beam waists as well as the effect of a small power imbalance is negligible.

Conclusion The different effects discussed above result in an anti-trapping in-plane potential in the central layer, while layers ≥ 1 are trapping along z and anti-trapping along x. However, in our setup the radial potential is strongly dominated by the harmonic confinement provided by the 850 nm CDT. Although the vertical trapping frequency ω_y decreases with higher layers, the difference is below 10% for layers ≤ 2. Hence, these layers are nearly equally suitable.

However, in case of a possible future implementation of a 2D box potential, e. g. via a DMD, the situation is different. In an otherwise flat potential, the in-plane potential created by the lattice beams becomes relevant as it perturbs the homogeneity of the box potential. This is particularly relevant for degenerate bosonic systems as their characteristic energy scale, given by the chemical potential, is much lower than compared to degenerate fermionic systems, where the characteristic energy scale is given by the Fermi energy. Therefore, it is strongly recommended to load the atoms into the central layer where the in-plane trapping frequencies are lowest. Furthermore, in contrast to higher layers, the in-plane potential in the central layer is radially nearly symmetric and purely anti-trapping which allows to compensate the potential by an additional magnetic confinement. The magnetic confinement that can be provided with our coil setup is slightly lower than the anti-trapping of the ground state potential, though. Thus, the remaining anti-trapping would need to be compensated by the DMD.[36]

[36] In principle the DMD could be used to compensate any in-plane potential of any layer. The drawback is that this compensating potential is an optical potential. Therefore, it increases the intensity at the atom position which gives rise to off-resonant scattering.

Chapter 5

Perspectives on studying 2D bosonic bulk systems

In the previous chapters we discussed how our experimental setup was re-designed and re-built to create two-dimensional Bose gases. The key features are the ability to prepare, image and to drive transitions between multiple spin states and hence to create *spin mixtures*, furthermore *tunable interactions* provided by a variety of suitable intra- as well as interstate Feshbach resonances and the *high-resolution imaging* enabled by the in-vacuo microscope objectives with an NA of 0.75 corresponding to a diffraction-limited resolution of $\sim 0.62\,\mu\text{m}$ at the imaging wavelength of $\sim 767\,\text{nm}$.

In this chapter we will discuss how these features can be utilised to study degenerate 2D Bose gases. Therefore, we will first give a short overview of previous work on 2D bosonic bulk systems with atomic BECs, followed by a brief presentation of the rich physics of binary spin mixtures. Then, we will discuss two phenomena in more detail. First, we will summarise measurements on 2D Bose polarons that were performed by [76] with the experimental setup described in this thesis. Then we will discuss how 2D droplets could be realised with our experimental setup.

5.1 Previous work

Since the first realisation of a BEC confined to two dimensions in 2001 [116] the field has greatly expanded. Several experiments were built to create and study quasi-2D Bose gases employing various atomic species, schemes to achieve the 2D confinement and in-plane potentials, thus allowing to focus on different aspects and hence to cover a variety of physical phenomena. Before we present the scientific research conducted in the field of 2D bosonic bulk systems with atomic BECs, we will give a brief overview of the experiments that are arguably most relevant in this context:

- the rubidium experiment in the group of J. Dalibard in Paris where the BKT transition in cold atoms was observed for the first time [23]. It is the first experiment where an accordion lattice providing the 2D confinement was employed for achieving tunable interactions [143]. This mechanism limits the coupling strength to $0.08 < \tilde{g} < 0.26$ but can be a useful tool for atomic species such as rubidium that lack suitable Feshbach resonances.
  Further noteworthy scientific contributions include e. g. the observation of superfluidity [144] and of transverse condensation [109] in a quasi-2D Bose gas.

- the 2D potassium experiment in the group of Z. Hadzibabic where the 2D confinement is realised via a combination of DMD and phase plate that creates a TEM_{01}-like mode which also allows to employ accordion schemes [145]. Particularly noteworthy are the observation of a smooth connection between the interaction-driven BKT and BEC phase transitions in a trapped 2D Bose gas [146] as well as the first observation of second sound in a 2D Bose fluid [118] that were achieved at this experiment.

- the caesium experiment in the group of C. Chin in Chicago where the availability of suitable Feshbach resonances is exploited to study e. g. the equation of state [147], the dynamics of driven systems via modulated interactions, especially including so-called Bose fireworks [148, 149], or the transition from an atomic to a molecular BEC [150], which is the bosonic analog to the BEC-BCS crossover in a Fermi gas.

- the caesium experiment in the group of C. Hung at the Purdue University in Indiana with a considerably high imaging resolution enabled by their objective with an NA of 0.6. Noteworthy techniques employed at this experiment include quenches, in particular interaction quenches from repulsive to attractive to induce a modulational instability leading to the formation of Townes solitons [151], and box quenches leading to the formation of ring dark solitons [152].

- the rubidium experiment in the group of C. J. Foot in Oxford which was the first one to implement a multiple-radiofrequency-dressed adiabatic potential. This potential not only provides the 2D confinement, but also allows to transform it from a single-well into a state-selective double-well potential and thus to coherently split the sample into two atom clouds [153–155]. This enables e. g. to measure the first-order correlation function and vortex density via spatially resolved matter-wave interferometry and allowed to observe the universal scaling of the algebraic exponent and vortex density [156].

- the sodium experiment in the group of Y. Shin in Seoul which mainly functions as a spin-1 spinor BEC. It focusses on two-dimensional spin dynamics while the condensate is usually thermodynamically 3D and is used to study e. g. spin turbulence [157, 158].

- the rubidium experiment also in the group of Y. Shin in Seoul employing a 3D BEC which is highly oblate such that the vortex dynamics are 2D. Notably, the optical dipole trap providing the tight vertical confinement is formed by a truncated Gaussian beam allowing to create a large-area BEC [159].

- the 2D lithium experiment in the group of J. Choi at the Korean Advanced Institute of Science and Technology with 2D spin dynamics. Due to their relatively low vertical trapping frequency ω_z their sample does not fulfil $k_B T < \hbar\omega_z$, though. They mainly study a spin-1 spinor BEC which in contrast to rubidium or sodium spinor BECs has strong spin-dependent interactions due the properties of lithium [160]. Recent studies include the first classification of universal coarsening dynamics in a quenched 2D ferro-magnetic spinor Bose gas [161].

- the potassium experiment in the group of M. K. Oberthaler in Heidelberg which is the first one to use a 2D Bose gas as a quantum simulator for a relativistic scalar quantum field in curved space-time [162].

Further groups with 2D setups with ultracold Bose gases include the group of T. W. Neely and the group of K. Helmerson in Australia, the group of M. D. Hoogerland in New Zealand and the groups of T. Bourdel and H. Perrin in Paris.[1]

Especially early research focussed on the fundamental properties of 2D Bose gases such as the BKT crossover [23, 163, 164], the critical point [165], the equation of state [147, 166–168], and signatures of superfluidity [144, 169]; and also recent studies address e. g. the dynamics of the BKT transition [156, 170, 171], first and second sound [118, 172] as well as the formation and dynamics of vortex clusters [173, 174]. Furthermore, 2D BKT clouds have been very successfully used as an experimental platform to investigate, e. g. the Kibble-Zurek mechanism [109, 175–178], vortex shedding [179, 180], vortex turbulence [181–183] and very recently also wave turbulence [184, 185]. Various other research topics include dark solitons [152], Tan's contact [141], Anderson localisation [186], and light diffusion [187, 188].

[1] Of course there are also numerous groups working with 2D bosonic lattice systems which are not discussed here.

Experiments with suitable Feshbach resonances, as available for caesium, lithium and especially potassium, possess an additional degree of freedom since Feshbach resonances allow for tunable interactions. This also gives access to driven systems, where phenomena such as pattern formation [189], the spontaneous emergence of a square lattice state [190] and matter-wave jets, so-called Bose fireworks [148, 149], were observed. Tunable interactions also give rise to the possibility to perform interaction quenches. Townes solitons, for example, were observed as a result of a modulational instability induced by quenching the interaction from repulsive to attractive [151, 191, 192]. Further phenomena that were studied by employing tunable interactions are the universality of the 2D Bose gas [147], the interaction-driven BKT transition [146], self-oscillating supersonic flow [193], universal coarsening [194] and so-called breathers [195].

Taking one step further and going from single-component to multi-component 2D Bose gases by preparing spin mixtures led to a variety of new phenomena and also enabled new approaches to known phenomena. Spinor gases [196], i. e. degenerate Bose gases whose spin composition can vary and hence feature a spin degree of freedom, with 2D spin dynamics were used to observe skyrmions [197–199], spin turbulence [157, 158], matter-wave jets, that are not created by driven interactions, but by an unstable spin mixture resulting in a strong spin-momentum correlation [200], and very recently universal coarsening dynamics [161]. Further studies include wall-vortex composite defects [201] and critical spin superflow dynamics that lead to the generation of dark-bright solitons and transverse magnon excitations [202]. Another direction arising from the availability of multiple spin states are binary Bose mixtures[2]. While spinor gases focus on having the spin as a degree of freedom which requires low magnetic fields and hence prevents to make use of Feshbach resonances, binary spin mixtures are two-component gases that maintain their respective spin state and whose key characteristics are the varying intra- and especially interstate interactions. 2D binary Bose mixtures have been used to study Townes solitons [203] - in contrast to the generation via interaction quenches, the generation via binary mixture allows for a deterministic preparation - and also sound modes[3] of mixtures have been observed [204]. Otherwise very few of their rich physics has yet been explored since many experiments lack the possibility to tune the interstate interaction, especially relative to the intrastate interaction. In contrast to K39, neither Rb87 nor Na23 feature suitable interstate Feshbach resonances which makes the combination of tunable interactions and the ability to prepare bosonic spin mixtures very rare.

[2]Note that binary Bose mixtures can also be realised with two different atomic species which is especially in the 2D case experimentally more challenging and introduces a significant mass ratio.

[3]Note that while the observed spin mode was in the 2D regime, the observed density mode was more in the 3D regime.

5.2 Overview on the physics of binary spin mixtures

Weakly interacting Bose gases are typically well-described by the mean-field approximation. For contact interactions the mean-field energy per particle E/N of a uniform degenerate Bose gas with atom number N and density n can be approximated by [110]

$$\frac{E}{N} = \frac{1}{2}gn. \tag{5.1}$$

Consequently, the behaviour is determined by the coupling constant g yielding two regimes: For repulsive interactions, $g > 0$, the energy is minimised by minimising the density. The atomic cloud expands, corresponding to a gaseous phase. For attractive interactions, $g < 0$, the energy is minimised by maximising the density. The atomic cloud contracts and collapses when exceeding a critical atom number [205–207].[4]

However, binary spin mixtures consist of not one, but two components and hence are not only characterised by the intrastate coupling constants g_{11}, g_{22}, but also by an interstate coupling constant g_{12}. This additional degree of freedom results in a richer phase diagram compared to the single-component case as can be seen in fig. 5.1.

In binary spin mixtures, attractive intrastate interaction still results in a collapse of the respective component, but a collapse can also occur for repulsive intrastate interaction, namely when it is exceeded by attractive interstate interaction, $g_{12} < -\sqrt{g_{11}g_{22}}$ with $g_{12} < 0$ and $g_{11}, g_{22} > 0$ [97]. Furthermore, the regime with repulsive intrastate interaction features two stable ground states: a miscible phase in which the two components form a uniform mixture, and an immiscible phase in which the two components separate. The demixing point dividing these two phases can be easily derived. Following [110] we consider a homogeneous gas confined to the volume V. The energy in the miscible case is then given by

$$E_{\text{misc}} = \frac{g_{11}}{2}\frac{N_1^2}{V} + \frac{g_{22}}{2}\frac{N_2^2}{V} + g_{12}\frac{N_1 N_2}{V} \tag{5.2}$$

while the energy in the immiscible case takes the form

$$E_{\text{imm}} = \frac{g_{11}}{2}\frac{N_1^2}{V_1} + \frac{g_{22}}{2}\frac{N_2^2}{V_2} \tag{5.3}$$

where V_1, V_2 are the volumes occupied by the two components with $V_1 + V_2 = V$. In order to be in mechanical equilibrium the pressure exerted by both components in the immiscible phase has to be equal: $\partial E_{\text{imm}}/\partial V_1 = \partial E_{\text{imm}}/\partial V_2$ which yields $g_{11}(N_1/V_1)^2 = g_{22}(N_2/V_2)^2$.

[4] Below the critical atom number the atomic cloud can be stabilised by the kinetic energy.

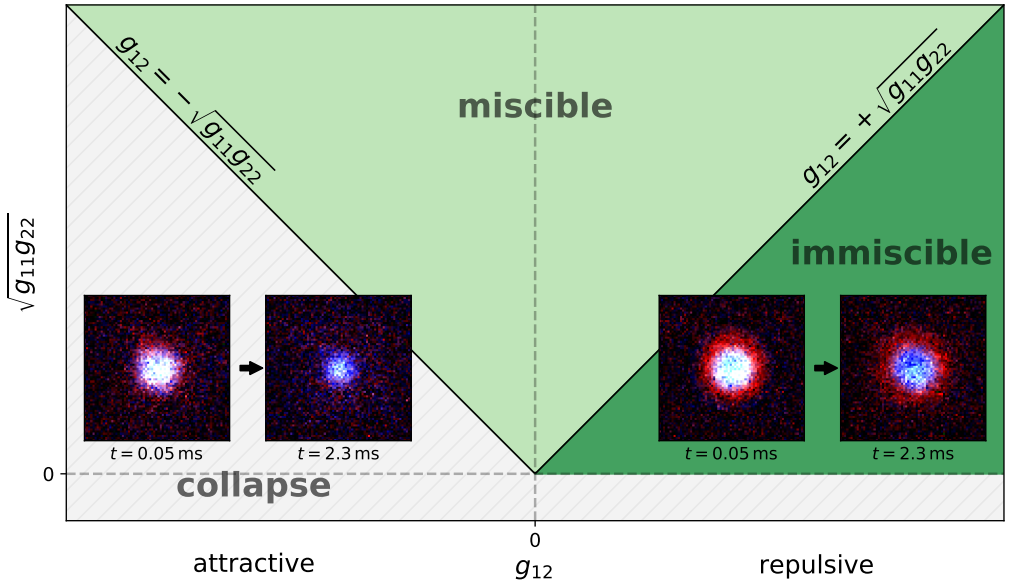

Figure 5.1: Ground state mean-field phase diagram of a binary Bose spin mixture in dependence of the interstate interaction g_{12} and the mean intrastate interaction $\sqrt{g_{11}g_{22}}$ assuming that g_{11} and g_{22} have the same sign. From a mean-field perspective there are three regimes. For attractive intrastate interaction $g_{11}, g_{22} < 0$ as well as for the case of attractive interstate interaction which exceeds repulsive intrastate interaction $g_{12} < -\sqrt{g_{11}g_{22}}$ with $g_{11}, g_{22} > 0$ the system collapses (grey shaded area): the system minimises its energy by maximising the density until the high density leads to severe three-body losses. For the case of repulsive interstate interaction which exceeds repulsive intrastate interaction $g_{12} > \sqrt{g_{11}g_{22}}$ with $g_{11}, g_{22} > 0$ the system is in the immiscible regime (dark green area): the system minimises its energy by spatially separating the two spin components. In contrast, for $-\sqrt{g_{11}g_{22}} < g_{12} < \sqrt{g_{11}g_{22}}$ the system is in the miscible regime (light green area): the system minimises its energy by minimising the density. The two spin components are in a gaseous state and maximise their spatial overlap. **Insets:** Measured density distribution in different regimes 0.05 ms and 2.3 ms after creating an imbalanced spin mixture by applying an RF pulse to a beforehand spin-polarised 2D BKT cloud in a harmonic confinement. Shown are averaged images where the majority component $|1,-1\rangle$ (blue) and the minority component $|1,0\rangle$ (red) were imaged in individual measurements, but with the same settings. Spatial overlap of the two components is marked white. The left images were taken in the collapse regime. After 0.05 ms, shortly after the RF pulse, the system barely had time to adapt and both components spatially overlap. With ongoing time the density increases and severe three-body losses occur. After 2.3 ms most of the minority atoms are lost and mainly majority atoms remain due to the initial imbalance. The right images were taken in the immiscible regime. While there is still significant spatial overlap 0.05 ms, i. e. shortly after the RF pulse, with ongoing time the minority component is pushed away from the trap center by the majority component and after 2.3 ms one can clearly see the phase separation. Insets are adapted from [76].

Using this, eq. 5.3 can be expressed as

$$E_{\mathrm{imm}} = \frac{g_{11}}{2}\frac{N_1^2}{V} + \frac{g_{22}}{2}\frac{N_2^2}{V} + \sqrt{g_{11}g_{22}}\frac{N_1 N_2}{V}. \tag{5.4}$$

Using eq. 5.2 and 5.4 one can easily see that the demixing point, where $E_{\mathrm{misc}} = E_{\mathrm{imm}}$, is given by

$$g_{12} = \sqrt{g_{11}g_{22}}. \tag{5.5}$$

The immiscible phase can also be interpreted as an instability of the spin mixture. Accordingly, collapse threshold and demixing point can also be derived by the requirement that the free energy density of the (miscible) spin mixture has to have a minimum. This yields the mean-field stability criteria $g_{11}, g_{22} > 0$ and $g_{12}^2 < g_{11}g_{22}$, retrieving the instability points $g_{12} = -\sqrt{g_{11}g_{22}}$ against collapse and $g_{12} = +\sqrt{g_{11}g_{22}}$ against spatial phase separation [208].

Naturally, the vicinity of these thresholds is of particular interest, especially since intra- and interstate interaction nearly balance each other in that regime. Accordingly, the mean-field term is weakened and quantum fluctuations become relevant which gives rise to beyond mean-field phases such as liquid-like droplets [7, 209] close to the collapse threshold and the formation of mixed bubbles near the demixing point predicted for $g_{11} \neq g_{22}$ [210].[5] But also the mean-field description features further regimes, e. g. when exploiting the degree of freedom given by the ratio of the two components. In highly imbalanced spin mixtures, for example, objects like Bose polarons [76] and Townes solitons [211] can be observed.

From this wealth of phenomena that can be studied with binary spin mixtures with tunable interactions we will discuss two in more detail. In sec. 5.3 we will summarise measurements of 2D Bose polarons that were performed by [76] on the very experimental setup described in this thesis. In sec. 5.4 we will then turn to a very different regime and discuss the realisability of 2D droplets in our experimental setup.

5.3 2D Bose polarons

The extreme case of a highly imbalanced spin mixture, an impurity in an otherwise spin-polarised bath, is a fundamental, yet non-trivial many-body problem. Due to

[5] Both regimes, droplets as well as mixed bubbles are not only predicted for the 2D case, but also for the 3D case. While 3D droplets have been observed in [8], 2D droplets and mixed bubbles have not yet been experimentally realised.

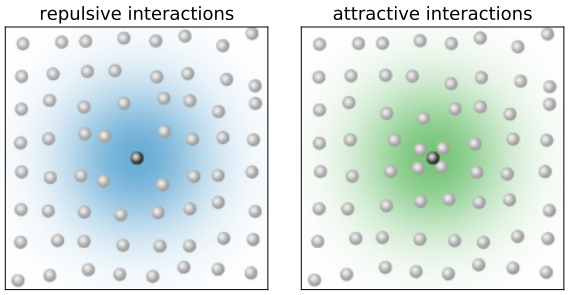

Figure 5.2: Polaron sketch. Due to impurity-bath interactions the impurity (black) locally modifies the density of the bath (white) which in turn modifies the motion of the impurity. The dressed impurity (blue/green) can be described as a quasi-particle, a so-called polaron. Adapted from [76].

impurity-bath interactions the bath density is modified by the impurity which in turn retro-acts on the impurity as sketched in fig. 5.2. The impurity gets dressed by the bath and the dressed impurity can be described as a quasi-particle known as polaron. The polaron concept was pioneered by Landau and Pekar [212–214] in the context of solid state physics where an electron moving through an ionic crystal gets dressed by phonons that are excited by the deformation of the crystal caused by the electron. It is relevant for a wide range of systems such as, most prominent, semiconductors [215] and high temperature superconductors [216], but also beyond condensed matter physics e. g. for the Higgs-mechanism [217]. The concept has been extended from Bose polarons, i. e. impurities in a bosonic bath as is the case for electrons in a phonon bath, to Fermi polarons, i. e. impurities in a fermionic bath as relevant e. g. for the Kondo effect [218]. Furthermore, different dimensions have been considered as the behaviour is also influenced by the dimensionality. Motivated by two-dimensional materials such as graphene and layered materials such as cuprate superconductors we studied 2D Bose polarons with the experimental setup described in this thesis. The measurements were performed and analysed by M. Schlederer and were the first realisation of 2D Bose polarons in a cold atoms environment. A detailed description and explanation is given in his thesis [76]. Here, we just give a brief partial summary.

The experiment starts with a spin-polarised 2D BKT cloud of $3{\cdot}10^3$ atoms in the $|1,-1\rangle$ state which acts as the bath state. The $|1,0\rangle$ state will be used as the impurity state. The interaction strength can be adjusted via the magnetic field by exploiting a Feshbach resonance. While the bath-bath interaction is weakly repulsive in the regime we are interested in, the impurity-bath interaction can be tuned from repulsive to attractive. After setting the magnetic field to a suitable value an RF pulse with detuning δ is applied where $\delta = 0$ corresponds to the resonance frequency of the $|1,-1\rangle \rightarrow |1,0\rangle$ transfer in the non-interacting case. Accordingly, when δ matches the interaction shift $g_{BI}n$, with impurity-bath coupling constant g_{BI} and bath density n, a small part of the atoms are transferred from the bath state into the impurity state and polarons are formed.[6] Both the impurity

[6]Due to interactions the Rabi oscillation driven by the RF transfer quickly decoheres and at most

state as well as the bath state can then be imaged in individual measurements via absorption imaging either in-situ or after time-of-flight allowing to extract the density distribution as well as the remaining condensate fraction and the remaining condensate atom number.

Due to the radially symmetric harmonic confinement the density $n = n(r)$ is spatially dependent where r is the radial coordinate. Consequently, the interaction-shifted resonance frequency is also spatially dependent as indicated in fig. 5.3 and thus, with different detunings δ polarons are created at different positions r. With repulsive interactions, for example, a higher detuning δ_1 transfers atoms at higher densities, i. e. near the trap center, while a lower detuning δ_2 creates polarons at lower densities further away from the trap center resulting in a ring-shaped structure. These shapes can be resolved with our high-resolution imaging as can be seen in fig. 5.3 (insets). Furthermore, the high resolution also allows to track the dynamics. When an atom is transferred into the impurity state the effective potential resulting from the interaction with the bath suddenly changes.

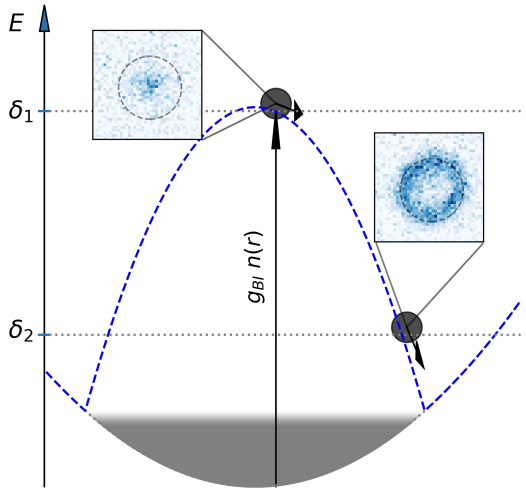

Figure 5.3: A polaron is created by transferring an atom from the bath state into the impurity state via an RF pulse. Due to impurity-bath interactions, the bath (grey) causes a spatially dependent interaction shift $g_{BI}n(r)$ (black arrow) of the resonance frequency for the transfer. Consequently, for different RF pulse detunings δ the polaron is created at different distances r from the trap center. For the illustrated repulsive case a lower δ matches the interaction shift for lower densities, i. e. further away from the trap center. This results in differently shaped density distributions of the impurity state as depicted in the insets. Furthermore, due to the interaction energy, the bath creates an effective potential (blue, dashed) for the impurity which for $g_{BI} > 0$ accelerates the impurity away from the trap center. Taken from [76].

For example repulsive impurity-bath interactions correspond to an effective repulsive potential as sketched in fig. 5.3 (blue, dashed) and this effective potential accelerates the impurity away from the trap center. This is similar to the phase separation that occurs in the immiscible regime as described in the previous section where one could see how the impurities moved away from the majority component in the trap center with ongoing time (see fig 5.1). Here, we can use the impurity as a probe for the bath since the acceleration of the impurity depends on the local slope of the effective potential given by the bath as well as on the local speed of sound above which the motion of the impurity gets damped due to friction. The resulting dynamics also reveal the 2D character of the bath which obeys the 2D rather than the 3D friction force.

$\sim 10\%$ of the atoms are transferred into the impurity state.

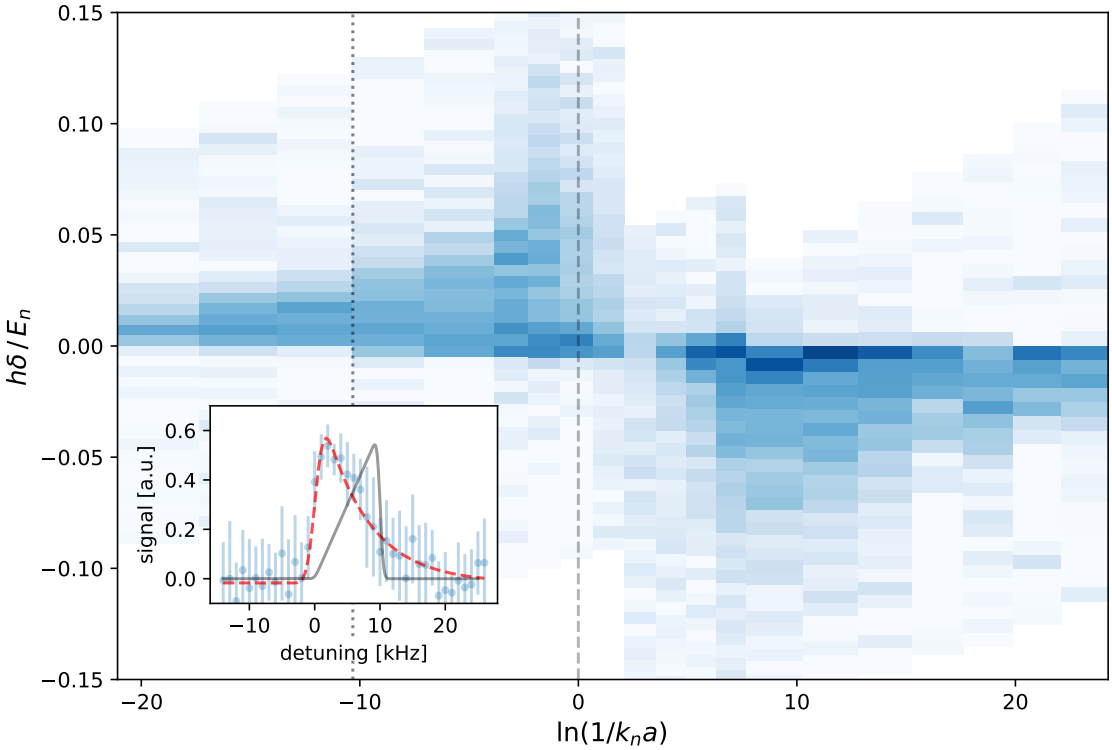

Figure 5.4: 2D Bose polaron spectra. Shown is the condensate atom number loss of the bath state in dependence of the energy corresponding to the RF pulse detuning δ for a wide range of the interaction parameter $\ln(1/k_n a)$ where $k_n = \sqrt{4\pi n}$ is the characteristic momentum corresponding to the peak density n. $h\delta$ is normalised to the natural energy scale $E_n = \hbar^2 k_n^2/(2m)$ and $\delta = 0$ corresponds to the resonance frequency for no interactions. The vertical dashed line indicates the center position of the Feshbach resonance. A negative (positive) interaction parameter corresponds to repulsive (attractive) interactions. **Inset:** Vertical cut through the main plot, exemplarily at $\ln(1/k_n a) = -10.3$ as indicated by the vertical dotted line. Illustrated are the measured data (blue dots) as well as two models. One model (grey, solid) only includes the broadening of the RF frequency and the volume factor of the density addressed by the RF frequency. The other model (red, dashed) additionally includes contributions from excited states. The agreement with the measured data indicates that these excited states are highly relevant. Adapted from [76].

The high tunability of the interactions furthermore allows to perform spectroscopic measurements from weakly to strongly interacting polarons both for repulsive as well as attractive interactions. The thereby extracted 2D polaron spectra are shown in fig. 5.4 where the condensate atom number loss of the bath state is plotted in dependence of the normalised applied RF pulse detuning δ and in dependence of the interaction parameter $\ln(1/k_n a)$ with $k_n = \sqrt{4\pi n}$ where n refers to the peak density. A single spectrum for a fixed interaction parameter is shown in the inset. From these spectra the polaron energy can be extracted which is especially interesting in the strongly interacting case where the mean-field description breaks down. Furthermore, the line shapes of the spectra are of particular

interest. Assuming that the energy required to create a polaron is proportional to the local density $\hbar\delta_{\mathrm{res}} \propto n(r)$ and including the volume factor of the addressed density as well as a frequency broadening due to the finite RF pulse width one would expect a line shape as illustrated in fig. 5.4 (inset) (grey, solid). This expectation does not match the observation, though. Instead the line shapes are well described by an alternative model, also illustrated in fig. 5.4 (inset) (red, dashed), introduced by [76] which takes significant contributions from excited polaron states into account. While these measurements, including the first published polaron spectrum in a degenerate 2D Bose gas, allowed to gain more insights on the creation and behaviour of 2D Bose polarons, there still remain open questions such as the nature and role of the indicated excited states which deserves further investigation.

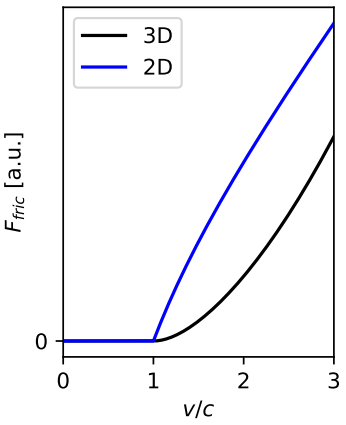

Figure 5.5: 2D and 3D friction force F_{fric} in dependence of the velocity v of the impurity in units of the speed of sound c. Calculated according to [76].

5.4 2D droplets

In the previous section we considered a highly imbalanced spin mixture where one of the spin states acts as an impurity. This impurity gets dressed by the atomic bath given by the majority spin component leading to the formation of a polaron, which is purely a mean-field effect. Turning to balanced spin mixtures on the other hand opens up new possibilities and gives access to beyond mean-field effects resulting in a new, liquid-like state of matter, the so-called quantum droplet. A more detailed discussion, especially including dipolar quantum droplets, can be found in the review by Böttcher *et al.* [219]. Here we will give a brief introduction focussing on quantum droplets in Bose-Bose mixtures and will then discuss the experimental realisability in our setup. We will derive the ground state phase diagram for different radial confinements of the quasi-2D system and highlight suitable parameter regimes for creating 2D droplets.

5.4.1 Quantum droplets in Bose-Bose mixtures

Typically, quantum fluctuations are negligible in weakly-interacting quantum gases, but using roughly balanced spin mixtures we can tune the interactions such that the intra- and interstate interaction contributions to the mean-field energy have opposite signs and

nearly cancel each other. In this regime, where $\delta g = g_{12} + \sqrt{g_{11}g_{22}} \ll g_{11}, g_{22}$ with intrastate coupling constants $g_{11}, g_{22} > 0$ and interstate coupling constant $g_{12} < 0$, the mean-field approximation breaks down: the mean-field term nearly vanishes and beyond mean-field corrections become relevant. The leading-order correction due to quantum fluctuations is the so-called LHY correction term [220] which is basically the zero-point energy corresponding to the Bogoliubov excitations. Due to its different scaling with the density, the LHY term can balance the remaining mean-field term: At an equilibrium density the ground state energy features a minimum. So instead of collapsing for $\delta g < 0$ as expected in the mean-field approximation as explained in section 5.2, the atomic cloud is stabilised by quantum fluctuations and forms a stable state: a quantum droplet.

Quantum droplets in Bose-Bose mixtures were predicted by Petrov in 2015 [7] and experimentally realised in 2018 [8, 221].[7] Unlike typical quantum gases that are well-described by the mean-field approximation and which hence either collapse or are in a gaseous phase, quantum droplets correspond to a liquid-like state: they exhibit incompressibility above a critical peak density, i. e. a flat-top density profile[8] and, arguably most characteristic, a self-bound nature just like a classical water droplet with no need for an external confinement. Furthermore, quantum droplets in Bose-Bose mixtures feature a unique property: they can self-evaporate. Petrov showed that there is a regime where there are no excitation modes below the particle emission threshold, i. e. where it is energetically more favorable to spill particles than to populate any excited mode [7]. However, the self-bound nature of the droplets prevents usual temperature probes such as time-of-flight measurements, which is why this self-evaporating effect still remains to be observed. Overall, further measurements of quantum droplets in Bose-Bose mixtures prove difficult since they suffer from a rather limited lifetime. Although several orders of magnitude more dilute than classical liquids, they are dense compared to BECs. The density differs by more than one order of magnitude resulting in severe three-body losses. With decreasing atom number the kinetic energy, corresponding to a repulsive force, becomes more dominant and drives a liquid-to-gas transition when reaching a critical atom number: the droplet dissociates [8].[9] Despite these experimental challenges, quantum

[7] Spin mixtures are not the only platform used to create quantum droplets. Besides hetero-nuclear mixtures that also rely on competing intra- and interstate contact interaction, quantum droplets are also studied using one-component quantum gases that feature significant dipole-dipole interaction. In that case there is no interstate interaction; instead the intrastate contact interaction is counter-acted by the dipole-dipole interaction. These so-called dipolar quantum droplets were first observed in 2016 [222, 223].

[8] This has been observed in dipolar quantum droplets [224]. Quantum droplets in Bose-Bose mixtures are typically below this critical peak density, i. e. their density profile is dominated by surface effects.

[9] This dissociation is strictly different from the self-evaporation mentioned above. Although a droplet can self-evaporate to its ground state as opposed to e. g. exhibiting excited surface modes, this ground state still corresponds to a droplet phase which is self-bound. The dissociation on the other hand corre-

droplets are of great interest as they provide insight on beyond mean-field physics and are subject to active research [225–231].

In lower dimensions the role of quantum fluctuations that stabilise the droplet against the mean-field collapse is enhanced. For that reason two-dimensional quantum droplets are of particular interest. In 2016 it was shown theoretically that quantum droplets in Bose-Bose mixtures also exist in two dimensions [209], but so far they were not observed experimentally. And indeed, 2D droplets are expected to behave significantly different from 3D droplets: Due to the peculiar scaling of the 2D LHY correction term there is in principle no critical atom number below which the droplet dissociates. A droplet solution exists as long as the intrastate interaction is weakly repulsive and the interstate interaction weakly attractive, i. e. for every atom number and also for $\delta g > 0$.

In the following we will discuss the experimental realisability of 2D droplets. As stated above droplets typically suffer from rather limited lifetimes as their density is usually sufficiently high to get significant three-body losses. Thus, after selecting a suitable spin combination, we will identify regimes with a suitable density. In order to do so we will estimate the equilibrium density and derive the ground state phase diagram by using a variational calculation technique (see e.g. [97]). This will also provide us with a better understanding of why the 2D droplet regime is less restrained than the 3D droplet regime. Furthermore, we will see that this only holds true in a flat potential. The presence of a weak anti-confinement as created by the vertical lattice providing the 2D confinement (see section 4.6.4) restores the existence of a critical atom number N_c below which the droplet dissociates. We will also discuss how the lower density limit corresponding to this critical atom number can be improved. A brief summary of the results can be found at the end of this section.

5.4.2 Selecting suitable spin states

As stated above the formation of 2D droplets requires repulsive intrastate and attractive interstate interaction, i. e. positive intrastate and negative interstate scattering lengths.[10] As can be seen in fig. 5.6 K39 features two regimes where this condition is fulfilled: preparing a spin mixture $|1,\text{-}1\rangle$, $|1,0\rangle$ and using magnetic fields around $B \approx 55\,\text{G}$ or preparing a spin mixture $|1,+1\rangle$, $|1,0\rangle$ and using magnetic fields around $B \approx 380\,\text{G}$.

sponds to a liquid-to-gas transition where the self-bound property is lost.

[10]Note that we refer to the 3D scattering lengths here. From the collisional perspective the system is basically 3D, since the scattering lengths are much smaller than the harmonic oscillator length $a_{ho,z}$ of the tightly confined axis. Accordingly, the 2D coupling constant $g_{ij} \propto a_{ij}/a_{ho,z}$ is mainly determined by the 3D scattering length a_{ij}.

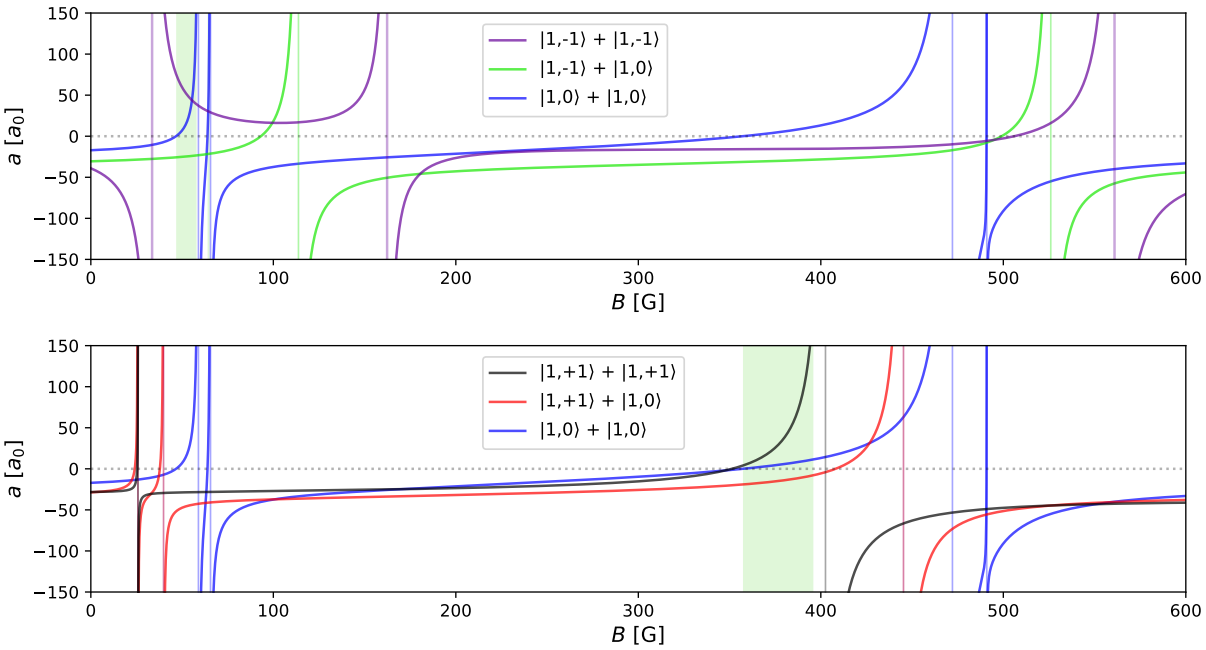

Figure 5.6: 3D s-wave scattering length a in dependence of the magnetic field B for a spin mixture of $|1,\text{-}1\rangle$, $|1,0\rangle$ (top) as well as $|1,+1\rangle$, $|1,0\rangle$ (bottom). The data is the same as in fig. 3.15. The regimes where the respective intrastate scattering lengths are positive while the respective interstate scattering length is negative as required for the formation of 2D droplets are shaded in green. Both spin mixtures feature a regime where this condition is fulfilled. However, for the mixture of $|1,+1\rangle$, $|1,0\rangle$, the $|1,0\rangle + |1,0\rangle$ scattering length is particularly low which makes the first spin combination $|1,\text{-}1\rangle$, $|1,0\rangle$ a more favorable choice.

As described in section 3.7.3 both spin states, $|1,\text{-}1\rangle$ as well as $|1,+1\rangle$ can be prepared and cooled to degeneracy and hence are experimentally accessible. However, the droplet formation also requires a nearly vanishing mean-field interaction energy, i. e. the system has to be close to the collapse threshold where $\delta g \ll g_{11}, g_{22}$ [232]. Since the $|1,0\rangle + |1,0\rangle$ scattering length around $B \approx 380\,\text{G}$ is very small, this drastically limits the suitable regime when using a $|1,+1\rangle$, $|1,0\rangle$ spin mixture. Hence, it is more favorable to prepare the quasi-2D system in the $|1,\text{-}1\rangle$ state and to then create a $|1,\text{-}1\rangle$, $|1,0\rangle$ spin mixture by applying an RF $\pi/2$-pulse.[11] Subsequently, the magnetic field can be ramped to small δg and the radial confinement given by the 850 nm crossed dipole trap can be switched off. The thereby created 2D quantum droplet can then be observed by measuring the density distribution via absorption imaging, especially allowing to infer the size of the atomic sample, in dependence of the time.

[11] In the following parameters corresponding to the $|1,\text{-}1\rangle$ state or the $|1,0\rangle$ state will be denoted by the index '1' or '2', respectively.

5.4.3 Estimating the droplet density

To estimate the equilibrium peak density of the 2D quantum droplet we employ a variational calculation technique (see e. g. [75, 97]). The idea is to determine the energy of the system $E(\phi) = \int \epsilon \, d\mathbf{r}$, where ϵ is the energy density functional, by making a variational ansatz for the spatial wave function $\phi(\mathbf{r})$. Using a parameter corresponding to the size of the atom cloud as a variational parameter and minimising the energy with respect to this parameter yields the ground state and allows to extract the corresponding density which is the equilibrium density.

The first step is to choose a suitable trial wave function. In the droplet regime, i. e. $\delta g = g_{12} + \sqrt{g_{11} g_{22}} \ll g_{11}, g_{22}$ with $g_{11}, g_{22} > 0$ and $g_{12} < 0$, the spin mode is suppressed which allows us to describe both spin modes with a common wave function as we will se in the following: Diagonalising the mean-field energy density yields

$$\epsilon_{\mathrm{MF}} = \frac{1}{2} \sum_{i,j=1,2} g_{ij} n_i n_j = \lambda_- n_-^2 + \lambda_+ n_+^2 \tag{5.6}$$

with coefficients $\lambda_+ \simeq (g_{11} + g_{22})/2$ and $\lambda_- \simeq \delta g \sqrt{g_{11} g_{22}}/(g_{11} + g_{22})$ [7, 232]. The density $n_+ = (n_1 \sqrt{g_{11}} - n_2 \sqrt{g_{22}})/(\sqrt{g_{11} + g_{22}})$ corresponds to a spin mode which is sensitive to the difference between the single component densities n_1 and n_2 while $n_- = (n_1 \sqrt{g_{22}} + n_2 \sqrt{g_{11}})/(\sqrt{g_{11} + g_{22}})$ corresponds to a density mode which is sensitive to the sum of the single component densities. $\delta g \ll g_{11}, g_{22}$ yields $|\lambda_-| \ll |\lambda_+|$ which means n_-, and hence the density mode, corresponds to a soft mode while n_+, and hence the spin mode, corresponds to a hard mode, i. e. the latter is energetically more costly. Accordingly, we can assume that $n_+ = 0$ in the ground state. Therefore, close to the ground state the ratio of the single components densities is fixed to

$$\frac{n_2}{n_1} = \sqrt{\frac{g_{11}}{g_{22}}}, \tag{5.7}$$

relative density fluctuations are suppressed and both single component densities are proportional to the soft mode density [232]

$$n_- = n_1 \sqrt{\frac{g_{11} + g_{22}}{g_{22}}} = n_2 \sqrt{\frac{g_{11} + g_{22}}{g_{11}}}. \tag{5.8}$$

The suppression of the spin mode can also be intuitively understood: Due to the attractive interstate interaction with $|g_{12}| \approx \sqrt{g_{11} g_{22}}$ maximising the spatial overlap of the two spin components is energetically favorable. Consequently, we assume that both spin

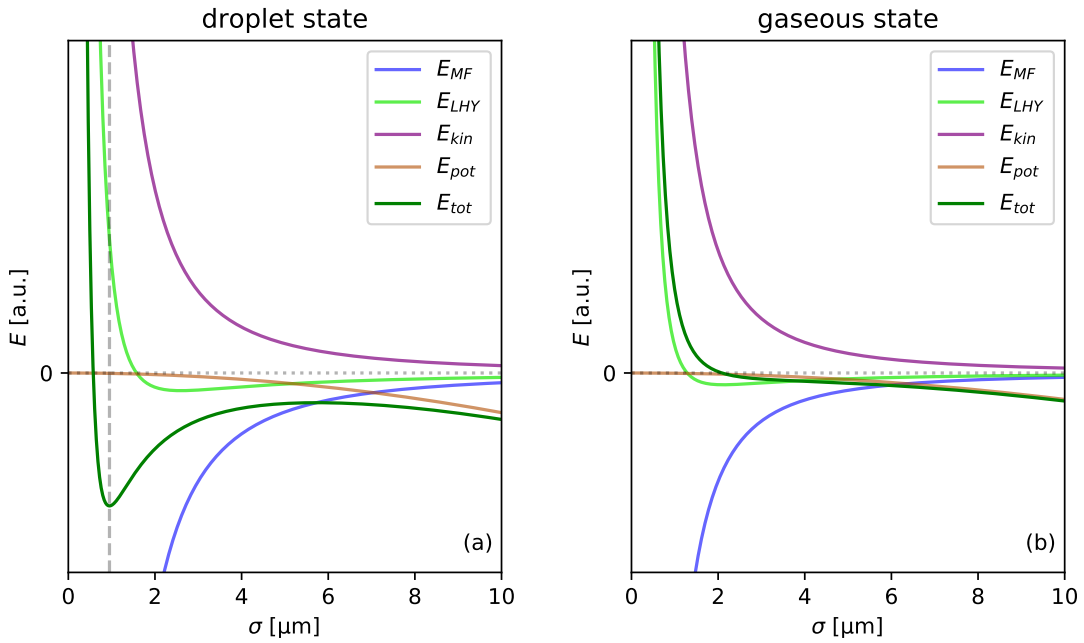

Figure 5.7: The system's total ground state energy E_{tot} as well as the individual energy contributions in dependence of the size σ of the atom cloud as derived by making a Gaussian ansatz for the spatial wave function (eq. 5.9) and integrating over the energy density (eq. 5.10) as explained in the main text. Exemplarily, the data for $\delta a = -4.3\,a_0$ and for the potential given by the central layer of the vertical lattice is shown for two different atom numbers. While the mean-field energy E_{MF} is purely attractive and the kinetic energy E_{kin} and the potential energy E_{pot} are purely repulsive, the structure of the LHY energy E_{LHY} is more complex featuring a minimum by itself. **(a)** For $N = 3 \cdot 10^3$ the attractive and repulsive forces balance each other at a finite value of σ. Hence, the total energy features a local minimum marked by the dashed vertical line. This stable state corresponds to a quantum droplet. **(b)** For $N = 2 \cdot 10^3$ the attractive and repulsive forces cannot compensate each other. The total energy is repulsive, i. e. the energy is minimised for $\sigma \to \infty$. The atom cloud cannot form a self-bound state, but continuously expands which corresponds to a gaseous state.

components occupy the same spatial mode, i. e. that we can describe them with a common spatial wave function for which we make a Gaussian ansatz

$$\phi(x,y) = \sqrt{n_0}\exp\left(-\frac{x^2}{2\sigma_x^2} - \frac{y^2}{2\sigma_y^2}\right) \tag{5.9}$$

with $n_0 = n_1 + n_2$. Proper normalisation yields $n_0 = N/(\pi\sigma_x\sigma_y)$. σ_x, σ_y correspond to the size of the atom cloud and will be used as variational parameters.

After choosing this trial wave function we proceed to the energy density functional, for which we consider four relevant contributions: the mean-field term ϵ_{MF} derived from equation 5.6 with $n_+ = 0$ and using equation 5.7 and 5.8, the LHY correction term ϵ_{LHY} [233], the kinetic term ϵ_{kin} which is determined by the curvature of the wave function and a potential term ϵ_{pot} describing the anti-trapping harmonic potential caused by the

vertical lattice:

$$\epsilon = \epsilon_{\mathrm{LHY}} + \epsilon_{\mathrm{MF}} + \epsilon_{\mathrm{kin}} + \epsilon_{\mathrm{pot}}$$

$$= \frac{1}{8\pi}\left(\frac{g_{11}+\sqrt{g_{11}g_{22}}}{1+\sqrt{g_{11}/g_{22}}}\right)^2 |\phi|^4 \ln\left(\sqrt{e}\, a_{ho,z}^2 \frac{g_{11}+\sqrt{g_{11}g_{22}}}{1+\sqrt{g_{11}/g_{22}}}|\phi|^2\right) \tag{5.10}$$

$$+ \delta g \frac{\sqrt{g_{22}/g_{11}}}{\left(1+\sqrt{g_{22}/g_{11}}\right)^2}|\phi|^4 + \frac{\hbar^2}{2m}|\nabla\phi|^2 - \frac{1}{2}m\left(\omega_x^2 x^2 + \omega_y^2 y^2\right)|\phi|^2$$

While the in-plane potential in the central layer is approximately radially symmetric, it becomes asymmetric in higher layers as it becomes confining along one of the axis (see sec. 4.6.4). The respective sign in the potential term is adapted according to the respective layer.

Combining equation 5.10 and 5.9 we can calculate the total energy of the 2D system $E_{\mathrm{tot}} = \int \epsilon\, d\mathbf{r}$ in dependence of the atom number N and the magnetic field B for variable size σ_x, σ_y of the atom cloud, where the magnetic field determines the 3D scattering lengths $a_{i,j}$ (see fig. 5.8) and thus the 2D coupling strengths $g_{i,j} = \hbar^2/m\sqrt{8\pi}a_{i,j}/a_{ho,z}$ [105]. By numerically minimising the energy with respect to σ_x, σ_y the ground state can be inferred: when there is a finite equilibrium density n_{eq} at which the attractive and repulsive forces corresponding to the energy terms balance each other, then E_{tot} features a minimum at a finite size σ_{eq} as shown in fig. 5.7 (a): The atom cloud is self-bound and this stable state corresponds to a quantum droplet. σ_{eq} can be extracted numerically and the equilibrium density can be determined from the normalisation condition of the wave function

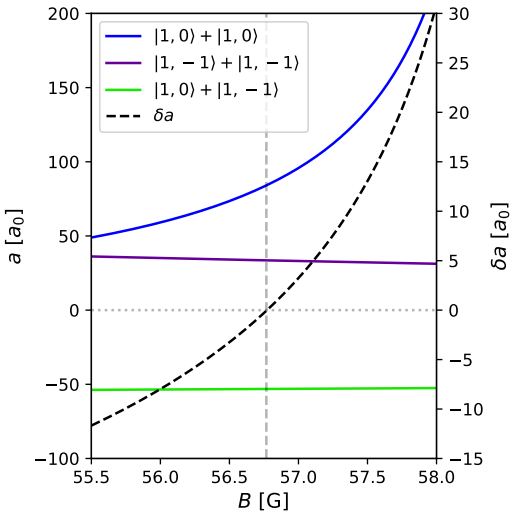

Figure 5.8: The scattering lengths a for the relevant spin combinations as well as $\delta a = a_{12} + \sqrt{a_{11}a_{22}}$ in dependence of the magnetic field B. The vertical dashed line denotes $\delta a = 0$. The data is taken from [8].

$$n_{eq} = \frac{N}{\pi\sigma_{eq,x}\sigma_{eq,y}}. \tag{5.11}$$

When on the other hand the repulsive terms outweigh the attractive ones, then the energy

is minimised for $\sigma \to \infty$ as shown in fig. 5.7 (b): The atom cloud is in a gaseous state and continuously expands. This analysis allows to derive the ground state phase diagram discussed in the following.

5.4.4 Droplets in free space

Let us first consider the free space case, i. e. neglecting the potential term.[12] The corresponding phase diagram, still assuming a 2D geometry, is shown in fig. 5.9. Remarkably, it exhibits only one phase. In the regime discussed here, i. e. $\delta g \ll g_{11}, g_{22}$ with $g_{11}, g_{22} > 0$ and $g_{12} < 0$, there is a droplet solution for every value of N and B, especially also for low atom numbers and for $\delta g > 0$ which contrasts the 3D case.

This can be understood when taking a closer look at the scalings of the individual energy terms for which we assume the symmetric case $\sigma = \sigma_x = \sigma_y$. In the 3D case the mean-field, LHY and kinetic energy all scale differently: $E_{\mathrm{MF,3D}} \propto N^2\sigma^{-3}$, $E_{\mathrm{LHY,3D}} \propto N^{5/2}\sigma^{-9/2}$ and $E_{\mathrm{kin,3D}} \propto N\sigma^{-2}$. For $\delta g < 0$ and low atom numbers the repulsive kinetic term becomes more relevant and together with the repulsive LHY term outweighs the attractive mean-field term resulting in a liquid-to-gas transition with decreasing atom number when reaching a critical atom number. For $\delta g > 0$ the mean-field term becomes repulsive and thus cannot balance the LHY and kinetic terms since they are repulsive as well. Consequently, there is no droplet solution for $\delta g > 0$.

In the 2D case on the other hand the situation is different. The 2D LHY correction term has the peculiar structure $E_{\mathrm{LHY}} \propto \sigma^{-2} \ln\left(c \cdot \sigma^{-2}\right)$ where $c > 0$ is constant for fixed N and B,[13] and the mean-field term E_{MF} as well as the kinetic term E_{kin} both scale with σ^{-2}.[14] Hence, the total energy exhibits the same structure as the LHY term, regardless of the sign of E_{MF}. Due to this structure the LHY term and thus also the total energy E_{tot} is not per se repulsive or attractive, but always features a local minimum at finite σ.[15]

This unique behaviour leads to a wide range of available equilibrium densities in the 2D case. The experimentally accessible densities, however, are subject to some limitations:

The main upper limit is given by three-body losses. For high densities scattering events involving three atoms cannot be neglected and losses occur due to three-body recombination processes which limits the lifetime of the atomic sample. The three-body

[12] Considering a box potential yields the same results as long as the box size is larger than σ_{eq} since a flat potential only results in a constant energy offset and hence features the same ground state.

[13] $c > 0$ as long as $g_{11}, g_{22} > 0$

[14] This corresponds to the scale invariance already mentioned in section 4.1.

[15] This can be easily seen from the derivative taking the form $\partial_\sigma E_{LHY} \propto -\sigma^{-3} \ln\left(c_2\sigma^{-2}\right)$ where $c_2 > 0$ is constant for fixed N and B and from $\partial_\sigma^2 E_{LHY}|_{\sigma=\sigma_{\mathrm{eq}}} > 0$.

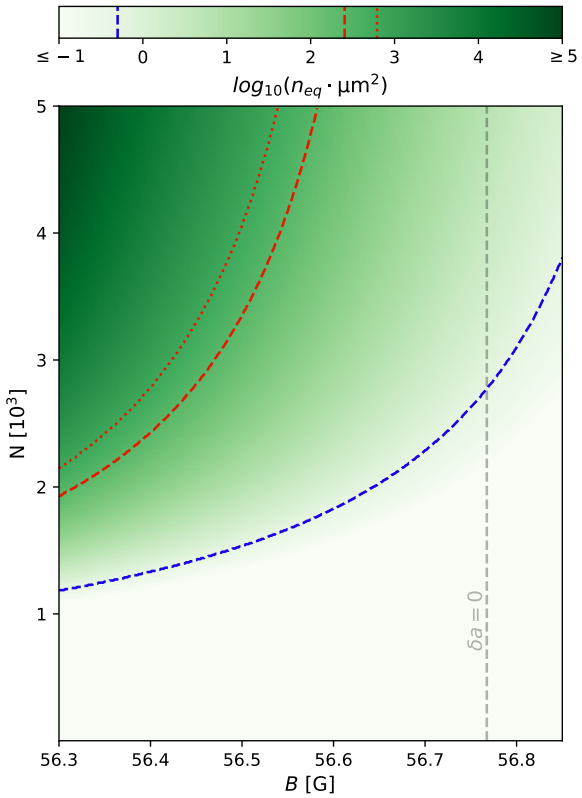

Figure 5.9: 2D ground state phase diagram for the free space case near the collapse threshold $\delta a = 0$. It exhibits only one phase since a droplet solution can be found for every parameter in the relevant regime $\delta a \ll a_{11}, a_{22}$. The logarithmic color scale illustrates the equilibrium density n_{eq} of the droplet in dependence of the magnetic field B and atom number N. Although a wide range of densities is covered, only a part of this range is experimentally accessible. The lower limit is given by the detection threshold (blue, dashed), upper limits are given by the validity of the 2D treatment (red, dotted) and by lifetime limitations due to three-body losses (red, dashed). Accordingly, the experimentally accessible regime is in between the dashed red and blue lines. Both upper limits have a weak dependency on B; the upper limits denoted in the color bar are averaged values. More details are given in the main text.

recombination rate K_3 has been measured in [75] for different spin compositions of K39 where it was found that K_3 for scattering events with three atoms in the $|1,0\rangle$ state is roughly two orders of magnitude higher than for any other spin combination of the states $|1,0\rangle$ and $|1,-1\rangle$. Thus, for estimating an upper density limit we neglect three-body recombination processes involving atoms in the $|1,-1\rangle$ state. With this approximation and assuming a constant volume[16] the three-body losses obey the differential equation $\dot{n}_{2,3\mathrm{D}} = K_3 n_{2,3\mathrm{D}}^3$ and hence, the 3D density $n_{2,3\mathrm{D}}(t)$ of atoms in the $|1,0\rangle$ state follows a power law. We then obtain an upper bound for the 3D density by demanding that

[16] Actually, with decreasing atom number the equilibrium size σ_{eq} of the droplet increases. Therefore, we underestimate the slope of the decreasing density by assuming a constant volume. Hence, we overestimate the three-body losses and therefore underestimate the lifetime.

$n_{2,3D}(t = 10\,\text{ms}) \geq 0.5 \cdot n_{2,3D}(t = 0)$ and convert the 3D density to a 2D density via the harmonic oscillator length of the tightly confined axis $n_2 = n_{2,3D} a_{ho,z}$.[17] Finally, by using equation 5.7 we derive an upper limit for the total 2D density.

An upper density limit is also given by the validity of the 2D treatment. To justify treating the droplet as two-dimensional and using the 2D LHY correction term the 2D confinement $a_{ho,z}$ needs to be smaller than the healing lengths ξ [234]. Since $\xi_i = 1/\sqrt{\tilde{g}_{ii} n_i}$ [105] depends on the coupling strength the corresponding density limit depends on B. However, in the relevant regime the upper density limit determined by the healing length is less strict than the upper density limit given by the three-body losses as can be seen in fig. 5.9.

A lower density limit is given by the signal-to-noise ratio. The lower the density, the lower the signal until it cannot be distinguished from noise. From this detection threshold we estimate a lower density limit of $0.5\,\mu\text{m}^{-2}$.

With these limits the parameter regime suitable for studying 2D droplets can be determined, the regime is illustrated in fig. 5.9. Note that this is an estimate which is based on static considerations. Further analysis including the dynamics by solving the extended Gross-Pitaevskii equation is beyond the scope of this thesis. Remarkably, the equilibrium density within the suitable regime covers more than two orders of magnitude, especially also very low densities in the order of a few atoms/μm^2 which would allow for much longer lifetimes than observed with 3D droplets.

Such low droplet densities can only be achieved in free space or flat potentials, though. The surface tension scales with $n_{eq}^{3/2}$ [209] and thus, becomes extremely low in these very dilute regimes. Hence, already a small anti-confinement as created by the vertical lattice providing the 2D confinement exerts a force that greatly exceeds the surface tension and can drive a liquid-to-gas transition.

5.4.5 Droplets in the central lattice layer

As discussed in section 4.6.4 the vertical lattice introduces an in-plane harmonic potential. In the central layer this potential is approximately radially symmetric and anti-confining with a trapping frequency of $\omega_{anti} \approx 2\pi \cdot 6\,\text{Hz}$. The presence of this anti-confinement significantly alters the phase diagram which now exhibits two phases as can be seen in fig. 5.10 (a). In contrast to the mean-field energy E_{MF} and the kinetic energy E_{kin}, both scaling with σ^{-2}, the potential energy scales with $E_{\text{pot}} \propto \sigma^2$. Consequently, the total

[17] In a truly two-dimensional system three-body losses are reduced due to the system's geometry. However, in our setup the scattering lengths a are small compared to the 2D confinement, $a \ll a_{ho,z}$, justifying the 3D treatment of the scattering processes.

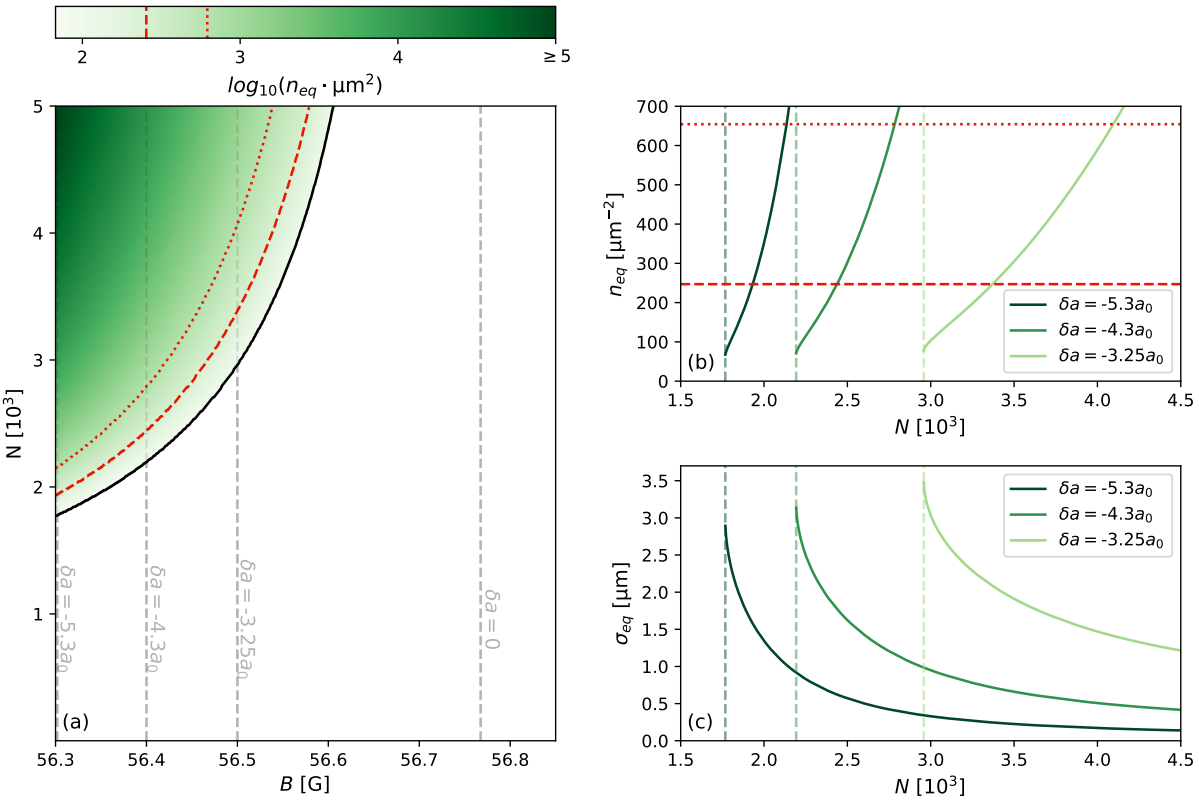

Figure 5.10: **(a)** 2D ground state phase diagram of an atomic sample prepared in the central layer of the vertical lattice which creates an approximately radially symmetric anti-confining potential with $\omega \approx 2\pi \cdot 6\,\mathrm{Hz}$. The logarithmic color scale illustrates the equilibrium density n_{eq} of the droplet in dependence of the magnetic field B and atom number N. White corresponds to a gaseous phase which does not support self-bound states. The critical atom number separating droplet and gaseous states is indicated by the black line. Also shown are upper density limits given by the validity of the 2D treatment (red, dotted) and by three-body losses (red, dashed). The upper limits exhibit a weak dependence on B, the values denoted in the color bar are the mean values. The experimentally accessible regime, in between the dashed red and the solid black line, is rather small. **(b)** Vertical cuts through (a). The respective critical atom number is denoted (vertical dashed lines) as well as the mean upper density limits given by validity of the 2D treatment (red, dotted) and by three-body losses (red, dashed). **(c)** The equilibrium size σ_{eq} of the droplet in dependence of atom number N for selected values of δa. Close to the respective critical atom number (vertical dashed lines), at which the liquid-to-gas transition takes place, the droplet size increases resulting in the decreasing density shown in (b).

energy E_{tot} no longer has the same structure as E_{LHY} and a gaseous phase can occur as was shown in fig. 5.7 (b). Due to $E_{pot} \propto \sigma^2$, while the other energy contributions decrease with increasing σ, the potential has little effect on small droplets, but a huge effect on large droplets. Since σ_{eq} increases with decreasing N as well as with decreasing δa (corresponding to increasing B) as can be seen in fig. 5.10 (c), the phase diagram for high values of N and δa is basically the same as in the free space case, while for decreasing N and δa the equilibrium density becomes smaller and smaller compared to the free space case until a critical value is reached, at which the droplet dissociates. This resembles the

3D case which also features a critical atom number N_c, below which there is no droplet solution.

The previously discussed upper density limits given by three-body losses and the healing length are not affected by the potential and due to the small trapping frequency these upper bounds follow nearly the same path in the parameter space as in the free space case. The lower limit on the other hand is now given by the critical atom number which is much stricter than the lower limit determined by the signal-to-noise ratio. Thus, the parameter regime and the density regime suitable for studying 2D droplets are rather small as illustrated in fig. 5.10 (a).

The achievable density and hence the lifetime is in the same order as observed for 3D droplets. To further prolong the lifetime it is favorable to use lower values of δa, i. e. a higher magnetic field. Due to the three-body losses the atom number axis also corresponds to a time axis[18] and as can be seen in fig. 5.10 (b) the slope of $n_{eq}(N)$ is less steep for decreasing δa, i. e. for the same initial density a higher atom number range is covered before the critical atom number is reached. Consequently, for the same initial density the lifetime is higher for lower values of δa. This regime is also favorable in terms of the droplet size. As can be seen in fig. 5.10 (c) σ increases with decreasing δa yielding a higher imaging resolution of the droplet.

Furthermore, the lifetime could be improved by reducing the critical atom number: Although the phase diagrams of 2D droplets in an anti-confining potential resembles the 3D case, the mechanism introducing the critical atom number is very different. While in the 3D case the liquid-to-gas transition is driven by the enhanced role of the kinetic energy for low atom numbers, in the 2D case the phase transition is driven by the anti-confinement which becomes more relevant for increasing σ_{eq}. The significant difference is that the kinetic energy depends, apart from N and σ, only on the atomic mass. The potential energy on the other hand also depends on the trapping frequency ω_{anti}, i. e. an external parameter which provides us with a handle on the critical atom number and hence on the corresponding lower density limit. As illustrated in fig. 5.11 reducing the anti-confinement allows access to lower droplet densities and thus to longer lifetimes.

However, reducing the anti-confinement would require a lower lattice power, which would loosen the 2D confinement, or an additional confining potential that is fine-tuned to compensate the anti-confinement. Another, much simpler method to reduce the lower density limit is to prepare the system in a non-central layer.

[18] Since the atom number decreases over time, the atom number axis corresponds to an inverse time axis. Also, the relation is non-linear.

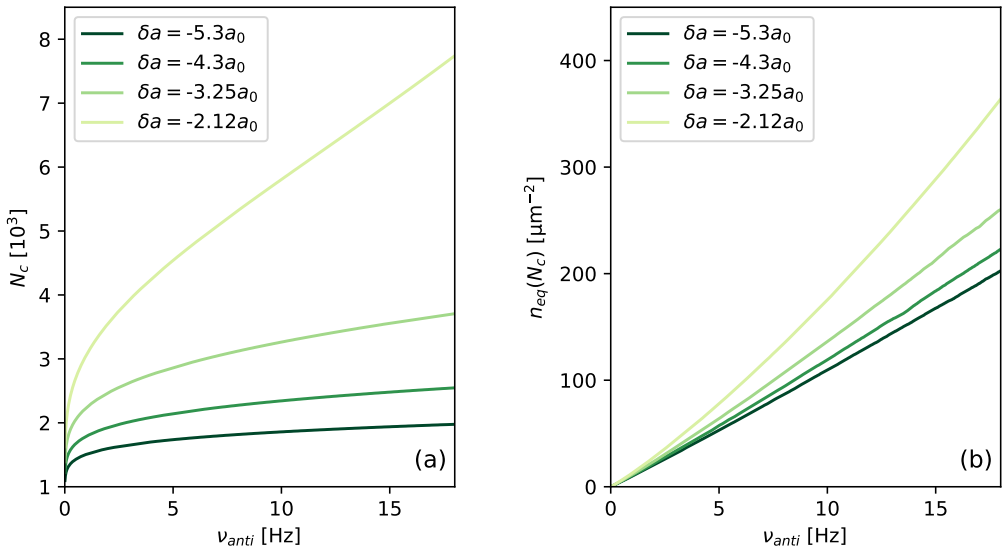

Figure 5.11: Critical atom number N_c (a) and the corresponding equilibrium density $n_{eq}(N_c)$ acting as a lower density limit (b) in dependence of the physical trapping frequency ν_{anti} corresponding to a radially symmetric harmonic anti-confinement for selected values of δa. For flat potentials $\nu_{\text{anti}} \to 0$ the critical atom number vanishes $N_c \to 0$ and the corresponding density continuously goes to zero $n_{eq}(N_c) \to 0$. Hence, the achievable lifetime can be increased by reducing the anti-confinement.

5.4.6 Droplets in non-central lattice layers

In contrast to the central layer, whose in-plane potential is approximately radially symmetric, the in-plane potential of non-central layers, e. g. the first layer, is not only asymmetric, but anti-confining along one axis and confining along the other axis (see section 4.6.4).

Due to $E_{pot} \propto (\omega_y^2\sigma_y^2 - \omega_x^2\sigma_x^2)$ this mainly affects the part of the phase diagram with larger droplet sizes, i. e. lower densities, as can be seen in fig. 5.12,(a), which is exactly the regime we are interested in. Compared to the central layer, the critical atom number is shifted to lower values, increasing the suitable parameter regime and decreasing the lower limit for achievable droplet densities. Both the increased atom number range covered within the suitable regime as well as the lower density improve the lifetime of the droplet compared to the central layer.

Furthermore, the asymmetry of the potential results in asymmetric, or more precisely elliptical, droplets. Since the potential becomes more relevant with increasing σ and hence decreasing N, the asymmetry becomes more pronounced towards the critical atom number. So as shown in fig. 5.12 (c) over time and hence with decreasing atom number, the droplet becomes more and more elongated until the critical atom number is reached and the droplet dissociates.

While the lower density limit decreases from central to first layer, it barely changes when going from first to second or even higher layers. The critical atom number on the

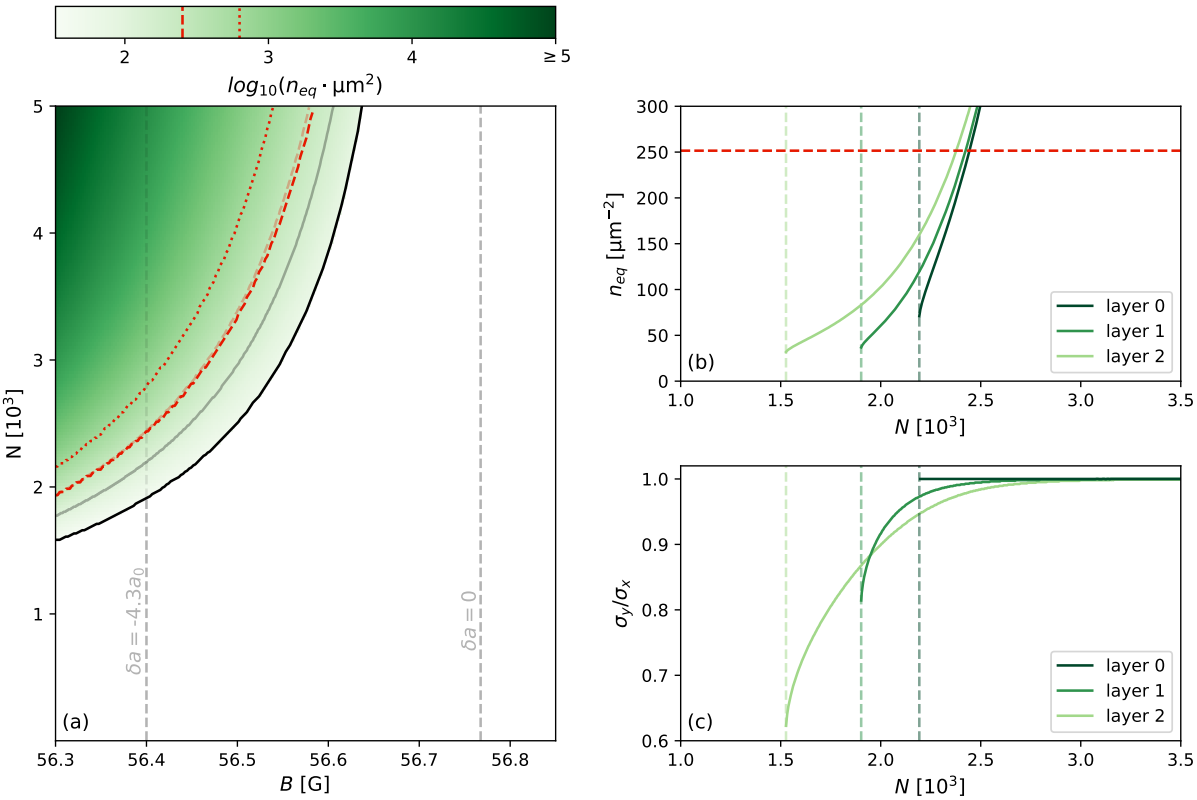

Figure 5.12: **(a)** 2D ground state phase diagram of an atomic sample prepared in the first layer of the vertical lattice. The corresponding in-plane potential is asymmetric as it is anti-confining along one axis with $\omega_x \approx 2\pi \cdot 5.8\,\mathrm{Hz}$ and confining along the other axis with $\omega_y \approx 2\pi \cdot 8.6\,\mathrm{Hz}$. The logarithmic color scale illustrates the equilibrium density n_{eq} of the droplet in dependence of the magnetic field B and atom number N. White corresponds to a gaseous phase which does not support self-bound states. The critical atom number separating droplet and gaseous states is indicated by the black line. Also shown are upper density limits given by the validity of the 2D treatment (red, dotted) and by three-body losses (red, dashed). The upper limits exhibit a weak dependence on B; the values denoted in the color bar are the mean values. The experimentally suitable parameter regime, in between the dashed red and black solid lines, is substantially larger than for the central layer. For comparison the suitable parameter regime for the central layer is denoted in fainter colors as well. **(b)** Vertical cuts through the phase diagram for central, first and second layer at $\delta a = -4.3\,a_0$. Denoted is the respective critical atom number (vertical dashed lines) as well as the mean upper density limit given by three-body losses (red dashed). With non-central layers lower densities and hence longer lifetimes can be achieved compared to the central layer. Additionally, the critical atom number decreases with higher layers which increases the accessible atom number range and hence further improves the lifetime. While the lower density effect saturates already after the first layer, the lifetime still improves with higher layers due to the atom number range effect. **(c)** The aspect ratio σ_y/σ_x of the droplet in dependence of atom number N for different lattice layers at $\delta a = -4.3\,a_0$. For non-central layers the droplet becomes more and more elliptical close to the critical atom number (vertical dashed lines) due to the asymmetry of the potential.

other hand further decreases. While this suggests that using outer layers is advantageous, this is not necessarily the case. The higher the layer, the lower the vertical trapping frequency determining the 2D confinement. That means the choice of the layer is a trade-off between droplet lifetime and tightness of the 2D confinement. The highest gain is

achieved when switching from central to first layer since in that case the vertical trapping frequency barely changes while the lifetime is improved by both, a lower critical atom number as well as by a reduced lower density limit.

5.4.7 Summary

In a regime with nearly vanishing mean-field energy, quantum fluctuations become relevant and can balance the mean-field term leading to the formation of self-bound objects. These so-called quantum droplets are a direct result of beyond mean-field effects and hence enable us to improve our understanding of beyond mean-field physics.

In comparison to the 3D case, the 2D droplet regime is less restrained due to the peculiar structure of the two-dimensional LHY correction term describing the quantum fluctuations: A droplet solution exists as long as the intrastate interaction is weakly repulsive and the interstate interaction weakly attractive. This holds true in free space and flat potentials, while the presence on an anti-confinement introduces a critical atom number below which a gaseous phase occurs which gives a lower bound for the achievable density.

One of the main experimental challenges is the droplet lifetime which is limited by three-body losses due to the rather high density compared to typical quantum gases. In our experimental setup we expect densities in the order of $\sim 100\,\mu\text{m}^{-2}$ when preparing the sample in the central layer of the vertical lattice which is comparable to the densities observed for 3D droplets. This could be further improved by instead preparing the sample in the first layer of the vertical lattice which is expected to reduce the density by a factor of ~ 2.

Chapter 6

Conclusion and outlook

In this thesis, the experimental realisation of a degenerate two-dimensional Bose gas using K39 was presented which exhibits the rare combination of three key features:

- the ability to prepare different spin states and especially to create *spin mixtures*. To study binary spin mixtures we typically prepare the sample in the $|^2S_{1/2}, F = 1, m_F = -1\rangle$ state and then drive an RF transition to transfer a part of the atoms into the $|^2S_{1/2}, F = 1, m_F = 0\rangle$ state. Both spin states can be imaged individually.

- *highly tunable interaction strength.* K39 exhibits several intra- as well as interstate Feshbach resonances within the $|^2S_{1/2}, F = 1\rangle$ manifold that allow to tune the interaction strength from weakly to strongly interacting as well as from attractive to repulsive.

- *high resolution imaging.* The experimental apparatus features two in-vacuo microscope objectives with a high numerical aperture of 0.75 corresponding to a diffraction-limited resolution of $\sim 0.62\,\mu\text{m}$ at the imaging wavelength of $\sim 767\,\text{nm}$.

In the beginning of this work, we employed fermionic potassium, K40, and used an all-optical cooling scheme to prepare small Fermi-Hubbard systems created by a 2x2 tweezer array. We were following a bottom-up approach by starting with this fundamental building block that was meant to be gradually extended in order to observe the emergence of many-body effects. In the course of this thesis, we implemented the reliable detection of single atoms trapped within the optical tweezers. Furthermore, to ensure a rapid repetition rate of the experiment, we employed Raman sideband cooling as a final cooling step to reach degeneracy. However, despite thorough optimisation and investigation of potential issues, we were not able to exceed a 3D ground state fraction of $\sim 40\%$.

Throughout this thesis, it is then discussed how the experimental setup was re-designed and re-built to create two-dimensional bosonic bulk systems using bosonic potassium K39. This mainly involves the experimental realisation of a K39 BEC via evaporation, including an accordingly modified experimental sequence and newly implemented dipole traps, as well as the subsequent transfer from the three-dimensional into the quasi-two-dimensional regime which is realised via a tight vertical confinement provided by a blue-detuned one-dimensional optical lattice. The experimental work furthermore covers modifications of the laser system in order to cool K39 rather than K40 and general improvements, such as reducing the decay time of induced eddy currents, implementing a modulation transfer spectroscopy for the D1 locking scheme and improving the stability of the air conditioning, not all of them discussed in this thesis. As a result the experimental setup allows to create a degenerate two-dimensional Bose gas of $\sim 3 \cdot 10^3$ atoms at a temperature of $\sim 50\,\mathrm{nK}$ corresponding to $\sim 0.2\,T_{\mathrm{BKT}}$. The two-dimensional system is harmonically confined and for our parameters, especially for the low temperature, we expect its character to be more that of a condensate rather than that of a quasi-condensate due to the system's finite size.

Measurements on 2D polarons performed by M. Schlederer [76] with this experimental setup are briefly presented, highlighting how the key features of the setup were utilised. Finally, a particularly interesting regime near the collapse threshold of a spin mixture is discussed that would allow for the formation of two-dimensional quantum droplets as a direct beyond mean-field effect. The peculiar shape of the two-dimensional LHY correction term, which stabilises the droplet against collapse, results in a much broader droplet regime in two dimensions compared to the three-dimensional case and suitable parameter regimes for studying two-dimensional droplets in our experimental setup were found.

A possible next step is to follow this promising research direction, starting with the creation of two-dimensional droplets which can be observed by their self-bound nature. It would then be interesting to map out the phase diagram and to compare it to the three-dimensional case. Further studies could focus on the excitation modes which are difficult to observe in three-dimensional droplets due to short lifetimes, while two-dimensional droplets are expected to exhibit longer lifetimes due to lower achievable densities. Furthermore, when implementing flexible in-plane potentials, e. g. via a DMD, one could realise a flat potential and observe dimensionality-driven gas-to-liquid transitions by preparing a vertically confined, but three-dimensional atom cloud in the mean-field stable regime, $\delta a > 0$, and then increasing the vertical confinement to enter the quasi-two-dimensional regime where, in contrast to the three-dimensional case, a droplet solution exists. A flexible in-plane potential is also expected to enable the realisation of potential-driven

gas-to-liquid transitions. Exploiting the high numerical aperture of our microscope objectives not only for high-resolution imaging, but also for high-resolution potential shaping would allow us to create a weak harmonic anti-confinement on the length scale of the two-dimensional droplets surrounded by an otherwise flat potential. In a suitable parameter regime, the two-dimensional atomic sample should be in a gaseous phase in the region of the anti-confinement and hence expand, but is expected to liquify as soon as it reaches the flat potential.

In addition, our experimental setup allows to study a variety of alternative research topics. An exciting possibility is to build on the previously discussed polaron measurements. The high numerical aperture of our microscope objectives enables the creation of small tweezers that provide localised light shifts for the transfer into the impurity state. This would enable a flexible spatial selection for the polaron formation which could be utilised e. g. for studying polaron-polaron interaction.

Another fascinating research direction is to study collapse dynamics. In contrast to the weak collapse observed in three-dimensions [207], a two-dimensional system is expected to undergo a strong collapse [235, 236]. Exploiting the capabilities of our experimental setup one could furthermore investigate how the collapse dynamics are affected by the presence of a second spin state with variable interstate interactions.

To give a final example, one could also pursue the study of turbulence which is an ongoing research topic. Only recently, Karailiev *et al.* [185] demonstrated an inverse turbulent-wave cascade in a spin-polarised two-dimensional Bose gas. Studying turbulence with spin mixtures gives rise to a variety of phenomena enabled by the interface between the two fluids [237] such as the Kelvin-Helmholtz instability [238, 239], the Rayleigh-Taylor instability [240, 241] and the Richtmyer-Meshkov instability [242].

In summary, the ability to study degenerate two-dimensional bosonic bulk systems with tunable interactions and with the possibilty to employ spin mixtures should bring a large range of fascinating quantum many-body phenomena into reach.

Publications

The following research article has been published in the course of this thesis:

- *Single-Atom Counting in a Two-Color Magneto-Optical Trap*
  M. Schlederer, A. Mozdzen, T. Lompe, and H. Moritz,
  Physical Review A, 103(**3**), (2021).

Bibliography

[1] M. H. Anderson, J. R. Ensher, M. R. Matthews, C. E. Wieman and E. A. Cornell. *Observation of Bose-Einstein Condensation in a Dilute Atomic Vapor.* Science **269**(5221):198 (1995).

[2] K. B. Davis, M. O. Mewes, M. R. Andrews, N. J. van Druten, D. S. Durfee, D. M. Kurn and W. Ketterle. *Bose-Einstein Condensation in a Gas of Sodium Atoms.* Phys. Rev. Lett. **75**:3969 (1995).

[3] B. DeMarco and D. S. Jin. *Onset of Fermi Degeneracy in a Trapped Atomic Gas.* Science **285**(5434):1703 (1999).

[4] C. J. Myatt, E. A. Burt, R. W. Ghrist, E. A. Cornell and C. E. Wieman. *Production of Two Overlapping Bose-Einstein Condensates by Sympathetic Cooling.* Phys. Rev. Lett. **78**:586 (1997).

[5] C. Baroni, G. Lamporesi and M. Zaccanti. *Quantum Mixtures of Ultracold Atomic Gases.* arXiv preprint arXiv:2405.14562 (2024).

[6] T.-L. Ho and V. B. Shenoy. *Binary Mixtures of Bose Condensates of Alkali Atoms.* Phys. Rev. Lett. **77**:3276 (1996).

[7] D. Petrov. *Quantum Mechanical Stabilization of a Collapsing Bose-Bose Mixture.* Physical Review Letters **115**(15) (2015).

[8] C. R. Cabrera, L. Tanzi, J. Sanz, B. Naylor, P. Thomas, P. Cheiney and L. Tarruell. *Quantum liquid droplets in a mixture of Bose-Einstein condensates.* Science **359**(6373):301–304 (2018).

[9] A. G. Truscott, K. E. Strecker, W. I. McAlexander, G. B. Partridge and R. G. Hulet. *Observation of Fermi Pressure in a Gas of Trapped Atoms.* Science **291**(5513):2570 (2001).

[10] F. Schreck, L. Khaykovich, K. L. Corwin, G. Ferrari, T. Bourdel, J. Cubizolles and C. Salomon. *Quasipure Bose-Einstein Condensate Immersed in a Fermi Sea.* Physical Review Letters **87**(8) (2001).

[11] C. Chin, R. Grimm, P. Julienne and E. Tiesinga. *Feshbach resonances in ultracold gases.* Rev. Mod. Phys. **82**:1225 (2010).

[12] S. Inouye, M. R. Andrews, J. Stenger, H.-J. Miesner, D. M. Stamper-Kurn and W. Ketterle. *Observation of Feshbach resonances in a Bose–Einstein condensate.* Nature **392**:151 (1998).

[13] P. Courteille, R. S. Freeland, D. J. Heinzen, F. A. van Abeelen and B. J. Verhaar. *Observation of a Feshbach Resonance in Cold Atom Scattering.* Phys. Rev. Lett. **81**:69 (1998).

[14] S. L. Cornish, N. R. Claussen, J. L. Roberts, E. A. Cornell and C. E. Wieman. *Stable 85Rb Bose-Einstein Condensates with Widely Tunable Interactions.* Physical Review Letters **85**(9):1795–1798 (2000).

[15] C. A. Regal, M. Greiner and D. S. Jin. *Observation of Resonance Condensation of Fermionic Atom Pairs.* Physical Review Letters **92**(4) (2004).

[16] M. W. Zwierlein, C. A. Stan, C. H. Schunck, S. M. F. Raupach, A. J. Kerman and W. Ketterle. *Condensation of Pairs of Fermionic Atoms near a Feshbach Resonance.* Physical Review Letters **92**(12) (2004).

[17] M. Bartenstein, A. Altmeyer, S. Riedl, S. Jochim, C. Chin, J. H. Denschlag and R. Grimm. *Crossover from a Molecular Bose-Einstein Condensate to a Degenerate Fermi Gas.* Physical Review Letters **92**(12) (2004).

[18] T. Bourdel, L. Khaykovich, J. Cubizolles, J. Zhang, F. Chevy, M. Teichmann, L. Tarruell, S. J. J. M. F. Kokkelmans and C. Salomon. *Experimental Study of the BEC-BCS Crossover Region in Lithium 6.* Physical Review Letters **93**(5) (2004).

[19] D. M. Stamper-Kurn, M. R. Andrews, A. P. Chikkatur, S. Inouye, H.-J. Miesner, J. Stenger and W. Ketterle. *Optical Confinement of a Bose-Einstein Condensate.* Phys. Rev. Lett. **80**:2027 (1998).

[20] M. Greiner, O. Mandel, T. Esslinger, T. W. Hänsch and I. Bloch. *Quantum phase transition from a superfluid to a Mott insulator in a gas of ultracold atoms.* Nature **415**:39 (2002).

[21] T. Kinoshita, T. Wenger and D. S. Weiss. *Observation of a One-Dimensional Tonks-Girardeau Gas.* Science **305**(5687):1125 (2004).

[22] B. Paredes, A. Widera, V. Murg, O. Mandel, S. Fölling, I. Cirac, G. V. Shlyapnikov, T. W. Hänsch and I. Bloch. *Tonks–Girardeau gas of ultracold atoms in an optical lattice.* Nature **429**:277 (2004).

[23] Z. Hadzibabic, P. Krüger, M. Cheneau, B. Battelier and J. Dalibard. *Berezinskii–Kosterlitz–Thouless crossover in a trapped atomic gas.* Nature **441**(7097):1118–1121 (2006).

[24] W. S. Bakr, J. I. Gillen, A. Peng, S. Fölling and M. Greiner. *A quantum gas microscope for detecting single atoms in a Hubbard-regime optical lattice.* Nature **462**(7269):74–77 (2009).

[25] P. Wieburg. *A Novel Fermionic Quantum Gas Microscope: Concept, Design and Construction.* Ph.D. thesis, University of Hamburg (2019).

[26] R. Vollmer. *Aufbau und Charakerisierung eines RF-Setups zur Spinmanipulation ultrakalter Quantengase.* bachelor thesis, Universität Hamburg (2016).

[27] B. DeMarco. *Quantum Behavior of an Atomic Fermi Gas.* Ph.D. thesis, University of Colorado (2001).

[28] T. G. Tiecke. *Properties of Potassium* (2019). (accessed on 22024-06-12).

[29] C. Darsow-Fromm. *Laserkühlung von ^{39}K und ^{40}K Atomen mit einer Kombination aus zwei- und dreidimensionaler magneto-optischer Falle.* master thesis, Universität Hamburg (2016).

[30] G. Dudle, N. Sagna, P. Berthoud and P. Thomann. *Anisotropic magneto-optical trapping of atoms: capture efficiency and induced drift velocities.* Journal of Physics B: Atomic, Molecular and Optical Physics **29**(20):4659 (1996).

[31] J. Catani, P. Maioli, L. De Sarlo, F. Minardi and M. Inguscio. *Intense slow beams of bosonic potassium isotopes.* Phys. Rev. A **73**:033415 (2006).

[32] E. L. Raab, M. Prentiss, A. Cable, S. Chu and D. E. Pritchard. *Trapping of Neutral Sodium Atoms with Radiation Pressure.* Phys. Rev. Lett. **59**:2631 (1987).

[33] G. Salomon, L. Fouché, P. Wang, A. Aspect, P. Bouyer and T. Bourdel. *Gray-molasses cooling of 39K to a high phase-space density.* Europhysics Letters **104**(6):63002 (2014).

[34] D. R. Fernandes. *Trapping and cooling of fermionic alkali atoms to quantum degeneracy. Sub-Doppler cooling of Potassium-40 and Lithium-6 in gray molasses.* Ph.D. thesis, Université Pierre at Marie Curie (2014).

[35] M. Tarnowski. *Implementation and Characterization of a Gray Molasses and of Tunable Hexagonal Optical Lattices for ^{40}K.* master thesis, Universität Hamburg (2015).

[36] G. Grynberg and J.-Y. Courtois. *Proposal for a Magneto-Optical Lattice for Trapping Atoms in Nearly-Dark States.* Europhysics Letters **27**(1):41 (1994).

[37] D. R. Fernandes, F. Sievers, N. Kretzschmar, S. Wu, C. Salomon and F. Chevy. *Sub-Doppler laser cooling of fermionic 40K atoms in three-dimensional gray optical molasses.* Europhysics Letters **100**(6):63001 (2012).

[38] A. T. Grier, I. Ferrier-Barbut, B. S. Rem, M. Delehaye, L. Khaykovich, F. Chevy and C. Salomon. *Λ-enhanced sub-Doppler cooling of lithium atoms in D_1 gray molasses.* Phys. Rev. A **87**:063411 (2013).

[39] K. N. Jarvis, J. A. Devlin, T. E. Wall, B. E. Sauer and M. R. Tarbutt. *Blue-Detuned Magneto-Optical Trap.* Phys. Rev. Lett. **120**:083201 (2018).

[40] J. Hubbard. *Electron correlations in narrow energy bands.* Proc. R. Soc. Lond. A **276**:238 (1963).

[41] W. P. Su, J. R. Schrieffer and A. J. Heeger. *Solitons in Polyacetylene.* Phys. Rev. Lett. **42**:1698 (1979).

[42] E. J. Meier, F. A. An and B. Gadway. *Observation of the topological soliton state in the Su–Schrieffer–Heeger model.* Nature Communications **7**(1) (2016).

[43] J. Struck, C. Ölschläger, M. Weinberg, P. Hauke, J. Simonet, A. Eckardt, M. Lewenstein, K. Sengstock and P. Windpassinger. *Tunable Gauge Potential for Neutral and Spinless Particles in Driven Optical Lattices.* Phys. Rev. Lett. **108**:225304 (2012).

[44] P. G. Harper. *Single Band Motion of Conduction Electrons in a Uniform Magnetic Field.* Proceedings of the Physical Society. Section A **68**(10):874 (1955).

[45] D. R. Hofstadter. *Energy levels and wave functions of Bloch electrons in rational and irrational magnetic fields.* Phys. Rev. B **14**:2239 (1976).

[46] M. Aidelsburger, M. Atala, M. Lohse, J. T. Barreiro, B. Paredes and I. Bloch. *Realization of the Hofstadter Hamiltonian with Ultracold Atoms in Optical Lattices.* Physical Review Letters **111**(18) (2013).

[47] M. E. Tai, A. Lukin, M. Rispoli, R. Schittko, T. Menke, D. Borgnia, P. M. Preiss, F. Grusdt, A. M. Kaufman and M. Greiner. *Microscopy of the interacting Harper–Hofstadter model in the two-body limit.* Nature **546**(7659):519 (2017).

[48] M. Harland, M. I. Katsnelson and A. I. Lichtenstein. *Plaquette valence bond theory of high-temperature superconductivity.* Physical Review B **94**(12) (2016).

[49] A. Ashkin. *Trapping of Atoms by Resonance Radiation Pressure.* Phys. Rev. Lett. **40**:729 (1978).

[50] S. Chu, J. E. Bjorkholm, A. Ashkin and A. E. Cable. *Experimental Observation of Optically Trapped Atoms.* Phys. Rev. Lett. **57**:314 (1986).

[51] A. Ashkin, J. M. Dziedzic, J. E. Bjorkholm and S. Chu. *Observation of a single-beam gradient force optical trap for dielectric particles.* Opt. Lett. **11**:288 (1986).

[52] C. Monroe, D. M. Meekhof, B. E. King, S. R. Jefferts, W. M. Itano, D. J. Wineland and P. Gould. *Resolved-Sideband Raman Cooling of a Bound Atom to the 3D Zero-Point Energy.* Phys. Rev. Lett. **75**:4011 (1995).

[53] A. M. Kaufman, B. J. Lester and C. A. Regal. *Cooling a Single Atom in an Optical Tweezer to Its Quantum Ground State.* Phys. Rev. X **2**:041014 (2012).

[54] J. D. Thompson, T. G. Tiecke, A. S. Zibrov, V. Vuletić and M. D. Lukin. *Coherence and Raman Sideband Cooling of a Single Atom in an Optical Tweezer.* Phys. Rev. Lett. **110**:133001 (2013).

[55] A. Mozdzen. *Entwicklung eines optischen Aufbaus zur Realisierung von kleinen Fermi-Hubbard Systemen.* master thesis, Universität Hamburg (2018).

[56] T. Grünzweig, A. Hilliard, M. McGovern and M. F. Andersen. *Near-deterministic preparation of a single atom in an optical microtrap.* Nature Physics **6**(12):951 (2010).

[57] B. J. Lester, N. Luick, A. M. Kaufman, C. M. Reynolds and C. A. Regal. *Rapid Production of Uniformly Filled Arrays of Neutral Atoms.* Phys. Rev. Lett. **115**:073003 (2015).

[58] A. Kaufman. *Laser cooling atoms to indistinguishability: Atomic Hong-Ou-Mandel interference and entanglement through spin exchange.* Ph.D. thesis, University of Colorado (2015).

[59] C. Tuchendler, A. M. Lance, A. Browaeys, Y. R. P. Sortais and P. Grangier. *Energy distribution and cooling of a single atom in an optical tweezer.* Physical Review A **78**(3) (2008).

[60] M. A. Norcia, A. W. Young and A. M. Kaufman. *Microscopic Control and Detection of Ultracold Strontium in Optical-Tweezer Arrays.* Phys. Rev. X **8**:041054 (2018).

[61] Y. Yu, N. R. Hutzler, J. T. Zhang, L. R. Liu, J. D. Hood, T. Rosenband and K.-K. Ni. *Motional-ground-state cooling outside the Lamb-Dicke regime.* Phys. Rev. A **97**:063423 (2018).

[62] L. W. Cheuk, M. A. Nichols, M. Okan, T. Gersdorf, V. V. Ramasesh, W. S. Bakr, T. Lompe and M. W. Zwierlein. *Quantum-Gas Microscope for Fermionic Atoms.* Phys. Rev. Lett. **114**:193001 (2015).

[63] N. Lorenz, L. Festa, L.-M. Steinert and C. Gross. *Raman sideband cooling in optical tweezer arrays for Rydberg dressing.* SciPost Physics **10**(3) (2021).

[64] N. Lorenz. *A Rydberg Tweezer Platform with Potassium Atoms.* Ph.D. thesis, Ludwig-Maximilians-Universität München (2021).

[65] A. Kramida, Yu. Ralchenko, J. Reader and and NIST ASD Team. NIST Atomic Spectra Database (ver. 5.11), [Online]. Available: `https://physics.nist.gov/asd` [2024, June 13]. National Institute of Standards and Technology, Gaithersburg, MD. (2023).

[66] American Elements: The Materials Science Manufacturer. *Francium.* Online: https://www.americanelements.com/francium.html (accessed on 2024-06-11).

[67] M. Horvath, S. Dhar, A. Das, M. D. Frye, Y. Guo, J. M. Hutson, M. Landini and H.-C. Nägerl. *Bose-Einstein condensation of non-ground-state caesium atoms.* Nature Communications **15**(3739) (2024).

[68] N. R. Claussen, S. L. Cornish, J. L. Roberts, E. A. Cornell and C. E. Wieman. *85Rb BEC near a Feshback resonance.* AIP Conference Proceedings **551**(1):325 (2001).

[69] A. Marte, T. Volz, J. Schuster, S. Dürr, G. Rempe, E. G. M. van Kempen and B. J. Verhaar. *Feshbach Resonances in Rubidium 87: Precision Measurement and Analysis.* Physical Review Letters **89**(28) (2002).

[70] R. G. Hulet, J. H. V. Nguyen and R. Senaratne. *Methods for preparing quantum gases of lithium.* Review of Scientific Instruments **91**(1) (2020).

[71] S. E. Pollack, D. Dries and R. G. Hulet. *Universality in Three- and Four-Body Bound States of Ultracold Atoms.* Science **326**(5960):1683–1685 (2009).

[72] M. Zaccanti, B. Deissler, C. D'Errico, M. Fattori, M. Jona-Lasinio, S. Müller, G. Roati, M. Inguscio and G. Modugno. *Observation of an Efimov spectrum in an atomic system.* Nature Physics **5**(8):586–591 (2009).

[73] M. Fischer. *A Matter-Wave Microscope for Lithium Atoms in a Tunable Optical Lattice.* Ph.D. thesis, University of Hamburg (2023).

[74] Z. A. Geiger. *An Apparatus for Dynamical Quantum Emulation Using Ultracold Lithium.* Ph.D. thesis, University of California Santa Barbara (2018).

[75] C. R. C. Córdova. *Quantum liquid droplets in a mixture of Bose-Einstein condensates.* Ph.D. thesis, UPC, Institut de Ciències Fotòniques (2018).

[76] M. Schlederer. *High Resolution Imaging of Quantum Gases: From Counting Fermions in Optical Tweezers to Tracking Impurities in 2D Bose Gases.* Ph.D. thesis, University of Hamburg (2024).

[77] T. Loftus, C. A. Regal, C. Ticknor, J. L. Bohn and D. S. Jin. *Resonant Control of Elastic Collisions in an Optically Trapped Fermi Gas of Atoms.* Phys. Rev. Lett. **88**:173201 (2002).

[78] T. Hänsch and A. Schawlow. *Cooling of gases by laser radiation.* Optics Communications **13**(1):68 (1975).

[79] D. Wineland and H. Dehmelt. *Proposed $10^{14}\Delta\nu < \nu$ laser fluorescence spectroscopy on Tl^{+} mono-ion oscillator III.* Bull. Am. Phys. Soc. **20**(4):637 (1975).

[80] D. J. Wineland, R. E. Drullinger and F. L. Walls. *Radiation-Pressure Cooling of Bound Resonant Absorbers.* Phys. Rev. Lett. **40**:1639 (1978).

[81] W. Neuhauser, M. Hohenstatt, P. Toschek and H. Dehmelt. *Optical-Sideband Cooling of Visible Atom Cloud Confined in Parabolic Well.* Phys. Rev. Lett. **41**:233 (1978).

[82] J. A. Devlin and M. R. Tarbutt. *Three-dimensional Doppler, polarization-gradient, and magneto-optical forces for atoms and molecules with dark states.* New Journal of Physics **18**(12):123017 (2016).

[83] T. Murase, S. Nakagawa, S. Kinoshita, A. Shimizu, S. Okamura, M. Isobe, G. Xiong, Y. Xu, H. Liu, H. Liu and D. Yin. *Eddy current analyses for vacuum vessel of CFQS quasi-axisymmetric stellarator.* Fusion Engineering and Design **161**:111869 (2020).

[84] C. Ramsauer. *Über den Wirkungsquerschnitt der Gasmoleküle gegenüber langsamen Elektronen.* Annalen der Physik **369**(6):513 (1921).

[85] J. L. Bohn, J. P. Burke, C. H. Greene, H. Wang, P. L. Gould and W. C. Stwalley. *Collisional properties of ultracold potassium: Consequences for degenerate Bose and Fermi gases.* Phys. Rev. A **59**:3660 (1999).

[86] C. D'Errico, M. Zaccanti, M. Fattori, G. Roati, M. Inguscio, G. Modugno and A. Simoni. *Feshbach resonances in ultracold 39K.* New Journal of Physics **9**(7):223–223 (2007).

[87] M. Landini. *A tunable Bose-Einstein condensate for quantum interferometry.* Ph.D. thesis, Universita degli Studi di Trento (2012).

[88] R. Chapurin. *Precise Measurements of Few-Body Physics in Ultracold ^{39}K Bose gas.* Ph.D. thesis, University of Colorado (2019).

[89] D. Comparat, A. Fioretti, G. Stern, E. Dimova, B. L. Tolra and P. Pillet. *Optimized production of large Bose-Einstein condensates.* Physical Review A **73**(4) (2006).

[90] E. Majorana. *Atomi orientati in campo magnetico variabile.* Il Nuovo Cimento (1924-1942) **9**(2):43 (1932).

[91] M. Landini, S. Roy, G. Roati, A. Simoni, M. Inguscio, G. Modugno and M. Fattori. *Direct evaporative cooling of 39K atoms to Bose-Einstein condensation.* Physical Review A **86**(3) (2012).

[92] J. Etrych, G. Martirosyan, A. Cao, J. A. P. Glidden, L. H. Dogra, J. M. Hutson, Z. Hadzibabic and C. Eigen. *Pinpointing Feshbach resonances and testing Efimov universalities in ^{39}K.* Physical Review Research **5**(1) (2023).

[93] C. D'Errico, M. Zaccanti, M. Fattori, G. Roati, M. Inguscio, G. Modugno and A. Simoni. *Feshbach resonances in ultracold ^{39}K.* New Journal of Physics **9**(7):223–223 (2007).

[94] D. S. Petrov. *Three-Boson Problem near a Narrow Feshbach Resonance.* Physical Review Letters **93**(14) (2004).

[95] W. Ketterle and N. V. Druten. *Evaporative Cooling of Trapped Atoms.* volume 37 of *Advances In Atomic, Molecular, and Optical Physics*, pages 181–236. Academic Press (1996).

[96] K. M. O'Hara, M. E. Gehm, S. R. Granade and J. E. Thomas. *Scaling laws for evaporative cooling in time-dependent optical traps.* Phys. Rev. A **64**:051403 (2001).

[97] C. J. Pethick and H. Smith. *Bose-Einstein Condensation in Dilute Gases.* Cambridge University Press, second edition edition (2008). ISBN 978-0-521-84651-6.

[98] F. Dalfovo, S. Giorgini, L. P. Pitaevskii and S. Stringari. *Theory of Bose-Einstein condensation in trapped gases.* Rev. Mod. Phys. **71**:463 (1999).

[99] H. Wagner. *Long-wavelength excitations and the Goldstone theorem in many-particle systems with "broken symmetries".* Zeitschrift für Physik pages 273–299 (1966).

[100] N. D. Mermin and H. Wagner. *Absence of Ferromagnetism or Antiferromagnetism in One- or Two-Dimensional Isotropic Heisenberg Models.* Phys. Rev. Lett. **17**:1133 (1966).

[101] N. D. Mermin. *Crystalline Order in Two Dimensions.* Phys. Rev. **176**:250 (1968).

[102] P. C. Hohenberg. *Existence of Long-Range Order in One and Two Dimensions.* Phys. Rev. **158**:383 (1967).

[103] V. L. Berezinskiĭ. *Destruction of Long-range Order in One-dimensional and Two-dimensional Systems having a Continuous Symmetry Group I. Classical Systems.* Soviet Journal of Experimental and Theoretical Physics **32**:493 (1971).

[104] J. M. Kosterlitz and D. J. Thouless. *Ordering, metastability and phase transitions in two-dimensional systems.* Journal of Physics C: Solid State Physics **6**(7):1181 (1973).

[105] Z. Hadzibabic and J. Dalibard. *Two-dimensional Bose fluids: An atomic physics perspective.* La Rivista del Nuovo Cimento **34**(6):389–434 (2011).

[106] D. Petrov, D. M. Gangardt and G. V. Shlyapnikov. *Low-dimensional trapped gases. Journal de Physique IV (Proceedings)*, volume 116, pages 5–44. EDP sciences (2004).

[107] Z. Hadzibabic, P. Krüger, M. Cheneau, B. Battelier and J. Dalibard. *The Atomic Bose Gas in Flatland.* AIP Conference Proceedings **869**(1):155 (2006).

[108] D. S. Petrov, M. Holzmann and G. V. Shlyapnikov. *Bose-Einstein Condensation in Quasi-2D Trapped Gases.* Physical Review Letters **84**(12):2551 (2000).

[109] L. Chomaz, L. Corman, T. Bienaimé, R. Desbuquois, C. Weitenberg, S. Nascimbène, J. Beugnon and J. Dalibard. *Emergence of coherence via transverse condensation in a uniform quasi-two-dimensional Bose gas.* Nature Communications **6**(1) (2015).

[110] L. Pitaevskii and S. Stringari. *Bose-Einstein Condensation.* Oxford University Press (2003). ISBN 978-0-19-850719-2.

[111] S. K. Adhikari. *Quantum scattering in two dimensions.* American Journal of Physics **54**(4):362 (1986).

[112] D. S. Petrov and G. V. Shlyapnikov. *Interatomic collisions in a tightly confined Bose gas.* Physical Review A **64**(1) (2001).

[113] N. Bogoliubov. *On the theory superfluidity.* J. Phys. (USSR) **11** (1947).

[114] E. P. Gross. *Structure of a quantized vortex in boson systems.* Il Nuovo Cimento (1955-1965) **20**:454 (1961).

[115] L. P. Pitaevskii. *Vortex Lines in an Imperfect Bose Gas.* JETP **13**(2):451 (1961).

[116] A. Görlitz, J. M. Vogels, A. E. Leanhardt, C. Raman, T. L. Gustavson, J. R. Abo-Shaeer, A. P. Chikkatur, S. Gupta, S. Inouye, T. Rosenband and W. Ketterle. *Realization of Bose-Einstein Condensates in Lower Dimensions.* Phys. Rev. Lett. **87**:130402 (2001).

[117] N. L. Smith, W. H. Heathcote, G. Hechenblaikner, E. Nugent and C. J. Foot. *Quasi-2D confinement of a BEC in a combined optical and magnetic potential.* J. Phys. B: At. Mol. Opt. Phys. **38**:223 (2005).

[118] P. Christodoulou, M. Gałka, N. Dogra, R. Lopes, J. Schmitt and Z. Hadzibabic. *Observation of first and second sound in a BKT superfluid.* Nature **594**(7862):191 (2021).

[119] C. Orzel, A. K. Tuchman, M. L. Fenselau, M. Yasuda and M. A. Kasevich. *Squeezed States in a Bose-Einstein Condensate.* Science **291**:2386 (2001).

[120] S. Burger, F. S. Cataliotti, C. Fort, P. Maddaloni, F. Minardi and M. Inguscio. *Quasi-2D Bose-Einstein condensation in an optical lattice.* Europhysics Letters (EPL) **57**(1):1 (2002).

[121] G. Modugno, F. Ferlaino, R. Heidemann, G. Roati and M. Inguscio. *Production of a Fermi gas of atoms in an optical lattice.* Physical Review A **68**(1) (2003).

[122] Z. Hadzibabic, P. Krüger, M. Cheneau, B. Battelier and J. Dalibard. *Berezinskii–Kosterlitz–Thouless crossover in a trapped atomic gas.* Nature **441**(7097):1118 (2006).

[123] T. C. Li, H. Kelkar, D. Medellin and M. G. Raizen. *Real-time control of the periodicity of a standing wave: an optical accordion.* Opt. Express **16**(8):5465 (2008).

[124] S. Al-Assam, R. A. Williams and C. J. Foot. *Ultracold atoms in an optical lattice with dynamically variable periodicity.* Phys. Rev. A **82**:021604 (2010).

[125] J. L. Ville, T. Bienaimé, R. Saint-Jalm, L. Corman, M. Aidelsburger, L. Chomaz, K. Kleinlein, D. Perconte, S. Nascimbène, J. Dalibard and J. Beugnon. *Loading and compression of a single two-dimensional Bose gas in an optical accordion.* Phys. Rev. A **95**:013632 (2017).

[126] K. Hueck, N. Luick, L. Sobirey, J. Siegl, T. Lompe and H. Moritz. *Two-Dimensional Homogeneous Fermi Gases.* Physical Review Letters **120**(6) (2018).

[127] A. L. Gaunt, T. F. Schmidutz, I. Gotlibovych, R. P. Smith and Z. Hadzibabic. *Bose-Einstein Condensation of Atoms in a Uniform Potential.* Physical Review Letters **110**(20) (2013).

[128] N. Navon, R. P. Smith and Z. Hadzibabic. *Quantum gases in optical boxes.* Nature Physics **17**(12):1334 (2021).

[129] F. Gerbier and Y. Castin. *Heating rates for an atom in a far-detuned optical lattice.* Phys. Rev. A **82**:013615 (2010).

[130] S. Friebel, C. D'Andrea, J. Walz, M. Weitz and T. W. Hänsch. *CO2 -laser optical lattice with cold rubidium atoms.* Phys. Rev. A **57**(1):R20 (1998).

[131] T. A. Savard, K. M. O'Hara and J. E. Thpmas. *Laser-noise-induced heating in far-off resonance optical traps.* Phys. Rev. A **56**(2):R1095 (1997).

[132] D. S. Jin, J. R. Ensher, M. R. Matthews, C. E. Wieman and E. A. Cornell. *Collective Excitations of a Bose-Einstein Condensate in a Dilute Gas.* Phys. Rev. Lett. **77**(3):420 (1996).

[133] L. P. Pitaevskii and A. Rosch. *Breathing modes and hidden symmetry of trapped atoms in two dimensions.* Physical Review A **55**(2):R853 (1997).

[134] B. R. Holstein. *Anomalies for pedestrians.* American Journal of Physics **61**:142 (1993).

[135] B. R. Holstein. *Understanding an anomaly.* American Journal of Physics **82**:591 (2014).

[136] M. Olshanii, H. Perrin and V. Lorent. *Example of a Quantum Anomaly in the Physics of Ultracold Gases.* Phys. Rev. Lett. **105**:095302 (2010).

[137] F. Chevy, V. Bretin, P. Rosenbusch, K. W. Madison and J. Dalibard. *Transverse Breathing Mode of an Elongated Bose-Einstein Condensate.* Physical Review Letters **88**(25) (2002).

[138] C. Gao and Z. Yu. *Breathing mode of two-dimensional atomic Fermi gases in harmonic traps.* Physical Review A **86**(4) (2012).

[139] M. Holten, L. Bayha, A. Klein, P. Murthy, P. Preiss and S. Jochim. *Anomalous Breaking of Scale Invariance in a Two-Dimensional Fermi Gas.* Physical Review Letters **121**(12) (2018).

[140] K. M. Hueck. *A homogeneous, two-dimensional Fermi gas.* Ph.D. thesis, University of Hamburg (2017).

[141] Y.-Q. Zou, B. Bakkali-Hassani, C. Maury, E. Le Cerf, S. Nascimbene, J. Dalibard and J. Beugnon. *Tan's two-body contact across the superfluid transition of a planar Bose gas.* Nature Communications **12**(1) (2021).

[142] W. Ketterle, D. Durfee and D. M. Stamper-Kurn. *Making, probing and understanding Bose-Einstein condensates.* arXiv: Condensed Matter arXiv:cond-mat/9904034 (1999).

[143] J. L. Ville, T. Bienaimé, R. Saint-Jalm, L. Corman, M. Aidelsburger, L. Chomaz, K. Kleinlein, D. Perconte, S. Nascimbène, J. Dalibard and J. Beugnon. *Loading and compression of a single two-dimensional Bose gas in an optical accordion.* Physical Review A **95**(1) (2017).

[144] R. Desbuquois, L. Chomaz, T. Yefsah, J. Léonard, J. Beugnon, C. Weitenberg and J. Dalibard. *Superfluid behaviour of a two-dimensional Bose gas.* Nature Physics **8**(9):645–648 (2012).

[145] P. Christodoulou. *Superfluidity in a uniform two-dimensional Bose gas.* Ph.D. thesis, University of Cambridge (2021).

[146] R. J. Fletcher, M. Robert-de Saint-Vincent, J. Man, N. Navon, R. P. Smith, K. G. Viebahn and Z. Hadzibabic. *Connecting Berezinskii-Kosterlitz-Thouless and BEC Phase Transitions by Tuning Interactions in a Trapped Gas.* Physical Review Letters **114**(25) (2015).

[147] C.-L. Hung, X. Zhang, N. Gemelke and C. Chin. *Observation of scale invariance and universality in two-dimensional Bose gases.* Nature **470**(7333):236–239 (2011).

[148] L. W. Clark, A. Gaj, L. Feng and C. Chin. *Collective emission of matter-wave jets from driven Bose–Einstein condensates.* Nature **551**(7680):356–359 (2017).

[149] L. Feng, J. Hu, L. W. Clark and C. Chin. *Correlations in high-harmonic generation of matter-wave jets revealed by pattern recognition.* Science **363**(6426):521–524 (2019).

[150] Z. Zhang, L. Chen, K.-X. Yao and C. Chin. *Transition from an atomic to a molecular Bose–Einstein condensate.* Nature **592**(7856):708–711 (2021).

[151] C.-A. Chen and C.-L. Hung. *Observation of Universal Quench Dynamics and Townes Soliton Formation from Modulational Instability in Two-Dimensional Bose Gases.* Physical Review Letters **125**(25) (2020).

[152] H. Tamura, C.-A. Chen and C.-L. Hung. *Observation of Self-Patterned Defect Formation in Atomic Superfluids–from Ring Dark Solitons to Vortex Dipole Necklaces.* Physical Review X **13**(3) (2023).

[153] T. L. Harte, E. Bentine, K. Luksch, A. J. Barker, D. Trypogeorgos, B. Yuen and C. J. Foot. *Ultracold atoms in multiple radio-frequency dressed adiabatic potentials.* Physical Review A **97**(1) (2018).

[154] A. J. Barker, S. Sunami, D. Garrick, A. Beregi, K. Luksch, E. Bentine and C. J. Foot. *Realising a species-selective double well with multiple-radiofrequency-dressed potentials.* Journal of Physics B: Atomic, Molecular and Optical Physics **53**(15):155001 (2020).

[155] A. J. Barker, S. Sunami, D. Garrick, A. Beregi, K. Luksch, E. Bentine and C. J. Foot. *Coherent splitting of two-dimensional Bose gases in magnetic potentials.* New Journal of Physics **22**(10):103040 (2020).

[156] S. Sunami, V. P. Singh, D. Garrick, A. Beregi, A. J. Barker, K. Luksch, E. Bentine, L. Mathey and C. J. Foot. *Universal scaling of the dynamic BKT transition in quenched 2D Bose gases.* Science **382**(6669):443–447 (2023).

[157] S. Kang, S. W. Seo, J. H. Kim and Y. Shin. *Emergence and scaling of spin turbulence in quenched antiferromagnetic spinor Bose-Einstein condensates.* Physical Review A **95**(5) (2017).

[158] S. W. Seo, B. Ko, J. H. Kim and Y. Shin. *Observation of vortex-antivortex pairing in decaying 2D turbulence of a superfluid gas.* Scientific Reports **7**(1) (2017).

[159] Y. Lim, J. Goo, H. Kwak and Y. Shin. *Large-area ^{87}Rb Bose-Einstein condensate in a clipped-Gaussian optical dipole trap.* Physical Review A **103**(6) (2021).

[160] S. Huh, K. Kim, K. Kwon and J.-y. Choi. *Observation of a strongly ferromagnetic spinor Bose-Einstein condensate.* Physical Review Research **2**(3) (2020).

[161] S. Huh, K. Mukherjee, K. Kwon, J. Seo, J. Hur, S. I. Mistakidis, H. R. Sadeghpour and J.-y. Choi. *Universality class of a spinor Bose–Einstein condensate far from equilibrium.* Nature Physics **20**(3):402–408 (2024).

[162] C. Viermann, M. Sparn, N. Liebster, M. Hans, E. Kath, A. Parra-López, M. Tolosa-Simeón, N. Sánchez-Kuntz, T. Haas, H. Strobel, S. Floerchinger and M. K. Oberthaler. *Quantum field simulator for dynamics in curved spacetime.* Nature **611**(7935):260–264 (2022).

[163] J.-y. Choi, S. W. Seo and Y.-i. Shin. *Observation of Thermally Activated Vortex Pairs in a Quasi-2D Bose Gas.* Physical Review Letters **110**(17) (2013).

[164] P. Cladé, C. Ryu, A. Ramanathan, K. Helmerson and W. Phillips. *Observation of a 2D Bose Gas: From Thermal to Quasicondensate to Superfluid.* Physical Review Letters **102**(17) (2009).

[165] P. Krüger, Z. Hadzibabic and J. Dalibard. *Critical Point of an Interacting Two-Dimensional Atomic Bose Gas.* Physical Review Letters **99**(4) (2007).

[166] S. P. Rath, T. Yefsah, K. J. Günter, M. Cheneau, R. Desbuquois, M. Holzmann, W. Krauth and J. Dalibard. *Equilibrium state of a trapped two-dimensional Bose gas.* Physical Review A **82**(1) (2010).

[167] T. Yefsah, R. Desbuquois, L. Chomaz, K. J. Günter and J. Dalibard. *Exploring the Thermodynamics of a Two-Dimensional Bose Gas.* Physical Review Letters **107**(13) (2011).

[168] R. Desbuquois, T. Yefsah, L. Chomaz, C. Weitenberg, L. Corman, S. Nascimbène and J. Dalibard. *Determination of Scale-Invariant Equations of State without Fitting Parameters: Application to the Two-Dimensional Bose Gas Across the Berezinskii-Kosterlitz-Thouless Transition.* Physical Review Letters **113**(2) (2014).

[169] C. D. Rossi, R. Dubessy, K. Merloti, M. d. G. d. Herve, T. Badr, A. Perrin, L. Longchambon and H. Perrin. *Probing superfluidity in a quasi two-dimensional Bose gas through its local dynamics.* New Journal of Physics **18**(6):062001 (2016).

[170] S. Sunami, V. Singh, D. Garrick, A. Beregi, A. Barker, K. Luksch, E. Bentine, L. Mathey and C. Foot. *Observation of the Berezinskii-Kosterlitz-Thouless Transition in a Two-Dimensional Bose Gas via Matter-Wave Interferometry.* Physical Review Letters **128**(25) (2022).

[171] J. Goo, Y. Lee, Y. Lim, D. Bae, T. Rabga and Y. Shin. *Universal Early Coarsening of Quenched Bose Gases.* Physical Review Letters **128**(13) (2022).

[172] J. Ville, R. Saint-Jalm, E. Le Cerf, M. Aidelsburger, S. Nascimbène, J. Dalibard and J. Beugnon. *Sound Propagation in a Uniform Superfluid Two-Dimensional Bose Gas.* Physical Review Letters **121**(14) (2018).

[173] G. Gauthier, M. T. Reeves, X. Yu, A. S. Bradley, M. A. Baker, T. A. Bell, H. Rubinsztein-Dunlop, M. J. Davis and T. W. Neely. *Giant vortex clusters in a two-dimensional quantum fluid.* Science **364**(6447):1264–1267 (2019).

[174] O. R. Stockdale, M. T. Reeves, X. Yu, G. Gauthier, K. Goddard-Lee, W. P. Bowen, T. W. Neely and M. J. Davis. *Universal dynamics in the expansion of vortex clusters in a dissipative two-dimensional superfluid.* Physical Review Research **2**(3) (2020).

[175] L. Corman, L. Chomaz, T. Bienaimé, R. Desbuquois, C. Weitenberg, S. Nascimbène, J. Dalibard and J. Beugnon. *Quench-Induced Supercurrents in an Annular Bose Gas.* Physical Review Letters **113**(13) (2014).

[176] M. Kim, T. Rabga, Y. Lee, J. Goo, D. Bae and Y. Shin. *Suppression of spontaneous defect formation in inhomogeneous Bose gases.* Physical Review A **106**(6) (2022).

[177] T. Rabga, Y. Lee, D. Bae, M. Kim and Y. Shin. *Variations of the Kibble-Zurek scaling exponents of trapped Bose gases.* Physical Review A **108**(2) (2023).

[178] J. Goo, Y. Lim and Y. Shin. *Defect Saturation in a Rapidly Quenched Bose Gas.* Physical Review Letters **127**(11) (2021).

[179] Y. Lim, Y. Lee, J. Goo, D. Bae and Y. Shin. *Vortex shedding frequency of a moving obstacle in a Bose–Einstein condensate.* New Journal of Physics **24**(8):083020 (2022).

[180] W. J. Kwon, J. H. Kim, S. W. Seo and Y. Shin. *Observation of von Kármán Vortex Street in an Atomic Superfluid Gas.* Physical Review Letters **117**(24) (2016).

[181] S. P. Johnstone, A. J. Groszek, P. T. Starkey, C. J. Billington, T. P. Simula and K. Helmerson. *Evolution of large-scale flow from turbulence in a two-dimensional superfluid.* Science **364**(6447):1267–1271 (2019).

[182] W. J. Kwon, G. Moon, J.-y. Choi, S. W. Seo and Y.-i. Shin. *Relaxation of superfluid turbulence in highly oblate Bose-Einstein condensates.* Physical Review A **90**(6) (2014).

[183] M. T. Reeves, K. Goddard-Lee, G. Gauthier, O. R. Stockdale, H. Salman, T. Edmonds, X. Yu, A. S. Bradley, M. Baker, H. Rubinsztein-Dunlop, M. J. Davis and T. W. Neely. *Turbulent Relaxation to Equilibrium in a Two-Dimensional Quantum Vortex Gas.* Physical Review X **12**(1) (2022).

[184] M. Gałka, P. Christodoulou, M. Gazo, A. Karailiev, N. Dogra, J. Schmitt and Z. Hadzibabic. *Emergence of Isotropy and Dynamic Scaling in 2D Wave Turbulence in a Homogeneous Bose Gas.* Physical Review Letters **129**(19) (2022).

[185] A. Karailiev, M. Gazo, M. Gałka, C. Eigen, T. Satoor and Z. Hadzibabic. *Observation of an inverse turbulent-wave cascade in a driven quantum gas.* arXiv preprint arXiv:2405.01537 (2024).

[186] D. H. White, T. A. Haase, D. J. Brown, M. D. Hoogerland, M. S. Najafabadi, J. L. Helm, C. Gies, D. Schumayer and D. A. W. Hutchinson. *Observation of two-dimensional Anderson localisation of ultracold atoms.* Nature Communications **11**(1) (2020).

[187] L. Corman, J. L. Ville, R. Saint-Jalm, M. Aidelsburger, T. Bienaimé, S. Nascimbène, J. Dalibard and J. Beugnon. *Transmission of near-resonant light through a dense slab of cold atoms.* Physical Review A **96**(5) (2017).

[188] R. Saint-Jalm, M. Aidelsburger, J. L. Ville, L. Corman, Z. Hadzibabic, D. Delande, S. Nascimbene, N. Cherroret, J. Dalibard and J. Beugnon. *Resonant-light diffusion in a disordered atomic layer.* Physical Review A **97**(6) (2018).

[189] Z. Zhang, K.-X. Yao, L. Feng, J. Hu and C. Chin. *Pattern formation in a driven Bose–Einstein condensate.* Nature Physics **16**(6):652–656 (2020).

[190] N. Liebster, M. Sparn, E. Kath, K. Fujii, S. Görlitz, T. Enss, H. Strobel and M. K. Oberthaler. *Emergence of crystalline steady state in a driven superfluid.* arXiv preprint arXiv:2309.03792 (2023).

[191] C.-A. Chen, S. Khlebnikov and C.-L. Hung. *Observation of Quasiparticle Pair Production and Quantum Entanglement in Atomic Quantum Gases Quenched to an Attractive Interaction.* Physical Review Letters **127**(6) (2021).

[192] C.-A. Chen and C.-L. Hung. *Observation of Scale Invariance in Two-Dimensional Matter-Wave Townes Solitons.* Physical Review Letters **127**(2) (2021).

[193] H. Tamura, S. Khlebnikov, C.-A. Chen and C.-L. Hung. *Observation of self-oscillating supersonic flow across an acoustic horizon in two dimensions.* arXiv preprint arXiv:2304.10667 (2024).

[194] M. Gazo, A. Karailiev, T. Satoor, C. Eigen, M. Gałka and Z. Hadzibabic. *Universal Coarsening in a Homogeneous Two-Dimensional Bose Gas.* arXiv preprint arXiv:2312.09248 (2024).

[195] R. Saint-Jalm, P. Castilho, E. Le Cerf, B. Bakkali-Hassani, J.-L. Ville, S. Nascimbene, J. Beugnon and J. Dalibard. *Dynamical Symmetry and Breathers in a Two-Dimensional Bose Gas.* Physical Review X **9**(2) (2019).

[196] G. E. Marti and D. M. Stamper-Kurn. *Spinor Bose-Einstein gases.* arXiv: Quantum Gases arXiv:1511.01575 (2015).

[197] J.-y. Choi, W. J. Kwon and Y.-i. Shin. *Observation of Topologically Stable 2D Skyrmions in an Antiferromagnetic Spinor Bose-Einstein Condensate*. Phys. Rev. Lett. **108**:035301 (2012).

[198] J. yoon Choi, W. J. Kwon, M. Lee, H. Jeong, K. An and Y. il Shin. *Imprinting Skyrmion spin textures in spinor Bose–Einstein condensates*. New Journal of Physics **14**(5):053013 (2012).

[199] J.-y. Choi, S. Kang, S. W. Seo, W. J. Kwon and Y.-i. Shin. *Observation of a Geometric Hall Effect in a Spinor Bose-Einstein Condensate with a Skyrmion Spin Texture*. Physical Review Letters **111**(24) (2013).

[200] K. Kim, J. Hur, S. Huh, S. Choi and J.-y. Choi. *Emission of Spin-Correlated Matter-Wave Jets from Spinor Bose-Einstein Condensates*. Physical Review Letters **127**(4) (2021).

[201] S. Kang, S. W. Seo, H. Takeuchi and Y. Shin. *Observation of Wall-Vortex Composite Defects in a Spinor Bose-Einstein Condensate*. Physical Review Letters **122**(9) (2019).

[202] J. H. Kim, S. W. Seo and Y. Shin. *Critical Spin Superflow in a Spinor Bose-Einstein Condensate*. Physical Review Letters **119**(18) (2017).

[203] B. Bakkali-Hassani, C. Maury, Y.-Q. Zou, E. Le Cerf, R. Saint-Jalm, P. Castilho, S. Nascimbene, J. Dalibard and J. Beugnon. *Realization of a Townes Soliton in a Two-Component Planar Bose Gas*. Physical Review Letters **127**(2) (2021).

[204] J. H. Kim, D. Hong and Y. Shin. *Observation of two sound modes in a binary superfluid gas*. Physical Review A **101**(6) (2020).

[205] J. M. Gerton, D. Strekalov, I. Prodan and R. G. Hulet. *Direct observation of growth and collapse of a Bose–Einstein condensate with attractive interactions*. Nature **408**(6813):692–695 (2000).

[206] E. A. Donley, N. R. Claussen, S. L. Cornish, J. L. Roberts, E. A. Cornell and C. E. Wieman. *Dynamics of collapsing and exploding Bose–Einstein condensates*. Nature **412**(6844):295–299 (2001).

[207] C. Eigen, A. L. Gaunt, A. Suleymanzade, N. Navon, Z. Hadzibabic and R. P. Smith. *Observation of Weak Collapse in a Bose-Einstein Condensate*. Physical Review X **6**(4) (2016).

[208] E. Timmermans. *Phase Separation of Bose-Einstein Condensates.* Phys. Rev. Lett. **81**:5718 (1998).

[209] D. Petrov and G. Astrakharchik. *Ultradilute Low-Dimensional Liquids.* Physical Review Letters **117**(10) (2016).

[210] P. Naidon and D. Petrov. *Mixed Bubbles in Bose-Bose Mixtures.* Physical Review Letters **126**(11) (2021).

[211] B. Bakkali-Hassani and J. Dalibard. *Townes soliton and beyond: Non-miscible Bose mixtures in 2D.* arXiv:2210.14045 (2022).

[212] L. D. Landau. *Über die Bewegung der Elektronen in Kristallgitter.* Phys. Z. Sowjetunion **3**:644 (1933).

[213] S. Pekar. *Autolocalization of the electron in an inertially polarizable dielectric medium.* Zh. Eksp. Teor. Fiz **16**:335 (1946).

[214] L. D. Landau and S. I. Pekar. *Effektivnaya Massa Polyarona.* Zhurnal Eksperimentalnoi i Teoreticheskoi Fiziki **18(5)**:419 (1948).

[215] M. E. Gershenson, V. Podzorov and A. F. Morpurgo. *Colloquium: Electronic transport in single-crystal organic transistors.* Rev. Mod. Phys. **78**:973 (2006).

[216] E. Dagotto. *Correlated electrons in high-temperature superconductors.* Rev. Mod. Phys. **66**:763 (1994).

[217] P. W. Higgs. *Broken Symmetries and the Masses of Gauge Bosons.* Phys. Rev. Lett. **13**:508 (1964).

[218] J. Kondo. *Resistance Minimum in Dilute Magnetic Alloys.* Progress of Theoretical Physics **32**(1):37 (1964).

[219] F. Böttcher, J.-N. Schmidt, J. Hertkorn, K. S. H. Ng, S. D. Graham, M. Guo, T. Langen and T. Pfau. *New states of matter with fine-tuned interactions: quantum droplets and dipolar supersolids.* Reports on Progress in Physics **84**(1):012403 (2020).

[220] T. D. Lee, K. Huang and C. N. Yang. *Eigenvalues and Eigenfunctions of a Bose System of Hard Spheres and Its Low-Temperature Properties.* Phys. Rev. **106**:1135 (1957).

[221] G. Semeghini, G. Ferioli, L. Masi, C. Mazzinghi, L. Wolswijk, F. Minardi, M. Modugno, G. Modugno, M. Inguscio and M. Fattori. *Self-Bound Quantum Droplets of Atomic Mixtures in Free Space.* Phys. Rev. Lett. **120**:235301 (2018).

[222] H. Kadau, M. Schmitt, M. Wenzel, C. Wink, T. Maier, I. Ferrier-Barbut and T. Pfau. *Observing the Rosensweig instability of a quantum ferrofluid.* Nature **530**(7589):194–197 (2016).

[223] I. Ferrier-Barbut, H. Kadau, M. Schmitt, M. Wenzel and T. Pfau. *Observation of Quantum Droplets in a Strongly Dipolar Bose Gas.* Phys. Rev. Lett. **116**:215301 (2016).

[224] F. Böttcher, M. Wenzel, J.-N. Schmidt, M. Guo, T. Langen, I. Ferrier-Barbut, T. Pfau, R. Bombín, J. Sánchez-Baena, J. Boronat and F. Mazzanti. *Dilute dipolar quantum droplets beyond the extended Gross-Pitaevskii equation.* Phys. Rev. Res. **1**:033088 (2019).

[225] G. Spada, S. Pilati and S. Giorgini. *Quantum droplets in two-dimensional Bose mixtures at finite temperature.* arXiv preprint arXiv:2405.09368 (2024).

[226] Y. V. Kartashov and D. A. Zezyulin. *Enhanced mobility of quantum droplets in periodic lattices.* Chaos, Solitons & Fractals **182**:114838 (2024).

[227] Y. Fei, X. Du, X.-L. Chen and Y. Zhang. *Collective excitations in two-dimensional harmonically trapped quantum droplets.* Physical Review A **109**(5) (2024).

[228] S. Nikolaou, G. M. Kavoulakis and M. Ögren. *Rotating quantum droplets confined in an anharmonic potential.* Physical Review A **109**(4) (2024).

[229] T. A. Flynn, N. A. Keepfer, N. G. Parker and T. P. Billam. *Harmonically trapped imbalanced quantum droplets.* Phys. Rev. Res. **6**:013209 (2024).

[230] K. Abbas and A. Boudjemâa. *Quantum liquid droplets in Bose mixtures with weak disorder.* Physical Review A **107**(3) (2023).

[231] Y. Hu, Y. Fei, X.-L. Chen and Y. Zhang. *Collisional dynamics of symmetric two-dimensional quantum droplets.* Frontiers of Physics **17**(6) (2022).

[232] P. Zin, M. Pylak, T. Wasak, M. Gajda and Z. Idziaszek. *Quantum Bose-Bose droplets at a dimensional crossover.* Physical Review A **98**(5) (2018).

[233] Y. Ma and X. Cui. *Quantum-fluctuation-driven dynamics of droplet splashing, recoiling, and deposition in ultracold binary Bose gases.* Phys. Rev. Res. **5**:013100 (2023).

[234] E. Shamriz, Z. Chen and B. A. Malomed. *Suppression of the quasi-two-dimensional quantum collapse in the attraction field by the Lee-Huang-Yang effect.* Phys. Rev. A **101**:063628 (2020).

[235] Y. Kagan, E. L. Surkov and G. V. Shlyapnikov. *Evolution and Global Collapse of Trapped Bose Condensates under Variations of the Scattering Length.* Phys. Rev. Lett. **79**:2604 (1997).

[236] C. Sulem and P.-L. Sulem. *The Nonlinear Schrödinger Equation: Self-Focusing and Wave Collapse.* Springer New York, NY (1999). ISBN 978-0-387-98611-1.

[237] D. Kobyakov, V. Bychkov, E. Lundh, A. Bezett, V. Akkerman and M. Marklund. *Interface dynamics of a two-component Bose-Einstein condensate driven by an external force.* Phys. Rev. A **83**:043623 (2011).

[238] R. Blaauwgeers, V. B. Eltsov, G. Eska, A. P. Finne, R. P. Haley, M. Krusius, J. J. Ruohio, L. Skrbek and G. E. Volovik. *Shear Flow and Kelvin-Helmholtz Instability in Superfluids.* Physical Review Letters **89**(15) (2002).

[239] H. Takeuchi, N. Suzuki, K. Kasamatsu, H. Saito and M. Tsubota. *Quantum Kelvin-Helmholtz instability in phase-separated two-component Bose-Einstein condensates.* Phys. Rev. B **81**:094517 (2010).

[240] D. Sharp. *An overview of Rayleigh-Taylor instability.* Physica D: Nonlinear Phenomena **12**(1):3 (1984).

[241] S. Gautam and D. Angom. *Rayleigh-Taylor instability in binary condensates.* Phys. Rev. A **81**:053616 (2010).

[242] A. Bezett, V. Bychkov, E. Lundh, D. Kobyakov and M. Marklund. *Magnetic Richtmyer-Meshkov instability in a two-component Bose-Einstein condensate.* Phys. Rev. A **82**:043608 (2010).

Eidesstattliche Versicherung

Hiermit versichere ich an Eides statt, die vorliegende Dissertationsschrift selbst verfasst und keine anderen als die angegebenen Hilfsmittel und Quellen benutzt zu haben.

Sofern im Zuge der Erstellung der vorliegenden Dissertationsschrift generative Künstliche Intelligenz (gKI) basierte elektronische Hilfsmittel verwendet wurden, versichere ich, dass meine eigene Leistung im Vordergrund stand und dass eine vollständige Dokumentation aller verwendeten Hilfsmittel gemäß der Guten wissenschaftlichen Praxis vorliegt. Ich trage die Verantwortung für eventuell durch die gKI generierte fehlerhafte oder verzerrte Inhalte, fehlerhafte Referenzen, Verstöße gegen das Datenschutz- und Urheberrecht oder Plagiate.

Hamburg, den 27.06.2024

Unterschrift der Doktorandin / des Doktoranden